ISN 02-25

Université Joseph Fourier - Grenoble I
Formation doctorale en physique

THÈSE

présentée à l'Institut des Sciences Nucléaires de Grenoble
pour obtenir le titre de

Docteur en Sciences

Spécialité: Astrophysique des particules

par

Ching-Yuan HUANG

Étude du flux d'antiprotons d'origine atmosphérique au voisinage de la terre

Soutenue le 14 mai 2002 devant le jury composé de:

M.	BUÉNERD:	Directeur de thèse
J.	CARBONELL:	Rapporteur
J.	COLLOT:	Président
A.	MENCHACA-ROCHA:	Rapporteur
C.	TAO:	Rapporteur

Thèse préparée à l'Institut des Sciences Nucléaires de Grenoble, IN2P3/CNRS - UJF

ISN 02-25

Université Joseph Fourier - Grenoble I
Doctoral Formation in Physics

THESIS

presented at Institut des Sciences Nucléaires de Grenoble to obtain the title of

Doctor of Sciences

Speciality: Particle Astrophysics

by

Ching-Yuan HUANG

Study of Antiproton Flux of Atmospheric Origin in Neighbourhood of the Earth

Defend on the 14 May 2002 in the Presence of the Committee of:

M.	BUÉNERD:	Supervisor of Thesis
J.	CARBONELL:	Reporter
J.	COLLOT:	President
A.	MENCHACA-ROCHA:	Reporter
C.	TAO:	Reporter

Thesis Prepared at Institut des Sciences Nucléaires de Grenoble
IN2P3/CNRS - UJF

夫水之積也不厚則載大舟也無力覆杯水於坳堂之上則芥為之舟置杯焉則膠水淺而舟大也風之積也不厚則負大翼也無力故九萬里則風斯在下矣而後乃今培風背負青天而莫之夭閼者而後乃今將圖南

莊子　逍遙遊

If there is not the sufficient depth, water will not float large ships. Upset a cupful into a hole in the yard, and a mustard-seed will be the boat. But, if one trys to float the cup, it will be grounded, due to the disproportion between the water and the vessel. So, for the air, if there is not the sufficient depth, it cannot support large wings. And, for this bird, a depth of ninety thousand li is essential to bear it up. Then, gliding upon the wind, with nothing save the clear sky above, and no obstacles on the way, it could start upon its journey to the extreme south.

A Happy Excursion
Chuang Tzu, 369-286 B.C.

Résumé

Cette thèse a pour objet l'étude de la production d'antiproton dans l'atmosphère. Une paramétrisation de la section efficace inclusive pour la production d'antiprotons dans les collisions $p + p$ et $p + A$ est présentée, basée sur les règles de comptage de quarks, la phénoménologie de Regge et l'ajustement aux données. Cette paramétrisation est en accord avec les données expérimentales pour une énergie incidente du nucléon au moins jusqu'à 24 GeV/n dans le laboratoire. Selon l'analyse de la distribution de la multiplicité moyenne d'antiprotons, cette paramétrisation peut être étendue sa validité jusqu'au moins $\sqrt{s} \simeq 25$ GeV dans le centre de masse. Avec cette paramétrisation, le modèle des nucléons touchés est appliqué pour obtenir la section efficace de production d'antiprotons lors d'une collision $A + A$.

Le flux atmosphérique d'antiprotons aux altitudes des ballons et des satellites est calculé en incluant les protons et héliums cosmiques. Les collisions générées par l'hélium contribuent pour environ 30% au flux total d'antiprotons atmosphérique. Pour l'étude de l'origine exotique d'antiprotons, par exemple l'annihilation de la matière sombre supersymétrique (les neutralinos) et l'évaporation des trous noirs primordiaux, les énergies incidentes des particules cosmiques jusqu'à $E = 200$ GeV/n contribuent le plus magnifiquement à la production d'antiprotons atmosphériques.

Il est montré que le flux atmosphérique d'antiprotons utilisé pour corriger le flux d'antiprotons au dessus de l'atmosphère est sous-estimé dans certains travaux précédents. Dans ce travail, le flux d'antiprotons au dessus de l'atmosphère est donc diminué de 10-15% par rapport au résultat original dans le domaine d'énergie $E_k > 1$ GeV. Une expérience de mesure d'antiprotons au sol est proposée pour valider la justesse de la production d'antiprotons calculés par les différents groupes. Les résultats de l'expérience BESS 1999 à l'altitude de 2.77 km ont confirmé la justesse de ce travail. À l'altitude d'AMS, le flux d'antiprotons mesuré par cette expérience dans la région polaire est pratiquement exclusivement constitué d'antiprotons cosmiques, avec une composante de seulement 2-3% d'antiprotons atmosphériques.

Il est observé que, même à très haute altitude, quelques milliers de kilomètres par exemple, il existe encore un flux résiduel d'antiprotons atmosphériques dont les trajectoires sont très compliquées et ne peuvent pas être bien expliquées au moyen des variables habituelles.

Finalement, le flux atmosphérique de protons dans l'atmosphère est calculé. La déviation entre les calculs et les données ainsi que les origines possibles de cette déviation sont discutées.

Mots clés: flux d'antiprotons secondaires au dessus de l'atmosphère, section efficace inclusive, règles de comptage de quarks, phénoménologie de Regge, multiplicité moyenne, modèle des nucléons touchés, matière sombre supersymétrique, neutralino, trous noirs primordiaux.

Abstract

Secondary atmospheric antiprotons are studied. A parametrisation of the inclusive cross section for the $\bar{p}$ production in $p+p$ and $p+A$ collisions is developed, based on the Quark Counting Rule, the Regge Phenomenology and data fitting. This parametrisation is shown to have a good agreement with experimental data for incident nucleon energy at least up to 24 GeV/n in the laboratory frame. By the analysis of the $\bar{p}$ mean multiplicity distribution, this parametrisation can extend at least up to the centre of mass energy $\sqrt{s} \simeq 25$ GeV. Based on this parametrisation, the Wounded Nucleon Model is used to obtain the $\bar{p}$ production cross section in $A+A$ collisions.

By including cosmic protons and heliums, the atmospheric $\bar{p}$ flux at high balloon and satellite altitudes are calculated. The He-induced collisions are shown to contribute about 30% in the total secondary atmospheric $\bar{p}$ flux. It is observed that, for the interest of the $\bar{p}$ exotic origins such as the annihilation of supersymmetric dark matter (neutralino) and the evaporation of primordial black holes, the energy range up to $E = 200$ GeV/n for cosmic particles generating the secondary atmospheric $\bar{p}$ production is the most important.

It is shown that the secondary atmospheric $\bar{p}$ flux used to correct the $\bar{p}$ flux at TOA was underestimated in the previous works. In this work, the $\bar{p}$ flux at TOA is then reduced by 10-15% compared to the previous results, for the energy range $E_k > 1$ GeV. A $\bar{p}$ measurement experiment at the ground level is used to test the accuracy of secondary atmospheric $\bar{p}$ production calculated by different works. The résults of the BESS 1999 experiment at 2.77 km have confirmed the correctness of the present approach. At the AMS altitude, it is shown that the $\bar{p}$ flux measured by this experiment is almost the exact $\bar{p}$ flux at TOA, with only 2-3% of the atmospheric $\bar{p}$ component.

It is found that, even at very high altitudes, thousands of kilometres above the Earth, there still exists some residual atmospheric antiproton flux with very complex trajectories which cannot be well explained by the usual variables.

Finally, the secondary atmospheric p flux at low altitudes are calculated. The deviation between the calculation and the measurements and the possible origins of this deviation are discussed. Comments, remarks and conclusions are given.

Keywords: secondary antiproton flux, Top of Atmosphere (TOA), inclusive cross section, Quark Counting Rule, Regge Phenomenology, mean multiplicity, Wounded Nucleon Model, supersymmetric dark matter, neutralino, primordial black holes, trapped particles, Earth magnetosphere

Remerciements

Tout d'abord, je remercie Joël Chauvin de m'avoir accueilli au sein de l'Institut des Sciences Nucléaires de Grenoble.

Je tiens à exprimer toute ma gratitude à nôtre capitaine du groupe d'AMS, Michel Buénerd, pour avoir dirigé mon travail pendant ma thèse. Merci à lui pour ses entraîements sévères et aussi pour m'avoir toujours appris à penser logiquement physiquement.

De plus, je voudrais remercier les membres de mon jury: Jaume Carbonell, Johann Collot, Arturo Menchaca-Rocha et Charling Tao, qui ont bien lu mon manuscrit. Les commentaires, corrections et aussi les questions qu'ils ont soulevées ont premis d'améliorer la qualité de cette thèse.

Je veux bien aussi remercier James M. Nester, professeur au Department de Physique, National Central University Taïwan. Prof. Nester m'a extrêmement encouragé à venir en France; en conséquence, j'ai changé mon sujet d'étude de la physique mathématique à l'astrophysique des particules.

Je tiens à remercier les personnes avec qui j'ai pu collaborer sur AMS. Un grand merci à Laurent Derome, pour sa générosité de la collaboration pendant le progrès de mon travail. Je souhaite particulièrement remercier Aurélien Barrau et Gaëlle Boudoul, pour leurs gentillesses ainsi leurs encouragements. Je veux bien aussi manifester ma gratitude à eux pour leur enthousiasme de m'avior aidé à préparer le pot après la soutenance. De plus, je tiens à faire des compliments à Aurélien pour ses commentaires importants sur les chapitres de l'astrophysique des rayonnements cosmiques et la cosmologie de cette thèse. Je veux bien remercier Frédéric Mayet et Thomas Thuillier, pour leur patience et leur aide tout au début de ma arrivée. Un grand merci particulier va aussi à Frédéric pour sa enthousiasme et les discussions entre nous. Il est très gentil de m'appeler sur le lien entre nos travaux.

Pour les autres collègues à Grenoble, je tiens à exprimer mes compliments à Bruny Baret, Rémy Duperray, Konstantin Protassov, Cécile Renault et Marciano Vargas-Trevino, pour leur sympathie et leur gentillesse. Ils n'avaient jamais perdu leur patience contre mon mauvais français. J'avais certainement du plaisir à travailler à Grenoble.

Je dois aussi remercier Madame Claudine Tur, la bibiothécaire de l'Institut des Sciences Nucléaires de Grenoble, qui m'avait aidé à chercher quelques articles anomaux.

Je tiens à découvrir mes compliments à quelques personnes à Taïwan: mon meilleur ami Chung-Heng, et les familles de Fung-Ju, Madame Lin, Da-J et 2-J, pour leurs mille gentillesses et leurs encouragements depuis longtemps. Je me réjouis des amitiés avec Chung-Heng et ainsi de nôtre même intérêt à nos études individuelles de la philosophie

et de la science. Je remercie les familles de Fang-Ju qui m'avaient tout de même fait la gentillesse depuis que Fang-Ju est partie pour le monde avec Dieu.

Enfin, je voudrais exprimer toute ma gratitude la plus profonde à mes bien-aimés familles et Tien pour leur ferme soutien et leur confiance inconditionnelle et continue. La gratitude à mon coeur est au-dessus de toute parole. Je dédie donc cette thèse à mes familles.

Acknowledgements

At first, I would like to thank Joël Chauvin, Director of the Institut des Sciences Nucléaires de Grenoble, for his reception of my doctoral work.

I am deeply indebted to my supervisor, Michel Buénerd, for his helpful supervision and instruction. He had helped find the right direction for my work. His careful reading and also the corrections of my manuscript are greatly appreciated. I have benefited a lot from his severe requirement and training. I appreciate that he always teaches and reminds me to think physically logically.

I also like to express with appreciation to all the members of the committee of my thesis: Jaume Carbonell, Johann Collot, Arturo Menchaca-Rocha and Charling Tao, for their careful reading of my manuscript. Their comments, corrections and questions as well have increased the quality of this thesis.

I also greatly appreciate James M. Nester, professor at Department of Physics, National Central University Taiwan. Because of his encouragement, I came to France to undertake the work on a new field, switching my subject from Mathematical Physics to Particle Astrophysics.

I also like to record my compliments to some people at Grenoble. My thanks go especially to Laurent Derome, Aurélien Barrau, Gaëlle Boudoul, Frédéric Mayet and Thomas Thuillier. I thank Laurent for his generosity of helping me during the progress of my work and also the collaboration. I am thankful to Aurélien and Gaëlle, for their kindly and generous concerns and encouragement during this period. I am also grateful for their enthusiasm for the preparation of the party after the defense of my thesis. In addition, I appreciate Aurélien especially for his important comments on the chapters of Cosmic Ray Astrophysics and Cosmology in this thesis. I thank Frédéric and Thomas for their patience and help at early stage after my arrival. A grand appreciation goes to Frédéric for his enthusiasm for the discussions between us and also his reminding me to have a look at his work together with mine.

For other colleagues at Grenoble, my thanks go to Bruny Baret, Rémy Duperray, Konstantin Protassov, Cécile Renault and Marciano Vargas-Trevino, for their kindness and patience of bearing my awkward French. It is really a great pleasure to work here at Grenoble.

I should also convey my thanks to Madame Claudine Tur, the librarian of the Institut des Sciences Nucléaires de Grenoble, for her kindness and effort of looking for some hard-to-get articles for me.

For those people at Taiwan, I would like to express my compliments to my best friend,

Chung-Heng, and Fang-Ju's families- Madame Lin, Da-J and 2-J, for their long-term concerns and encouragement. Although the subjects of Chung-Heng's and mine are quite different from each other, due to our friendship and interest, there still exists a dialogue window for us between philosophy and science. I appreciate that Fang-Ju's families still have kept their concerns about me since Fang-Ju was recalled by God years ago.

Finally, I would like to express my deepest gratitude to my beloved families and Tien for their unconditional and continuous trust and support. They have accompanied me for a long journey, from Taiwan to England, and then from England to France. The gratitude in my heart is beyond the words which could be spoken out. I am grateful to dedicate this thesis to them.

Contents

Chapter 1

Introduction

The study of the particle populations in the Earth environment has been a field of intense research activity in the last few decades [?]. After a short-term seclusion, this field has returned to its renaissance of research interest. This is attributed to the improvement of detector and experimental techniques in both balloon and satellite experiments. Current experiments, such as balloon-borne IMAX, MASS, HEAT, BESS, CAPRICE and space-borne AMS, have opened, especially the latter, new prospects for data with good quantity and quality, thus allowing a new generation of high precision studies of the interactions of cosmic ray particles in the atmosphere and also of particle dynamics in the magnetosphere.

Antiprotons are a rare component of cosmic rays. The origin of cosmic antiprotons has been attracting a lot of attention since their first observation reported by Golden *et al.* in 1979 [?]. The major part of cosmic antiprotons is believed to be the interaction products of the high energy cosmic ray particles with the interstellar media in our Galaxy. These antiprotons are called secondary galactic. In addition to the secondary products, other antiproton contributions of primary origin are of great interest: the annihilation products of supersymmetric dark matter (neutralinos) spreading in the Galactic halo [?, ?, ?] and the evaporation products of primordial black holes formed in the early epoch of our Universe [?, ?]. With these speculations, their contributions to the observed $\bar{p}$ flux can be evaluated. And, the distinctive spectral shape of the observed $\bar{p}$ flux with a maximum at 2 GeV and a sharp decrease towards lower energies can be used as a unique probe of the antiproton origin.

In measuring the $\bar{p}$ flux in the neighbourhood of the Earth, antiprotons have to be distinguished from a large background of e^- and shortlived μ^- and π^-, which are produced by interacting cosmic ray particles with atmospheric nuclei. This difficulty can be overcome by the improvement in the identification techniques of the detectors currently used. In addition, the measured $\bar{p}$ flux is in fact a superposition of cosmic ray antiprotons and a significant contribution of secondary atmospheric antiprotons produced from the collisions of cosmic ray particles with atmospheric nuclei. So, a correction for the production of secondary atmospheric antiprotons may be required as to obtain the cosmic $\bar{p}$ flux. Both secondary galactic antiprotons and secondary atmospheric antiprotons are

produced by the same mechanism. Thus, an important input for such a correction in order to obtain the cosmic $\bar{p}$ flux and also the evaluation of secondary galactic $\bar{p}$ flux to verify the $\bar{p}$ primary origins is the $\bar{p}$ production cross section in nuclear collisions. Unfortunately, unlike $p + p$ collisions, experimental data for the $\bar{p}$ production on nuclei are scarce in the energy range of interest and, the available parametrisation [?] shows a poor agreement with the available experimental data.

Therefore, the first and the most basic work for such issues is to obtain a good expression of the $\bar{p}$ production cross section in nuclear collisions. In this work, the parametrised inclusive antiproton production cross section in $p + p$ and $p + A$ collisions, based on the Quark Counting Rule [?, ?] and the Regge Phenomenology [?, ?, ?] is studied. Furthermore, in order to correctly evaluate the atmospheric $\bar{p}$ flux, the antiprotons produced in $A + A$ collisions, especially $He + He$, $He + N$ and $He + O$ collisions, have to be included. However, neither the parametrisation nor the experimental data for $A + A$ collisions are available. In this work, the Wounded Nucleon Model [?] is used, together with the parametrisation for the $\bar{p}$ production in $p + p$ and $p + A$ collisions developed in parallel.

With the developed parametrisation for $\bar{p}$ production in $p + p$, $p + A$ and $A + A$ collisions, the secondary atmospheric $\bar{p}$ flux are calculated at different altitudes by a simulation approach, including both cosmic p-incident and He-incident collisions in the atmosphere. The cosmic $\bar{p}$ flux corrected by the atmospheric $\bar{p}$ component calculated in the previous work [?] are then modified by the secondary atmospheric $\bar{p}$ flux evaluated in the present work. More results and discussions are available in the chapters of this thesis.

The structure of this thesis is arranged as follows. In Chapter ??, cosmic ray astrophysics is roughly reviewed. Some important features of cosmic rays and their propagation are discussed. Cosmic rays entering the Solar system and near the Earth are discussed separately. The related potential study of ultra high energy cosmic rays is outlined. In Chapter ??, the relation between the antiproton study and Cosmology is discussed. The possible origins of cosmic antiprotons are emphasised in this chapter. Chapter ?? discusses the principles of particle detection which are applied in the related detectors and experiments. The experiments whose data are used to compare the results obtained by the present work are reviewed and discussed. Chapter ?? discusses the theoretical models for the $\bar{p}$ production in nuclear collisions, including the approach of Quantum Field Theory, nucleon-nucleon interactions, Quark Counting Rule and Regge Phenomenology. From Chapter ??, the results achieved in the present work are discussed chapter by chapter. In Chapter ??, the parametrisation for the $\bar{p}$ production in nuclear collisions is compared with the experimental data. The energy range of its validity is given. The Wounded Nucleon Model applied to the $\bar{p}$ production cross section in $A + A$ collisions is discussed, so are the results. Chapter ?? introduces and discusses the simulation technique used to evaluate the secondary atmospheric $\bar{p}$ flux. The important elements applied in the simulation technique, such as generating cosmic ray spectra and their composition, the solar modulation, the model of the Earth geomagnetic field, particle equations of motion, atmospheric model and the collisions between antiprotons and other nuclei, are discussed in independent sections. Chapters ??, ?? and ?? present series of results. Chapter ?? dis-

cusses the evaluated atmospheric $\bar{p}$ flux and their features at different altitudes, from sea level to the AMS altitude. The corrections to the previous experimental works are given and discussed as well. Chapter **??** discusses the trajectories of secondary atmospheric antiprotons at very high altitudes. Discussions of possible future work on this issue are given. The short chapter, Chapter **??**, gives the atmospheric proton flux at different altitudes, in comparison with the measurements. The deviation between the present calculations and the experimental data at some specific low altitudes are discussed. Some possible future work directions are also given here before the work is concluded.

Chapter 2

Cosmic Ray Astrophysics

Cosmic rays have been the subject of intense scientific study during the past several decades for various reasons. Firstly, they are ionised nuclei arriving at the Earth. Most of them are protons and helium nuclei. Such particles are distinguished by their high energies. It is worth reminding that some discoveries in particle physics were achieved using cosmic rays [?]. Secondly, cosmic rays are quite abundant, with a galactic energy density about 1 eV/cm^3 [?]. Such an energy density is comparable to that contained in the galactic magnetic field [?], in the starlight luminosity or in microwave background radiation [?]. It is possible to estimate the galactic containment time to be of the order of 10^7 years [?].[1] With such energy features, the energy source needed to power the cosmic radiation must have a total luminosity exceeding about 10^{40} ergs/sec [?]. Therefore, these energy sources must be renewed during the lifetime of the Galaxy in order to continually re-power the cosmic rays. In addition, there is evidence that cosmic rays have existed for as long as the Galaxy itself ($\approx 10^{10}$ yrs) [?]. Yet, cosmic ray particles are the largest source of material reaching the Earth from outside our Solar System. So, the chemical composition of these particles reflects the acceleration history and the nucleosynthetic processes at their origin [?]. Recently, ultrahigh energy cosmic rays with energies E $> 10^{20}$ eV have been detected [?, ?]. They provide evidence for astrophysical accelerations. In addition, such extremely high energy cosmic rays will offer clues to their sources and potentially some important signatures of new physics.

In this chapter, some issues on cosmic rays are drawn: their discovery, their applications in particle physics at early stage [?, ?], their important and unique characteristics and also their link with interests of modern astrophysics.

2.1 Discovery of Cosmic Rays

Cosmic rays are high energy particles propagating in the outer space of the Earth. The mystery of cosmic rays began around 1900 when it was found that electroscopes dis-

[1] The containment time is defined as the time scale of a cosmic ray particle propagating in the galactic confinement volume until it escapes.

charged even if they were kept in the dark well away from sources of natural radioactivity (see Figure **??**). During that period, the electroscope was a key instrument in early experiments in radioactivity. The rate at which the leaves of the electroscope came together could provide a measure of the amount of ionisation. The origin of such a behaviour was a major puzzle and various experiments were carried out to explain this issue. It was found later by Rutherford that, most of the ionisation was due to natural radioactivity, either in rocks or from radioactive contamination of the equipment. Soon followed by a tantalising experiment carried out by Wulf in 1910 by using the best electrometer constructed at that time, he found that the ionisation fell from 6×10^6 ions m^{-3} to 3.5×10^6 ions m^{-3} as he ascended the Eiffel Tower, at a height about 330 m. γ-rays were the most penetrating particles of the ionising radiations known at that time and their absorption coefficient in the air was well known. If the ionisation had been due to γ-rays originating at the surface of the Earth, the intensity of ions should have decayed to one half in 80 m and would have been negligible at the top of the Eiffel Tower.

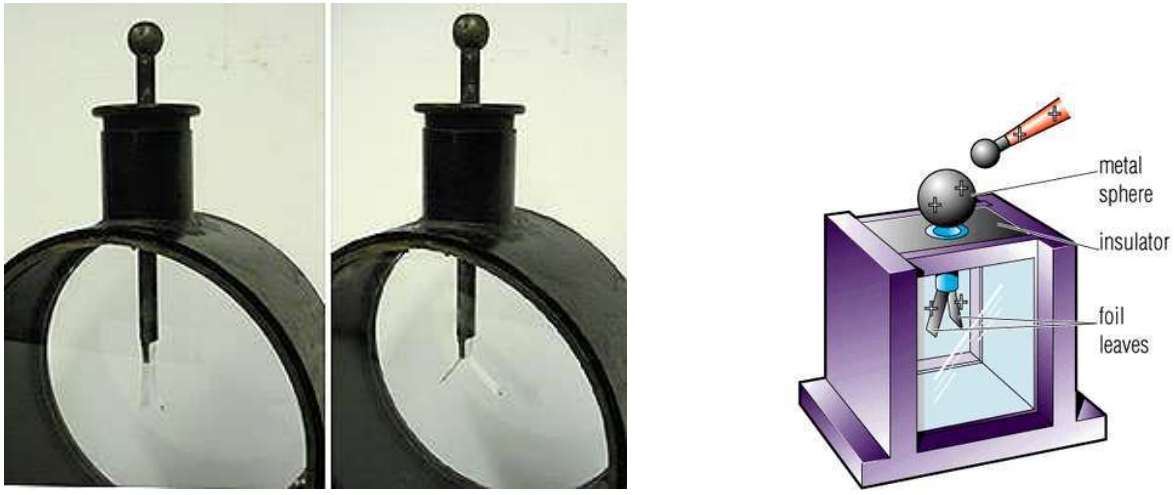

Figure 2.1: *Left: An example of a traditional electroscope before and after induction. Right: The gold-leaf electroscope. The gold-leaf system, consisting of two leaves attached together. When a charged object is approaching the metal sphere, the opposite charges will be removed to the leaves which will turn to separate. The amount of ionisation is then measured by observing the rate at which the charged gold-leaves move towards each other as the gold-leaves discharged due to the leakage currents associated with the ionisation.*

The big milestone came in 1912 and 1913 when Hess and then Kolhörster made the balloon flights in which they measured the ionisation of the atmosphere with increasing altitudes. In 1912, Hess had flown to 5 km and then Kolhörster had made the flight up to 9 km in 1914. It was Hess who discovered the first evidence that the source of the ionising radiation was extraterrestrial.

Hess and Kolhörster found the surprising results that the average ionisation increased with respect to its value at sea level above about 1.5 km (see Table **??**). This result shows evidence that the source of the ionising radiation must be originating from above

the Earth's atmosphere. From the observed number decrease of ions $n(x)$ at a distance x through the atmosphere, the attenuation constant α, defined as

$$n(x) = n_0 e^{-\alpha x} \tag{2.1}$$

can be derived. According to the result in Table **??**, the value of α corresponding to about 10^{-3} m^{-1} was found and this can be compared with the absorption coefficient for the γ-rays from radium, Ra, which in the air has a value of 4.5×10^{-3} m^{-1}, i.e., the γ-rays from Ra are at least five times less penetrating than this ionising radiation which must originate from above the atmosphere.

In 1929, Skobeltsyn constructed a cloud chamber to study the properties of β-rays emitted in radiative decays. The experiment involved placing the chamber within the jaws of a strong magnet so that the curvature of their tracks could be measured. Among the tracks, Skobeltsyn noted some of them which were hardly deflected and which looked like electron-type particles with energies greater than 15 MeV. He then identified them with secondary electrons produced in the Hess ultra γ-radiation. This claim happened to be incorrect but it was the first picture of the tracks of cosmic rays.

In 1929, it was possible to detect individual cosmic rays by the Geiger-Müller detector. In an experiment performed by Bothe and Kolhörster in the same year, they tried to distinguish whether the cosmic radiation consists of high energy γ-rays or charged particles. They found that two detectors discharged simultaneously even if a strong absorber was placed in between. This result indicated that cosmic radiation consists of charged particles which have sufficiently penetrating power to pass through both detectors. If the cosmic radiation were γ-rays, the particles detected by Geiger counters would have had to be secondary electrons and two separated events would take place in the two detectors initiated by a single γ-ray. In the mean time, Bothe and Kolhörster also showed the flux of these particles could account for the observed intensity of cosmic rays at sea level. These particles were very energetic since they could pass through a long range in matter. They then estimated the energies of these particles to be 10^9-10^{10} eV.

2.2 Cosmic Rays and Particle Physics

The elementary unit of matter has drawn great attention in the history of human civilisation. In modern physics, William Crookes discovered electron in cathode rays in 1879 and J. J. Thomson, later in 1897, measured the charge-mass ratio e/m of electron. Rutherford, by using α-scattering, found the structure of atoms in 1898. In 1910s, C. T. R. Wilson invented a significant equipment, the cloud chamber, which helped accelerate the study of atomic nuclei. It was found soon that a typical nucleus has a mass about two or more times the proton mass value. Rutherford, Chadwick and Pauli postulated the neutral mass might be in the form of new particles and started a series of experiments to find the evidence for such new particles which became known as neutrons.

Bothe and Becker in 1930 and also Irène Joliot-Curie and Frédéric Joliot in 1932, discovered that neutral penetrating radiation was emitted when light elements were bom-

Table 2.1: *The variation of ionisation with altitude from the observation of Kolhörster [?].*

Altitude (km)	Difference between observed ionisation and that at sea level (10^6 ions m^{-3})
0	0
1	-1.5
2	+1.2
3	+4.2
4	+8.8
5	+16.9
6	+28.7
7	+44.2
8	+61.3
9	+80.4

barded by α-particles. They supposed the radiation would be some form of γ-radiation but such radiation was later confirmed to be the neutron by Chadwick.

The discovery of cosmic rays was confirmed in 1929. Between 1930s and early 1950s, the cosmic radiation provided a natural source of very high energy particles which were energetic enough to penetrate the nucleus. This procedure turned out to be the key technique to discover new particles until the early 1950s. In 1930, Millikan and Anderson studied the tracks of particles passing through the cloud chamber in magnetic field. Anderson observed some curved tracks identical to those of electrons but corresponding to particles with positive electric charge, which were confirmed to be positrons by Blackett and Occhialini in 1933 by using an improved technique in which the cloud chamber was only triggered after a cosmic ray had passed through [?]. These positrons were found to be created by cosmic ray interactions with the body of the apparatus and the reaction is actually the decay of bound protons in atom A via the basic process

$$(Z, A) \to (Z - 1, A + 1) + e^+ + \nu_e \tag{2.2}$$

where ν_e is the electron neutrino.[2]

The discovery of positron coincided with Dirac's theory of the electron. Dirac succeeded in deriving the relativistic wave equation for the electron which not only predicted its

[2]The inverse β-decay process for the creation of positrons

$$\bar{\nu}_e + p \to e^+ + n \tag{2.3}$$

could also be observed. However, the cross section of such a process is extremely small [?].

spin and magnetic moment but also the existence of the antiparticle of the electron, the positron [**?**].

In his experiment, Anderson also noticed some penetrating positive and negative tracks which corresponded to particles with a mass about 200 m_e. In 1936, Anderson and his colleague, Neddermeyer, were sufficiently confident of their discovery of new types of particles, nowadays known as muons (μ^+, μ^-), which come from the weak interaction processes

$$\nu_\mu + n \rightarrow \mu^- + p \quad ; \quad \bar{\nu}_\mu + p \rightarrow \mu^+ + n \tag{2.4}$$

The muon particles are unstable, with lifetime about 2.2×10^{-6} s [**?**] and can subsequently decay into e^- and e^+ respectively.

$$\mu^- \rightarrow e^- + \bar{\nu}_e + \nu_\mu \quad ; \quad \mu^+ \rightarrow e^+ + \nu_e + \bar{\nu}_\mu \tag{2.5}$$

The same work continued. In 1947, Rochester and Butler reported the discovery of two new particles, one was neutral and the other charged and both had mass about half of the proton and now are referred to as the charged and neutral kaons (K^+, K^-, K^0). In the meantime, they also noticed some examples of neutral particles with long lifetimes and with mass greater than that of the proton. These particles are now known as the lambda particles (Λ).

Meanwhile, another powerful technique, photographic emulsion, for the study of particle collisions was developed by Powell's group at Bristol University. Photographic emulsions are activated by the passage of charged particles which would leave tracks showing their paths through the emulsions. In 1947, in cosmic rays interactions, Powell and his colleagues discovered the pion, π, which was the particle predicted by Yukawa in 1936 for the strong interactions [**?**], generated via processes

$$\begin{aligned} p + p &\rightarrow p + n + \pi^+ && (2.6)\\ &\rightarrow p + p + \pi^0 && (2.7)\\ &\rightarrow p + p + \pi^+ + \pi^- && (2.8) \end{aligned}$$

The charged pions could decay predominantly by the reactions

$$\pi^+ \rightarrow \mu^+ + \nu_\mu \quad ; \quad \pi^- \rightarrow \mu^- + \bar{\nu}_\mu \tag{2.9}$$

The photographic emulsions showed clearly the production of π^+ and π^- with lifetimes of $2 \sim 3 \times 10^{-8}$ s [**?**] and then their decay into muons (Eq. (**??**)) which subsequently decayed into electrons or positrons and invisible neutrinos (Eq. (**??**)).

Two more types of particle were discovered through cosmic ray studies. The Ξ^- particle left a very clear signature in a bubble chamber photograph recorded by the Manchester group in 1952. The decay took place in the cloud chamber and showed a decay chain which ended up with the production of a proton. The Σ particle was discovered in 1953.

From 1953, the accelerator technology became more mature. It was then possible to produce particles in the laboratory with energies comparable to those available in cosmic

rays. These produced particles had a great advantage that the beams could be produced with required energies and could be directed precisely onto the targets in the collisions. After 1953 therefore, accelerators have replaced the application of cosmic rays in high energy physics and the interest in cosmic rays then shifted to the mystery of their origin and their propagation history from their sources to the Earth.

Recently, some cosmic particles with extremely high energy, up to 10^{20} eV, have been detected in ultrahigh energy cosmic ray spectra in extensive cosmic ray air shower [?, ?]. Such particles have a centre of mass energy $\sqrt{s} \simeq 500$ TeV, about 35 times the energy of the Large Hadron Collider, LHC, whose centre of mass energy level is about 14 TeV. Thus, these extremely high energy cosmic rays and the atmosphere themselves provide a natural accelerator with energies beyond human technique capability. These particles could then provide important clues to their origins, the interactions during their propagation and also test on models of cosmic rays, galaxies and Cosmology. Due to the inconsistence in spectra between measurement and prediction at energies above 10^{19} eV, new particles are supposed to be produced at this energy level [?, ?].

2.3 Cosmic Ray Astrophysics

The astrophysical study of the origin and the propagation of cosmic ray particles began when cosmic rays detectors could be launched to terrestrial altitudes. The answer to the question of the origin of cosmic rays is still not yet well known. It is clear, however, that nearly all of them must come from outside the Solar System but from within the Galaxy. Most of the cosmic ray particles observed are secondary. They are produced by the collisions of interacting primary cosmic rays with nuclei in the interstellar medium (ISM). By the cross section of spallation, the mean amount of matter traversed for the bulk of the cosmic rays is of the order $\xi \sim$ 5-10 g/cm^2 [?]. The density ρ_N in the disc of the Galaxy is of the order of about one proton per cm^3 [?]. So, the thickness of material corresponds to a distance of

$$l = \frac{\xi}{m_p \rho_N} \approx 1000 \quad \text{kpc} \tag{2.10}$$

Cosmic ray particles might spend some time in the more diffuse galactic halo, and Eq. (??) then shows a lower limit to the distance a cosmic ray particle has travelled, $l \gg 150$ pc, half the thickness of the disc of the Galaxy. This implies that cosmic confinement is a diffusive process in which the particles drift around for a long time before escaping into the intergalactic space [?].

The chemical composition of cosmic rays draws a great attention to cosmic ray astrophysics since the chemical composition of cosmic rays is observed to be similar to the abundance of elements in the Sun, with just some important exception in lithium (Li), beryllium (Be) and boron (B), which appear in relatively high abundance in the cosmic rays [?]. Most of the knowledge of cosmic ray propagation in the Galaxy relies on the study of secondary species, such as Li, Be and B (Z=3-5) and the spallation products

of Fe (Z=21-24) that are almost certainly produced solely in cosmic ray interactions but rarely in cosmic ray sources. Their spectra and isotropic ratios are then a good way to understand the acceleration history of cosmic rays and their sources. These observations provide evidence about the chemical composition of cosmic rays as they leave their sources and also the modifications which take place during the propagation from their sources until being observed. These cosmic ray observations are significant for high energy astrophysics since they are the only particles which can be detected and have traversed a considerable distance through ISM and were accelerated in events such like supernovae in relatively recent past, about the galactic containment time ($\simeq 10^7$ years) [?]. Current measurements of $LiBeB$ at low metallicities [?, ?], defined as the function of iron to helium ratio, Fe/H, have raised the questions of the cosmic ray origin, requiring acceleration out of fresh supernova ejecta and have also implied their production at all epochs of Galactic evolution by cosmic rays having the same spectra and source compositions as those at the current epoch.

Observations show that the energy spectra of cosmic ray particles are almost exactly the same as the typical spectra of high energy particles inferred to be present in both Galactic and extragalactic non-thermal radio sources [?]. In the region of the energy spectrum that is not affected by the propagation of the particles to the Earth through the Solar Wind, the energy spectra of the cosmic ray particles have a power-law relation with energy $N(E)dE \propto E^{-\alpha}dE$, with $\alpha \approx$ 2.5-3.0. Such a relation is found to be applicable to protons, electrons and nuclei with energies in the range 10^9-10^{14} eV [?].

A very low flux of particles with energies up to 10^{20} eV is also detected by air shower arrays located on the surface of the Earth [?, ?]. The arrival directions seem isotropic and, they are not significantly influenced by the magnetic field in our Galaxy since the cosmic ray particles with such high energies have gyroradii in typical galactic magnetic fields which are larger than the size of the Galaxy. Due to the Greisen-Zatsepin-Kuzmin cutoff at around 5×10^{19} eV [?, ?], cosmic ray particles with energies higher than the cutoff must come from the vicinity of the Galaxy, so that they can arrive at the Earth before travelling long energy-sapping distances. The scale is estimated to be 50 Mpc [?]. However, spectra measured from cosmic ray air shower show no apparent signature of cutoff. The solution to this puzzle still remains open.

In addition, the problem of the atmospheric neutrino anomaly has also drawn a lot of attention recently. Neutrino oscillations proposed by the SuperKamiokande Collaboration [?], based on the direction dependent deficit of atmospheric muon neutrinos generated by incident cosmic ray particles could provide potential clues of new physics beyond the Standard Model and are one of the principal interests on neutrino astrophysics. The ISN team has also approached this issue [?].

2.4 Features of Cosmic Rays

The information about cosmic rays from which, one hopes to learn about their origin, are the relative abundance of the different nuclei (chemical composition) and the energy

spectrum of each component. The comparison with the chemical composition of other various astrophysical objects, for example, the Sun, ISM, supernovae or neutron stars, can give clues about the environment in which cosmic rays are injected into the acceleration processes while the energy spectra could be characteristic of certain acceleration mechanisms.

Among the high energy particles in cosmic rays arriving at the top of atmosphere (TOA), about 98% of the particles are protons and nuclei, and about 2% are electrons. In the component of protons and nuclei, about 87% are protons, 12% are helium nuclei and the remaining 1% are heavier nuclei, carbon (C), nitrogen (N), oxygen (O), magnesium (Mg), silicon (Si), iron (Fe)... Particles with energy up to 1 TeV per nucleon can be well directly measured from space experiments. Particles with energies greater than 100 TeV can be detected but their energies are derived from the phenomenon of cosmic air shower (cascade) at TOA [?, ?].

2.4.1 Energy Spectrum

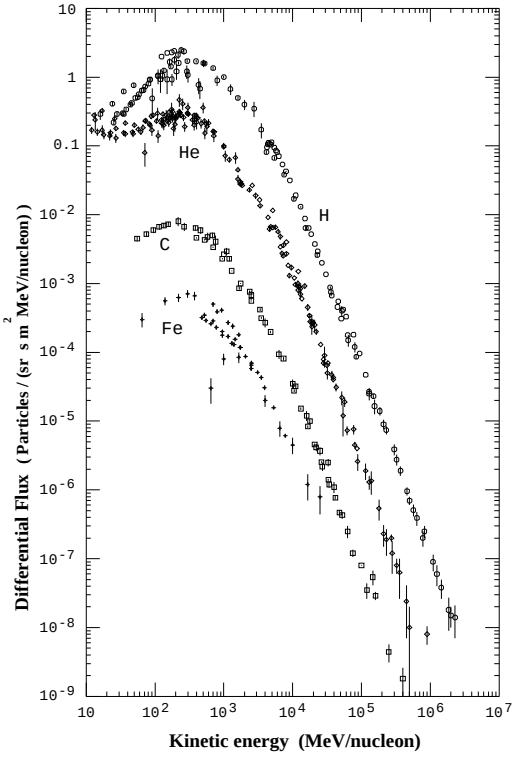

Figure 2.2: *The differential energy spectra of cosmic rays as measured at the Earth from observation made from the Top of Atmosphere (TOA) [?]. The spectra for hydrogen, helium, carbon and iron are shown.*

Figure ?? [?] shows the differential flux of cosmic ray species, proton, helium, carbon and iron, in function of kinetic energy per nucleon. The energy spectra of cosmic rays span a wide range from several MeVs up to several TeVs. The differential energy spectra of various cosmic ray species follow a power-law energy distribution which can be well expressed over the energy range between 1 GeV and 100 TeV per nucleon as

$$N(E)dE = KE^{-\alpha}dE \tag{2.11}$$

where α lies in the range of 2.5-3.0, depending on the cosmic ray species. Cosmic rays under 100 TeV are supposed to come from standard supernova acceleration [?]. A supernova remnant disspates a significant fraction of its energy to cosmic rays [?], which are then accelerated by strong diffusive shock waves propagating through interstellar space. Such strong shocks generate power-law spectra, with the power index $\alpha \simeq 2$ [?]. During the propagation, cosmic rays are actually loosely confined in the Galaxy by the galactic magnetic field. The Leaky Box Model incorporates a rate of escape from the galaxy that is energy dependent by a spectral index $\alpha \simeq 0.6$ [?], which is supported by measurement of the ratio of the secondary cosmic ray flux to the primary flux [?]. Figure ?? show some important features of cosmic ray particles.

(i) At energies less than 1 GeV per nucleon, the energy spectra of all species show an attenuation relative to the power-law observed at higher energies. The energy and the shape of the cut-off vary with the phase of the Solar Cycle so that the flux of low energy particles decrease during the period of high solar activity and reach a maximum during phases of low solar activity. The cut-off results from the fact that cosmic ray particles have to diffuse in towards the Earth from interstellar space through out-flowing Solar Wind. Such a phenomenon is referred to as solar modulation of the flux of cosmic rays. The Solar Wind with embedded magnetic field would exclude low energy cosmic ray particles from the heliosphere: the greater the solar activity, the greater the disturbances in the interplanetary magnetic field which would impede the propagation of cosmic ray particles with energies less than about 1 GeV/nucleon to the Earth.

(ii) In the energy spectrum of helium nuclei, there is a turn-up below 60 MeV. This component is referred to as the anomalous ^4He component. The spectral turn-up was found in 1972 and its intensity began to decrease again in 1981. Thus, such a turn-up is affected by the solar activity. The nature of this component, however, is still unclear so far. It is also found that the flux of these anomalous ^4He increases with increasing distance from the Sun. Such a fact suggests that the component particles are accelerated in outer regions of the heliosphere.

(iii) Although in Figure ??, the spectra of all cosmic ray species look remarkably similar, there are, however, significant differences between the energy spectra of different elements, especially for the heavier elements. Up to now, the energy spectra of cosmic nuclei with Z up to 28 have been measured [?] and their best-fitted spectra have been parametrised by applying all available data [?]. Figure ?? shows the

spectrum index in power law spectrum Eq. (??) in function of atomic number Z. In this figure, it shows that the spectra of cosmic ray species with $3 \leq Z \leq 5$ and $10 \leq Z \leq 24$ are significantly steeper than the spectra of C and Fe respectively, which are presumably the primary cosmic rays and also the sources producing these species by spallation. This distinction comes from the fact that, if the production is throughout the time of transport, then the secondaries are expected to present a steeper spectra; if on the other hand, the spallation is mostly already in the source region, then the secondary spectra should be the same as that of the primaries. Thus, this characteristic suggests that the difference between these cosmic ray species can be attributed to the difference in their path length for spallation as a function of particle energy [?].

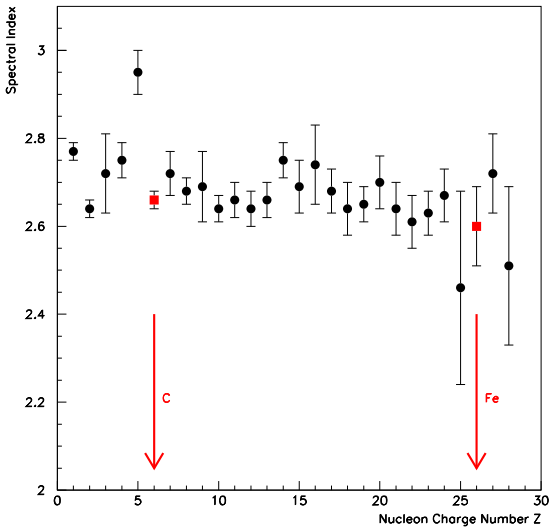

Figure 2.3: *The spectral indices for the various cosmic elements as a function of the charge number Z. The values are given by fitting all available data from cosmic ray abundance measurements [?]. Proposed primary species C and Fe are indicated.*

As discussed above, Figure ?? is coupled with solar modulation and the power-law spectra Eq. (??) is valid only at $E > 1$ GeV/n. A modified power-law of cosmic ray spectra is achieved by fitting the data from experiments, which are classified into three categories: i) spectra measured during minimum solar activity, ii) those measured during maximum solar activity, and iii) measurements at high energies, where the solar modulation becomes negligible. The best fitting form is then given by an expression of the type [?]

$$N(E)dE = A(E+B)^{-\alpha}E^{\beta}dE \qquad \text{particles}/(\text{m}^2 \text{ sr s GeV/n}) \tag{2.12}$$

for protons, heliums and $(C+O)$ nuclei. The best-fit parameters A, B, α and β are give in Table **??**. Eq. (**??**) with the parameters on Table **??** has shown an agreement with measurement data of protons, helium and $(C+O)$ nuclei, with energies that span up to 2 TeV during both maximum and minimum solar activities. For light nuclei secondarily produced from spallation, the spectra are steeper and are almost compensated by the relatively flatter spectra of heavier nuclei [**?**]. From the observed cosmic ray abundance as a function of energy [**?**], it is found that the spectrum of all nuclei with $Z > 2$ is equivalent to 2.25 times the $(C+O)$ spectrum and this weighting factor stays nearly energy-independent within the measurement uncertainty [**?**]. The same conclusion is made for all nuclei with $Z > 1$ whose spectrum is the helium spectrum multiplied by a factor of 3.5.

Eq. (**??**) shows that, at high energies, $E \gg B$, the energy spectra reduces to the typical power law $\propto E^{-2.75}$, for all proton, helium and $(C+O)$ spectra at both minimum and maximum solar activities. The solar modulation is then drawn off for high energy particles. While at low energies, solar modulation starts to pull down the spectra once energy E is comparable to B and at solar maximum, the spectra are pulled down from a higher energy. For energies $E \ll B$, the spectra correspond to E^{β}, which decreases exponentially with respect to diminishing energies.

Table 2.2: *Parameters of Cosmic Ray Spectra Fits [**?**].*

Minimum solar modulation				
	A	B	α	β
P	18000	0.92	4.00	1.25
He	850	0.76	3.52	0.77
C+O	62	1.05	3.25	0.50

Maximum solar modulation				
	A	B	α	β
P	18000	1.61	3.83	1.08
He	850	1.17	3.63	0.88
C+O	62	1.15	3.75	1.00

2.4.2 Chemical Abundance

The chemical abundances of cosmic rays provide important clues to their origin and also to the processes of their propagation from their sources to the Earth. If one can deduce from these data the abundances of cosmic rays at their sources, this could provide an important astrophysical clue to potential sites of acceleration.

The relative abundances of cosmic rays can be compared with the abundances of elements in the Solar System. Figure **??** reveals the overall similarities and differences

between the abundances in cosmic rays and those of the typical Solar System. On the figure, some features are apparent.

(i) The abundance peaks at C, N, and O and at the iron group are present both in the cosmic ray and the Solar System abundances.

(ii) Both the cosmic ray and the Solar System abundances show the odd-even effect in the relative stabilities of the nuclei according to atomic number, with the tightly bound, even Z nuclei being more abundant. This phenomenon would emphasise the importance of helium burning in both cosmic ray sources and in the material sources in the Solar System [**?**].

(iii) Two groups of elements Li, Be, B and Sc, Ti, Cr, Mn are grossly more abundant, in cosmic rays than in the Solar System. These elements are essentially absent and are not the end products of stellar nucleosynthesis destroyed in stars. They are believed to originate the most likely from the fragmentation of heavier primary nuclei, $C - O$ and Fe respectively. That is to say, the primary cosmic rays are accelerated in their sources and propagate through the ISM to reach the Earth, and during the propagation, they suffer the fragmentation collisions with ISM.

(iv) There is an underabundance of hydrogen and helium in cosmic rays relative to other heavy elements [**?**]. This could be attributed to H and He being relatively hard to ionise for injection into the acceleration processes [**?**], otherwise, it would reflect an original difference in the element composition at the sources of cosmic rays [**?**, **?**].

Cosmic ray isotope abundances also draw a great amount of attention in modern astrophysics. Cosmic ray isotopic component is believed to provide more direct constraints on the type of cosmic rays sources, because it cannot be affected by atomic selection effects, and is therefore indicative of the nucleosynthetic origin of cosmic rays [**?**]. First of all, the light elements (^1H, D) and (^3He, ^4He) form a characteristic group of isotopes. Only ^1H and ^4He are found with very high abundances in ISM but the rare isotopes, D and ^3He, are present in much greater abundances in cosmic rays than they are in ISM [**?**]. D and ^3He come from two origins: they are either the primordial remnants of the Big Bang or the secondary products in the propagation of cosmic rays. Thus, D and ^3He play as a good probe to test the propagation models [**?**, **?**] and also allow a lower limit to their primordial component. In standard Cosmology [**?**], the light elements D, ^3He and ^4He are partly, if not wholly, primordial in origin. Current stellar processes cannot make them in sufficient quantity but, instead, will tend to reduce their abundances. However, they could be synthesised in significant abundances in the Standard Hot Big Bang as products of the main *pp*-chain

$$\begin{aligned} p + n &\longleftrightarrow D + \gamma \\ D + D &\longleftrightarrow {}^3H + p \longleftrightarrow {}^3He + n \\ {}^3H + D &\longleftrightarrow {}^4He + n \end{aligned} \tag{2.13}$$

As the secondary products, the measured ^3He [?], which is mainly produced by the fragmentation of ^4He, tests the propagation of He, and the $^3He/^4He$ ratio measurement that proves the prediction by using the escape length derived from B/C [?]. D nuclei are produced partially by the fragmentation of heavier nuclei (mainly ^4He) and partially by the interactions of cosmic ray protons with ISM protons. This pp interaction has produced a peak in D spectrum around 150-160 MeV/c [?]. It is reported [?] that such pp-interaction contributes for about 50% to the measured D flux in the measurements [?]. Thus, D measurement can also be used to test the propagation of cosmic protons.

It is found that the most common isotopes of the heavier elements are the same as the most common isotopes found in the Solar System and also in the local interstellar (LIS) medium. But, some significant abundances of rare isotopes are found in cosmic ray particles. A greater abundance compared with the Solar System of some neutron rich isotopes are found in cosmic rays. For example, the value of $^{22}Ne/^{20}Ne$ and $^{18}O/^{16}O$ ratios are about 4 times greater in the cosmic rays than that found in the Solar System, $^{25}Mg/^{24}Mg$, $^{26}Mg/^{24}Mg$, $^{29}Mg/^{28}Mg$ and $^{30}Si/^{28}Si$ about 1.6 times greater while $^{10}Be/^{9}Be$ about 2 times greater and $^{60}Ni/^{58}Ni$ about 2.6 times greater [?, ?]. These enrichments are important clues about the sites of acceleration of the cosmic ray particles, i.e., the nucleosynthesis of cosmic rays is different from that of the Solar system [?]. A very possible resolution, for ^{22}Ne for example, would be helium burning via the following nuclear reactions [?].

$$\begin{aligned} {}^{14}N + {}^{4}He &\rightarrow {}^{18}F + \gamma \\ {}^{18}F &\rightarrow {}^{18}O + e^{+} + \nu_e \\ {}^{18}O + {}^{4}He &\rightarrow {}^{22}Ne + \gamma \end{aligned} \tag{2.14}$$

It must be noted that these ratio values are the averages derived from several experiments. Since the isotopic ratios at low solar modulation Φ are presumably closer to the interstellar ratios than those at high Φ [?], the isotopic ratio measurements are of more importance at lower modulation which becomes non-negligible at lower energies. For example, $^{18}O/^{16}O$ ratio at 150 MeV/n increases by a factor of 1.5 [?] when Φ changes from 325 MeV to 1400 MeV. Such a fact points out that the isotopic ratio measurement at the same energy but at different times or locations in the heliosphere cannot be compared directly.

2.4.3 Cosmic Ray Clocks

Another important aspect of the cosmic ray isotope abundances is the fact that some of the isotope species produced in spallation reactions are radioactive, for example, ^{10}Be, ^{14}C, ^{26}Al, ^{36}Cl and ^{54}Mn, which can be considered as cosmic ray clocks or propagation clock nuclei. Hence, if the production rates of the different isotopes of a given element are known, information can be carried by these species about the duration of the time these samples have taken in the journey from their sources until reaching the Earth. The most important example is the ^{10}Be isotope, which has a radioactive half-life of

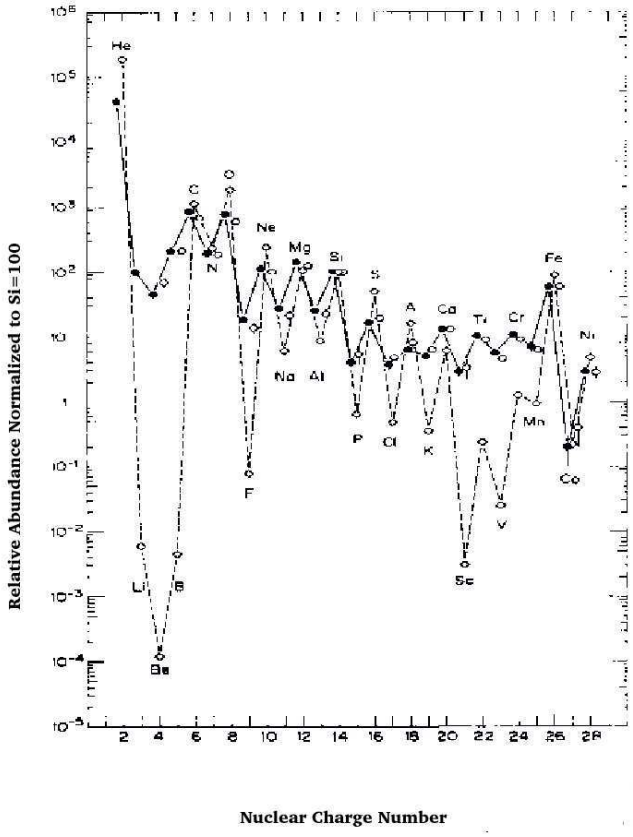

Figure 2.4: *The reproduced cosmic element abundances (He-Ni) in cosmic rays measured at TOA compared with the Solar System abundances [?]. The data have been normalised to [Si]= 100. The solid circles are low energy data (70-280 MeV per nucleon), the open circles show a compilation of high energy measurements (1-2 GeV per nucleon) and the diamonds represent the Solar System abundances.*

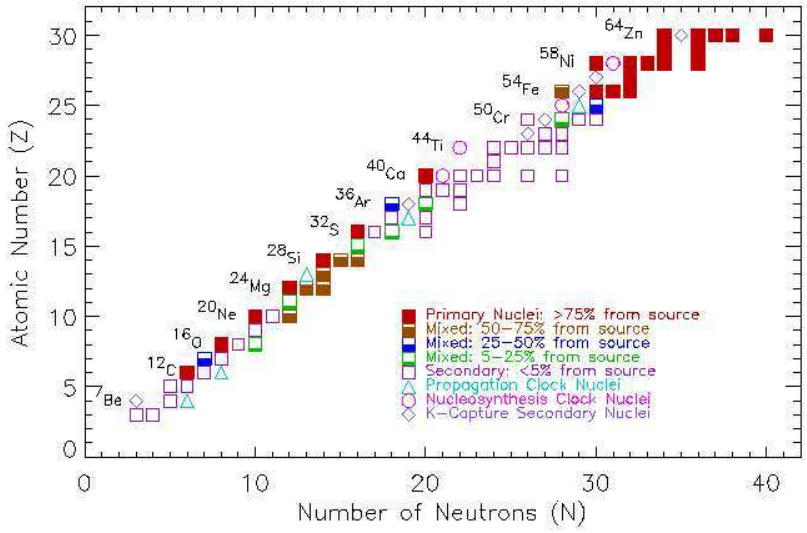

Figure 2.5: *The abundance classification of primary-secondary isotopes in cosmic ray for Z=3-30 [?].*

about 1.5×10^6 years. Because of its long lifetime, the ^{10}Be isotope is used as a galactic chronometer for the measurement of the confinement time of cosmic rays in the Galaxy [?, ?, ?]. The measurement of the momentum dependence of the $^{10}Be/^9Be$ ratio will provide a determination of important transport parameters and galactic variables: the mean ISM density in the Leaky Box Model [?, ?], and the size of the confinement halo in the diffusion model [?].

Figure ?? [?] shows the abundance classification of primary-secondary cosmic isotopes with atomic number Z=3-30 with respect to the neutron number. It's apparent that all the isotopes of light elements in cosmic rays, such as Li, Be and B, are secondary products, so are species ^{15}N, ^{17}O, ^{18}O, ^{19}F and ^{21}N. And, the elements just lighter than Fe, for example from Sc to Mn, are the fragmentation products of Fe. On the other hand, for common elements like carbon, oxygen, neon, magnesium, silicon and iron, a substantial fraction of each has survived from the spallation destruction between the sources and the Earth. The heaviest cosmic ray particles are all primary while they are very difficult to be produced by cosmic ray interactions. Thus, they must be directly created from their sources, arriving at the Earth with a fraction of spallation loss.

2.4.4 Energy Density

The charged cosmic ray particles propagate in the galactic magnetic field. It is impressing that the energy density of cosmic rays is comparable to the energy density in magnetic fields. The relation between flux Φ (particles/cm^{2}s sr) and number density of cosmic rays, ρ_{CR}, is

$$\Phi = \frac{\rho_{CR}\beta c}{4\pi} \tag{2.15}$$

Therefore, the energy density, ρ_E, is

$$\rho_E = 4\pi \int E \frac{dN}{dE}\frac{dE}{\beta c} = \int \frac{4\pi E^2}{\beta c}\frac{dN}{dE} d\ln E \tag{2.16}$$

By using the energy spectra in Eq. (??) with the parameters in Table ?? for both minimum and maximum solar activities [?], one could calculate ρ_E. Figure ?? shows the differential of the energy density integral from Eq. (??) for the spectra of proton and helium at periods of minimum and maximum solar activities. The area under the proton curve at period of minimum solar activity is about 0.75 eV/cm^3, and helium and other heavier nuclei contribute another amount about 0.3 eV/cm^3. This is comparable to a magnetic field energy density $\epsilon \approx 0.25$ eV/cm^3 in a typical galactic field of $B \approx 3$ μGauss [?], the local thermal energy density of the interstellar gas that pervades the space between stars, $\epsilon \approx 0.3$ eV/cm^3 and the energy density of the Cosmic Microwave Background Radiation (CMB), $\epsilon \approx 0.3$ eV/cm^3 [?]. These two energy densities between cosmic rays and any one from the other three are comparable in consequence of the mutuality of the interactions between cosmic ray particles and the other, with field configuration being

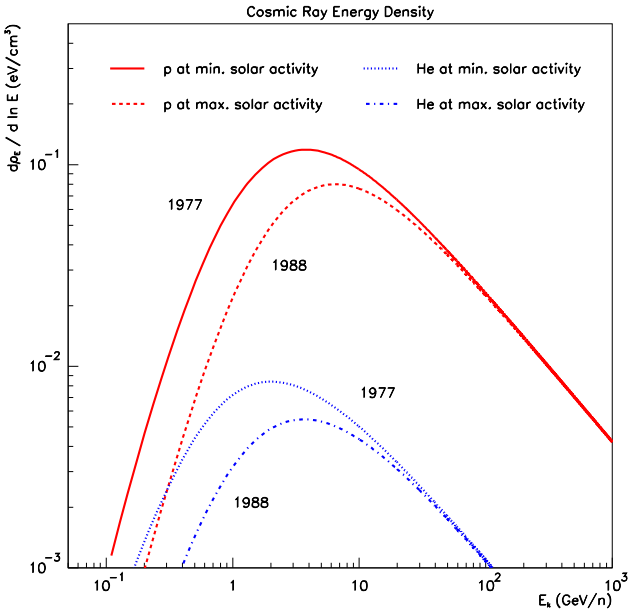

Figure 2.6: *The distribution of the energy density, ρ_E, for proton and helium in cosmic rays at periods of minimum and maximum solar activities. The values are calculated by applying the parametrisation in [?].*

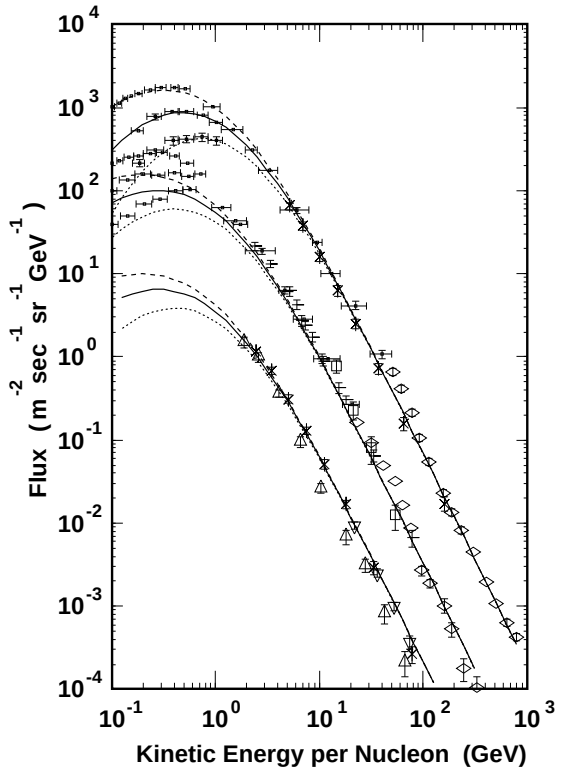

Figure 2.7: *The differential energy spectra of hydrogen, helium and C+O nuclei in cosmic rays as a function of the phase of the Solar Cycle [?, ?]. The data were measured in the period of 1964-1973. In each set of spectra, the top curve shows the measurements at the time of minimum sun-spot number and the bottom curve at sun-spot maximum. The middle curve shows the spectra at intermediate levels of sun-spot number. Solid lines are the parametrisations of Eq. (??) and (??) for the relevant three time periods.*

influenced by cosmic rays and vice versa [?]. Generally, the relation between the power Q, of the sources needed to maintain the observed energy density in cosmic rays is

$$Q \sim \frac{\rho_E}{\tau_e} \tag{2.17}$$

where τ_e is the typical time that a cosmic ray particle takes to escape from the Galaxy. By measuring stable ^{11}B spectrum [?], the confinement time τ_e is given as

$$\rho_H \tau_e \sim 10^7 \cdot \left(\frac{R}{4.7 \text{ GV/c}} \right)^{-0.6} \quad \text{yrs}, \quad R > 4.7 \text{ GV} \tag{2.18}$$

where ρ_H is the galactic hydrogen number density, $R = pc/Ze$, is the magnetic rigidity. The median energy of all cosmic rays is about 3 GeV/nucleon [?]. Thus Eq. (??) gives $\tau_e \approx 10^7$ years. The power required to maintain the supply of cosmic ray radiation then becomes

$$Q = \int_{V_{galaxy}} dV \int \frac{1}{\tau_e} E \frac{dN}{dE} dE \quad \sim \; 5.5 \times 10^{40} \;\; \text{erg/s} \tag{2.19}$$

This amount sets the lower limit of the power of the cosmic ray source. Although with a large uncertainty, this power was suggested as a few efficient percent of the likely power output of the supernova blast waves [?].

2.5 Cosmic Rays in the Solar System and Near the Earth

Once cosmic rays enter the Solar system, they will undergo strong influence from the Solar Wind and the Earth geomagnetic field. After reaching a radial distance of about $10R_E$, R_E the mean Earth radius, where the Earth geomagnetic field turns to be dominant, their propagation is strongly influenced by this field.

2.5.1 Solar Modulation

When cosmic rays enter the Solar system, they undergo strong influence from the Solar Wind. The Solar Wind is the corpuscular outflow from the Sun, carrying the magnetic field of the Sun through space, thus producing an outward convection effect upon cosmic ray particles. The Solar Wind then drives back part of the cosmic ray particle flux entering into the Solar Sphere and prevent this interstellar flux of cosmic rays from reaching the Earth. This effect is called solar modulation and occurs only for lower energy cosmic rays. The strength of the Solar Wind varies with the solar activity, for which, a measure is the number of spots on the surface of the Sun that varies with a period of 11 years. There exists a correlation between relative sun-spot number and geomagnetic index showing that the local degree of turbulence in the geomagnetic field is strongly correlated with the level

of activity of the Sun and there also exists an anti-correlation between these quantities with the intensity of cosmic rays [?]. As a result, the spectrum shape becomes dependent of the solar activity: during solar maxima, the repulsion of Solar Wind on cosmic rays is also maximal, thus the particle spectra are at minimum. Some features of Solar Wind are shown in Table ??.

Table 2.3: *Typical parameters of the Solar Wind [?]. These parameters refer to the normal Sun and can vary with the solar activity. In high speed streams, velocities up to 700-800 km s^{-1} are found and the particle concentrations are* $\sim 5 \times 10^6$ m^{-3}, *so that the particle flux is more or less the same in all cases.*

Particle velocity	~ 350 km s^{-1}
Particle flux	$\sim 150 \times 10^{12}$ m^{-2} s^{-1}
Particle concentration	$\sim 10^7$ m^{-3}
Energy of proton	~ 500 eV
Energy density of protons	$\sim 8 \times 10^{-10}$ J m^{-3}
Temperature	$\sim 4 \times 10^6$ K

The effect of solar modulation is calculated by a transport equation assuming spherical symmetry including the effects of diffusion, convection and adiabatic deceleration [?], for which, the propagation of cosmic rays into the Solar System is described by the Fokker-Planck equation [?]

$$\frac{1}{r}\frac{\partial}{\partial r}(r^2 VU) - \frac{1}{3}\left[\frac{1}{r^2}\frac{\partial}{\partial r}(r^2 V)\right]\left[\frac{\partial}{\partial E}(\alpha E U)\right] - \frac{1}{r^2}\frac{\partial}{\partial r}\left(r^2 \kappa \frac{\partial U}{\partial r}\right) = 0 \qquad (2.20)$$

where U is the cosmic ray density, V is the Solar Wind velocity, E is the kinetic energy, r is the radial distance from the Sun and $\alpha = (E + 2m_0)/(E + m_0)$ [?]. The diffusion coefficient κ has the form $\kappa = \frac{1}{3} v\lambda$, where $\lambda = \lambda(r, R, t)$ is the scattering mean free path [?], where R is the particle rigidity, $R = \frac{pc}{Ze}$. Since the path of a charged particle in a steady magnetic field is determined by its initial direction and its rigidity, λ can then be approximated by a separable function of r and R such that [?, ?]

$$\kappa = \beta\kappa_1(r)\kappa_2(R) \simeq \beta\kappa_1(r)R \simeq \beta C_0 \exp(r/r_0)R \qquad (2.21)$$

where κ_1 is the diffusion coefficient multiplier constant. C_0 can be determined by taking $\kappa = 10^{22}$ cm^2 s^{-1} for protons with energy $E = 6$ GeV at r=1 AU. The modulation strength is parametrised with one parameter Φ, which is given as [?]

$$\Phi(r) = \frac{1}{3}|Ze| \int_r^{r_B} \frac{V(r)}{\kappa_1(r)} dr \simeq 140|Ze| \left(\frac{r_0}{r_E}\right) \exp\left(\frac{r - r_E}{r_0}\right) \qquad (2.22)$$

where V is taken as the typical velocity of the Solar Wind, V= 400 km s^{-1}, r_B is the modulation boundary and is taken to be 100 AU, r_E is the Earth radius and r_0 is a bounded limit on radius, $0.8 \leq r_0/r_E \leq 1.6$, for the need of fitting. Φ then immediately

gives estimates of the mean energy loss of cosmic ray particles. Applying Φ, the relation between the modulated and unmodulated cosmic ray flux can be expressed as [?]

$$N(E) = N(E)_{modulated} = \frac{E^2 + 2m_pE}{(E + Ze\Phi)^2 + 2m_p(E + Ze\Phi)} N_{unmodulated}(E + Ze\Phi) \quad (2.23)$$

The parameter Φ varies between 350 and 1500 MV from the solar minimum to the solar maximum. It must be noted that the detailed measurements of energy spectra under solar modulation are very laborious. However, a simpler but less detailed monitoring of the magnitude of solar modulation than measuring energy spectra is possible by measuring the flux of secondary neutrons produced in the atmosphere by interacting cosmic rays [?]. Thus, the variation of Φ can be correlated by using CLIMAX Neutron Monitor Counting Rate Data [?, ?] and the updated CLIMAX data can be found in [?].

The solar modulation reflects directly on the measured primary cosmic ray flux. The flux for various levels of solar activity is parametrised as a function of the count rate of a neutron monitor N by [?]

$$N(E)dE = \gamma_i u^{-2.585} M(R, N)dE \quad (2.24)$$

where the index i stands for the kind of nucleus, H, He, $CNO, \ldots$, R for the rigidity in unit of GeV/cZ, and u for the total energy per nucleon in GeV. The absolute flux value for each species is determined by γ_i, for which, γ_H, γ_{He} and γ_{CNO} are 10.85×10^3, 5.165×10^2 and 3.3×10^{-2} m^2 s^{-1} sr^{-1} GeV^{-1} respectively. The function $M(R, N)$ is the modulation function defined as

$$M(R, N) = \exp\left[-\frac{1.15 + 14.9(1 - N/N_{max})^{1.12}}{0.97 + R}\right] \quad (2.25)$$

where N is the count rate of the neutron monitor with N_{max}= 2465 count/hr. For various levels of solar activity, solar minimum, solar intermediate and solar maximum, N is taken as a number of 2445, 2300 and 2115 respectively. Such a parametrisation is plotted in Figure ?? and is compared with measurement data [?].

Figure ?? shows the differential energy spectra for cosmic ray proton, helium and $C + O$ nuclei [?]. The results of the parametrisation in Eq. (??) show a good agreement with the data except over the energy range $E \leq 10$ GeV/n. Solar modulation influences considerably particles with energies $E \leq 1$ GeV/n. The flux difference at solar maximum and solar minimum is more than a factor of 2.0 for 1 GeV/c cosmic rays while it decreases to about 10% at $E = 10$ GeV/n.

Attention has to be drawn to the fact that, in reality, the solar modulation strength Φ in Eq. (??) is also a function of time. In addition, the measurement of CLIMAX Neutron Monitor shows some large fluctuations [?]. This fact is the result of the irregular activity of the Sun. If there are some instantaneous and irregular solar phenomena, such as solar flares etc., when a cosmic ray measurement is performed, the solar modulation could be correlated to a higher value [?, ?].

As discussed, the solar activity is irregular in reality and the measurements show some large fluctuations. So, the solar modulation is in fact very uncertain, with a diffusion coefficient κ in Eq. (??) being complicated in reality. Such an uncertainty reflects directly on the cosmic ray flux measurements at low energies, $E \leq 2$ GeV/n that is derived [?] and approximated using Eq. (??) and (??):

$$\begin{aligned} \frac{\triangle N}{N} &= \frac{1}{E}\left[-\frac{2(E+m)}{E+2m}+\frac{\partial \ln N}{\partial \ln E}\right]\frac{R}{\kappa_2(R)}\frac{\triangle \Phi}{Ze} \\ &\simeq \frac{-1}{E}\left[\frac{2(E+m)}{E+2m}+\frac{\alpha E}{E+B}-\beta\right]\frac{\triangle \Phi}{Ze} \end{aligned} \tag{2.26}$$

where the parameters α, β, B are defined in Table ?? and m is the particle mass. In Eq. (??), it is shown that such an uncertainty depends on particle mass, energy, time and spectrum index. For example, suppose there is 10% of uncertainty in the solar modulation parameter. In this case, for H at energy $E = 1$ GeV/n during the minimum solar period, the uncertainty is still as large as about 21% while for He, it is as large as 12%; at $E =$ 0.5 GeV/n, the uncertainty turns to be 27% for H and 17% for He. During the maximum solar period, the uncertainty is much larger at low energies: for H, it is 17% at $E = 1$ GeV/n and 20% at $E = 0.5$ GeV/n, while for He, the uncertainty is 10% at $E = 1$ GeV/n and 13% at $E = 0.5$ GeV/n. However, at $E = 5$ GeV/n, the uncertainty reduces to less than 10% during both solar minimum and solar maximum.

2.5.2 Geomagnetic Cutoff

Cosmic rays being charged particles, their trajectories reaching the Earth neighbourhood are bent by the geomagnetic field, which will affect the arrival directions of cosmic rays, block lower energy cosmic rays, and trap some (secondary) particles in the radiation belts. The geomagnetic field consists of two parts, the internal field (main field) produced by magnetic moments of the Earth and the external field driven by the Solar Wind plasma. These two fields merge and form the magnetosphere at a radial distance about $r \simeq 10\ R_E$ [?], where R_E is the mean Earth radius.

The geomagnetic field determines the minimum energy with which a cosmic ray particle can arrive at the Earth. This effect is caused by the magnetic shield effect for low energy cosmic rays [?]. Since the dynamics of a charged particle in a magnetic field is determined by its rigidity, for cosmic ray particles, the minimum energy for arriving at the Earth is then determined by their minimum rigidity. Below this threshold, the cutoff, cosmic rays cannot penetrate through the geomagnetic field into the forbidden region; particles with rigidity below the cutoff cannot escape from the geomagnetic field either. The rigidity cutoff is a function of the entering position on the Earth and the arrival direction (zenith angle θ and azimuth angle ϕ) of the particles. The realistic geomagnetic field is represented by a multipole expansion of the spherical harmonic function as [?]

$$B_r = -\frac{\partial \psi}{\partial r} \qquad B_\theta = -\frac{1}{r}\frac{\partial \psi}{\partial \theta} \qquad B_\phi = \frac{1}{\sin\theta}\frac{\partial \psi}{\partial \phi} \tag{2.27}$$

with the potential function

$$\psi = R_E \sum_{n=1}^{\infty} \left(\frac{R_E}{r}\right)^{n+1} \sum_{m=0}^{n} (g_n^m \cos m\phi + h_n^m \sin m\phi) P_n^m(\cos\theta) \tag{2.28}$$

where $P_n^m(\cos\theta)$ is the associated Legendre function with Schmit normalisation of degree n and order m. g_n^m and h_n^m are Gaussian coefficients determined by the magnetic field. Unfortunately, multipole equations (??) and (??) have no analytic solution. Thus, it is frequent to simplify the main field as a dipole field, i.e., $n = 1$ in Eq. (??). This simplification reduces the potential function in Eq. (??) to

$$\psi = R_E \left(\frac{R_E}{r}\right)^2 g_1^0 \cos\theta \tag{2.29}$$

In a dipole field (??), the rigidity cutoff, called Störmer cutoff [?], can be well expressed analytically. It is given in the form [?, ?]

$$R_{cutoff} = \frac{M\cos^4\lambda}{r^2(1+\sqrt{1-\zeta\cos\theta_{EW}\cos^3\lambda})^2} = \frac{59.6\cos^4\lambda}{(r/R_E)^2(1+\sqrt{1-\zeta\cos\theta_{EW}\cos^3\lambda})^2} \tag{2.30}$$

in unit of GV/c where M is the Earth dipole moment, λ the geomagnetic latitude, r the radial distance, ζ the sign of the particle charge, θ_{EW} is the incident angle from the east. The Störmer cutoff shown in Eq. (??) is found to have an error as large as 30% in some regions [?]. In the realistic geomagnetic field, the cutoff becomes more complicated and cannot be formulated as a simple formula but turns to a band of intermittent transition, which is referred to penumbra [?].

2.5.3 Cosmic Ray Trajectory Near the Earth

A particle with a rest mass m_0 and a charge e in electromagnetic unit moving in a magnetic field will experience a force $\boldsymbol{F} = e\boldsymbol{H} \times \boldsymbol{v}$, with $\boldsymbol{H}$ the field vector and $\boldsymbol{v}$ the particle velocity. A variable s, the arc of the particle trajectory, $s = vt$, happens to be more convenient and the equation of motion can be rewritten as

$$\begin{aligned}
\frac{mv}{e}\frac{d^2x}{ds^2} &= H_y\frac{dz}{ds} - H_z\frac{dy}{ds} \\
\frac{mv}{e}\frac{d^2y}{ds^2} &= H_z\frac{dx}{ds} - H_x\frac{dz}{ds} \\
\frac{mv}{e}\frac{d^2z}{ds^2} &= H_x\frac{dy}{ds} - H_y\frac{dx}{ds}
\end{aligned} \tag{2.31}$$

with $m = m_0\gamma = m_0(1-\beta^2)^{-1/2}$.

The realistic geomagnetic field is a multipole field. However, with the purpose to understand the characteristic and important features, the dipole approximation is considered here. For a dipole with moment M, one can have

$$\boldsymbol{H} = \boldsymbol{\nabla} V = \boldsymbol{\nabla}\left(\frac{Mz}{r^3}\right) \tag{2.32}$$

where V is the magnetic potential and r is the radial distance. Eq. (??) provides the components of magnetic vector field as

$$H_x = -M\frac{3xz}{r^5}, \quad H_y = -M\frac{3yz}{r^5}, \quad H_z = -M\frac{3z^2 - r^2}{r^5} \tag{2.33}$$

With an appropriate choice of unit, the equations of motion can be reduced to [?]

$$\begin{aligned} r^5\frac{d^2x}{ds^2} &= 3yz\frac{dz}{ds} - (3z^2 - r^2)\frac{dy}{ds} \\ r^5\frac{d^2y}{ds^2} &= (3z^2 - r^2)\frac{dx}{ds} - 3xz\frac{dz}{ds} \\ r^5\frac{d^2z}{ds^2} &= 3xz\frac{dy}{ds} - 3yz\frac{dx}{ds} \end{aligned} \tag{2.34}$$

by a choice of a special unit of length (Störmer unit) [?, ?]

$$l_{ST} = \sqrt{\frac{M|e|}{mv}} \tag{2.35}$$

As it can be seen, the quantity l_{ST} is characterised as the radius of the circular orbit in the dipole equatorial plane.

Unfortunately, there is no general solution to the equations of motion (??). However, the theory enables limits to be set to those regions of the magnetic field configuration which are accessible to the particles coming from infinity.

Transform Eq. (??) to cylindrical coordinates (R, θ, z) where R is the projection of the radius vector $\boldsymbol{r}$ in the xy-plane and θ is the angle between the x axis and the meridian plane (Rz-plane). The coordinate configuration is shown in Figure ??. Thus, the equations of motion can be rewritten as

$$\frac{d^2R}{ds^2} = R\left(\frac{d\theta}{ds}\right)^2 + \frac{R(r^2 - 3z^2)}{r^5}\frac{d\theta}{ds} \tag{2.36}$$

$$\frac{d^2z}{ds^2} = \frac{3R^2z}{r^5}\left(\frac{d\theta}{ds}\right) \tag{2.37}$$

$$\frac{d}{ds}\left(R^2\frac{d\theta}{ds}\right) = \frac{d}{ds}\left(\frac{R^2}{r^3}\right) \tag{2.38}$$

From Eq. (??), a relation can be obtained immediately

$$R^2\frac{d\theta}{ds} = \frac{R^2}{r^3} + 2b \tag{2.39}$$

where b is the integration constant of the motion. Let ψ be the angle between the particle velocity and the meridian plane. Then, together with Eq. (??), one has

$$\sin\psi = R\frac{d\theta}{ds} = \frac{R}{r^3} + \frac{2b}{R} \quad \Longrightarrow \quad r^2\sin\psi\cos\phi - 2br - \cos^2\phi = 0 \tag{2.40}$$

Eq. (??) is the equation in polar coordinate, for the loci of the intersection points between the particles trajectories and the meridian plane. Note that the solution of the equations of motion (??) has two parameters b and $\sin\psi$, with the particle momentum hidden in r and b since the Störmer unit is used. The parameter $\frac{-2b}{\cos\phi}$ can be viewed as an impact parameter with respect to the dipole axis at the geomagnetic latitude ϕ [?].

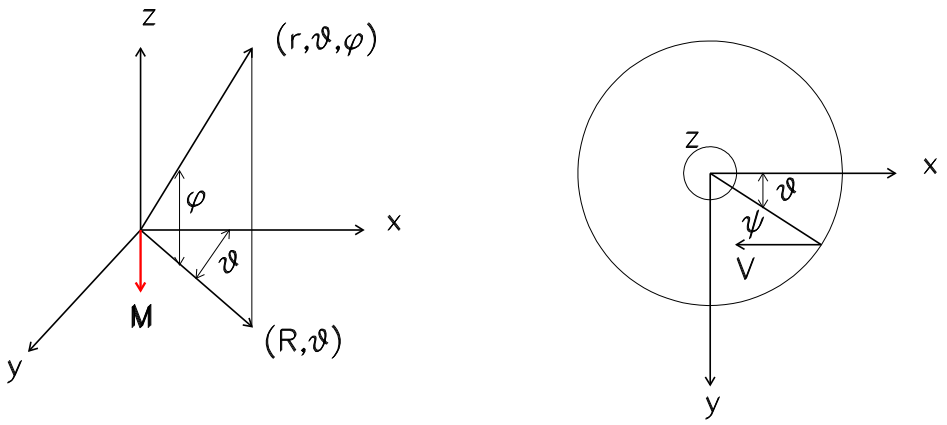

Figure 2.8: *Left: The coordinate system in which the dynamics of charged particles in a dipole field are defined. Right: The coordinate system viewed from z-axis showing the definition of the angle ψ, the angle between the particle velocity and the meridian plane (Rz-plane).*

Figure ?? shows some examples of the permitted and forbidden regions for the particle trajectories in the Earth geomagnetic field for different values of b. It can be seen that a critical value happens at $b = -1$. So, there is a critical particle momentum with which, a cosmic ray particle can reach the Earth from infinity. In the case of a proton, for example, the critical momentum is found to be about $p \simeq 59.6$ GeV/c. This value has provided the minimum rigidity needed for a proton to reach the Earth from infinity. Forbidden regions have $|sin\psi| > 1$. In Figure ??, for the cases $b = -1.1$ and $b = -1.01$, two disconnected allowed regions are found but a particle cannot reach the inner allowed region from outer region by passing through the forbidden region. However, for $b > -1$, these two regions turn to be connected so a particle can reach the inner region from infinity.

Charged particles propagating in the geomagnetic field might be trapped by the Earth. Discussions on this will be given in Chapter ?? and Chapter ??.

Since there doesn't exist an analytic solution for Eq. (??), a numerical integration method is applied for a system of differential equations of the 2nd order for a dipole case [?, ?]. For a realistic case of the multipole geomagnetic field, the equations of motion become more complicated but the dipole case can still give the principal features of the geomagnetic dynamics.

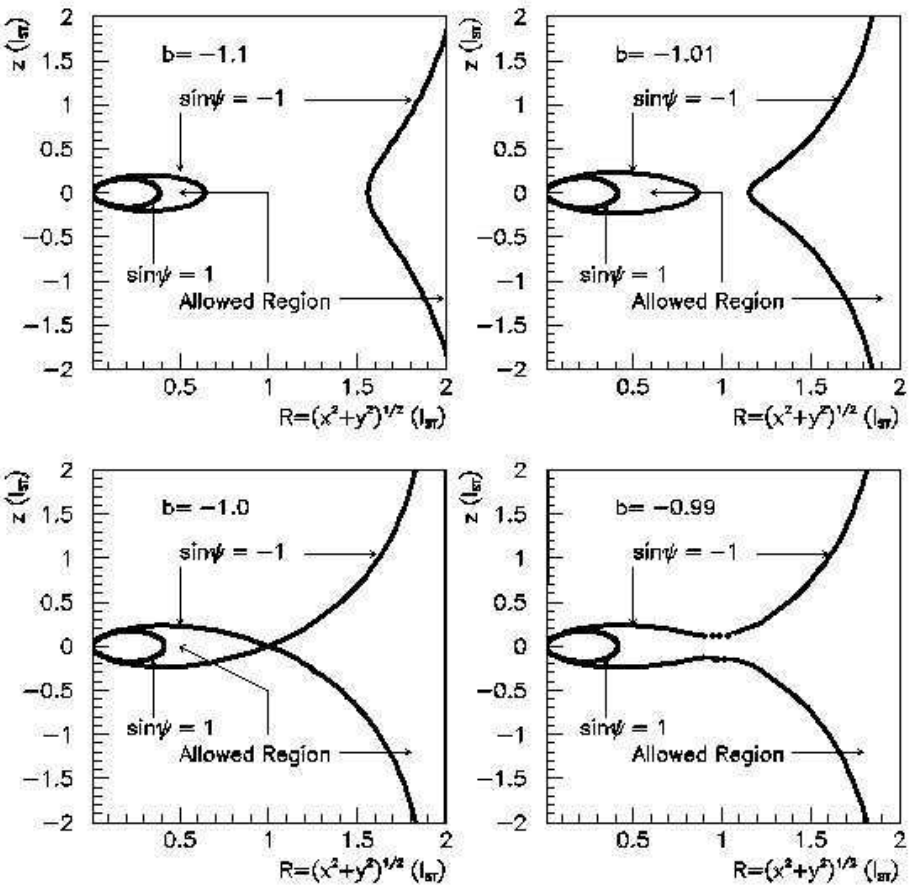

Figure 2.9: *Diagrams illustrating the regions in polar coordinate which are accessible and forbidden for the charged particle entering the geomagnetic field from infinity. Forbidden regions cannot have the relation* $|\sin\psi| \leq 1$ *to be satisfied. Boundaries between the allowed and forbidden regions are indicated.*

2.5.4 Cosmic Ray Air Shower

An air shower is a cascade of particles generated by the interaction of a single high energy primary cosmic ray particle or photon near TOA. Although cosmic ray particles are abundant, they would however, practically never hit the ground of the Earth directly but collide with nuclei in the atmosphere. During the collisions, typically for hadron interaction energies above the particle emission threshold, say, 1 GeV, secondary particles will be produced, in which, most of them are pions and nucleons. Neutral pions decay very quickly into two γ-rays. Charged pions also decay, Eq. (**??**), but with a longer lifetime [**?**, **?**]. Thus secondary pions might collide with another nucleus in the atmosphere before decaying off. These processes can produce muons and neutrinos. The fragments of the incident nucleus can also take part in the collision cascade.

A cosmic ray induced air shower has three components, electromagnetic, hadronic and muonic [**?**]. Electromagnetic cascades are initiated by high energy cosmic electrons or γ-rays. A high energy photon generates an electron-positron pair production ($\gamma \rightarrow e^+ + e^-$), each of which in turn generates high energy photons by bremsstrahlung, each of which then generates another electron-positron pair production... and so on. Because of the rapid multiplication of electromagnetic cascade, electrons and positrons turn to be the most numerous particles in cosmic ray air showers, with only a relatively small fraction of muons after a few generations [**?**]. Thus, most of the shower energy is eventually dissipated by ionisation losses of the electrons and positrons. Hadronic cascades are generated by nuclear collisions of high energy cosmic ray nucleons, for which, the secondary nucleons and charged pions could have sufficient energy to continue to multiply in successive generations of nuclear collisions until the energy per particle drops below the pion production threshold. In the process of hadronic cascades, the initial energy of the high energy nucleons or nuclei is degraded into the energy of secondary nucleons, antinucleons, pions, kaons or strange particles, which are called hadronic products. This process is referred to as hadronisation. During the hadronisation, the decays of the lower energy charged pions and kaons will contribute to the muonic component of the cascade. Particles with energies below 1 GeV are however rapidly absorbed and disappear from the shower [**?**].

Unlike electrons and positrons, the number of muons doesn't multiply but just increases as the shower develops until reaching a plateau because muons rarely interact catastrophically but only lose energy slowly by ionisation while traversing the atmosphere. An important feature for muonic shower component is that, the ratio between muons and electrons, N_μ/N_e, is sensitive to primary composition [**?**]. This fact results from that, at a fixed observation level, N_e is smaller for a heavy nucleus initiated shower than for a proton initiated one of the same energy. However, N_μ is comparable for both, even larger, for a heavy nucleus initiated shower. Thus, since muons come from hadronic decays, a measurement of muons can be a good probe for evaluating the signal to background ratio in proton-induced showers [**?**].

When a shower starts to develop, the number of particles increases rapidly as the shower moves downwards in the atmosphere. On their way and in each interaction however, the particles also lose energy. So, after some point, the number of particles reaches a

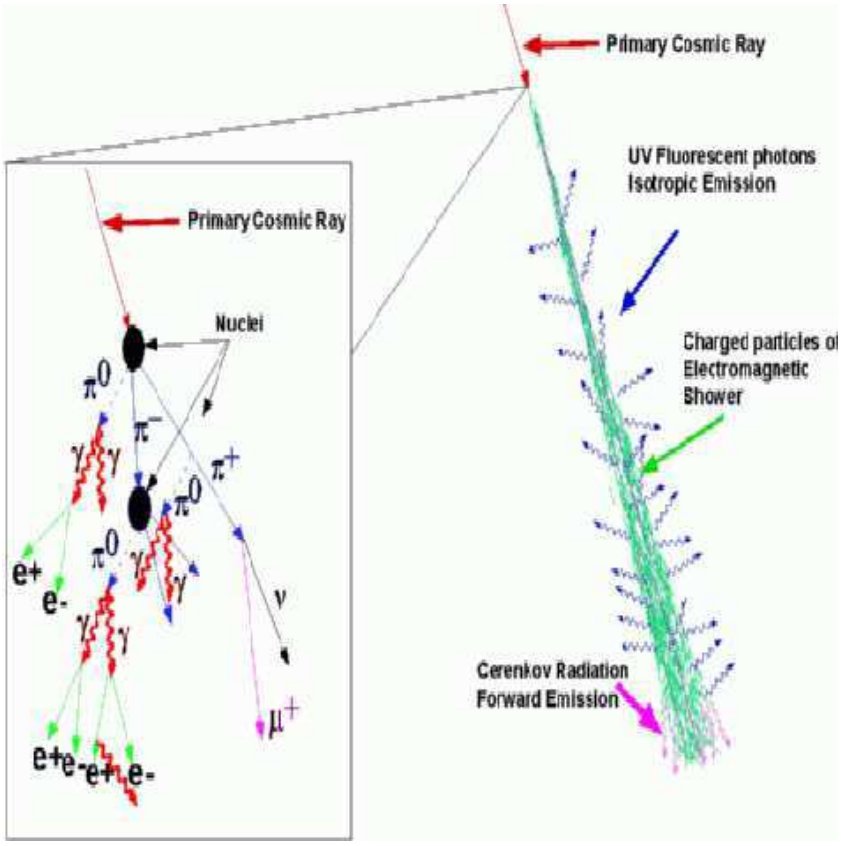

Figure 2.10: *A schematic diagram showing the development of an extensive cosmic ray air shown in the atmosphere [?]. Downwards the primary particle is the shower axis. A cosmic ray particle initiates a cascade followed by the production of pions, which in turn, decay into electromagnetic particles or yield non-hadron particles. γ-rays from neutral pion decays or bremsstrahlung of electrons/positrons form pair production speed and multiply the electromagnetic cascade. Charged pions decays contribute the muonic cascade. Čerenkov radiation and fluorescence light are also emitted with the growth of the shower. Along the shower axis, the shower grows broader and more intense and a disc-like (shower cone) distribution forms. In the cone, the innermost contains mesons and heavier particles, embedded by muonic cascade and with electromagnetic cascade the outermost.*

maximum but eventually attenuates as more and more particles fall below the threshold for further particle production. Along the direction of the primary particle generating the cascades, there is an axis, along which, most particle can be found in a kind of disc (shower cone). In the shower, particles might also emit lights in two ways: Čerenkov radiation, which is a form of shock wave and is emitted along the shower axis with only a small angle, resulting from the energetic particles whose velocities are greater than the light speed in the atmosphere; fluorescence light, which is emitted in all direction, resulting from particles which are passing nearby the molecules, for example, nitrogen, in the atmosphere, inducing transitions. A schematic diagram of an air shower developed in the air is shown in Figure **??**.

Only a small fraction of the particles could eventually reach the Earth ground. The amount of such particles depends on the energy and type of the incident cosmic ray generating the cascade. Nevertheless, actual numbers are subject to large fluctuations [**?**, **?**].

When a very high energy cosmic particle initiates a cascade and a great amount of secondary particles are produced, an extensive air shower (EAS) develops. The extensive air shower is the unique methodology to study ultrahigh energy cosmic rays. With fluorescence detectors [**?**, **?**], it is possible to reconstruct the shower profiles. Then, with the measured profile of particle density, the energy of the primary particle generating a shower is calculated; from the number of muons, the shape of shower front and the rise time of the pulse in the detectors, the particle mass is then calculated. However, the measurements are subject to the fluctuations in shower development. Measurements made by fluorescence detectors and ground arrays agree with each other remarkably well. The determination of energies obtained from two different methods agree within 20-30%, with the error estimated as 15-20% for the good events [**?**].

2.6 Ultra High Energy Cosmic Rays

Cosmic Rays with energies up to 10^{14} eV can be directly detected [**?**] while 'Ultra-High Energy Cosmic Rays' (UHECR), with $E > 10^{18}$ eV can only be detected by EAS.

Figure **??** [**?**] shows the all particle spectrum, i.e., the differential flux of the total number of cosmic ray particles as a function of energy for which, no identification by particle type is made. The figure shows that the energy spectrum exhibits little structure and can be well expressed with a broken power law $\propto E^{-\alpha}$: At the energy $E \simeq 4 \times 10^{15}$ eV, called the 'knee', the flux is characterised by a spectrum index $\alpha \simeq 3.0$. Above the so called 'ankle' at $E \simeq 5 \times 10^{18}$ eV, the spectrum turns again to a characteristic spectrum index $\alpha \simeq 2.8$.

The breaks of slope of the spectrum on Figure **??** imply three regimes and possibilities for the origins of cosmic rays. Below the knee, the bulk of cosmic rays are believed to be generated by strong supernova shocks [**?**, **?**]. The change of slope at the knee could imply that cosmic rays have experienced a different acceleration from a different origin [**?**]. Some suggest that the knee is the result of acceleration at a single, nearby and young

supernova [?]. Some propose the knee to be a signature of the production of a new and weakly interacting particle which has taken away the energy so that one cannot see it in the atmospheric cascades [?]. The actual spectrum is then with no modification at all and the break of the slope is a signal of phenomenon of the production of new particles in the cascades.

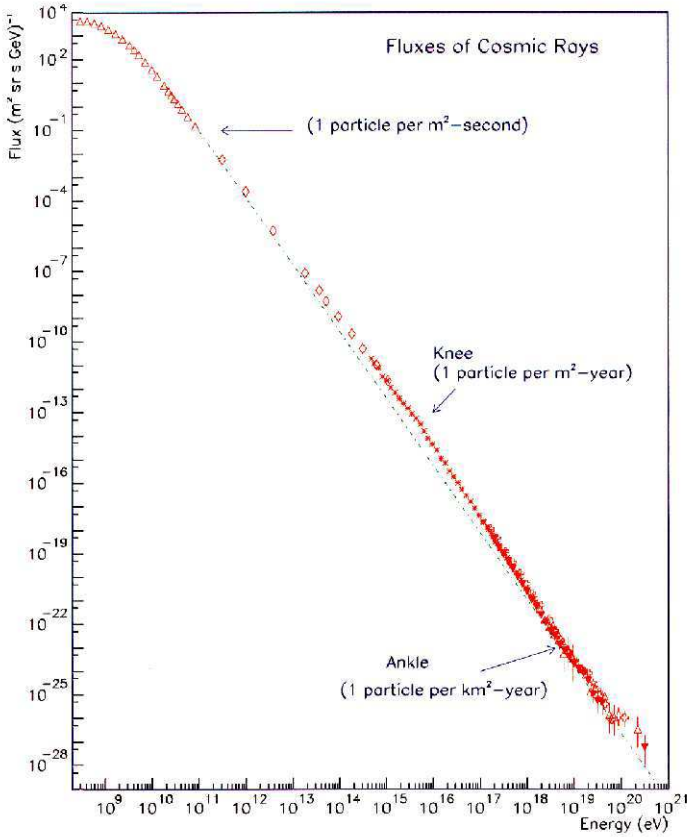

Figure 2.11: *All particle spectrum in function of energy for three regimes of the propagation of cosmic rays [?].*

For particles with energies $E > 10^{20}$ eV, the ordinary signal carriers such as protons, nuclei, electrons and photons, will suffer interactions with the omnipresent 2.73 K microwave background radiation (CMB), the thermal relics of the Big Bang, that limit the attenuation length of the highest energy particles to less than 50 Mpc [?]. For example, a high energy proton embedded in CMB will produce pion ($p + \gamma_{2.73K} \rightarrow N + \pi$) with a threshold [?]

$$E_{th} = \frac{m_\pi(m_p + m_\pi/2)}{\varepsilon} \simeq 5 \times 10^{19} \left(\frac{\varepsilon}{10^{-3}\text{eV}}\right)^{-1} \quad \text{eV} \tag{2.41}$$

where $\varepsilon \sim 10^{-3}$ eV is a typical CMB photon energy. For $E \geq E_{th}$, the proton will lose a significant amount of energy on a length scale of $l_\pi \simeq 1/(\sigma_\pi n_{CMB}) \simeq 20$ Mpc, where

$n_{CMB} \simeq 422$ cm^{-3} is the number density of CMB photons, and the pion production cross section is taken $\sigma_\pi \simeq 100$ mbarn $= 10^{-25}$ cm^2. So, the energy spectrum will exhibit a depletion of particle above E_{th}. This is the so called Greisen-Zatsepin-Kuzmin (GZK) cutoff [?, ?]. Such a character is caused by the fact that the production of pions needs the photons from the high energy tail of their distribution and the number of these photons exponentially increases when the proton energy becomes higher [?]. The same phenomenon also occurs for nuclei, electrons and photons [?]: UHE nuclei lose energy due to e^-/e^+ pair production in the collisions with CMB photons; UHE electrons are losing energy very fast on microwave radiation; UHE photons are absorbed on extragalactic radio background. Numerically, the energy of the GZK cutoff is generally given for a model where sources are uniformly distributed in the extragalactic region. However, the measurement data of energy spectrum do not confirm such a cutoff [?, ?]. So far, two experiments have measured two reliable UHECRs: the Fly's Eye array [?], by detecting fluorescence light produced by EAS, gets the primary energy being $3^{+0.36}_{-0.54} \times 10^{20}$ eV; the AGASA array [?], by detecting the distribution of shower particles, estimates the primary energy being 1.7-2.6$\times 10^{20}$ eV. Thus, the spectrum measurement above the GZK cutoff then provides a test of potential models for UHECR sources. At this moment, because of the conflict between the observations and the models, neither a galactic nor an extragalactic origin is excluded [?, ?, ?, ?, ?]. In addition, the astrophysical solution to UHECR problem is strongly disfavoured today. Therefore, some new understandings of the elementary particle solutions are proposed [?, ?]. Since this subject is beyond the discussion of this thesis, only the draft of conclusions are listed below.

In the Left-Top of Figure ??, the proton spectra are calculated for a model where the sources are uniformly distributed in the Universe with cosmological evolution of the sources and without it. The evolutionary case is given as $(1+z)^m$ with $m = 4$, where z is redshift parameter. The case without evolution, $m = 0$, is calculated with different cutoffs of generation spectra described by maximal energies $E_{max} = 3 \times 10^{20}$, 1×10^{21} and ∞ eV. The calculations are compared with AGASA data [?]. In this model, the GZK cutoff is clearly seen, in contrast to the observed spectrum. In the Right-Top of Figure ??, a model of overdensity is compared with the observed spectrum data, the model with uniformly distributing sources and observed local overdensity, $n/n_0 = 2$. This model shows that the GZK cutoff will be less pronounced with much higher overdensity. However, this result is in contrast to the observation of cosmological isotropy. The result by applying a model of galactic origin is shown in the Left-Bottom in Figure ??. The model shows no GZK cutoff but gives a higher anisotropy, shown in the Right-Bottom in Figure ??, which is calculated as the ratio of the flux from the direction of the disc to the total flux.

Some new physics solutions are suggested since the astrophysical solution is disfavoured. They are [?, ?, ?]:

- *Superheavy Dark Matter* Longlived Superheavy Dark Matter Particles could be accumulated in galactic halos. These particles are naturally produced at post-inflationary epoch and can close the Universe or contribute some fraction to Cold Dark Matter. These particles can be longlived, with lifetime exceeding the age of the Universe. Decay of these particles produce UHECR without GZK cutoff.

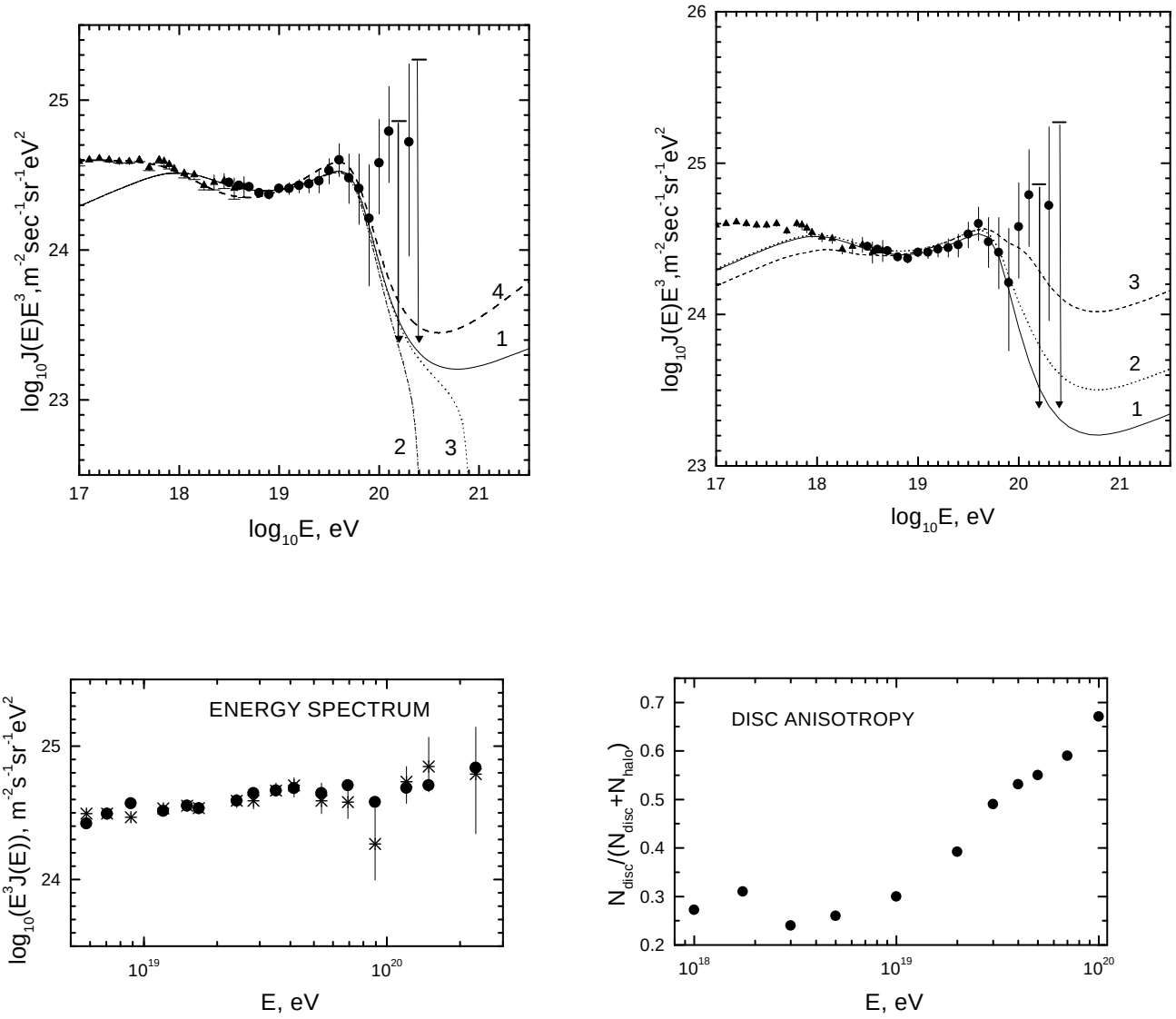

Figure 2.12: *Left Top: Calculated diffuse spectra for uniform distribution of UHECR sources in the Universe in case of cosmological evolution of the sources (curve 4) and without evolution (curves 1-3). Right Top: Diffuse energy spectra with local overdensity of UHECR sources. Curves 1, 2 and 3 are given for uniform distribution of the sources, for overdensity* $n/n_0 = 2$ *and* $n/n_0 = 10$*, respectively. Left Bottom: Energy spectra of UHECR of galactic origin, with the calculated flux* • *and the data* ∗*. Right Bottom: Disc anisotropy of model of UHE iron nuclei. Figures are referred from [?]. Data compared are referred from [?].*

- *Topological Defects (TD)* There are different mechanisms of production of UHE particles by TD. In some cases, TD become unstable and decompose to constituents fields (superheavy Higgs and gauge bosons), which then decay to ordinary particles. This mechanism works for cusps and superconducting cosmic strings. In case of monopoles and antimonopoles connected by strings, high energy particles are produced at annihilation of monopole-antimonopole pairs. The most promising candidates are necklaces and monopole-antimonopole pairs connected by strings. UHECR from TD has spectrum with a soft GZK cutoff which does not contradict the observations.

- *Resonant Neutrinos* Very high energy neutrinos are resonantly absorbed by target neutrinos comprising Hot Dark Matter (HDM): $\nu + \bar{\nu}_{HDM} \to Z^0 \to$ hadrons. In the case of HDM neutrinos have locally enhanced density, the GZK cutoff is absent or softened. Very large flux of primary neutrinos with superhigh energies are needed for this hypothesis.

- *Light Gluino* Light gluinos can be effectively produced by TD or in pp-collisions in astrophysical sources. They weakly degrade in energy in interacting with microwave radiation. The interaction of UHE light gluino with nucleons is similar to that of UHE proton. Light gluino is disfavoured by accelerator experiments.

- *Strongly Interacting Neutrino* In extra-dimension theories, for example, neutrinos can have large scattering cross section off the nucleon. In this case, neutrinos can be the carriers of UHE signal from remote astrophysical sources.

- *Lorentz Invariance Breaking* In the case for protons with energies of 10^{20} eV and even higher, the centre of mass energy could be insufficient for the production of pions in collisions with microwave photos.

2.7 Propagation of Cosmic Rays

2.7.1 Propagation Equation (Diffusion Equation)

The propagation of cosmic rays in the Galaxy is understood as a diffusion process where the galactic magnetic irregularities serve as scattering centres. Consider a control volume in a coordinate space, with a frame with respect to the galactic centre with $\hat{z}$ as a perpendicular unit vector to the disc that is shown in Figure **??**. The evolution equation of population of particles of species i, $N_i(t, \boldsymbol{r}, E)$, in the Galaxy in the energy interval $(E, E + dE)$ is given as [**?**, **?**, **?**]

$$\begin{aligned}\frac{\partial N_i}{\partial t} &= \boldsymbol{\nabla} \cdot (D \boldsymbol{\nabla} N_i) - \boldsymbol{\nabla} \cdot (N_i V_c \hat{z}) + Q_i + \frac{\partial}{\partial E}\left[\left\langle \frac{\partial E}{\partial t} \right\rangle_i^{ion} N_i\right] \\ &+ \left(\sum_{j \neq i} n v \sigma_{ji} N_j - n v \sigma_i N_i\right) + \left(\sum_{j \neq i} \frac{N_j}{\tau_{ji}} - \frac{N_i}{\tau_i}\right)\end{aligned}$$

$$+ \quad \left(\frac{\partial}{\partial E} \left[\left\langle \frac{\partial E}{\partial t} \right\rangle_i^{reac} N_i \right] - \frac{1}{2} \frac{\partial^2}{\partial E^2} \left[\frac{\triangle E^2}{\triangle t} N_i \right] \right) \tag{2.42}$$

- $\frac{\partial N_i}{\partial t}$ is the time variation of the population of particle species i. Since the data on cosmogenic isotopes, on meteorites and on lunar rock show that the intensity of cosmic rays on the Earth has not changed more than a factor of 2 within the last $t \simeq 4 \times 10^9$ years [**?**], a stationary picture of the propagation of cosmic rays are often considered within typical escape time scale.

- $\boldsymbol{\nabla} \cdot (D \boldsymbol{\nabla} N_i)$ represents the diffusion of cosmic rays in the galactic magnetic field. D is generally a tensor but can be approximated by supposing the diffusion of cosmic rays are isotropic in the Galaxy. D depends principally on energy while the dependence of others can be negligible.

- $\boldsymbol{\nabla} \cdot (N_i V_c \hat{z})$ is the convection term of the ions. The z-component can be viewed as the resultant of all individual contributions from the sources distributed in the galactic disc. The convection model [**?**] sets an upper limit on the velocity $V_c \leq$ 20 km/s with a gradient $\partial V_c / \partial z \leq$ 7 km s^{-1} kpc^{-1}. It must be emphasised that this term is just an approximation and that the general phenomenon is much more complicated.

- Q_i is the term of the rate of injection of particles of species i from sources per unit volume. In particular, $Q_i = 0$ for secondary particles.

- $\frac{\partial}{\partial E} \left[\left\langle \frac{\partial E}{\partial t} \right\rangle_i^{ion} N_i \right]$ takes account of the effect of energy gains and losses of the ions in ISM upon the energy spectrum, in the interval $(E, E + dE)$. The principal two contributions are the energy losses due to ionisation in neutral material and the Coulomb interaction in the ionised regions. This term is important at low energies and becomes negligible for $E \geq$ 300-400 MeV/n.

- $\left(\sum_{j \neq i} n v \sigma_{ji} N_j - n v \sigma_i N_i \right)$ characterises the particle gain and loss term for species i. It consists of a term of the production of species i by fragmentation of heavier elements on the ISM, and also a term of destruction corresponding to the fragmentation of i on other lighter nuclei. σ_{ij} is the production cross section of species i by another species j. n is the density of the interstellar gas and v is the velocity of the nucleus. σ_i is the inelastic cross section of nuclear spices i with nuclei of the interstellar gas.

- $\left(\sum_{j \neq i} \frac{N_j}{\tau_{ji}} - \frac{N_i}{\tau_i} \right)$ takes into account the effect of radioactive decay. τ_{ji} is the lifetime of radioactive nucleus of type j decaying to type i and τ_i is the lifetime of a nucleus of type i with respect to decay.

- $\frac{\partial}{\partial E} \left[\left\langle \frac{\partial E}{\partial t} \right\rangle_i^{reac} N_i \right]$ takes into account the reacceleration of cosmic rays of species i. The reacceleration takes place when cosmic ray particles are scattered with magnetohydrodynamic turbulences in ISM during its diffusion. This term becomes more

noticeable for light elements, particularly H and He [?] and more important at low energy $E \leq 400$ MeV/n [?].

- $\frac{1}{2}\frac{\partial^2}{\partial E^2}\left[\frac{\triangle E^2}{\triangle t}N_i\right]$ takes into account the fluctuations in the systematic energy gain. This second-order term introduces more difficulties in solving the diffusion equation. However, this term can be evaluated as a dependence of rigidity [?].

Generally, a complete solution of the diffusion equation (??) requires all kinds of nuclei. So, one has to write down a system of coupled equations for each species by requiring the parameters, such as observable density, diffusion coefficient, fragmentation and inelastic cross sections, lifetime due to decay and escape time for each species are all known. In addition, the form and the size of the propagation region of cosmic rays in the Galaxy and the distribution of interstellar medium and also of the sources have to be introduced.

Apparently, Eq. (??) is non-linear and there doesn't exist an analytic solution for this 3-D transport problem. However, a generalised analytic solution is possible with some assumptions [?, ?]:

(i) the propagation region of cosmic rays in the Galaxy is a cylindrical symmetry of radius $R = 15$ kpc and height $2h_h$. The cosmic ray sources are distributed in a disc of thickness $2h_g$, $h_g \simeq$ 100 pc, inside the cylinder;

(ii) the spatial distribution of the sources and their time evolution are independent of the kind of nuclei. Thus, $Q_i(t, \boldsymbol{r}, E) = q_i(E)\chi(t, \boldsymbol{r})$ where q_i is the constant which determines the relative abundance of nucleus i in the sources;

(iii) the density of the gas inside the disc is $n_g = 1$ cm^{-3} and, outside the disc, called halo, the density is n_h, $n_h \ll n_g$. Practically, $n_h \leq 10^{-2}$-$10^{-3} n_g$. So, the halo medium doesn't significantly affect the fragmentation of cosmic rays. Thus, $n_h = 0$ is used in this approach. The length scale of the halo, h_h, is in fact an adjustable parameter, of the order of 3-10 kpc;

(iv) the diffusion tensor D is isotropic. The diffusion coefficients of cosmic rays are D_g and D_h in the disc and in the halo respectively;

(v) relevant boundary conditions for the propagation equation. At the boundaries of the halo, $\Sigma: \ z = \pm h_h$, and of the disc edge in r-direction, $r = \pm R$, cosmic ray particles can escape freely into the intergalactic space, but, the density of cosmic rays at the boundary is negligible. At the boundary between the disc and the halo, the density and the diffusion flux follow the continuity conditions. Sources are distributed in the disc region but there is neither source nor flux at $z = 0$. In brief, the boundary conditions are written as

$$Q_i|_{z=o} = 0, \quad \left.\frac{\partial N_i}{\partial z}\right|_{z=0} = 0, \quad N_i|_{r=\pm R} = 0, \quad N_i|_{z=\pm h_h} = 0 \tag{2.43}$$

(vi) the energy-dependent term is neglected because the energies of the particles interested are above the fragmentation threshold, which is larger than several hundred MeV. So, the term taking into account the ionisation losses can be neglected. With such energies, the particles can be considered as being free of solar modulation effects and reacceleration as well.

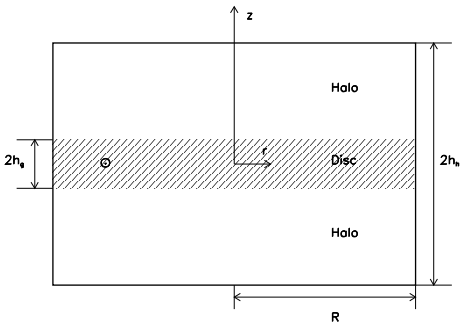

Figure 2.13: *Schematic modelisation of the propagation region of cosmic rays in the Galaxy according to [?]. The symbol ⊙ denotes the position of the Solar System.*

The diffusion equation (**??**) can then be treated analytically under these simplifications on the basis of Bessel functions and the solution can provide the principal characteristics of the flux. Nevertheless, it is clear that an analytic treatment quickly becomes limited as soon as more realistic models are desired. Global complete solution for Eq. (**??**) can be achieved only numerically. Numerical techniques without neglecting the effects of convection, energy loss or reacceleration are performed basically on the analytic solution with the conditions that all the non-linear terms are for the secondaries [**?**, **?**, **?**] and have shown good agreement with the measurements.

2.7.2 Weighted Slab Model

For the transport equation (**??**) under the simplifications mentioend above, there exists an analytic solution which can be approached by different models. In solving Eq. (**??**), one can change the function N_i by introducing a Green function and a new function $N_i^{(\sigma)}$, which represents the population of nuclei i after traversing a path length, ξ, in the

interstellar material, such that [?]

$$N_i(t, \boldsymbol{r}) = \int_0^\infty N_i^{(\sigma)}(\xi) G(t, \boldsymbol{r}, \xi) d\xi \tag{2.44}$$

where ξ is in unit of g/cm^2. It can be seen that the function G here weights the contribution of each path length ξ that is referred to 'Path Length Distribution'. With relation of Eq. (??), Eq. (??) can then be decomposed into two equations for G and $N_i^{(\sigma)}$ separately, i.e.,

$$nv\frac{\partial G}{\partial \xi} + \frac{\partial G}{\partial t} \quad - \quad \nabla \cdot (D \nabla G) = \chi \delta(\xi) \tag{2.45}$$

$$\frac{dN_i^{(\sigma)}}{d\xi} = \left(\sum_{j \neq i} \sigma_{ji} N_j^{(\sigma)} - \sigma_i N_i^{(\sigma)} \right) \quad + \quad \left(\sum_{j \neq i} \frac{N_j^{(\sigma)}}{nv\tau_{ji}} - \frac{N_i^{(\sigma)}}{nv\tau_i} \right) + q_i \delta(\xi) \tag{2.46}$$

From Eq. (??) and (??), it is clear to see that the diffusion of the particles and their fragmentation can be independently investigated: G doesn't depend on the fragmentation and can be analytically solved as a combination of Bessel functions thus allowing to study specifically the diffusion of the nuclei in the Galaxy; $N_i^{(\sigma)}$ satisfies a first-order differential equation that is analytically resolvable in ξ. The technique in solving Eq. (??) is similar to that in the diffusion equation. In addition, Eq. (??) is equivalent to the equation for the density of cosmic rays in the 'Slab Model' [?], in which, it is assumed that all particles traverse the same amount of material between 0 and ξ, i.e., there exists a 1-1 relation between path length ξ and the produced species. This is identical to the path length distribution by setting

$$G(t, \boldsymbol{r}, \xi) = \delta(\xi - \xi_0) \tag{2.47}$$

It is obvious that the Slab Model is an oversimplification while in reality, high energy particles are found to span over a wide range of different lengths, behaving like a double exponential distribution [?]. However, the Slab Model can still represent some rough but important characteristics of the propagation of cosmic rays, especially the ratios of secondaries to primaries or spallation products to spallation sources. In reality, all one has to do is to modify the results calculated by the Slab Model by considering an appropriate path length distribution

2.7.3 Leaky Box Model

Another approach is the Leaky Box Model, which is currently and widely used. This model has the advantage of a system with analytically linear equations and also presents good predictions.

Typically, high energy particles traverse about 5-10 g/cm^2 of ISM material [?]. This deduces a time scale of about 10^7 years that cosmic ray particles remain within the Galaxy. But, with a typical dimension of the Galaxy, of the order $\sim$ 10 kpc, if high energy cosmic

rays propagate freely at a velocity close to that of light, they would escape the interstellar space in $3 \sim 4 \times 10^4$ years, which is not enough to produce the spallation products. Thus, the particles must propagate by much more tortuous paths until they escape from the Galaxy. Therefore, there exists a confinement volume, within which, cosmic rays propagate before they escape.

In the Leaky Box Model, it is assumed that high energy cosmic rays diffuse freely inside the confinement volume and they are reflected at the boundaries, with an escape time scale. In this case, the diffusion is assumed to take place rather rapidly so that the density of cosmic rays in the whole Galaxy remains constant. Under such conditions, the link between the diffusion model and the Leaky Box Model is [?, ?]

$$\boldsymbol{\nabla} \cdot (D \boldsymbol{\nabla} N_i) \longleftrightarrow -\frac{N_i}{\tau_i^{esc}} \tag{2.48}$$

where τ_i^{esc} is the parameter in time which characterises the escape of cosmic rays from the Galaxy. In addition, the physical parameters describing the Galaxy are taken as the mean values

$$n \longleftrightarrow \bar{n} \qquad Q_i \longleftrightarrow \bar{Q}_i \tag{2.49}$$

With the relations (??) and (??), the diffusion equation (??) is then changed to

$$\frac{\partial N_i}{\partial t} + \frac{N_i}{\tau_i^{esc}} = \bar{Q}_i + \left(\sum_{j \neq i} \bar{n} v \sigma_{ji} N_j - \bar{n} v \sigma_i N_i \right) + \left(\sum_{j \neq i} \frac{N_j}{\tau_{ji}} - \frac{N_i}{\tau_i} \right) \tag{2.50}$$

The Leaky Box Model immediately leads to an exponential path length distribution. Consider the case of stable nuclei, then Eq. (??) is changed to

$$\bar{n} v \frac{\partial G}{\partial \xi} + \frac{G}{\tau_{esc}} = \chi \delta(\xi) \quad \Longrightarrow G(\xi) = C_0 \exp\left(-\frac{\xi}{\xi_{esc}} \right) + \tau_{esc} \chi \delta(\xi) \tag{2.51}$$

where $\xi_{esc} = \bar{n} v \tau_{esc}$ is the amount of material traversed by cosmic ray particles from their sources until they escape.

This exponential path length distribution, however, is an oversimplification. Current studies conclude that the path length distribution is not a pure exponential. The measured secondary-to-primary ratios [?] at energies greater than a few GeV/n, is found to decrease with increasing energy. This fact is interpreted as the consequence of the decrease with increasing energy of the mean amount of matter traversed by the observed cosmic ray particles, i.e., decreasing as an inverse power law in total energy or in rigidity. In addition, by taking into account the effect of solar modulation, the path length distribution below 1 GeV/n is also energy dependent [?]. Taking all observed data, the best-fit path length distribution is given as [?]

$$\xi_{esc} = \begin{cases} 31.6 \beta R^{-0.6}, & R > 4.7 \text{ GeV} \\ 12.5 \beta, & R < 4.7 \text{ GeV} \end{cases} \tag{2.52}$$

under the solar modulation $\Phi = 500$ MV where ξ is in unit of g/cm^2, $\beta = v/c$ and R is the magnetic rigidity.

The Leaky Box Model is widely used because of its simplicity. However, if all cosmic ray informations are be taken into account, (e.g., the energy loss by ionisation), or the interactions between cosmic rays and cosmic plasma, (e.g., the reacceleration), the diffusion approximation is, in turn, better substantiated. And, the characteristic path length distribution then depends on the type of magnetic field irregularities: $\xi_{esc} \propto R^{-1/3}$ in the case of a Kolmogorov-type spectrum of turbulence and $\xi_{esc} \propto R^{-1/2}$ in the case of a Kraichnan-type turbulence [**?**].

2.7.4 Examples of Solution

?? *(a) Spectral Index*

Consider the steady Leaky Box Model without the effect of solar modulation, with energies greater than 1 GeV/n. Diffusion Eq. (**??**) then reduces to

$$\bar{Q}_i(E) \simeq N_i(E)\left(\frac{1}{\tau_i^{esc}(E)} + \frac{1}{\tau_i^{spall}}\right) = \frac{N_i(E)}{\tau_i^{esc}(E)}\left(1 + \frac{\tau_i^{esc}(E)}{\tau_i^{spall}}\right) \tag{2.53}$$

The production rate of component i through spallation of heavier nuclei is relatively small compared to the most abundant primary nuclei so this term is not taken into account for the sake of simplicity. Thus, for high energy cosmic rays, Eq. (**??**) gives the relation for the cosmic ray components between the source spectra and the observed spectra

$$N_i(E) \simeq \bar{Q}_i(E) \cdot \tau_i^{esc}(E) \tag{2.54}$$

with $\tau_i^{spall}=1/(\bar{n}v\sigma_i) \simeq\ 4 \times 10^7$ years $>\ \tau_i^{esc}$. From the energy-dependent path length distribution in Eq. (**??**), one gets

$$N_i(E) \propto E^{-0.6}\bar{Q}_i(E) \tag{2.55}$$

where $\bar{Q}_i$ is the source spectrum of species i. As it will be indicated later in Section **??**, such a source spectrum would follow a power law, $\bar{Q}_i(E) \propto E^{-\alpha}$, with $\alpha \simeq$ 2.0-2.3, under the acceleration by strong shock waves of supernova remnants. So, Eq. (**??**) gives the observed spectrum of cosmic rays with a spectral index $\alpha \simeq$ 2.6-2.9, which is the index experimentally ovserved for cosmic ray spectra. Thus, the prediction by this model is in good agreement with the observations.

?? *(b)* $^3He/^4He$ *Ratio*

The rare isotope ^3He is produced by interactions of cosmic ray ^4He in the Galaxy and the $^3He/^4He$ ratio is an excellent probe of the propagation history of cosmic ^4He. Since ^3He is rare in nature, with a ratio $^3He/^4He \sim\ 3 \times 10^{-4}$ in the solar wind, cosmic ^3He is

believed to be due to the breakup of primary ^4He. In order to obtain the ratio value of $^3He/^4He$, Eq. (**??**) for such nonradioactive nuclei can be rewritten as

$$-\frac{N_i}{\tau_i^{esc}} + \sum_{j\neq i} \bar{n} v \sigma_{ji} N_j - \frac{N_i}{\tau_i^{spall}} = 0 \Longrightarrow N_i = \frac{\sum_{j\neq i} \bar{n} v \sigma_{ji} N_j}{(1/\tau_i^{esc}) + (1/\tau_i^{spall})} \tag{2.56}$$

Since ^3He is produced from the primary ^4He, the $^3He/^4He$ ratio can then be written by applying Eq. (**??**)

$$\frac{[^3He]}{[^4He]} = \frac{\tau_{esc}^{-1}(^4He) + \tau_{spall}^{-1}(^4He)}{\tau_{esc}^{-1}(^3He) + \tau_{spall}^{-1}(^3He)} \cdot \frac{\bar{n} v (^3He) \sigma_{^4He \to ^3He} N(^4He)}{\bar{Q}(^4He)} \tag{2.57}$$

where τ_{esc} can be replaced by ξ_{esc} in Eq. (**??**) by using the relation $\xi_{esc} = \bar{n} v \tau_{esc}$ and $\bar{Q}(^4He)$ can be replaced by other parameters by applying Eq. (**??**). It is necessary to know the production cross section of ^3He from the principal interaction

$$^4He + p \longrightarrow ^3He + X \tag{2.58}$$

The experiment has shown that such a process has an almost constant cross section, 54 mb, with incident energy 1 GeV/n $\leq E \leq$ 10 GeV/n [**?**]. In addition, the lifetimes of the spallation for ^3He and ^4He have to be known. With the relation between τ_{spall} and total inelastic cross section σ_{inel}^{total}, $1/\tau_{spall} = \bar{n} v \sigma_{inel}^{total}$, Eq. (**??**) can then be worked out immediately with an additional formula on σ_{inel}.

Since cosmic protons are the most abundant, the collisions between protons and helium nuclei should dominate the spallation. For $p+A$ collisions, the total inelastic cross section can be parametrised as [**?**]

$$\sigma_{inel}^{total} = \sigma_0[1 - 0.62\exp(-E_k/200)\sin(10.9E_k^{-0.28})] \quad \text{(mb)} \tag{2.59}$$

where E_k is the kinetic energy in MeV. The factor σ_o is

$$\sigma_0 = 45A^{0.7}[1 + 0.016\sin(5.3 - 2.63\ln A)] \tag{2.60}$$

where A is the mass of target in amu unit. With all the parameters fixed, Eq. (**??**) can be solved. Figure **??** shows the result of this approximation. Although with great simplification, the prediction is acceptable with an error range within 20%. For the complete calculation, one must consider the ^3He-production from the spallation of ^4He colliding with other heavier nuclei in the ISM. Such a production is scaled to a target dependence with a scaling factor of $A_T^{0.31}$ [**?**]. In addition to protons, the collisions between helium and heavier nuclei shall be considered too. The total inelastic cross sections for such $A + A$ collisions can be parametrised as [**?**]

$$\sigma_{inel}^{total} = 10\pi r_0^2 (A_p^{1/3} + A_t^{1/3} - \delta)^2 \tag{2.61}$$

where r_0=1.47, δ=1.12 and A_p and A_t are the mass numbers of the projectile particle, ^3He or ^4He, and the target respectively. The actual $^3He/^4He$ ratio is then the resultant of all contributions.

It must be indicated that, with a systematic study [?], different parameters present different weights of effect on the $^3He/^4He$ ratio. It is found that each of the path length distribution and also the production cross section of ^3He from the spallation of ^4He contributes about 10% uncertainty to the ratio prediction while the inelastic cross section, solar modulation and others denote an uncertainty less than 5% for each.

The $^2H/^3He$ ratio measurement is currently of particular interest. The reacceleration effects are stronger for lighter elements [?] hence the ^2H and ^3He data impose stronger constraints on the reacceleration parameter than the B/C, $^{sub}Fe/Fe$ data etcetera. Measurements of $^2H/^3He$ ratio over a wide energy range during the solar minimum can then provide a good test for this model. And, at higher energies, where the solar modulation effects can be neglected, the ^2H and ^3He data are directly comparable to the precise B/C and $^{sub}Fe/Fe$ data available above $\sim$ 700 MeV/n [?].

During the last decade, there have been a number of space and balloon experiments with improved sensitivity and statistics. They then impose more and more severe constraints on cosmic ray propagation models. Now, it is generally proposed that, there doesn't exist a simple model that can simultaneously reproduce all data related to cosmic ray origin and propagation [?]. This is still a big question in cosmic ray studies.

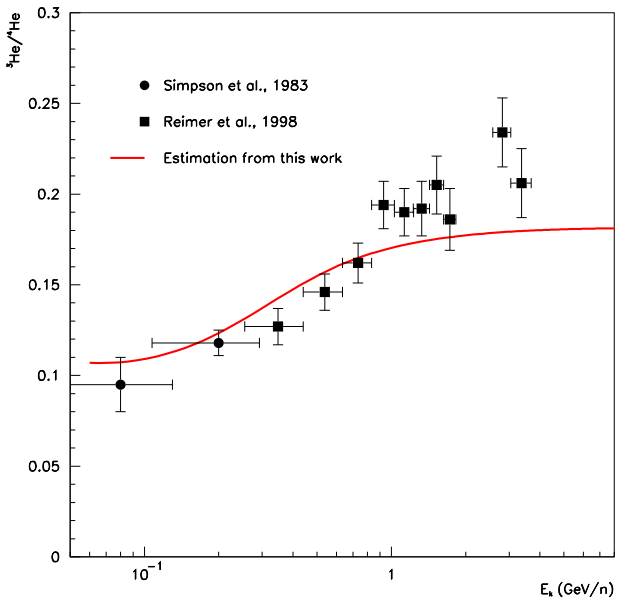

Figure 2.14: *Prediction of $^3He/^4He$ ratio for lower solar modulation, Φ = 500 MV. The production cross section of ^3He from $^4He + p \rightarrow {}^3He + X$ is taken as 54 mb for low energies [?]. The result is compared with the measurement data [?, ?].*

2.7.5 Acceleration of Cosmic Rays: Fermi Acceleration

Fermi first proposed a model for the acceleration of cosmic rays in 1949 that became known as the 'Second Order Fermi Mechanism' [?]. In this model, particles collide stochastically with magnetic clouds in the ISM and are reflected by these magnetic mirrors, which are assumed to move randomly with a typical velocity V. Those particles are involved in head-on collisions and following collisions with the mirrors. During the collisions, the particles will gain energy by head-on collisions and lose some energy by following collisions. However, head-on collisions are more probable. Thus on average, Fermi showed the particles could be accelerated statistically during the collisions.

This mechanism naturally predicts a power-law energy spectrum. This surprising result can be well understood by following Fermi's approach [?, ?].

Consider the collision between the particle and a mirror, or massive cloud, takes place such that the angle between the initial direction of the particle and the normal to the surface of the mirror is θ. Since the cloud is assumed very massive, the velocity of the particle is unchanged in the collisions. In the centre of mass frame, the mirror is moving at a velocity V. Under Lorentz transformation, the energy of the particle in this frame is

$$E' = \gamma(E + Vp\cos\theta), \qquad \gamma = \left(1 - \frac{V^2}{c^2}\right)^{-1/2} \tag{2.62}$$

The x component of the relativistic 3-momenta in the centre of mass frame is

$$p'_x = p'\cos\theta' = \gamma\left(p\cos\theta + \frac{VE}{c^2}\right) \tag{2.63}$$

Because the mirror is massive, the energy of the particle is conserved in the collisions but the x-momentum is reversed. So, after a collision, the quantity in the observer's frame (the laboratory frame) becomes

$$E'' = \gamma(E' + Vp'_x) = \gamma^2 E\left[1 + \frac{2Vv\cos\theta}{c^2} + \left(\frac{V}{c}\right)^2\right] \tag{2.64}$$

with v as the velocity of the particle. So, the energy change after a collision is

$$\frac{\triangle E}{E} = \frac{E'' - E}{E} \simeq \frac{2Vv\cos\theta}{c^2} + 2\left(\frac{V}{c}\right)^2 + \mathcal{O}\left(V^3/c^3\right) \tag{2.65}$$

Since the particle is randomly scattered by hydromagnetic waves or irregularities in the magnetic field, the probability of a collision within the angles θ to $\theta + d\theta$ is proportional to $\sin\theta d\theta$. In the case of a relativistic particle with $v \simeq c$, the average value of Eq. (??) then becomes

$$\left\langle\frac{\triangle E}{E}\right\rangle = 2\left(\frac{V}{c}\right)^2 + \left\langle\frac{2V\cos\theta}{c}\right\rangle = 2\left(\frac{V}{c}\right)^2 + \left(\frac{2V}{c}\right)\frac{\int_{-1}^{1} x\left[1 + \frac{V}{c}x\right]dx}{\int_{-1}^{1}\left[1 + \frac{V}{c}x\right]dx} = \frac{8}{3}\left(\frac{V}{c}\right)^2 \tag{2.66}$$

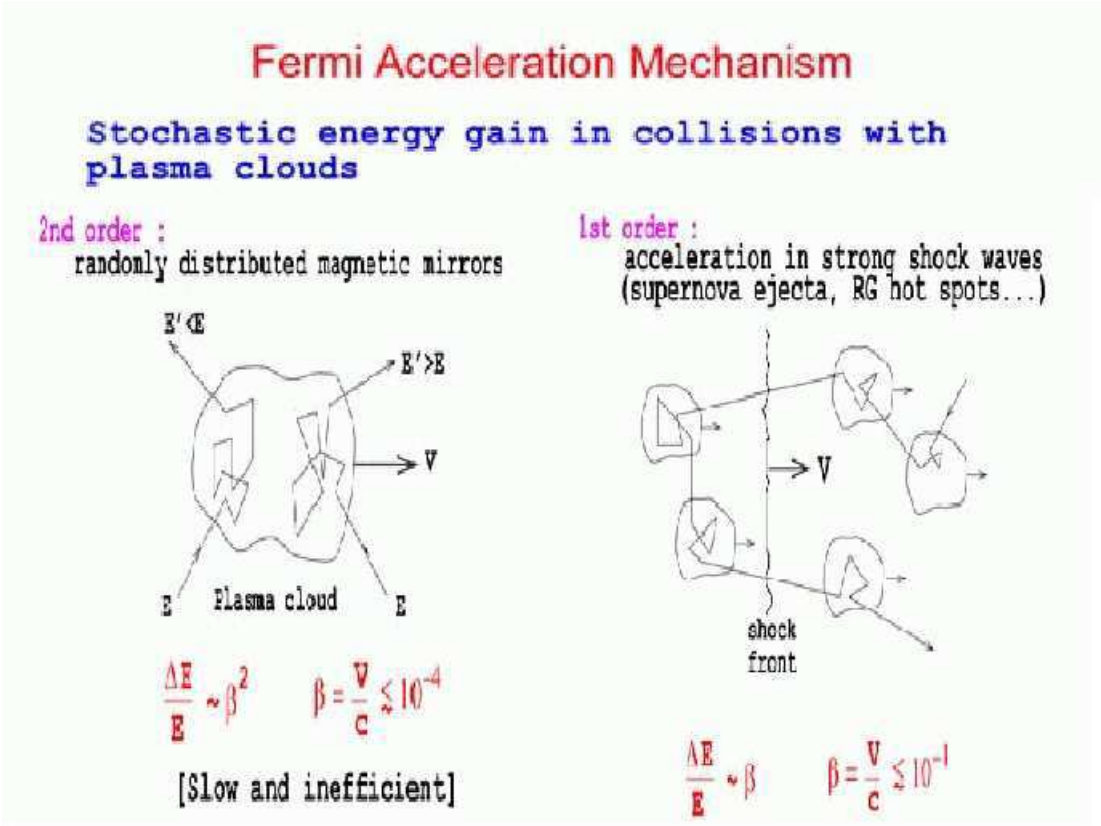

Figure 2.15: *A schematic diagram of Fermi mechanics [?]. In the second order process, particles collide stochastically with massive, randomly distributed magnetic mirrors, which in turn reflect the particles. The particles suffer both head-on and following collisions. In the first order process, velocity distribution of particles is isotropic. Particles near a shock wave can cross the shock front from either upstream or downstream region and recross the front on the way round.*

where $x = \cos\theta$. Eq. (??) illustrates the result that the average increase in energy is just a second order of V/c. Suppose the mean free path of the particle along a field line is L, then the time between two adjacent collisions is approximately $L/c\cos\theta$, which leads to an average value of $\frac{2L}{c}$. So, the average energy increase rate is

$$\frac{dE}{dt} = \frac{4}{3}\left(\frac{V^2}{cL}\right)E = \alpha E \tag{2.67}$$

Define τ as the confinement time that the particle remains in the acceleration region. Consider the simplest case that only one single particle is involved during the acceleration, the steady-state solution of Eq. (??) can then be reduced to

$$\begin{aligned} \frac{\partial}{\partial E}[b(E)N(E)] - \frac{N}{\tau} = 0 \quad &\Longrightarrow \quad -\frac{d}{dE}[\alpha E N(E)] - \frac{N}{\tau} = 0 \\ &\Longrightarrow \quad \frac{dN(E)}{dE} = -\left(1 + \frac{1}{\alpha\tau}\right)\frac{N(E)}{E} \end{aligned} \tag{2.68}$$

with $b(E) = -\frac{dE}{dt}$. So, Eq. (??) leads to a solution

$$N(E) = \text{constant} \times E^{-x} \tag{2.69}$$

where $x = 1 + (\alpha\tau)^{-1}$. Apparently, the solution has given a power-law energy spectrum.

Although the acceleration derived from the collisions between the particles and heavy interstellar clouds has given a power-law energy spectrum, it also shows that the power index in Eq. (??) depends on the local details of the model and would not give rise to a universal power law for cosmic rays arriving from the outer space of the Earth. In addition, the random velocities of interstellar clouds in the Galaxy are very small, about $V/c \leq 10^{-4}$ [?]. And, the typical mean free path of cosmic rays in ISM is about 1 pc [?]. Thus, a cosmic ray particle collides about once per year. Furthermore, energy loss by ionisation will drag the acceleration. Energy loss by ionisation becomes important when the particle energies are low. So, if cosmic rays are accelerated by this mechanism, it must accelerate the particles from low energy regions, by overcoming the energy loss by ionisation or, it must accelerate the particles very rapidly in order to contribute an average increase in energy. However, Eq. (??) shows the energy increase is very small at low energy and, the collision rate, once per year, is too slow and too insufficient to play a key role in particle acceleration. Thus, another more efficient mechanism, the so called 'First Order Fermi Acceleration' is then considered, which proposes that the acceleration is driven by shock waves.

Although second-order Fermi acceleration is not the principal mechanism dominating the acceleration of cosmic rays during their propagation, it characterises, by theoretical derivation, the reacceleration of cosmic ray particles that results from their interactions with the turbulent magnetic fields [?].

2.7.6 Acceleration of Cosmic Rays: Strong Shock Waves

??(a) Aspects of Shock Waves

Shocks waves are found ubiquitously in high energy astrophysics and play a key role in many different astrophysical environments. Shock waves form when a wave source or a disturbance is propagating at a velocity greater than the speed of sound in the medium. There is then a discontinuity between the regions behind and ahead of the disturbance. Shocks arise in astrophysical situations such as the stellar explosions or charged particles in magnetic interstellar regions.

In formulating the equations of shock waves, assume there is an abrupt discontinuity between two regions of fluid flow. In the undisturbed region ahead of the shock wave, the gas is at rest with pressure P_1, density ρ_1 and temperature T_1. Behind the shock wave, the gas moves supersonically with pressure, density and temperature P_2, ρ_2 and T_2 respectively. A more convenient way is to take a reference frame moving at a velocity U in which the shock wave becomes stationary. Thus, the undisturbed gas then flows towards the discontinuity at velocity $v_1 = |U|$ and, after it passes through the shock front, its velocity becomes v_2 with respect to the reference frame. The behaviour of the gas on crossing the shock front is described by some conservation laws in fluid dynamics:

$$\text{Continuity Equation} \qquad \rho_1 v_1 = \rho_2 v_2 \tag{2.70}$$

$$\text{Conservation of Energy Flux} \qquad \rho_1 v_1 \left(\frac{1}{2}v_1^2 + w_1\right) = \rho_2 v_2 \left(\frac{1}{2}v_2^2 + w_2\right) \tag{2.71}$$

$$\text{Conservation of Momentum Flux} \qquad P_1 + \rho_1 v_1^2 = P_2 + \rho_2 v_2^2 \tag{2.72}$$

where w is the enthalpy per unit mass, $w = \varepsilon_m + PV$, ε_m is the internal energy per unit mass and V is the specific volume $V = \rho^{-1}$. For simplicity, consider the case of shock waves in a perfect gas for which, the enthalpy is $w = \gamma PV/(\gamma - 1)$, in which, γ is the ratio of specific heats. Applying the defined w to Eq. (**??**), (**??**) and (**??**), and using the perfect gas law $\frac{PV}{T}$=constant, the ratios of pressures, densities and temperatures can be calculated as

$$\frac{P_2}{P_1} = \frac{2\gamma M_1^2 - (\gamma - 1)}{(\gamma + 1)} \simeq \frac{2\gamma M_1^2}{(\gamma + 1)} \quad (\text{if } M_1 \gg 1) \tag{2.73}$$

$$\frac{\rho_2}{\rho_1} = \frac{v_1}{v_2} = \frac{(\gamma + 1)}{(\gamma - 1) + 2/M_1^2} \simeq \frac{(\gamma + 1)}{(\gamma - 1)} \quad (\text{if } M_1 \gg 1) \tag{2.74}$$

$$\frac{T_2}{T_1} = \frac{[2\gamma M_1^2 - (\gamma - 1)][2 + (\gamma - 1)M_1^2]}{(\gamma + 1)^2 M_1^2} \simeq \frac{2\gamma(\gamma - 1)M_1^2}{(\gamma + 1)^2} \quad (\text{if } M_1 \gg 1) \tag{2.75}$$

where the Mach number of the shock wave is defined as

$$M_1^2 = \left(\frac{v_1}{c_1}\right)^2 = \left(\frac{v_1}{(\gamma P_1/\rho_1)^{1/2}}\right)^2 = \frac{v_1^2}{\gamma P_1/\rho_1} = \frac{v_1^2}{\gamma P_1 V_1} \tag{2.76}$$

and $c_1 = \sqrt{(\gamma P_1/\rho_1)}$ is the sound speed in the undisturbed region. The results in Eq. (??), (??) and (??) show that in the limit of very strong shock waves, the temperature and pressures can become arbitrarily large. That is to say, the undisturbed gas is both heated and accelerated when it passes through the shock front. But, the density ratio attains the finite value of $(\gamma + 1)/(\gamma - 1)$ in Eq. (??). For example, for a monoatomic gas, $\gamma = 5/3$ and hence $\rho_2/\rho_1 = 4$ in the limit of strong shock wave case. These results demonstrate how efficiently strong shock waves can heat gas to higher temperatures and it is found to be the physical phenomenon in supernova explosions and supernova remnants [?, ?, ?].

??*(b) Particle Acceleration in Strong Shocks*

As seen in Section ??, the second order Fermi acceleration is not efficient at all. A more efficient approximation is to consider 'First Order Fermi Acceleration'. The key difference of the first order Fermi acceleration from the second order is that, only the head-on collisions are possible between the particles and the mirror [?] so the energy increase is then $\frac{\triangle E}{E} \propto \frac{2V}{c}$. This argument remains applicable to strong shock waves. A flux of high energy particles are assumed to appear both in front and behind the shock front. For particles with high energies, the velocity of the shock is much less. So, the thickness of the shock will be normally much smaller than the gyroradius of a high energy particle. Thus, when the particles pass through the shock front in either direction, because of turbulence behind the shock front and irregularities ahead, the particles are scattered so that their velocity distribution rapidly becomes isotropic on either side of the shock front [?]. The distributions are then isotropic with respect to the reference frames in which the fluid is at rest on either side of the shock.

In formulating the first order Fermi acceleration, define $E = \beta_e E_0$ as the average energy of the particle after one collision and P_c as the probability that the particle remains within the acceleration region after one collision. Then, after k collisions, there will be $N = N_o P_c^k$ particles with energies $E = E_o \beta_e^k$ in the region. This satisfies

$$\frac{\ln(N/N_0)}{\ln(E/E_0)} = \frac{\ln P_c}{\ln \beta_e} \Longrightarrow \frac{N}{N_0} = \left(\frac{E}{E_0}\right)^{\ln P_c/\ln \beta_e} \tag{2.77}$$

Eq. (??) then presents a power law

$$N(E)dE \propto E^{-1+(\ln P_c/\ln \beta_e)}dE \tag{2.78}$$

Now consider the case of a strong shock propagating at a supersonic, but non-relativistic speed U through a stationary interstellar gas. Figure ??(a) shows the situation in the rest frame of the gas: the density, pressure, and temperature of the gas upstream and downstream of the shock front are ρ_2, P_2, T_2 and ρ_1, P_1 and T_1 respectively. When viewed in the rest frame of the shock front as in Figure ??(b), particles are arriving from downstream with a speed $v_1 = |U|$ and exiting upstream at a speed v_2. Eq. (??) gives $v_1/v_2 = 4$ with $\gamma = 5/3$ for a fully ionised plasma. Transforming into the rest frame of the downstream medium, the upstream particles appear to flow into the shock front

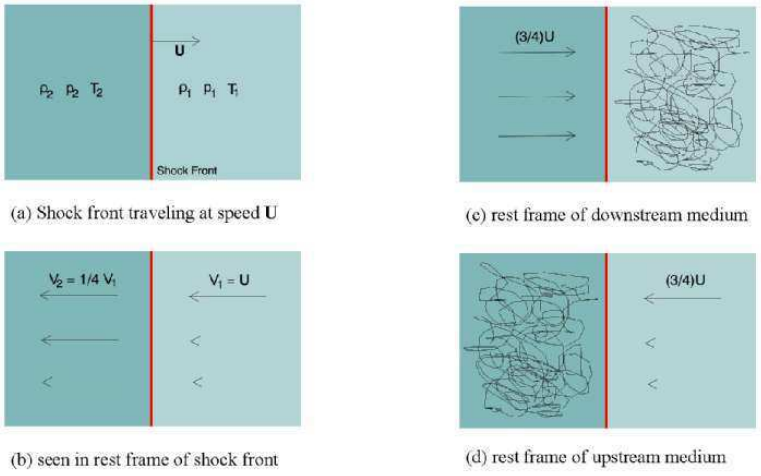

Figure 2.16: *The schematic dynamics of high energy particles in the vicinity of a strong shock wave [?]. (a) A strong shock wave propagating at a supersonic velocity, U, through a region of stationary interstellar gas with pressure, P_1, density ρ_1 and temperature T_1. Behind the shock wave, they are flow of interstellar gas in the vicinity of the shock front in a reference frame such that the shock front is at rest. In this reference frame, the ratio of the upstream to the downstream velocity is $v_1/v_2 = (\gamma+1)/(\gamma-1)$ (Eq. (??)). In the case of fully ionised plasma, the monoatomic perfect gas gives $\gamma = 5/3$ so that ratio v_1/v_2=4. (c) The flow of gas is observed in the reference frame in which the upstream gas is stationary and the velocity distribution of the high energy particles is isotropic. (d) Same argument as (c) but in the reference frame in which the downstream gas is stationary.*

with a speed of $\frac{3U}{4}$. Similarly, the downstream particles appear to flow into the shock front with a speed of $\frac{3U}{4}$ as seen in the rest frame of the downstream medium. These are illustrated in Figure **??**(c) and (d). A particle crossing from either side of the shock front is more likely to suffer a head-on collision, which then tends to send it back in the opposite direction with an increase in energy.

Under the performance of the same steps in Section **??**, the energy of a particle at a velocity $V = \frac{3U}{4}$ when passing into the downstream region from the upstream is given by the Lorentz transformation

$$E' = \gamma(E + p_x V) \tag{2.79}$$

where x is taken to be perpendicular to the shock front. Assume the shock moves non-relativistically, $V \ll c$, but the particles are relativistic. So that, $E = pc$, $p_x = (E/c)\cos\theta$. Thus, when a particle crosses a shock front, it gets an energy increase by an amount of

$$\triangle E = p_x V = pV\cos\theta \Longrightarrow \frac{\triangle E}{E} = \frac{V}{c}\cos\theta \tag{2.80}$$

The number of particles within the angles θ to $\theta + d\theta$ is proportional to $\sin\theta d\theta$ but the rate at which they approach the shock front is proportional to the orthogonal component of their velocities, i.e., $c\cos\theta$. So, the probability distribution over all particles approaching the shock is then

$$\mathcal{P}(\theta) = 2\sin\theta\cos\theta d\theta \tag{2.81}$$

Thus, the average increase of energy for particles crossing the shock front is

$$\left\langle \frac{\triangle E}{E} \right\rangle = \frac{V}{c}\int_0^{\pi/2} 2\cos^2\theta\sin\theta d\theta = \frac{2}{3}\frac{V}{c} \tag{2.82}$$

Shown in Figure **??**(d), the velocity vector of the particle is randomised without energy loss by scattering in the downstream region and it can then recross the shock front, in which, the particle gains another energy increase by the same amount. So, in a loop of crossing the shock, the average energy increase becomes

$$\left\langle \frac{\triangle E}{E} \right\rangle = \frac{4}{3}\frac{V}{c} \tag{2.83}$$

This is the Fermi first order approximation. So, by definition

$$\beta_e = \frac{E}{E_0} = 1 + \frac{4}{3}\frac{V}{c} \tag{2.84}$$

By applying the argument in [**?**], the number of particles which cross the shock is $\frac{1}{4}Nc$, which is the average number of particle crossing the shock in either direction. In the downstream region, some particles are removed from the shock at a rate $N(U - \frac{3}{4}U) = \frac{1}{4}NU$, shown in Figure **??**(b). Therefore, the fraction of the particles which have drifted

away per time is $\frac{1}{4}NU/\frac{1}{4}Nc = U/c \ll 1$. Thus, $P_c = 1 - \frac{U}{c}$. By solving Eq. (??), one can get

$$\ln P_c = \ln\left(1 - \frac{U}{c}\right) \simeq -\frac{U}{c} \quad ; \quad \ln \beta_e = \ln\left(1 + \frac{4V}{3c}\right) \simeq \frac{4V}{3c} = \frac{U}{c} \tag{2.85}$$

with $U \ll c$. So,

$$\frac{\ln P_c}{\ln \beta_e} = -1 \tag{2.86}$$

This relation predicts a differential energy spectrum of high energy particles Eq. (??) as

$$N(E)dE \propto E^{-2}dE \tag{2.87}$$

Although different from the observed spectrum, Eq. (??) derived from the first order Fermi mechanics shows the characteristic power-law spectrum. The strong waves with the velocity vectors of the high energy particles being randomised on either side of the shocks have a great applicability to most sources of high energy particles, such as, supernova remnants, active galactic nuclei and the diffuse components of external radio sources [?, ?].

On the other hand, this mechanism has an energy limit for the acceleration [?]. This model relies on the fact that the particles must be scattered in both the upstream and downstream regions by magnetic irregularities. Near the shock, the particles diffuse back and forth across the wave front and are confined for some time, which is typically about 10^5 years [?], and the upper limit of energy of particles which can be accelerated in typical supernova explosions is that for which, the gyroradii of the accelerated cosmic particles become of the same order of the shock size, such that this acceleration mechanism cannot function. The maximal possible energy a charged particle can be accelerated by this mechanism is

$$E_{max} = |Ze| r_{gyro} B \simeq 10^{15} \quad \text{eV} \tag{2.88}$$

where B is the galactic magnetic field.

Other approaches have also been proposed. In pulsars, very strong magnetic fields and very strong electric potentials can develop within the magnetospheres where particles can be accelerated to very high energies with a limit about 3×10^{19} eV [?]. Ultra-relativistic shock wave mechanism has also been considered [?]. This is similar to the original Fermi acceleration but involves highly relativistic shock waves. This mechanism gives a characteristic spectrum index 2.2-2.3, with an energy limit about 10^{18} eV/n but with large anisotropies of the velocity distribution of the accelerated particles near the shocks.

Chapter 3

Antiprotons and Study of the Universe

Antiprotons are a topic of great interest in Relativistic Heavy Ion Physics [?, ?, ?, ?, ?], because the enhanced production of antiprotons may result from the formation of the Quark Gluon Plasma (QGP) [?] and also because antiprotons might provide an experimental measurement of the density of baryonic matter produced in $A + A$ collisions due to the large $\bar{p} - p$ annihilation cross section [?]. In addition, antiprotons are also of astrophysical interest since they are a rare component of cosmic rays, of the order of $\bar{p}/p \sim 10^{-5}$. The origin of cosmic ray antiprotons has attracted a lot of attention since the first observation reported by Golden *et al.* [?]. The major part of the $\bar{p}$ flux is believed to result from the interactions of high energy cosmic ray particles with the ISM in the Galaxy. However, the measured data [?] of antiprotons appear to be higher than the expectation if these particles are assumed to be produced by such interactions. This overabundance of antiprotons has led to speculations about their origins, ranging from models where they are produced in the shrouded supernovae [?] to the annihilation of Majorana fermions created during the Big Bang [?]. In addition to the secondary galactic $\bar{p}$ component, other contributions of primary origin and of major astrophysical interest, have been considered. Contributions from the annihilation of dark matter (DM) constituents [?, ?, ?], and from the existence of primordial black holes (PBHs) [?, ?] to the cosmic ray $\bar{p}$ flux have been discussed recently. All these speculations have predicted different energy spectra at high energies [?].

In this chapter, the motivation for studying cosmic antiproton is discussed. An important AMS-related prospect for the study on the Universe, dark matter and primordial black holes, is reviewed. The existence of dark matter in the Galactic halo is investigated, dynamically and observationally. A dark matter candidate, the supersymmetric neutralino, is especially discussed. The formation of primordial black holes in the Early Universe is also investigated. The individual contribution to the cosmic antiprotons from the interaction production in the interstellar medium, the annihilation of supersymmetric dark matter and the evaporation of primordial black holes is separately discussed. Comments on this issue are given at the end.

3.1 Dark Matter in the Universe

The nature of dark matter (DM) remains one of the great mysteries of the Universe. A considerable uncertainty remains as to whether our Universe is open ($\Omega < 1$), flat ($\Omega = 1$) or closed ($\Omega > 1$), but it is quite sure that the dominant constituents of the Universe are invisible.

3.1.1 Estimates of the Density Parameter Ω

The mass density of matter in the Universe is usually given in terms of the ratio

$$\Omega_i = \frac{\rho_i}{\rho_c} \tag{3.1}$$

where ρ_i is the density of the i-th kind of matter, $\rho_c = 10.5h^2$ keV/cm^3 [?] is the critical density of the Universe, with $h = H/100$, in which, H= 50-100 km s^{-1}Mpc^{-1} as the measured value of Hubble constant. However, the density of the Universe cannot be measured directly. One way to estimate the density of the Universe is from the anisotropy of the CMB. Figure ?? [?] shows the predicted and the measured CMB anisotropy power spectra. With the adiabatic models, the location of the first acoustic peak in the spectra is predicted to be [?]

$$l \simeq \frac{220}{\sqrt{\Omega_0}} \tag{3.2}$$

giving the density of the Universe about

$$\Omega \simeq 1.0 \pm 0.2 \tag{3.3}$$

Another way to estimate the density in the Universe is to be inferred from the dynamical observations: firstly the mass of a representative class of nearby galaxies must be found by using the dynamical consideration, determining the typical relation between the luminosity and the mass of a galaxy- the mass-to-light ratio, $\Upsilon = M/L$; secondly one uses Υ to integrate over the observed galaxy luminosity function [?] to determine the overall mass density.

The mass density of luminous matter is determined by observing the solar neighbourhood. The mass-to-light ratio of the solar neighbourhood is $\Upsilon \approx 5h\ M_\odot/L_\odot$, giving $\Omega_{lum} = 0.003h^{-1}$= 0.003-0.007 [?], where $M_\odot$ is the solar mass and $L_\odot$ is the solar luminosity. If the solar neighbourhood is typical, the amount of material in stars, dust and gases, within the optical radius of galaxies yields an estimate for the mass density about [?, ?]

$$\Omega_{lum} \simeq 0.005\ (\pm 0.002) \tag{3.4}$$

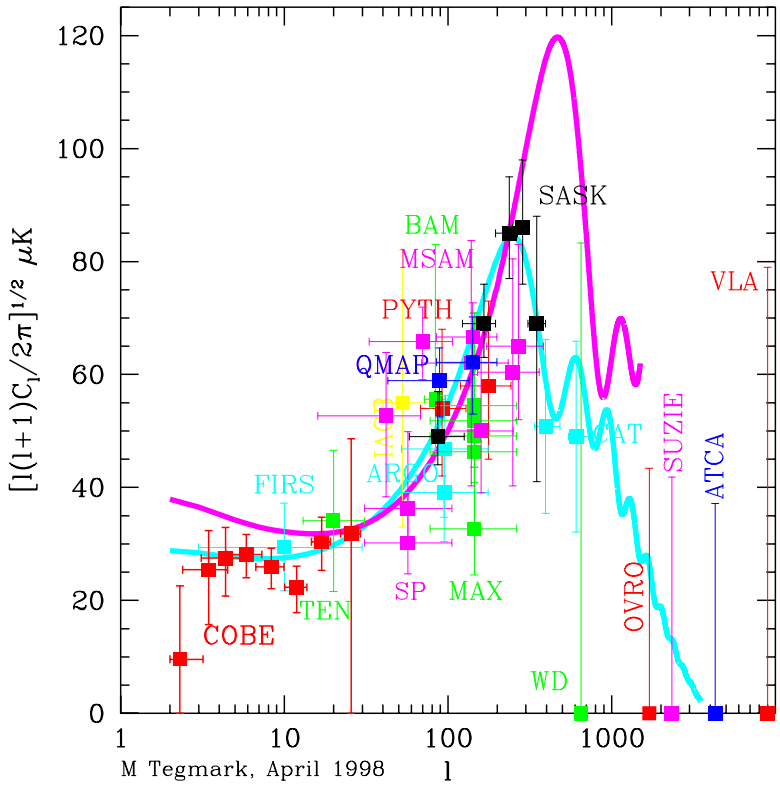

Figure 3.1: *Theoretical predictions of CMB anisotropy power spectra together with the measurement results from COBE, and a wide range of ground based and balloon borne experiments [?].*

Dynamics of cluster of galaxies constrained by the virial theorem [?] suggests a universal nonrelativistic-matter density of [?]

$$\Omega_{cluster} \simeq 0.2\ (\pm 0.1) \tag{3.5}$$

This is a reasonable range if the Universe is an open one with $\Omega < 1$. However, if the Universe is composed of all these matters, the duration of the epoch of the structure formation would be quite short, therefore requiring the fluctuations in the microwave background to be larger than the observed [?, ?]. So, this argument suggests $\Omega_{cluster} > 0.3$. In addition, if the current value of Ω is of the order of unity, then at the Planck time, it must have been 1 ± 10^{-60} [?], leading to Ω exactly unity for the aesthetic reason. This same conclusion is also given by Inflationary Cosmology [?], which provides a satisfying explanation for the homogeneity of the microwave background and requires the total density parameter of the Universe be equal to unity.

Dynamical estimates [?] for the mass-to-light ratio of elliptical galaxies by the virial theorem typically yield $\Upsilon \simeq 7h\ M_\odot/L_\odot$. For spirals, the measurement of disk rotation curves out to the optical radius yields $\Upsilon \approx$ 4-10$h\ M_\odot/L_\odot$. So, the mass in the Universe

related to such kinds of matters is

$$\Omega_{cluster} \simeq 0.016 \tag{3.6}$$

In fact, the rotation curves of spirals can be measured further out into the halos by observing globular clusters beyond the disk. In general, there is up to 10 times more invisible matter mass associated with each spiral galaxy [?]. Newton's law implies galactic dark halos with mass yielding

$$\Omega_{halo} \simeq 0.15\ (\pm 0.05) \tag{3.7}$$

Big Bang Standard Cosmology [?, ?, ?] predicts the light abundance ratios, D/H, $^4He/H$ etc, from the primordial nucleosynthesis.[1] These abundances are a sensitive function of the baryonic density Ω_B which is given with a constraint by observation [?]

$$\Omega_B \simeq 0.02\ (\pm 0.002)h^{-2} \tag{3.8}$$

This constraint is widely accepted. Figure ?? [?] shows the theoretical prediction of ^4He, D, ^3He and ^7Li abundances, from the Big Bang Nucleosynthesis. The baryon density of the primordial abundance of deuterium is given as $\Omega_B h^2 = 0.019 \pm 0.0024$, based upon the measurement [?]. The baryon density ρ_B is related to the baryon-to-photon ratio η as [?]

$$\rho_B \simeq 9 \times 10^8 h L_\odot \left(\frac{M}{L}\right)\left(\frac{L_\odot}{M_\odot}\right) \quad \mathrm{Mpc}^{-3} \quad = 9 \times 10^8 h L_\odot \left(\frac{\eta}{\eta_\odot}\right) \quad \mathrm{Mpc}^{-3} \tag{3.9}$$

However, some problems exist. First, the measurement of the baryonic density in the hot gas region of the rich cluster from X-ray emissions [?] due to bremsstrahlung $e^- + e^- \rightarrow e^- + e^- + \gamma$ in the galactic magnetic field provides the baryonic mass M_B relative to the total dynamical mass M_{total} as [?]

$$\frac{M_B}{M_{total}} \geq 0.009 + 0.05h^{-3/2} \tag{3.10}$$

Eq. (??) is in contrast to the Big Bang Nucleosynthesis constraint (??). This is called "baryon cluster crisis" [?] since it cannot be reconciled with a Universe of $\Omega_{total} = 1$. However, some arguments for the resolution of baryon cluster crisis are raised by applying more complicated inhomogeneous nucleosynthesis models, making constraint (??) slightly altered and weakened [?, ?].

In Conclusion, dynamical arguments have led to the assumption that there is a great fraction of the mass in the Universe invisible, i.e., there is a great deal of non-luminous (or dark) matter. However, weighting its density parameter is a challenge. By using relatively rare celestial objects, rich clusters, which form from the density perturbation of comoving size around 10 Mpc [?], the total matter density can be inferred because such

[1] See also Chapter ?? in this thesis.

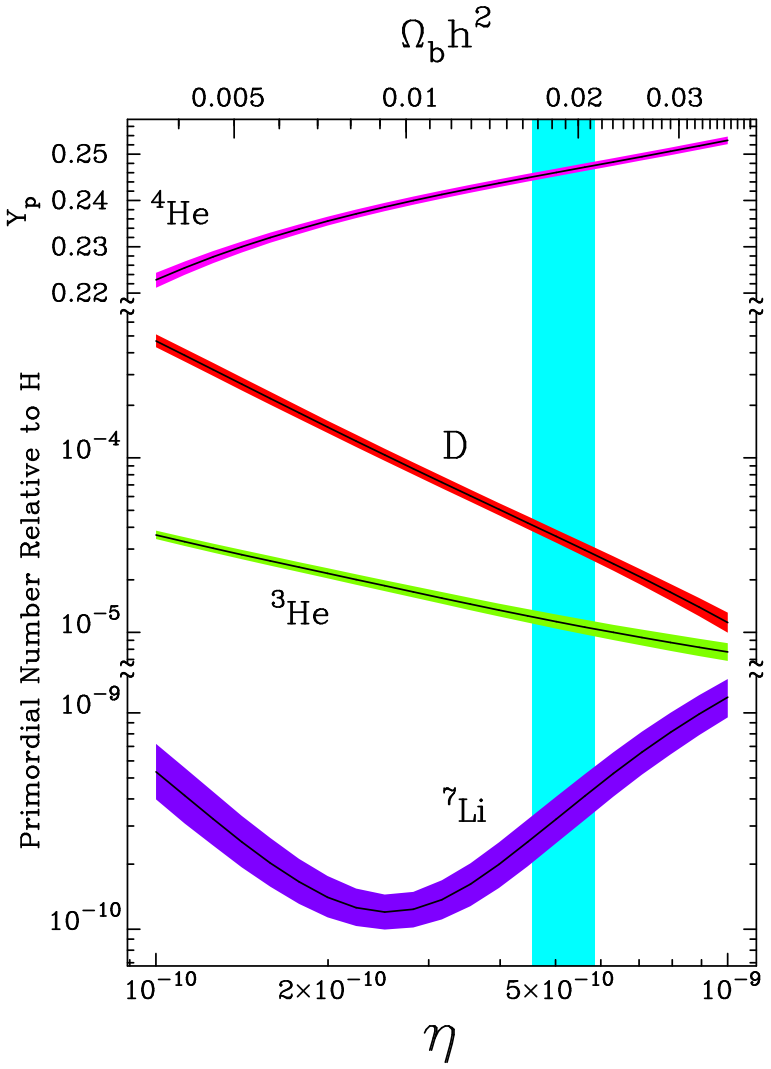

Figure 3.2: *Predicted abundances of ^4He (mass fraction), D, ^3He and ^7Li (number relative to hydrogen) as a function of the baryon-to-photon ratio η and the baryon density parameter $\Omega_B h^2$ [?]. The shadow band embedding each curve indicates 2σ theoretical uncertainty. The dark band shows the determination of the baryon density based upon the recent measurement of the primordial abundance of deuterium, $\Omega_B h^2 = 0.019 \pm 0.0024$ [?]. The baryon density ρ_B is calculated by the baryon-to-photon ratio η [?].*

clusters gather material together from a large region of space thus play as a sample of matter in the Universe. Most baryons in clusters are in the hot diffusive intracluster gas which glows in X-rays and donot reside in the galaxies [?]. Thus, a variable, so called the gas-to-total mass ratio, can be applied to determine the total baryon mass and also the total matter mass. The gas mass is determined by measuring the X-ray flux from the intracluster gas or mapping the Sunyaev-Zel'dovich CMB distortion [?, ?] caused by CMB photons scattering off hot electrons in the intracluster gas. The total cluster mass, on the other hand, can be determined by the dynamics of cluster galaxies and the virial theorem, or by mapping the cluster mass by gravitational lensing, or by the hydrodynamics of gas emitted from the cluster. With the gas-to-total mass ratio from the X-ray measurements, the reliable estimates of the mean matter density parameter is reported to lie in the range [?]

$$\Omega_M = 0.4 \pm 0.1 \tag{3.11}$$

Evidently, the matter with the matter density parameter (??) is still far from composing a flat Universe (??). In addition, the observational evidence based on measurements of type Ia supernovae carried out by two groups, the Supernova Cosmology Project (SCP) [?] and the High-z Supernova Team (HZSST) [?, ?], has pointed to an accelerating Universe. Such results have suggested that our Universe has a large missing energy component with negative pressure, i.e., another form of energy, dark energy [?]. So far, the Universe is believed to made up with dark energy with a density parameter about 2/3, dark matter with a density parameter about 1/3 and luminous matter with a very small density parameter, only about 1/200 [?]. The dark energy problem is still one of the great puzzles in Modern Cosmology.

3.1.2 Evidence of Existence of Dark Matter

From Eqs. (??) and (??), one has the estimated total density of the Universe $\Omega_0 \simeq 1$, much greater than the density of the visible matters in the Universe, $\Omega_{visible} \simeq \Omega_{star} \simeq \Omega_{lum} \simeq 0.005$. This fact suggests that there might be a great amount of invisible dark matter contributing to the Universe. The most robust and physical evidence of the existence of dark matter comes from the observations of rotation curves of the gas clouds of the spiral galaxies. Fig. ?? [?] shows the rotation velocity for the spiral galaxy NGC6503. The velocities of the gas clouds of the galaxy are measured in function of r, the distance from the centre of the galaxy. In the figure, it is apparent that, after a rise near $r = 0$, the circular velocities of clouds remain constant out as far as can be measured. By Newton's law,

$$\frac{GM(r)}{r^2} = \frac{v^2}{r} \tag{3.12}$$

it implies the density distribution

$$\rho(r) \approx \frac{1}{r^2} \tag{3.13}$$

at large radius so that $M(r) \propto r$. If the mass of the galaxy is all concentrated in luminous matter, one then expects the circular velocity v_r behaves as $\propto r^{1/2}$. However, this is not seen at all. Another example is the rotation curve of galaxy NGC3198 [?], which implies $\Upsilon > 30h\ M_\odot/L_\odot$, $\Omega_{halo} > 0.017$. The discrepancy between this number and Ω_{lum} is found in many external galaxies and is the strongest evidence that a big fraction of the mass in the galaxy is contained in a dark halo.

3.1.3 Dark Matter Candidates

The inconsistency between the estimates of the mass directly related to luminous matter and the mass inferred from the dynamical consideration has implied the Universe is predominantly made up of dark matter in some forms. The inconsistency between Big Bang Nucleosynthesis constraint (??) and Eq. (??) shows that dark matter might be non-baryonic. So far, some dark matter candidates, both baryonic and non-baryonic, are popularly accepted.

Most of the baryons are in the hot, intracluster gas which glows in X-rays around clusters [?]. The gas outweighs stars by around 10 to 1. However, only about 5% of galaxies are in great clusters of galaxies [?]. Another principal baryonic candidate is the MAssive Compact Halo Object (MACHO) class of candidates [?, ?], which include brown dwarfs, white dwarfs, neutron stars, planetary-type objects and Jupiter-like objects. Using microlensing effort, which is based on the fact of the light deflection when a compact massive object lies near the line of sight to the background star, several experimental groups have reported some MACHO events by monitoring millions of stars in the Large Magellanic Cloud Galaxy in our Milky Way or our Galactic bulge: groups of SCP [?, ?], EROS [?] and MACHO [?], by undertaking the search for microlensing in the Large Magellanic Cloud Galaxy and groups of SCP [?], OGLE [?] and DUO [?], by observing the microlensing in the Galactic bulge, have reported 3 to tens of MACHO events. These MACHOs are reported to contribute a fraction of 0.1-0.5 to our Galaxy's halo mass.

Among the non-baryonic dark matter candidates, two classes are distinguished by whether they were created in large quantity, thermally or non-thermally, in the phase transition during the Early Universe: Axion [?], which is created non-thermally, arises in the solution of the strong CP-problem in QCD; Weakly Interacting Massive Particle (WIMP) [?], which is created thermally, arises in supersymmetric extension of Standard Model. In addition, particle dark matter like massive neutrinos from the case of neutrino oscillations presented by the SuperKamiokande Collaboration [?], based upon the direction dependent deficit of atmospheric muon neutrinos, is also proposed. In AMS-related search for dark matter [?], the attention focuses on such supersymmetric particles.

Supersymmetry (SUSY) models suggest/require the existence of a new multiplicatively conserved quantum number, R-parity [?], in which, each ordinary particle is assigned $R = +1$, and each supersymmetric partner (superpartner) is assigned $R = -1$. This quantum number implies that supersymmetric particles must be created or destroyed in pairs, and then guarantee that lightest supersymmetric particles (LSP), or say, neutralino χ, are absolutely stable. So, if SUSY exists and R-parity is conserved, some LSPs should

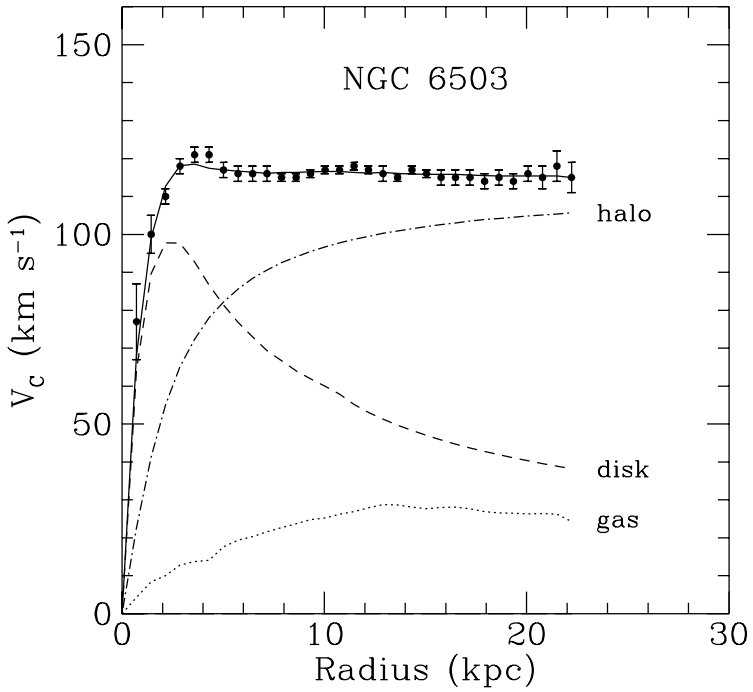

Figure 3.3: *Rotation curve for the spiral galaxy NGC6503 [?]. The points are the measured circular rotation velocities as a function of distance from the centre of the galaxy. The dashed and dotted curves are the contribution to the rotational velocity due to the observed disk and gas, respectively. The dot-dash curve is the contribution from the dark halo.*

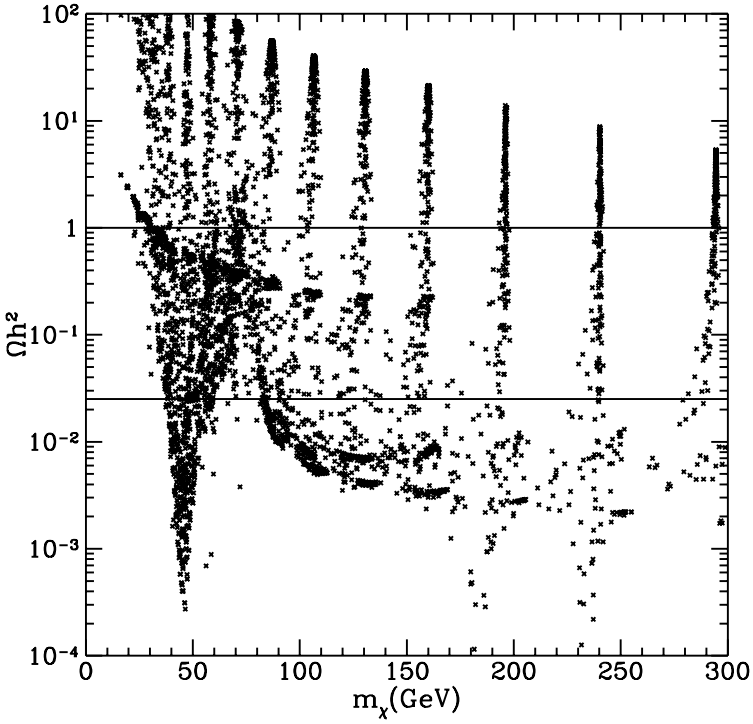

Figure 3.4: *Scatter plot of relic neutralino density versus neutralino mass for the set of SUSY models [?]. Models between the lines at* $\Omega_\chi h^2 = 0.025$ *and* $\Omega_\chi h^2 = 1$ *are compatible with neutralino dark matter.*

exist from the Early Universe.

If WIMPs do populate the Galactic halo, they could be detected directly or indirectly. The idea of the direct detection of WIMPs is based on WIMPs elastically scattering off nuclei in the detector [?]. Once the SUSY model parameters are chosen, the elastic scattering cross section and also the event rate in the detector can be calculated [?]. When a WIMP scatters off a nucleus, the nucleus recoils, causing perturbations in the crystal lattice (phonons or heat), and also the ionisation. The principal difficulties of the direct detection of WIMPs are the fact that the events are quite rare and there exists a huge amount of background which can also deposit energy in the nucleus in the detector. So, the most important work for the experiments is to increase the scattering rate and to discriminate the nuclear recoil signal from the background. For this reason, the experiments are frequently performed by increasing the mass of the detector in order to increase the scattering rate and, the detectors are generally operated deep underground at mini-Kelvin temperature and heavily shielded. The majority of the background comes from gamma rays which would deposit a great fraction of their energy in ionisation while the WIMPs signals are nuclear recoils which deposit the energy in the form of phonons or heat. Thus in experiments, by simultaneously measuring the energy deposited in heat and the energy deposited in ionisation, it is possible to discriminate around 99% of background of gamma rays.

The idea of the indirect detection of WIMPs is based on the conjecture that WIMPs might occasionally elastically scatter off nuclei in the Sun or the Earth [?, ?]. They then would occasionally lose enough energy, or change their direction of motion, to become gravitationally captured by the Sun or the Earth. The captured WIMPs in the bent orbits would repeatedly intersect the Sun or the Earth, resulting in the eventually settling of these WIMPs into the core. As the number density increases over time, the self-annihilating rate of $\chi\chi \to \nu\bar{\nu}$ would increase too, resulting in a stream of neutrinos produced in the core. Neutrinos can easily escape the core and are detectable on the Earth. The properties of very high energy and minority in number make these neutrinos distinguishable from the solar neutrinos. Another important indirect detection of WIMPs is based on neutralino as Majorana particle [?] equivalent to its antiparticle. Two neutralinos can then annihilate into quarks, gluons, gauge boson, Higgs bosons or leptons. These particles will decay into some stable ordinary particles such as $\bar{p}$, e^+ and γ. For the issue of the direct and indirect detections of supersymmetric dark matter, details can be found in [?].

Given a SUSY model, the cross section for neutralino annihilation to lighter particles can be calculated. One can obtain the cosmological mass of dark matter [?]

$$\Omega_\chi = \frac{m_\chi n_\chi}{\rho_c} \simeq \frac{10^{-26}\ \mathrm{cm}^{-3}\ \mathrm{sec}^{-1}}{<\sigma v>} \tag{3.14}$$

where σ is the thermally averaged cross section for two neutralinos to annihilate into ordinary particles, v is the neutralino velocity in the Galactic halo, n_χ is the χ number

density, coming from the solution of Boltzmann equation in the Early Universe [?]

$$\frac{dn_\chi}{dt} = -3Hn_\chi - n_\chi^2 < \sigma v > (\chi\chi \to f\bar{f}) + n_\chi^2 < \sigma v > (f\bar{f} \to \chi\chi) \tag{3.15}$$

where H is the Hubble constant. The third term at the right hand side is the increase term due to particle production and can be simplified by quoting the fact that the ordinary particles such as quarks and electrons stay in thermal equilibrium throughout the evolution period during which, n_χ freezes out [?]. So, if thermal equilibrium is reached, Eq. (??) is then reduced to a more useful equation

$$\frac{dn_\chi}{dt} = -3Hn_\chi - (n_\chi^2 - (n_\chi^{eq})^2) < \sigma v >_{annihilation} \tag{3.16}$$

It has to be noted that the Global-SUSY model provides a vast region of neutralino relic abundance for different masses [?]. Figure ?? shows the relic neutralino density relative to neutralino mass. As shown in the figure, a great deal of SUSY models give neutralino relative density with $0.025 \leq \Omega_\chi h^2 \leq 1$, being compatible with neutralino dark matter. Data from e^+e^- annihilation at Large Electron Positron Collider (LEP) combined with the cosmological constraints has given a lower limit on the mass of neutralino χ [?]

$$m_\chi \geq 21.4 \quad \text{GeV} \tag{3.17}$$

Another categorisation scheme of dark matter is the hot or cold classification, depending on their mean velocities when they decouple from thermal equilibrium. This categorisation is important for structure formation and there is the possibility to determine whether the dark matter is hot or cold from the studies of the galaxy formation. Primordial black holes (PBHs) for example, can be the MACHO candidates and also the tracers of the Cold Dark Matter [?] that have produced part of the large structure.

3.2 Characteristic and Origin of Cosmic Antiprotons

Cosmic antiprotons have been carefully studied, both theoretically and experimentally. The first experimental evidence of cosmic antiprotons dates from the 1970's from balloon-borne experiments. Antiprotons detected at that time were speculated to originate from an anti-Universe.[2] Today, it is already clear that most cosmic antiprotons are galactic secondaries. In addition to the galactic origin, other possible sources, such as supersymmetric dark matter and primordial black holes are also proposed.

The distinctive spectral shape of antiprotons with a maximum at 2 GeV and a sharp decrease towards lower energies makes antiprotons a unique probe of the models for the production source and also the mechanism, in the window at energies $E < 1$ GeV, and

[2]Since antiprotons can be produced in nuclear collisions while antihelium nuclei have never been seen in nuclear interactions, the study of the remnant from the anti-Universe is the search for antihelium nuclei rather than antiprotons.

also the propagation condition in the Galaxy and modulation in the heliosphere [?, ?, ?, ?, ?, ?, ?].

Antiproton measurements are quite important because these particles are mostly secondarily produced from the interactions of cosmic ray protons. On the other hand, most of our knowledge on cosmic ray history comes from the studies of secondary nuclei such as Li, Be, B [?, ?], and sub-iron elements [?] whose heavy nucleus parents have not necessarily had the same history as the much more plentiful protons. Positrons could serve as tracers of proton cosmic history since they come from, mostly p-interactions. However, the positron spectrum is easily distorted by electromagnetic interactions subsequent to their creation. Thus, antiprotons provide a unique channel for the study of proton cosmic history. In addition, the kinematics of antiproton production greatly suppresses the creation of antiprotons in the low energy range so that their expected spectrum differs evidently from the slowly changing power laws of other cosmic ray particles [?]. So, the antiproton spectrum should behave sensitively to energy changing stochastic processes which might act upon the cosmic particles during the propagation in interplanetary and interstellar region [?].

3.2.1 $\bar{p}$ from Interaction Production in ISM

Galactic antiprotons are predominantly produced by standard nuclear interactions of cosmic ray nuclei, mostly protons, with nuclei in the ISM. In order to study the possible exotic sources of cosmic antiprotons, accurate measurement of the $\bar{p}$ spectrum, especially at low energies, about 100 MeV to 10 GeV, is mandatory [?]. This requirement should be achieved in the near future by the forthcoming experiments like AMS, BESS, CAPRICE, PAMELA, LEAP, etc.

In addition, it is also necessary to theoretically and accurately evaluate the $\bar{p}$ spectrum in the required energy range. So, a more refined treatment of the diffusion of cosmic rays in the magnetic fields of the Galaxy has to be taken into account. Nowadays, there has already been great progress in such a consideration [?]:

- The inelastic non-annihilation cross section for $\bar{p}$-induced collisions has been developed [?, ?, ?] and has given rise to the so called "tertiary contribution".
- $p + He_{ISM} \rightarrow \bar{p}$ contribution has been considered by means of a geometric approach [?].
- The reacceleration of cosmic ray propagation has been taken into account [?, ?].
- The propagation of cosmic rays has been modelled in a more realistic two-zone diffusion model [?, ?].
- The reactions of cosmic p and He with p and He in the ISM have been re-estimated in a more complete nuclear Monte Carlo simulation [?].

As discussed in Section ?? for cosmic ray propagation, there doesn't exist a model which can solve all cosmic ray problems. So, one can only choose either an easy-to-solve but less physical model, e.g., the Leaky Box Model, or a more physical but complicated model, e.g., the Diffusion Model. For the purpose of evaluating the galactic $\bar{p}$ spectrum as accurately as possible, one should apply the most realistic physical model. Even so, however, such a model is still coupled with an apparent uncertainty [?, ?, ?, ?, ?, ?] since the real physics in the system being treated is still not well known. The origin of the uncertainty can be itemised as follows:

- The propagation parameters are not yet well known. For example, the actual diffusion coefficient of cosmic ray propagation in Eq. (??) is not perfectly understood. It is reported [?] that the propagation parameters are severely constrained by the analysis of B/C ratio experimental results. Nevertheless, the B/C ratio itself is of great uncertainty [?, ?].

- Even the $\bar{p}$ production from p+p collisions [?, ?, ?] and p+A collisions [?, ?, ?, ?, ?] is well measured and the $\bar{p}$ production cross section and its mean multiplicity for both types of reaction are well parametrised [?, ?], the $\bar{p}$ production from $A+A$ collisions, especially from $He + He$ collisions which are important for galactic antiprotons, is, however, not yet clearly understood.

- The material composition of p and He in the ISM is not really well understood. The number density in the ISM is $n_{ISM} \equiv n_H + n_{He} \simeq 1$ cm^{-3}. The He to the ISM number density ratio n_{He}/n_{ISM} is usually assumed as 0.1. By scanning the variation of n_{ISM} and n_{He}/n_{ISM} [?], it is reported that the uncertainty of $\bar{p}$ spectrum due to the material composition in the ISM principally comes from the uncertainty in n_{He}: 10% uncertainty in n_{He}/n_{ISM} will lead to a few percent error in the $\bar{p}$ spectrum over the entire energy range.

- As discussed in Section ??, the cosmic ray spectra at low energies are strongly influenced by the solar modulation. Definitely, one can modulate cosmic ray spectra using Eq. (??) discussed in Section ??, this equation is, however, over simplified since the phenomenon of diffusion and convection within the heliosphere is quite complicated in reality. The only way to avoid the solar modulation is to measure the low energy $\bar{p}$ spectrum outside the heliosphere. The planned interstellar probe described in [?] could make such an experiment possible. This probe is expected to leave the Solar System at a velocity 20 AU/yr and to reach a region free of the solar magnetic field influence within 5-10 years. So, an exact measurement of absolute cosmic antiprotons is expected to be available in the near future.

3.2.2 $\bar{p}$ from Annihilation of Supersymmetric Dark Matter

Antiproton is one of the expected annihilation products of two self-annihilating neutralinos. In evaluating the $\bar{p}$ contribution from neutralino annihilation, a typical treatment

is to take into account the contribution in the antiproton energy spectrum from a single $\chi\chi$-annihilation and the $\bar{p}$ in the diffusion equation (**??**) and then perform the integration over the whole Galactic halo [**?**]. The differential rate (per unit volume per second) for the $\bar{p}$ production due to a single $\chi\chi$-annihilation is given by [**?**]

$$q_{\bar{p}}^{SUSY}(E_{\bar{p}}) =< \sigma v > f(E_{\bar{p}}) \left(\frac{\rho_\chi}{m_\chi}\right)^2 \tag{3.18}$$

where $E_{\bar{p}}$ is the antiproton energy, σ is the $\chi\chi$-annihilation cross section and v is the neutralino velocity in the Galactic halo, ρ_χ is the neutralino density and $f(E_{\bar{p}})$ is the antiproton energy spectrum for a single annihilation give as [**?**]

$$f(E_{\bar{p}}) \equiv \left(\frac{1}{\sigma}\right)\left(\frac{d\sigma(\chi\chi \to \bar{p}X)}{dE_{\bar{p}}}\right) = \sum_{F,f} B_{\chi f}^{(F)} \left(\frac{dN_{\bar{p}}^f}{dE_{\bar{p}}}\right) \tag{3.19}$$

where F is the $\chi\chi$-annihilation final state and $B_{\chi f}^{(F)}$ is the branching ratio into the quarks or gluons f in the channel F, and the differential distribution of the antiprotons generated by the hadronisation of quarks and of gluons is given by $dN_{\bar{p}}^f/dE_{\bar{p}}$.

It has to be noted that in Eq. (**??**), both the branching ratio $B_f^{(F)}$ and the distribution $dN_{\bar{p}}^f/dE_{\bar{p}}$ depend on the nature of the species f. In evaluating the $\bar{p}$ spectrum in a $\chi\chi$-annihilation, one has to calculate all annihilation final states, even those possible intermediate products such as gauge bosons Z^0Z^0, W^+W^-, Higgs bosons H^0H^0, H^+H^- and top quarks $t\bar{t}$. Such a work is laborious but could be achieved with Lund Monte Carlo programmes [**?**, **?**].

The neutralino density ρ_χ is also a challenge to deal with. Generally, the neutralino halo distribution is assumed spherically symmetric. The density profile is then given as [**?**]

$$\rho_\chi(r) = \rho_\chi(\odot)\left(\frac{r_0^2 + a^2}{r^2 + a^2}\right) \tag{3.20}$$

where r is the radius, $r_0 \simeq 8.5$ Kpc is the distance between the Sun from the Galactic centre, a is the core radius of the halo and $\rho_\chi(\odot)$ is the local neutralino halo density, i.e., the density near the Sun. Such a halo would give rise to a rotation curve [**?**]

$$v_h^2(r) = 4\pi G\rho_\chi(\odot)(r_0^2 + a^2)\left[1 - \frac{a}{r}\tan^{-1}\left(\frac{r}{a}\right)\right] \tag{3.21}$$

where G is Newton's constant. $\rho_\chi(\odot)$ and a in Eq. (**??**) are then determined by the rotation velocities of two points in the halo. According to Fig. **??**, at $r \gg 10$ Kpc, the halo velocity $v_h \approx 220$ km sec^{-1}. But, the local halo rotation curve is uncertain since there is the disk contribution. Nevertheless, the local halo density with $\rho_\chi(\odot) \simeq$ 0.3-0.5 GeV cm^{-3} is expectedly reasonable [**?**].

Moreover, there could be a supermassive black hole, with a mass of about $2.6 \times 10^6\ M_\odot$, at the centre of our Galaxy [**?**]. This superheavy black hole would much more largely

accumulate dark matter within the Galactic halo, enhancing the neutralino density ρ_χ in Eq. (??) with a power law as

$$\rho_\chi \propto r^{-\alpha}, \qquad \alpha \simeq 0.0 \sim 2.0 \tag{3.22}$$

The existence of such a supermassive black hole at the Galactic centre will aggravate the annihilation rate of neutralinos, weighing the $\bar{p}$ production from this origin.

3.2.3 $\bar{p}$ from Evaporation of Primordial Black Holes

A primordial black hole (PBH) is a black hole which formed during the Early Universe. In Standard Cosmology, a black hole forms because of self-gravitational collapse to within its Schwarzschild radius [?]. However, a primordial black hole forms in a different way.

In 1971, Hawking [?] published an article in which he showed that, in the Early Universe, fluctuations in the density of energy in regions could cause those regions to collapse to within their Schwarzschild radii and thus form black holes. Soon later, by Inflationary Cosmology [?, ?], another theory for the formation of PBHs in a period of inflation was introduced. The Inflation Theory states that the Universe underwent a very short period of very rapid expansion. During such an inflationary epoch, the energy density of the Universe would probably decrease dramatically, resulting in a possible but not absolutely necessary cosmological phase transition. When a cosmological phase transition occurred, it would cause some irregularities, which have been referred to as bubbles of broken symmetry [?]: if a phase transition is to produce PBHs, the production rate of these bubbles needs to be finely tuned; if the production is too high, the entire Universe will undergo a phase transition otherwise the bubbles will never collide if the rate is too low. In addition to the above two ways of formation of PBH, the formation of PBHs from the collapse, or the topological deflection, of cosmic strings in the Early Universe was also raised [?].

If a black hole exists, there should be some related observable evidences. Hawking [?, ?] first showed that a black hole could evaporate or emit particles, called Hawking Radiation nowadays, by quantum effects with an equivalent temperature, which is called Hawking temperature

$$T = \frac{\hbar c^3}{8\pi G M k} \simeq 1.06 \times 10^{13} \left(\frac{M}{g}\right)^{-1} \quad \text{GeV} \tag{3.23}$$

with G the gravitational constant and k the Boltzmann constant, thus noting that PBHs are the only ones with a mass small enough for the quantum emission rate to be significant, possibly yielding an observable effect.

The existence of PBHs has been applied in a variety of cosmological interests. PBHs are supposed to have heated the Early Universe by means of accretion, or have caused the formation of at least some of the galaxies or clusters observable today [?]. PBHs are also speculated to have formed in Inflationary Cosmology as MACHOs that have caused the gravitational microlensing effect of observations [?]. PBHs might be part of large scale structure formation of cold dark matter (CDM) [?], playing as the tracers for the

cold dark matter in the Galactic halo. As an ultimate irregularity/singularity formed in the Early Universe, PBHs are also believed to contribute the irregularities of the current Universe [?], likely forming the core of some galaxies.

Another important issue about PBHs is that, PBHs might have contributed to the cosmic radiation [?, ?, ?]. This radiation is the result of the evaporation of the black holes. An evaporating black hole captures one particle from a particle-antiparticle pair production taking place in its ergosphere, emitting the other as radiation. This process is completely a quantum effect. Among the particles emitted from black holes are photons, neutrinos, electrons and gravitons. And, when the black hole temperature increases, or the black hole mass decreases, heavier particles like hadrons might also be emitted. This emission results from the direct production of fundamental constituents and also from the hadronisation of quarks and gluons.

Although the average density of PBHs in the Universe is quite small, $\Omega_{PBH} \leq 10^{-8}$ [?], their signature in the spectra of some interested cosmic particles is not small at all. MacGibbon and Carr [?] first noticed that the emissions from PBHs might significantly contribute to the extragalactic photon and interstellar cosmic ray electron and positron spectra around 0.1-1 GeV. The γ spectrum in the energy range about 50-170 MeV fits well such PBH emission. In addition, the expected flux of antiprotons from PBH evaporation has been shown to increase with decreasing kinetic energy down to 0.2 GeV [?], thus providing a distinct signature below 1 GeV. Hence, searches for such low energy cosmic antiprotons can lead to some cosmological constrains on the density of PBHs and, in the mean time, demonstrate their existence as well. PBHs might also be one of the possible origins of extremely high energy cosmic rays [?], over an energy threshold about 10^{20} eV.

The $\bar{p}$ spectrum contributed by PBHs is determined by the properties of the black hole evaporation. The emission spectrum for a charge free, nonrotating black hole with a mass M, which emits particles with spin s and with total energy in an energy interval $(E, E + dE)$, is given as [?]

$$\frac{d^2n}{dtdE} = \frac{\Gamma_s}{2\pi\hbar}\left[\exp\left(\frac{E}{kT}\right) - (-1)^{2s}\right]^{-1} \tag{3.24}$$

where T is the black hole temperature defined in Eq. (??), Γ_s is the dimensionless absorption probability for the emitted species, with an optical limit (i.e., with energy $E \to \infty$) given as [?]

$$\Gamma_s \approx \frac{27E^2}{64\pi^2(kT)^2} \tag{3.25}$$

Considering all possible species emitted, the corresponding mass loss rate for a black hole can be described as [?]

$$\frac{dM}{dt} \approx -5.34 \times 10^{25} f(M)\left(\frac{M}{g}\right)^{-2} \quad \text{(g/sec)} \tag{3.26}$$

where $f(M)$ is a function of the number of emitted species that is normalised to unity for large M, $M \gg 10^{17}$ g, and increases with decreasing M. Following Eq. (??), there is a

critical mass for a black hole

$$M_c \simeq 5.3 \times 10^{14} \left(\frac{t_{BH}}{t_u}\right)^{1/3} \tag{3.27}$$

in which, the critical mass of a black hole is defined as the initial mass of a black hole that is expiring today, in other words, its initial lifetime t_{BH} is the same as the current age of the Universe t_u. For a black hole with an initial mass below its critical mass, it must have had completely evaporated out by today.

Eq. (??) gives the production rate of species in function of species energy at a temperature T. For each species j, a differential fragmentation function $dg_{\bar{p}}^{(j)}(E_{\bar{p}}, E)/dE_{\bar{p}}$ is defined as the fragmentation of each emitted species j with total energy E into antiprotons with total energy $E_{\bar{p}}$ and can be computed by Monte Carlo simulation code JETSET [?]. So, the contribution of PBHs to the $\bar{p}$ spectrum is then calculated by applying Eq. (??) onto $dg_{\bar{p}}^{(j)}(E_{\bar{p}}, E)/dE_{\bar{p}}$, summing over all species and all their degrees of freedom.

3.2.4 Comments on Cosmic Antiprotons

In summary, cosmic ray induced antiprotons as a principal background are mainly generated through $p + p \rightarrow \bar{p} + X$ collisions of cosmic protons with the ISM. The strategy to search for the exotic signals of antiprotons is to investigate the $\bar{p}$ spectrum in the low energy region, since the neutralino-induced or PBH-induced component doesn't drop fast at low energies [?, ?, ?, ?]. Figure ?? shows separately the $\bar{p}$ spectra from 3 sources: the interstellar source [?], the supersymmetric dark matter annihilation with m_χ= 62 GeV [?] and the the evaporation of primordial black holes [?].

It is clear enough from Figure ?? that, the hope of identifying antiprotons from exotic sources lies in the energy range $E < 1$ GeV. However, such a distinguishing spectrum shape will be blurred to a large extent by a tertiary component, resulting from the scattering of the secondary antiprotons with energy loss [?]. In addition, antiprotons produced from the collisions between heavier nuclei in the ISM, mostly primary helium nuclei, will also cause a significant $\bar{p}$ flux at low energies as well [?]. Figure ?? [?] shows the total spectrum together with its estimated individual components. As shown in this figure, the contribution from $p + He$ collisions and tertiary has flattened the shape of $\bar{p}$ spectrum at energies $E < 1$ GeV. This would definitely increase the challenge but the solution of the search for antiproton exotic sources is none but over there. On the contrary, if there exists a supermassive black hole at the centre of our Galaxy, the $\bar{p}$ spectrum component from the neutralino annihilation will be increased, making the resultant $\bar{p}$ spectrum at low energies even more distinctive. The precise measurement of $\bar{p}$ spectrum at low energy range could set good upper limits to these exotic sources or, even rule out their existence.

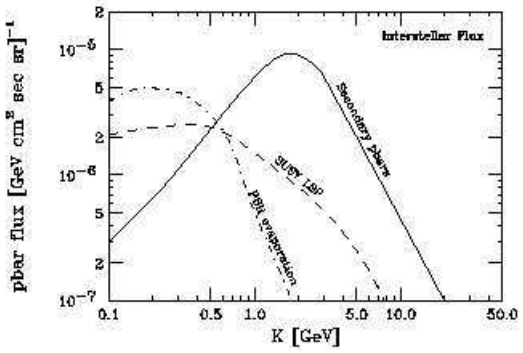

Figure 3.5: *Antiprotons from three regimes: galactic secondaries [?], neutralino annihilation with m_χ= 62 GeV [?] and evaporation of primordial black holes [?] respectively.*

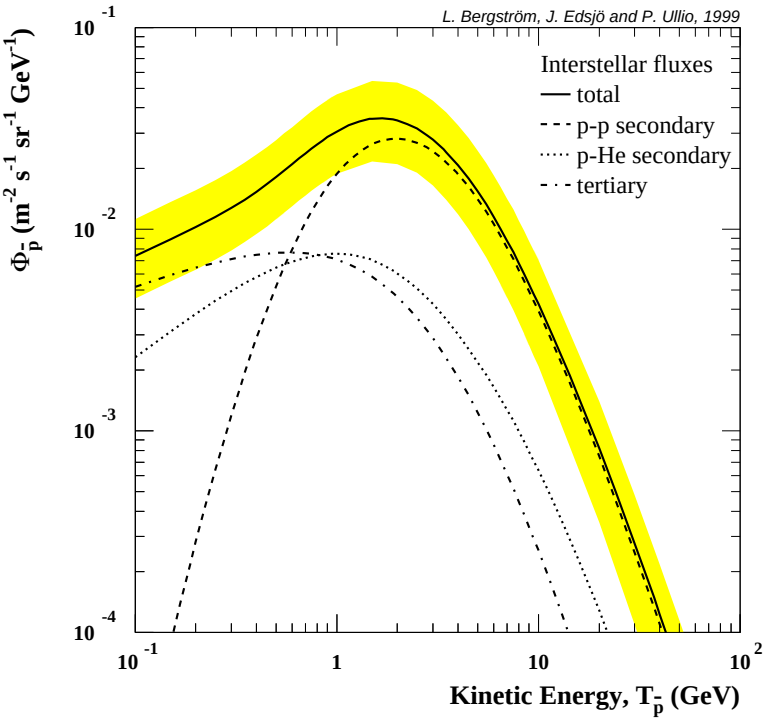

Figure 3.6: *The galactic antiproton flux and its individual contributions from $p+p$, $p+$ He collisions and tertiary [?]. The shadow embedding the total galactic $\bar{p}$ flux is the uncertainty due to the parametrisation of the primary proton spectrum.*

Chapter 4

Particle Detection and Experiments

A particle detector is designed to determine the physical properties of a particle based on some well developed physical theories. The ability of a detector is required to produce good resolutions in order to distinguish the particles from each other. A better resolution requires more advanced and mature detector techniques. No single detector can give all the physical properties of a particle thus in modern particle experiments, more than one detector are often arranged altogether in order to perform multiple measurements at the same time. Some properties are not determined directly. For example, the mass of a particle is not directly measured but determined from the measurements of velocity β and momentum p via

$$p = m\beta\gamma = \frac{m\beta}{\sqrt{1-\beta^2}} \tag{4.1}$$

thus giving the mass resolution

$$\frac{(\triangle m)^2}{m^2} = \frac{(\triangle p)^2}{p^2} + \frac{(\triangle \beta)^2}{\beta^4(1-\beta^2)^2} \tag{4.2}$$

So, the resolution of a value determined in this way is reduced.

In this chapter, the physics of particle detectors is reviewed. The experiments which are related to and are applied to test the results of this work are introduced and discussed. Comments are given along with the context in each section.

4.1 Measurement Methodology: Particle Interactions in Matter

Our knowledge of the subnuclear and nuclear world comes from the study of the interactions between particles and nuclei. The nature (mass, charge, momentum, spin, etc.) of the interacting particles created in these processes, their angular and energy distribution and the polarisation are measured by appropriate detectors. The detection of nuclear particles depends on the fact that, directly or indirectly, they transfer energy

to the medium they are traversing in the processes of ionisation or the excitation of the constituent atoms in the medium. This can be observed as charged ions, for example in a gas counter, or as a results of the scintillation light, Čerenkov radiation, etc., which is subsequently emitted. This information could be obtained principally in three ways: (a) by receiving a signal which is produced when the particles pass through a medium; (b) by passing the particles through an electromagnetic field and observing either directly or indirectly their trajectories; (c) by revealing the particles through the detection of the characteristic radiation they emit and of the variation with time of the rate of emission of this radiation. The methodology will be discussed in the following sections.

4.1.1 Ionisation Loss of Charged Particles

When a charged particle passes through matter, it loses energy by interactions with the atoms in the medium and as a result, they might be excited or ionised. Ionisation energy losses are very important for all charged particles in their passage and for particles other than electrons and positrons, for example, such energy losses would dominate over radiation energy losses at all but the highest attainable energy levels. The theory of such losses, which are predominantly due to Coulomb scattering from the atomic electrons, was given by Bethe and Bloch [**?**]

$$-\frac{dE}{dx} = \frac{z^2 e^4 N_e}{4\pi\epsilon_0 m_e v^2}\left(\ln\frac{2m_e c^2\beta^2\gamma^2}{\bar{I}} - \beta^2 - \frac{\delta(\gamma)}{2}\right) \tag{4.3}$$

where N_e is the number density of electron, m_e is the electron mass, z and v are the charge (in unit of e) and the velocity of the particle, $\beta = v/c$, and x is the distance the particle has travelled in the medium. More frequently, it is convenient to describe this energy loss in terms of path length, ξ, such that $\xi = \rho x$ where ρ is the mass density of the medium. So, Eq. (**??**) then changes to

$$-\frac{dE}{d\xi} = -\frac{1}{\rho}\frac{dE}{dx} = \frac{z^2 e^4}{4\pi\epsilon_0 m_e v^2}\frac{N_e}{\rho}\left(\ln\frac{2m_e c^2\beta^2\gamma^2}{\bar{I}} - \beta^2 - \frac{\delta(\gamma)}{2}\right) \tag{4.4}$$

The path length ξ in the medium is measured in g cm^{-2} or kg m^{-2}. The quantity $\bar{I}$ is an effective ionisation potential, averaged over all electrons, with an approximate magnitude $\bar{I} = 10Z$ eV. $\delta(\gamma)$ is a dielectric screening correction and is important only for highly relativistic particles, for which, it is given by [**?**]

$$\frac{\delta}{2} \approx \ln\frac{\hbar\omega_p}{\bar{I}} + \ln\beta\gamma - \frac{1}{2} \tag{4.5}$$

with

$$\hbar\omega_p = 28.816\sqrt{\rho(Z/A)} \quad \text{eV} \tag{4.6}$$

where ρ is in unit of g/cm^3, Z and A are the atomic charge and the atomic weight of the medium respectively.

Equation (??) shows that the energy loss dE/dx is independent of the mass M of the particle which passes through the medium but varies as a function of $1/\beta^2$, falling rapidly as the velocity increases from zero. However, after passing through a region of minimum ionisation for $E \simeq 3\ Mc^2$, it increases logarithmically with $\gamma = E/Mc^2 = (1-\beta^2)^{-1/2}$. As seen in Eq. (??) too, the magnitude of the energy loss also depends on the medium since N_e is given by

$$N_e = \rho N_0 Z/A \tag{4.7}$$

where N_0 is Avogadro's number. Thus, the mean energy loss is proportional to the density of the medium. However, the dependence on the medium is relatively weak since $Z/A \approx 0.5$ for all atoms except hydrogen and the heaviest elements. Numerically, $(dE/d\xi)_{min}$ for all particles spans over a range from 1 to several MeV cm^2/g.

The Bethe-Bloch formula for ionisation losses in Eq. (??) has three important uses in astrophysics that are itemised as follows.

(i) This formula provides one of the most important techniques by which particle diagnostics can be carried out in experimental studies of high energy particles while the ionisation is one of main processes in the propagation of the cosmic ray particles. In most particle physics and astrophysics detectors, it is applied to identify the particles passing through the detectors and their kinematics as well.

(ii) The losses will be very important as particles make their journey from their sources through ISM.

(iii) The heating and ionisation caused by high energy particles will be important in the heating and ionisation of molecular clouds [?].

Figure ?? shows the observed relativistic rise in ionisation loss as a function of momentum p (GeV/c) for relativistic particles, e, μ, π, K, p and D, in a gas (argon-methane mixture). For $\gamma \sim 20,\ 140,\ 190$ and 40 for $p,\ \pi,\ \mu$ and D respectively, the energy losses reach about 1.3 times their minimum values. The relativistic rise is associated with the fact that transverse electric field of the particles is proportional to γ, so that more and more distant collisions became important as the energy increases. Eventually however, when the impact parameter becomes comparable to the interatomic distances, polarisation effects in the medium halt any further increase. Such effects are important in solids at a much lower value of $\gamma \sim 10$, and this plateau value is about 10% larger than $(dE/d\xi)_{min}$ [?]. Part of the energy loss of a relativistic particle may be reemitted from the excited atoms in the form of coherent radiation at a particular angle. Such radiation is called Čerenkov radiation.

The bulk of the energy loss results in the formation of ion pairs (positive ions and electrons) in the medium. One can distinguish two stages in this process. In the first stage, the incident particle produces primary ionisation in atomic collisions. The electrons collided out in this stage have a distribution in energy E' roughly of the form $dE'/(E')^2$. Those of higher energy, called δ-rays, can produce new ions in traversing the medium.

This process is called secondary ionisation. Thus, the resultant total number of ion pairs is then 3-4 times the number of primary ionisations and is proportional to the energy loss of the incident particle in the medium. Note that formula (**??**) is the average value of the energy loss dE in the thickness dx. However, there are still some fluctuations around the mean value, dominated by the relatively small number of closed primary collisions. This is called Landau distribution around the mean value and is asymmetric, with a tail extending to values much greater than the average. However, these tails could be removed by sampling the number of ion pairs produced in the successive layers of gas and the mean ionisation energy loss can be then measured with a good precision.

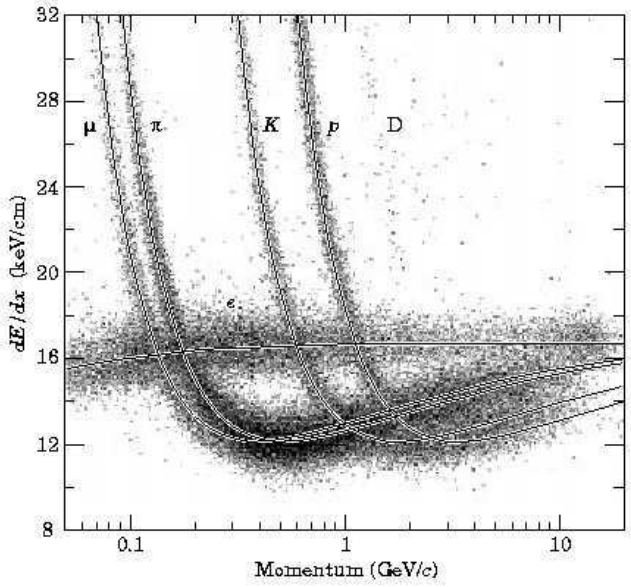

Figure 4.1: *PEP4/9-TPC dE/dx measurements (185 samples @8.5 atm Ar-CH_4 80-20%) in multihadron events [**?**]. The lines are the theoretical derivations. The electrons reach a Fermi plateau value of 1.4 times minimum. Muons from pion decays are separated from pions at low momentum; π/K are separated over all momenta except in the cross-over region. (Low-momentum protons and deuterons originate from hadron-nucleus collisions in inner materials such as the beam pipe.)*

4.1.2 Coulomb Scattering

A charged particle suffers electromagnetic interaction with both electrons and nuclei when passing through a medium. In Eq. (**??**), $dE/d\xi$ corresponds to the target mass of the medium. Thus, in comparison with electrons, the energy loss in Coulomb collisions with nuclei is negligible. However, transverse scattering of the particle appears to be

appreciable when the target mass is large. The differential cross section at a scattering angle θ for this transverse scattering is described by Rutherford formula

$$\frac{d\sigma(\theta)}{d\Omega} = \frac{1}{4}\left(\frac{1}{4\pi\epsilon_0}\right)^2 \left(\frac{Zze^2}{pv}\right)^2 \frac{1}{\sin^4(\theta/2)} \tag{4.8}$$

where p, v and z are the momentum, velocity and charge of the incident particle, Z is the charge of the nucleus but is assumed to act as a point charge. The cross section for small scattering angles is large so that in any given layer of medium, the net scattering is the resultant of a large number of small deviations, which are independent of each other. The resultant distribution in the net angle of multiple scattering follows a quasi-Gaussian distribution

$$P(\phi)d\phi = \frac{2\phi}{<\phi^2>} \exp\left(\frac{-\phi^2}{<\phi^2>}\right) d\phi \tag{4.9}$$

in which, the root-mean-square deflection in a layer t of the medium is given by [**?**]

$$\phi_{rms} = <\phi^2>^{1/2} = \frac{zE_s}{pv}\sqrt{\frac{t}{X_0}} \tag{4.10}$$

where

$$E_s = \sqrt{4\pi\alpha} m_e c^2 \quad ; \quad \frac{1}{X_0} = \frac{4Z(Z+1)r_e^2 N_0}{\alpha A} \ln\left(\frac{183}{Z^{1/3}}\right) \tag{4.11}$$

In Eq. (**??**), α is the fine structure constant, $\alpha = e^2/4\pi\epsilon_0\hbar c$, and $r_e = e^2/m_e c^2$ is the classical electron radius. The quantity X_0 is called the radiation length of the medium, and incorporates all the dependence of ϕ_{rms} on the medium in Eq. (**??**). Numerically, the rms angular deflection will be azimuthally symmetric about the trajectory of a particle while along one axis in the plane normal to the trajectory, it is $1/\sqrt{2}$ times the value in Eq. (**??**).

Coulomb scattering is of practical importance because it constrains the precision with which, the direction of a particle can be determined. For example, considers a high energy charged particle passing through a magnetic field $\mathbf{B}$. If there is no scattering, and the momentum of the particle doesn't change appreciably during the passage, the radius of curvature ρ is then given by $\rho = \frac{pc}{|\mathbf{B}|e}$. Thus after traversing a distance s, the deflection is then

$$\phi_{mag} = \frac{s}{\rho} = \frac{|\mathbf{B}|es}{pc} \tag{4.12}$$

From Eq. (**??**), the rms Coulomb scattering in the plane of the trajectory will be

$$\phi_{scat} = \frac{E_s}{\sqrt{2}p\beta c}\sqrt{\frac{s}{X_0}} \tag{4.13}$$

So that, the ratio between Eq. (??) and (??) then becomes

$$\frac{\phi_{scat}}{\phi_{mag}} \sim \frac{0.05}{|\mathbf{B}|\beta\sqrt{X_0 s}} \tag{4.14}$$

which is independent of the momentum for a relativistic particle ($\beta \sim 1$). Numerically for example, for iron, X_0=13.9 g/cm^2, X_0/ρ=0.0176 m, and take $|\mathbf{B}|$=1.5 Tesla, then, the ratio $\phi_{scat}/\phi_{mag} \sim 0.25$ for s=1 m, but this ratio drops to 0.10 when s=6 m. Some other examples can be obtained from Table ??.

4.1.3 Radiation Energy Loss

When a charged particle traverses matter, it can also lose energy by radiative collisions, especially with nuclei. The electric field of a nucleus will accelerate or decelerate the particles when they pass, causing them to radiate photons and then lose energy. Such a process is called bremsstrahlung (literally 'braking radiation' in German) and is a particularly important contribution to the energy loss of electrons and positrons. So, electrons suffer energy losses when passing through the medium in two ways: one is the ionisation energy loss in Eq. (??),[1] the other bremsstrahlung.

Bremsstrahlung is extremely important in different astrophysical contexts. Wherever there is a region of hot ionised gas in the Universe, it will emit free-free radiation or bremsstrahlung. Some of the astrophysical applications include the radio emission from compact regions of ionised hydrogen at temperature $T \approx 10^4$K, the X-ray emission of binary X-ray sources for which $T \approx 10^7$K and the diffuse X-ray emission from the hot intergalactic gas in clusters of galaxies, which might be as hot as $T \approx 10^8$K. In addition, in Section ??, bremsstrahlung is also a mechanism for relativistic electrons which plays a key role in electromagnetic cascade in cosmic rays.

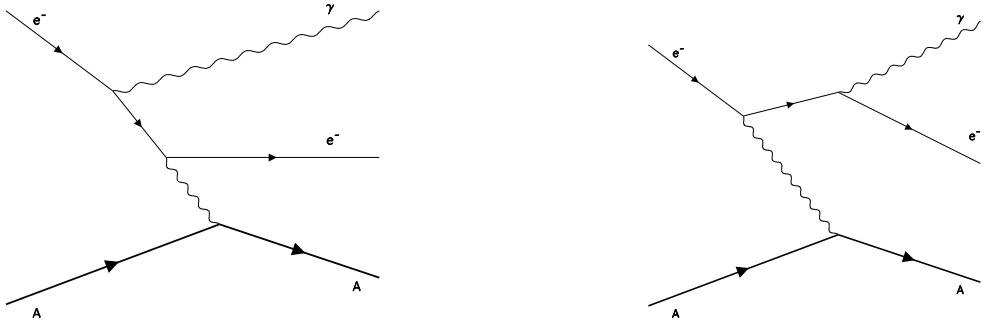

Figure 4.2: *The dominant Feynman diagrams for the bremsstrahlung process* $e^- + (Z, A) \to e^- + \gamma + (Z, A)$

The dominant Feynman diagrams for electron bremsstrahlung in the field of nucleus

$$e^- + (Z, A) \to e^- + \gamma + (Z, A) \tag{4.15}$$

[1]The formula of ionisation energy loss in (??) is for bosons. However, the corresponding formula for fermions differs very slightly.

are shown in Figure ??. The proper formula derived by Bethe and Heitler from the full relativistic quantum treatment is [?]

$$-\left(\frac{dE}{dt}\right) = \frac{Z(Z+1.3)e^6 N_e}{16\pi^3\epsilon_0^3 m_e^2 c^4 \hbar} E\left[\ln\left(\frac{183}{Z^{1/3}}\right) + \frac{1}{8}\right] \tag{4.16}$$

All the symbols are as defined as before. The term $(Z+1.3)$ comes from taking account of electron-electron interactions between the high energy electron and those bound to atoms of the ambient material.

Shown in Eq. (??), the relativistic bremsstrahlung energy loss rate is proportional to the energy of the electron E. Thus, by integrating over the whole spectrum, the average rate of bremsstrahlung energy loss in traversing a path length $d\xi$ of a medium can be expresses as

$$-\left(\frac{dE}{d\xi}\right)_{rad} = \frac{E}{X_0} \tag{4.17}$$

where X_0, the radiation length, is defined in Eq. (??). From Eq. (??) therefore, the average energy of a beam of electrons of initial energy E_o, after traversing a path length ξ in a medium, will be

$$< E >= E_0 \exp(-\xi/X_0) \tag{4.18}$$

Thus, the radiation length X_0 can be also defined simply as that path length the particles have travelled in the medium that would reduce the mean energy of a beam of electrons by a factor of e.

In Eq. (??) and Figure ??, it is evident that the rate of ionisation energy loss beyond the minimum value is proportional to the logarithm of the energy. In addition, such contribution of energy loss is approximately constant for high energy electrons. So, at high energies, bremsstrahlung dominates the energy loss. The energy, at which, these two interaction processes for electrons lead to equal energy losses, is defined as critical energy E_c and can be derived by combining Eq. (??), (??) and (??) as [?]

$$E_c \simeq \frac{550}{Z} \quad \text{MeV} \tag{4.19}$$

Table ?? lists the numerical data of the radiation lengths and the critical energies for some certain materials with electrons as the incident particles [?, ?]. It is easy to find that the radiation length and the critical energy as well, scale as the square of the mass of the incident particles. Thus, for other light particles, for example, muons μ, in medium A, it has

$$E_{c,A}^{\mu} \simeq \left(\frac{m_\mu}{m_e}\right)^2 E_{c,A}^{e} \quad ; \quad X_{0,A}^{\mu} \simeq \left(\frac{m_\mu}{m_e}\right)^2 X_{0,A}^{e} \tag{4.20}$$

Table 4.1: *The radiation length X_0 and the critical energy E_c for some various absorber materials with electrons as the incident particles [?, ?].*

Material	Z	A	X_0 (g/cm^2)	X_0/ρ (cm)	E_c (MeV)
Hydrogen	1	1.01	63	700000	350
Helium	2	4.00	94	530000	250
Lithium	3	6.94	83	156	180
Carbon	6	12.01	43	18.8	90
Nitrogen	7	14.01	38	30500	85
Oxygen	8	16.00	34	24000	75
Aluminum	13	26.98	24	8.9	40
Silicon	14	28.09	22	9.4	39
Iron	26	55.85	13.9	1.76	20.7
Copper	29	63.55	12.9	1.43	18.8
Lead	82	207.2	6.4	0.56	7.40
Air	7.3	14.4	37	30000	84
SiO_2	11.2	21.7	27	12	57
Water	7.5	14.2	36	36	83

4.1.4 Energy Loss by High Energy Photons in Matter

Processes which generate the interactions of high energy photons with atoms, nuclei and electrons are divided into types of photoelectric effect, Rayleigh scattering (coherent scattering), Compton scattering (incoherent scattering), photonuclear absorption and electron-positron pair production. Interactions of photons are fundamentally different from the ionisation processes of charged particles since in each photon interaction, the photon is either completely absorbed (photoelectric effect, photonuclear absorption, pair-production) or is scattered through a more or less large angle (Rayleigh effect, Compton effect).

For astrophysical interest, these processes are very important in studying high energy astrophysical phenomena, for example, the development of electron-photon cascades in which high energy electrons enter the atmosphere or in a particle detector. The arrival of very high energy γ-rays at TOA gives rise to showers of extremely energetic electron-positron pairs, in which, the produced pairs will afterwards generate Čerenkov radiation which can be observed at ground level. Such a technique has provided the remarkable evidence for ultrahigh energy γ-rays from cosmic sources. In addition, these properties meet very wide applicability in high energy astrophysics. Photoeletric absorption is found in the spectra of most X-ray sources at $E < 1$ KeV. Compton scattering appears numerously from the processes which take place in stellar interiors, to the spectra of binary X-ray sources and also the applications of inverse Compton scattering in objects involving intense radiation fields and high energy electrons. Pair production is bound to occur whenever there is significant flux of high energy γ-rays and is proven by the detection of

the 511 keV electron-positron annihilation line by observing the Galaxy.

Like charged particles, photons have a high probability of being absorbed or scattered through large angles by the atoms in matter. It is then impossible to define exactly a range for γ-rays. Statistically, a photon beam is approximately exponentially attenuated in matter:

$$I = I_0 e^{-\mu\xi} \tag{4.21}$$

after traversing a length ξ with an initial beam density I_0. The mass absorption coefficient μ is related to the cross sections for the various interaction processes of photons that is described as

$$\mu = \sum_i \mu_i = \frac{N_0}{A} \sum_i \sigma_i \tag{4.22}$$

where σ_i is the cross section for the process i, A is the atomic weight of the matter and μ is in unit of cm^2/g.

?? *(a) Photoelectric Effect*

Photoelectric effect

$$\gamma + A \rightarrow A^+ + e^- \tag{4.23}$$

is one of the principal sources of opacity in stellar interior and stellar atmosphere. An incident photon can eject an electron from the atom, ion, or molecule, if its energy is greater than the binding energy of that electron, $\hbar\omega \geq E_I$. The remaining energy ($\hbar\omega$-E_I) then transfers to that electron as the kinetic energy. This process can continue until $\hbar\omega < E_I$. In evaluating the absorption cross section, the cross section from the electrons in the K-shells (1s) of atoms is particularly important ($\approx 80\%$ of the total cross section σ_{PE}) [**?**]. This results comes from the fact that, according to the momentum conservation law, a photon cannot be completely absorbed by a free electron. The absorption of a photon by an atomic electron then requires a third collision partner, the atomic nucleus itself. So, the photon absorption by electrons in the K-shells of the atom is important because the atomic nucleus takes the recoil momentum. Analytically, the absorption cross section due to the ejection of electrons from the K-shells, σ_{PE}^K, is evaluated from the quantum theory of radiation [**?**]

$$\sigma_{PE}^K = 4\sqrt{2}\sigma_{Th}\alpha^4 Z^5 \left(\frac{m_e c^2}{\hbar\omega}\right)^{7/2} = \frac{e^{12} m_e^{3/2} Z^5}{192\sqrt{2}\pi^5 \epsilon^6 \hbar^4 c} \left(\frac{1}{\hbar\omega}\right)^{7/2} \tag{4.24}$$

where α is the fine structure constant and σ_{Th} is the Thomson cross section, $\sigma_{Th} = 8\pi r_e^2/3 = e^2/6\pi\epsilon_0^2 m_e^2 c^4$

The cross section shown in Eq. (**??**) corresponds to the removal of two K-shell electrons from the binding of the atom since both 1s electrons contribute to the opacity of the

material. Apparently, Eq. (??) has a strong dependence upon the atomic number Z. Thus, even though heavy elements are much less abundant than hydrogen, the effect from the $\omega^{-7/2}$ dependence and the Z^5 dependence shows that the rare heavy elements in the stellar atmosphere or in the interstellar region make important contribution to σ_{PE} at hard ultraviolet and X-ray energy levels [?]. In addition, Eq. (??) can help understand some characteristic features of X-ray absorption spectra observed in X-ray sources. Each atom has a characteristic X-ray term diagram showing the energies of the different stationary states (K, L, M, etc.) for the removal of an electron from within an atom. Such information is of great importance in the construction of proportional counters for the detections of X-rays since the photoelectric absorption spectra of the detector gas and the window material determine the efficiency and the sensitivity of the counter [?].

?? *(b) Compton Scattering*

The Compton scattering describes the process that the incoming photons collide with quasi-free stationary atomic electrons and transfer some of their energy and momentum to the electrons.

$$\gamma + e^- \rightarrow \gamma + e^- \tag{4.25}$$

In the treatment of this interaction process, the binding energy of the electrons is neglected. The relevant total cross section for Compton scattering per electron σ^e_{KN} is the Klein-Nishina formula [?]

$$\sigma^e_{KN} = 2\pi r_e^2 \left\{ \left(\frac{1+\varepsilon}{\varepsilon^2} \right) \left[\frac{2(1+\varepsilon)}{1+2\varepsilon} - \frac{1}{\varepsilon} \ln(1+2\varepsilon) \right] + \frac{1}{2\varepsilon} \ln(1+2\varepsilon) - \frac{1+3\varepsilon}{(1+2\varepsilon)^2} \right\} \tag{4.26}$$

where $\varepsilon = \hbar\omega / m_e c^2$. In cases of low and high energy photons, Eq. (??) then reduces to

$$\sigma^e_{KN} \simeq \frac{8\pi}{3} r_e^2 (1-2\varepsilon) = \sigma_{Th}(1-2\varepsilon) \approx \sigma_{Th} \qquad (\varepsilon \ll 1) \tag{4.27}$$

$$\sigma^e_{KN} \simeq \pi r_e^2 \frac{1}{\varepsilon} (\ln 2\varepsilon + \frac{1}{2}) \propto \frac{\ln \varepsilon}{\varepsilon} \qquad (\varepsilon \gg) \tag{4.28}$$

So, Eq. (??) shows that the cross section decreases roughly as ε^{-1} at the highest energies. If the atom has Z electrons, there are exactly Z electrons that can scatter the photons. So, the total cross section for Compton scattering, σ^A_C, is just Z times the σ^e_{KN}. Therefore,

$$\sigma^A_C = Z \cdot \sigma^e_{KN} \tag{4.29}$$

In addition to Compton scattering, another process, inverse Compton scattering also exists. In this case, the high energy electrons scatter low energy photons and transfer a fraction of their energy to photons, which consequently are blue shifted to higher energies. For example, radio, infrared or optical photons are scattered by very high energy electrons

and then turn to X-ray or γ-ray range. For this reason, the inverse Compton scattering is a means of producing high energy photons in the celestial bodies or terrestrial accelerators. Apparently, such a process is an inevitable drain of energy loss for high energy electrons whenever they pass through a region with a large energy density of photons. Typically, the energy loss rate of this process corresponds to $v^2\gamma^2$.

Compton scattering also takes place between photons and other charged particle, say the atomic nuclei. However, the atomic nuclei experience much less scattering than electrons, roughly by a factor of $(m_e/M_A)^2$ from Eq. (**??**).

?? *(c) Pair Production*

The production of electron-positron pairs

$$\gamma + (Z, A) \rightarrow (Z, A) + e^- + e^+ \tag{4.30}$$

in the Coulomb field of a nucleus is only possible if the photon energy exceeds a certain threshold, which is given by twice the electron mass plus the recoil energy that is transferred to the nucleus

$$\hbar\omega \geq 2m_e c^2 + 2\frac{m_e^2}{M_A}c^2 \sim 2m_e c^2 \qquad (\text{with } M_A \gg m_e) \tag{4.31}$$

If, however, the electron-positron pair production proceeds in the Coulomb field of an electron, then the threshold energy in Eq. (**??**) turns to be $4m_e c^2$. So, electron-positron pair production in the Coulomb field of an electron is strongly suppressed when compared to that in the Coulomb field of the nucleus.

The results for electron-positron pair production cross section, σ_{pair}, are given as follows.

Intermediate photon energies In the case of no screening, σ_{pair} for photons with energies in the range $1 \ll \hbar\omega/m_e c^2 \ll 1/\alpha Z^{1/3}$ is of the form [**?**]

$$\sigma_{pair} = \alpha r_e^2 Z^2 \left[\frac{28}{9}\ln\left(\frac{2\hbar\omega}{m_e c^2}\right) - \frac{218}{27}\right] \quad (\text{m}^2/\text{atom}) \tag{4.32}$$

Ultrarelativistic limit In the case of complete screening and for photons with energies $\hbar\omega/m_e c^2 \gg 1/\alpha Z^{1/3}$, σ_{pair} becomes [**?**]

$$\sigma_{pair} = \alpha r_e^2 Z^2 \left[\frac{28}{9}\ln\left(\frac{183}{Z^{1/3}}\right) - \frac{2}{27}\right] \quad (\text{m}^2/\text{atom}) \tag{4.33}$$

Note that for large energy photons, the pair production cross section approaches an energy independent value in Eq. (**??**). Further approximation can be reached by using definition X_0 in Eq. (**??**).

$$\sigma_{pair} \simeq \frac{7}{9}4\alpha r_e c^2 Z^2 \ln\left(\frac{183}{Z^{1/3}}\right) \simeq \frac{7}{9}\frac{A}{N_0}\frac{1}{X_0} \tag{4.34}$$

Eq. (??) together with the definition of γ-ray attenuation coefficient in Eq. (??) will lead to the attenuation for a beam of high energy photons with initial intensity I_0 by pair production after travelling a length ξ in medium as

$$I = I_0 \exp\left(-\frac{7\xi}{9X_0}\right) \tag{4.35}$$

which is the form applied to the electromagnetic cascades.

In summary, from Eq. (??), (??), (??) and (??), for the photon absorption in matter, the photoelectric cross section varies with photon energy as $1/E^{7/2}$, the Compton cross section as $1/E$ and pair production cross section stay essentially constant for high energy photons. Figure ?? shows the total and various mass attenuation coefficients defined in Eq. (??). All values are calculated by running NIST (National Institute of Standards and Technology) XCOM: Photon Cross Sections Database in Physical Reference Data. As shown in the figure, the mass attenuation coefficient depends strongly on the photon energy. For low energies, $E_{ion} \leq \hbar\omega \leq$100 KeV where E_{ion} is the ionisation energy, the photoelectric effect dominates; in the range of medium energies, 0.1 MeV $\leq \hbar\omega \leq$ 10 MeV, the Compton scattering dominates; at high energies, $\hbar\omega \geq$ 10 MeV, the pair production extremely dominates even though its cross section is almost constant. At low energies, Rayleigh scattering shows a more important contribution than Compton scattering but its cross section is negligible because it is about 10^{-3} of the cross section of the photoelectric effect.

4.2 Measurement Methodology: Particle Detectors

One of the main purposes of some astrophysical experiments is the detection of particles produced in astrophysical nuclear interactions. This detection must be done with a resolution sufficient enough to enable particles to be separated in both space and time in order to determine which are associated with a particle event. In addition, it is necessary to identify each particle and measure its momentum and velocity. Such performances cannot be achieved by a single detector and in practice, experiments are using different detectors in combination. The modern trend is to build large multicomponent detectors that integrate many different sub-detectors in a single device. Such systems rely on fast electronics and computer to monitor and control the sub-detectors and to coordinate, classify and record the vast amount of information flowing in from different parts of the apparatus.

In this section, the principles of detectors which are used in the related experiments to this work is discussed.

4.2.1 Time Resolution: Scintillation Counter

Scintillation counters make use of the property of certain chemical compound which emit short light pulses after excitation by the passage of charged particles. The light

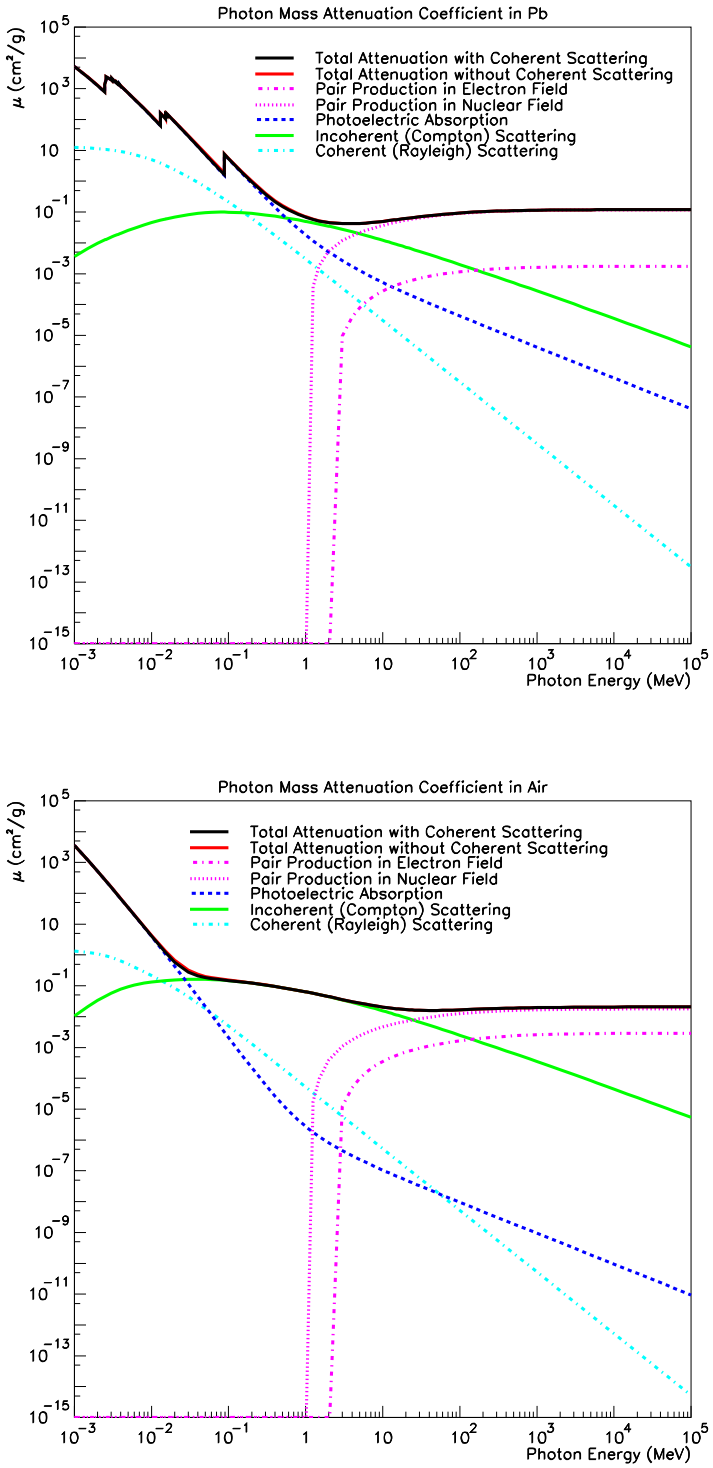

Figure 4.3: *Photon total mass attenuation coefficient as a function of energy in lead and air for the contributions of the various processes. The coefficients for carbon are similar to those for air. Values are calculated by running NIST XCOM: Photon Cross Sections Database in Physical Reference Data. The coherent scattering means, in the process, the atom is neither ionised nor excited. This is the process of Rayleigh scattering. The incoherent scattering, means a photon is scattered off an electron. This is the process of Compton scattering.*

emitted passes down the scintillator and is directed onto the face of a photomultiplier by multiple internal reflections along a shaped solid plastic tube called a light guide. Scintillation is characterised by the light yield, the absorption and emission spectrum, signal linearity and the pulse shape, and decay times as well, for which, the decay times range from less than 1 ns up to 5 μs [**?**]. Thus, the scintillation counter is ideal for timing devices, with a time resolution as good as 100 ps or better, and for fast event selection. It is also important for measuring the energy of particles by total absorption in sampling calorimeters.

Commonly used scintillators are inorganic single crystals (e.g. sodium iodide) or organic liquids and plastics. A modern complex detector might use detectors in combination with photomultiplier tubes (PMTs).

4.2.2 Measurement of Position

The devices providing measurements of a particle position detect ionisation, either by collecting the total ionisation products onto electrons by using an electric field, or by making the ionisation track visible in some form. A wide range of devices are available for this purpose. Bubble Chamber, Cloud Chamber and Photographic Emulsion were used in the early studies while nowadays, Proportional/Drift Chambers and Semiconductor Detectors are frequently used as current detectors. In this subsection, Proportional/Drift Chambers and Semiconductor Detectors are especially discussed since they are the most frequently used in modern experiments in particle physics and astrophysics.

- *Proportional and Drift Chambers*: The basis of proportional chambers is the observation that, if an electric field is established in a gas, the electrons released as a part of electron-ion pairs by the passage of a charged particle will drift towards the anode, with a velocity

$$v_D = \frac{e\tau E}{2m_e} \tag{4.36}$$

  where e is the electron charge, m_e is the electron mass, τ is the mean time between collisions and E is the electric field. If the field is strong enough, the electron will gain sufficient energy to result in secondary ionisation, and a chain of such processes leads to a avalanche of secondary electrons which can be collected as a pulse on the anode. The proportional counter, first established by using this idea, consists basically of a cylindrical tube filled with gas and maintained at a negative potential, and a fine central wire at a positive potential. If many anode wires are arranged in a plane between a common pair of cathode plates, then each wire acts as an independent detector. This is called multiwire proportional chamber (MWPC), which can achieve spatial resolutions of 500 μm or less [**?**], and has a typical time resolution of about 30 ns [**?**]. In order to reach better spatial resolution, drift chambers are used [**?**]. This applies the fact that the liberated electrons take some time to drift from the point where they are produced to the anode. Thus, the

time delay between the passage of a charged particle through the chamber and the creation of a pulse at the anode is related to the distance between the particle trajectory and the anode wire. In practice, a reference time has to be well defined, which can be done by allowing the particle to pass through a scintillator located somewhere in the experiment. The electrons drift for some time and are collected at the anode, thus providing a signal that the particle has passed. If the time resolution is good enough, then it is possible to translate this time resolution into spatial resolution, if the drift velocity is known. Generally, it is easy to get a spatial resolution of 100-200 μm [?], or even less. MWPCs and drift chambers are constructed in a variety of geometries, depending on the nature of the experiment.

- *Semiconductor Detectors*: Semiconductor detectors are essentially solid state ionised chambers. The principle of the operation is that, if an ionised particle penetrates the detector, it then produces electron-hole pairs along its track. In the presence of an externally applied electric field, the electrons and holes are separated and collected at the electrodes before they recombine, giving a signal proportional to the energy loss of the incident charged particle. The intrinsic energy resolution is related to the low energy threshold: only about 3.7 eV is necessary to produce an electron-hole pair [?], much lower than the ionisation energy in a gas, about 30 eV, and the extraction energy of an electron from a photocathode coupled to a plastic scintillator, which is about 300 eV. Semiconductor detector devices can be produced in a small size. For example, in a silicon microstrip detector, narrow strips of active detector are etched onto a thin slice of silicon, with gaps of an order of 10 μm. Arrays of such strips can then be used to form detectors with an accuracy of position localisation of an order of 5 μm [?]. However, being electronic devices, they are limited in the ability to withstand the radiation damage [?].

4.2.3 Measurement of Momentum

The momentum of a charged particle is usually determined from the curvature of its track in a magnetic field:

$$\rho = \frac{P}{z} = \frac{\gamma m_o \beta c}{z} \tag{4.37}$$

An apparatus which measures the momentum of a charged particle is called spectrometer, which consists of a magnet and a series of detectors to track the passage of the particles. Two popular types of magnet are used in particle spectrometers, depending on the experiments. Dipole magnets typically have their field perpendicular to the beam direction and have their best momentum resolution to particles emitted in the direction along the beam. For colliders, however, the most usual magnet shape is the solenoid where the field lines are parallel to the beam direction. This device is usually used in conjunction with cylindrically tracking detectors. For this, the device has its best momentum resolution for particles whose directions are perpendicular to that of the beam.

4.2.4 Particle Identification

Particle identification is usually based on determining the mass of the particle by position-sensitive detectors used for tracking, or calorimeters used for measuring particle energy. Particle identification relies on special properties of some particles, like muons, which carry charges but do not shower nor interact strongly, or, the electromagnetic shower characteristics for electrons and gammas. In most cases, mass measurement of a charged particle usually combines p (by spectrometer) versus β (by TOF, Čerenkov Counter and so on) or p versus the ionisation loss dE/dx (by Calorimeters).

?? *(a) Time of Flight*

The simplest way to measure the velocity of a particle is to measure the time of flight (TOF) between two scintillation counters. The velocity of a particle is then given by the TOF combined with the distance in between. Particle identification with TOF techniques requires an excellent time resolution. Suppose two particles of mass m_1 and m_2 have the same momentum and flight distance L, then the TOF difference is

$$\triangle t = L\left(\frac{1}{v_1}-\frac{1}{v_2}\right) = \frac{L}{c}\left(\frac{1}{\beta_1}-\frac{1}{\beta_2}\right) \tag{4.38}$$

$$= \frac{L}{c}\left\{\sqrt{\frac{\gamma_1^2}{\gamma_1^2-1}}-\sqrt{\frac{\gamma_2^2}{\gamma_2^2-1}}\right\} = \frac{L}{c}\left\{\sqrt{\frac{1}{1-\left(\frac{m_1c^2}{E_1}\right)^2}}-\sqrt{\frac{1}{1-\left(\frac{m_2c^2}{E_2}\right)^2}}\right\} \tag{4.39}$$

For relativistic particles, Eq. (**??**) changes to

$$\triangle t = \frac{L}{c}\left\{\sqrt{1+\left(\frac{m_1c^2}{E_1}\right)^2}-\sqrt{1+\left(\frac{m_2c^2}{E_2}\right)^2}\right\} \simeq \frac{Lc}{2p^2}(m_1^2-m_2^2) \tag{4.40}$$

For a mass seperation, a significance of $\triangle t = 4\sigma_t$ is demanded [**?**]. That is, a TOF difference 4 times the time resolution is required. Such a constraints has limited this method to low energy particles with momenta $p \leq 4$ GeV/n.

?? *(b) Čerenkov Radiation and Čerenkov Counter*

An important identification method for high energy particles is based on the Čerenkov effect. Whenever a charged particle with a velocity $\beta = v/c$ traverses a dispersive medium of refractive index n, excited atoms in the vicinity of the particle become polarised. If the particle velocity exceeds the light speed in the medium v_γ, $\beta > v_\gamma = 1/n$, the excited atoms turn back rapidly to their ground state and then emit a part of the excitation energy which reappears as coherent radiation, emitted at a characteristic angle θ relative to the direction of the particle velocity

$$\cos\theta = \frac{1}{\beta n} \tag{4.41}$$

Therefore, from Eq. (**??**), it is easy to see that the measurement of θ is a direct measurement of the particle velocity. Figure **??** presents schematically this phenomenon.

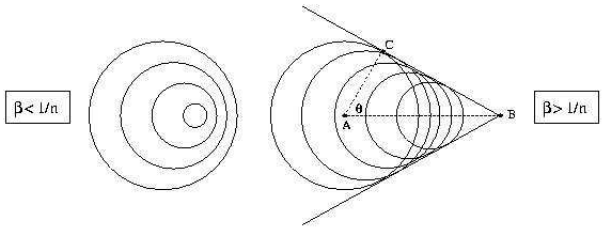

Figure 4.4: *Huygens construction for two velocities:* $\beta < 1/n$ *and* $\beta > 1/n$.

Eq. (**??**) shows that the asymptotic emission angle which is given as

$$\cos\theta_{max} = \frac{1}{n} \tag{4.42}$$

and also the thresholds for velocity and momentum of the particle

$$\beta_{th} = \frac{1}{n} \quad ; \quad P_{th} = \frac{mc}{\sqrt{n^2-1}} \tag{4.43}$$

Čerenkov radiation appears as a continuous spectrum and can be collected by a photosensitive detector. However, the problem is its modest light yield: the energy loss due to ionisation or excitation is 2 or 3 orders of magnitude higher than the energy lost in radiation Čerenkov light. But, in the photon energy range, photomultipliers can be used, about a few eV, or about 400 nm wavelength [**?**]. The photon yield per unit length in the wavelength interval $(\lambda, \lambda + d\lambda)$ is given as [**?**]:

$$\frac{dN}{dld\lambda} = \frac{2\pi\alpha Z^2}{\lambda^2}(1-\cos^2\theta) = \frac{2\pi\alpha Z^2}{\lambda^2}\left(1-\frac{1}{\beta^2 n^2}\right) \tag{4.44}$$

where N is the photon number, l is the length of traversed radiator, λ is the wavelength of Čerenkov light, α is the fine structure constant and Z is the charge of the incident particle. So, the photon yield after a traversed length can be obtained by integrating the range of sensitive wavelength.

Čerenkov counters are used to measure the particle velocity. They can be used as threshold counters, filtering the particles with velocities $\beta > 1/n$ or differential counters, accepting light only in a narrow range of angles, with a proposed β resolution. In Ring Imaging Čerenkov Counter (RICH), the Čerenkov radiation emitted at an angle θ is focused onto a ring on the detector surface, made of photomultiplier tubes (PMTs) or photosensitive MWPCs. β is then determined by a direct measurement of the radius of that ring.

?? *(c) Transition Radiation*

Also below Čerenkov threshold, a charged particle may emit electromagnetic radiation. When a charged particle traverses an interface, the charge, together with its mirror charge form an electric dipole, whose field strength varies in time, or, in other word, varies with the movement of the particles. The field strength vanishes when the particle enters the medium. Thus, the time dependent dipole electric field causes the emission of electromagnetic radiation, called transition radiation.

One of the most important features of transition radiation is that, the radiation energy increases with the Lorentz factor γ rather than its velocity [?]. The γ-dependent effect of transition radiation is extremely important for particle identification at high energies since most processes used for this purpose (ionisation energy loss, TOF, Čerenkov radiation,...) depend on β, thus providing only moderate possibility in identifying ultrarelativistic particles. Another important characteristic is that, the transition radiation photons are emitted in an angle, $\theta = \frac{1}{\gamma}$ [?], in the X-ray range [?], with the average energy about 5-25 KeV in the electron momentum range 1-4 GeV/c for typical standard radiator arrangements [?], which produce an effective threshold behaviour at a value of $\gamma \approx 1000$.

In general, a Transition Radiation Detector (TRD) is constructed by using a set of foils consisting of a material with Z as low as possible. As seen in Eq. (??), the photoabsorption cross section depends strongly on Z: $\propto Z^5$. Hence, a material with small Z has to be chosen otherwise, the transition radiation photons are not able to escape from the radiator.

Transition radiation is particularly useful in identifying high energy particles. With the threshold $\gamma \approx 1000$, pions, for example, with energies below 140 GeV cannot produce such radiation but only deposit the energy loss by ionisation and excitation in the detector. Thus, this provides a means to distinguish electrons from pions. Similarly, pions can be distinguished from kaons at relativistically high energies. For $E > 140$ GeV, pions will produce transition radiation while kaons, with $\gamma = 280$ at this energy, do not. Even in the TeV-region, a $\pi/K/p$ separation with TRDs still appears feasible.

4.2.5 Energy Measurement: Calorimeters (Shower Counters)

Calorimeters are used to measure the energy and the position of a particle by its total absorption. Calorimeters differ from other kinds of detectors in that the nature of the particle is changed during the passage, and, they can be applied to both neutral and charged particles. A calorimeter can be a homogeneous absorber, or detector, such as a block of lead glass used to detect photons by Čerenkov radiation, or, it can be a sandwich construction with separated layers of absorber and detector. During the absorption process, the particle interacts with the material of the absorber, generating secondary particles which will then generate further particles, and so on. So, a cascade then develops in the absorber. As discussed in Section ??, the shower is predominating in the longitudinal direction but will be subject to some transverse spreading due to Coulomb scattering and the transverse momentum of the produced particles. As a result, almost all of the primary energy is then deposited in the calorimeter and gives a signal in the detector component.

Calorimeters have some important characteristics, especially for high energy particles:

(i) they can detect neutral particles, by measuring the charged secondaries; (ii) the absorption process is statistical, so that the relative precision of energy measurement $\triangle E/E$ varies as $E^{-1/2}$ for large E [?], with a great improvement on high energy spectrometer for which, $\triangle E/E$ varies as E^2 [?]; and (iii) the signal produced by the cascades is fast of order 10-100 ns [?], and is thus suitable for triggering purpose.

Calorimeters are usually composed of different parts, built for optimal performance on different particles. Typically, incident electromagnetic particles, electrons and gammas, are fully absorbed in the electromagnetic calorimeter, whose construction takes advantages of the comparatively short and concentrated electromagnetic shower shape to measure energy and position with optimal precision. On the other hand, incident hadrons, may start their showering in the electromagnetic calorimeter, but will nearly always be fully absorbed only in hadronic calorimeter.

?? (a) Electromagnetic Showers

A high energy electron or positron interacts with the matter that the dominant energy loss is due to bremsstrahlung, and for the photons produced, the dominant absorption process is pair production. So, by these two processes, a incident electron will lead to a cascade of e^-e^+ pairs and photons. The cascade continues developing until the energy of the secondary falls below the critical energy in Eq. (??), $E_c \simeq 560$ MeV$/Z$ [?].

A shower development can be simply modelised by the qualitative features:

(i) each electron with energy $E > E_c$ travels one radiation length and then gives up half of its energy to a bremsstrahlung photon;

(ii) each photon with $E_\gamma > E_c$ travels one radiation length and then creates an e^+e^- pair, in which, each particle has half of the photon energy;

(iii) electrons with $E < E_c$ cease to radiate and lose all the rest energy by collisions with material;

(iv) ionisation losses are negligible with $E > E_c$.

So, suppose the initial electron energy $E_0 \gg E_c$, then after traversing ξ radiation lengths, the shower will have 2^ξ particles which consist of approximately the same amount of electrons, positrons and photons and each of which has the average energy

$$E(t) = \frac{E_0}{2^\xi} \tag{4.45}$$

And, the shower will cease until the particles have traversed the maximum radiation length, ξ_{max}, at which, $E(\xi) = E_c$. So that

$$\xi_{max} = \xi(E_c) = \frac{\ln(E_o/E_c)}{\ln 2} \tag{4.46}$$

Thus, the number of particles at ξ_{max} is just

$$N_{max} = \exp(\xi_{max} \ln 2) = \frac{E_0}{E_c} \tag{4.47}$$

Eqs. (??) and (??) show that maximum shower depth increases logarithmically with the incident energy and the maximum particle number in the shower is determined only by the primary energy. So, the physical size for calorimeters is required to increase slowly with the maximum energies of the particles to be detected. Electromagnetic showers have a shape that fluctuates within comparatively narrow limits and, and the energy resolution actually depends on the statistical fluctuations, which is typically [?]

$$\frac{\triangle E}{E} \simeq \frac{0.05}{\sqrt{E}} \tag{4.48}$$

where E is in unit of GeV.

?? *(b) Hadronic Showers*

Hadronic showers are similarly modelised as electromagnetic showers but are much more complex in reality. The complex features come from that many different processes will contribute to the inelastic production of secondary hadrons. The scale of the shower is determined by the nuclear absorption length defined as

$$l_a = \frac{1}{n\sigma_{inel}} \tag{4.49}$$

where n is the number density of the material. According to the formula of total inelastic cross section in Eq. (??) and the values of radiation length in Table ??, the absorption length is much larger than the radiation length. So, hadron calorimeters have to be much thicker than electromagnetic calorimeters.

Another major difference for hadron calorimeters is that, the calorimeters may also provide signatures for particles that are not absorbed: muons and neutrinos [?]. Muons do not shower in matter but their charges leave an ionisation signal, which can be identified in a calorimeter if the particles are sufficiently isolated, and then can be associated to a track detected in tracking devices inside, or in specific muon chambers. Neutrinos, on the other hand, leave no signal in a calorimeter but their existence can sometimes be inferred from energy conservation. And, a substantial fraction of the hadronic energy, of about 20% of the total energy [?], will be used to break up nuclear bonds. In the break-up of nuclear bonds, short range nuclear fragments are produced. However, such fragments do not contribute to the detection signal since they are absorbed before reaching the detection layers. Furthermore, stable neutral particles like neutrons, K^0 or neutrinos, can probably escape from the calorimeter. All these excitation and leakage of secondary muons and neutral particles will reduce the energy resolution. In addition, hadron calorimeters have a widely fluctuating shape. These features lead that the energy resolution is in general much worse than that of electromagnetic calorimeters, typically at least 10 times worse than Eq. (??) [?].

4.3 Experiments

Data of cosmic particles are available from both balloon-borne and space-borne experiments. The measurement results provide good sources to verify the related subjects on astrophysical studies. In this section, the related experiments to the work of this thesis are discussed. The performed experiments will be applied to verify the applicability of this work and this work is expected to explore its applicability to the probable results in the future experiments.

4.3.1 Isotope Matter Antimatter Experiment (IMAX)

The Isotope Matter-Antimatter Experiment (IMAX) shown is Figure **??** is a balloon-borne magnetic spectrometer designed to measure cosmic ray antiprotons, hydrogen isotopes and helium isotopes over an energy range from about 200 MeV/n to 3 GeV/n [**?**]. This energy range includes the intensity maximum in the light isotope spectra. In the energy range of about 1 to 3 GeV/n, differences from the antiproton spectral shape and intensity expected from interactions of cosmic rays with the ISM may indicate that antiprotons from exotic sources are present [**?**].

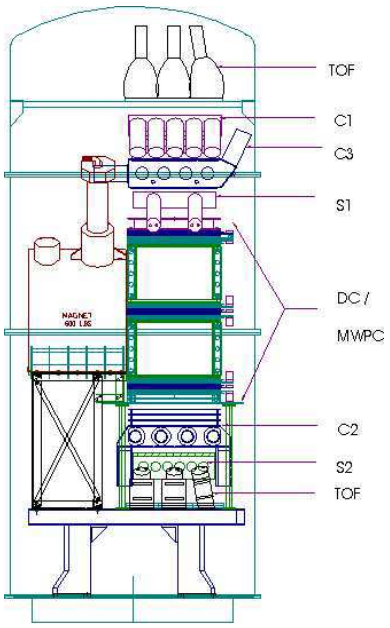

Figure 4.5: *Schematic drawing of the IMAX instrument [**?**]. IMAX has a useful geometry factor of 140* cm^2 sr. *As its basis, IMAX uses the NASA/NMSU Balloon-Borne Magnet Facility payload, with additional detectors and electronics supplied by the collaboration. See text for the abbreviations of all devices.*

Particle identification in IMAX is based on the determination of the charge Z, velocity

β, and magnetic rigidity R of incident particles. The rigidity is measured using a 61 cm diameter single-coil superconducting magnet, providing a magnetic field from 0.1 to 2.1 Tesla in the region of the tracking detectors [?]. The tracking system is a combination of drift chambers (DCs) and multiwire proportional chambers (MWPCs). The DC system consists of two identically manufactured DC modules with a hexagonal close-packed structure, which provide 12 measurements in the bending direction (x) and 8 in the non-bending direction (y). The average position resolution in the DCs is about 65 μm [?]. The set of MWPCs, placed above, below and between the two DC modules, provide another eight measurements in x and four in y.

Particle trajectories are measured in general with the full hybrid tracking system (DCs plus MWPCs), whereas both tracking subsystems can operate separately in order to provide two independent trajectory measurements. In addition, each single DC module is capable of measuring the trajectory of a charged particle in the magnetic field. The most probable maximum detectable rigidity (MDR), which is defined as the value at which the uncertainty in the rigidity measurement becomes 100% [?]:

$$\frac{dR}{R} = \frac{R}{\mathrm{MDR}} \tag{4.50}$$

and is determined by the path integral of the magnetic field and the trajectory resolution, is about 200 GV/c for Z=1 particles [?]. A large MDR is important while identifying particle charge sign at high energy.

Particle velocities are measured by a TOF system with a flight path of 2.54 m and two Čerenkov counters (C2 and C3) with n=1.043 silica-aerogel radiators [?]. For Z=1, $\beta \simeq$1 particles, the TOF resolution $\sigma \simeq$ 122 ps [?] while for Z=2 particles, $\sigma \simeq$ 92 ps [?]. Energy loss is measured by the TOF and scintillators S1 and S2.

The charge determination is performed by four independent ionisation energy loss measurements. Beside the two plastic scintillators of the TOF system, which form the event trigger, two large area light integrating counters S1 and S2 are used to separate particles by charge. The charge is determined by using a dE/dx versus β^2 method.

The IMAX flight took place in July 1992 [?]. The float altitude of 36 km (5 g/cm^2 of residual atmosphere) was reached about 7 hours after launch. During the flight, the geographic latitude varied between $55^0 58'$N and $57^0 35'$N, and the geographic longitude varied between $100^0 28'$W and $117^0 35'$W. The vertical geomagnetic cutoff rigidity varied between about 0.35 GV at departure position and 0.63 GV at the landing position. These cutoff rigidities correspond to energies for protons 70 MeV and 190 MeV and for ^4He, 17 MeV/n and 52 MeV/n respectively [?]. The geomagnetic cutoff is then well below the instrument cutoff owing to the instrumental grammage in the IMAX experiment and the residual atmosphere on the top of the instrument [?].

4.3.2 Balloon Borne Experiment with Superconducting Solenodial Spectrometer (BESS)

BESS, the Balloon Borne Experiment with a Superconducting Solenodial Spectrometer, shown in Figure **??**, was proposed and developed as a high resolution spectrometer for the mission to search for antihelium nuclei in the galactic cosmic rays. It is ideally suited to statistics limited studies of Z=1 and Z=2 components in cosmic rays, identifying antiprotons, measuring proton and helium spectra and separating isotopes as well [**?**, **?**].

BESS has been described in detail in articles on BESS [**?**, **?**, **?**]. The BESS detector has incorporated various new detector technologies developed for collider experiments. A uniform field of 1 Tesla is produced by a thin superconducting coil (4 g/cm^2 thick including the cryostat) [**?**], through which, particles can pass with small interaction probability. The magnetic field region is filled with central tracking devices. This configuration has achieved a geometrical acceptance of 0.3 m^2 sr [**?**], depending on the off-line fiducial cuts [**?**]. The r-ϕ tracking in the central region is performed by fitting up to 28 hit points, each with 200 μm resolution [**?**], in a jet-type drift (JET) chamber and two inner drift chambers (IDCs) resulting in a maximum detectable rigidity of 200 GV/c, corresponding to the momentum resolution of 0.5% at 1 GeV/c [**?**]. Tracking in the z-coordinate is done to an accuracy of 300 μm by fitting points in IDCs measured by vernier pads and points in the JET chamber measured by charge devision with an accuracy of 2 cm [**?**]. The continuous and redundant 3-dimensional position measurements with outer drift chambers (ODCs), IDCs and JET chamber, which are all equipped with multi-hit capacity, make it possible to recognise multi-track events and tracks having interactions and scattering, thus minimising the background originating from interactions [**?**]. The upper and lower scintillators hodoscopes measure two independent dE/dx and the TOF of particles. In addition, dE/dx in the DC gas is obtained as a truncated means of the integrated charges of the hit pulses. The scintillator hodoscopes consist of 10 upper and 12 lower plastic scintillators and PMTs are attached at each end of scintillators [**?**]. The hodoscopes are placed at outer-most radii and the timing resolution of each hodoscope is 50 ps rms, resulting in inverse velocity β^{-1} resolution of 0.008 [**?**]. A Čerenkov counter with silica-aerogel radiator is installed below the upper TOF hodoscopes. The refractive index of the radiator is variable, for example, n=1.032 for 1997 flight [**?**] while n=1.020 for 1998 flight [**?**].

BESS flights took place once a year during the solar minimum 1995-1998 [**?**, **?**, **?**, **?**], with the geographic latitude range between 66.57^{0}N and 62.82^{0}N, and the longitude range between 118.34^{0}W and 141.45^{0}W, where the cut-off rigidity ranged from 0.3-0.5 GV/c. The flight altitudes varied from 35-38 km, with residual air of 4.8-5.5 g/cm^2, with an average value of 5.3 g/cm^2 [**?**].

BESS recently measured $\bar{p}$ flux at ground level [**?**, **?**], which will be discussed in Chapter **??**.

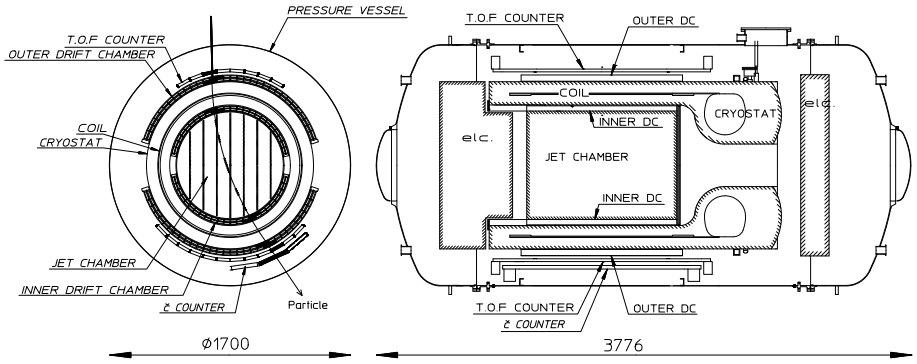

Figure 4.6: *Cross-sectional front and side views of the structure of BESS [?].*

4.3.3 Cosmic AntiParticle Ring Imaging Čerenkov Experiment (CAPRICE)

The main aim of the experiment of CAPRICE, Cosmic AntiParticle Ring Imaging Čerenkov Experiment, is to measure the flux of antiparticles, especially antiprotons and positrons, in the cosmic radiation. The balloon flights took place in 1994, 1997 and 1998 separately [?, ?, ?], between geographic latitudes and longitudes (56.5^0N, 101.0^0W) and (56.15^0N, 117.2^0W), at an atmosphere pressure of 3.2 to 4.5 mb, closely 36.0-38.1 km height, with an average residual atmosphere of 5.5 g/cm^2.

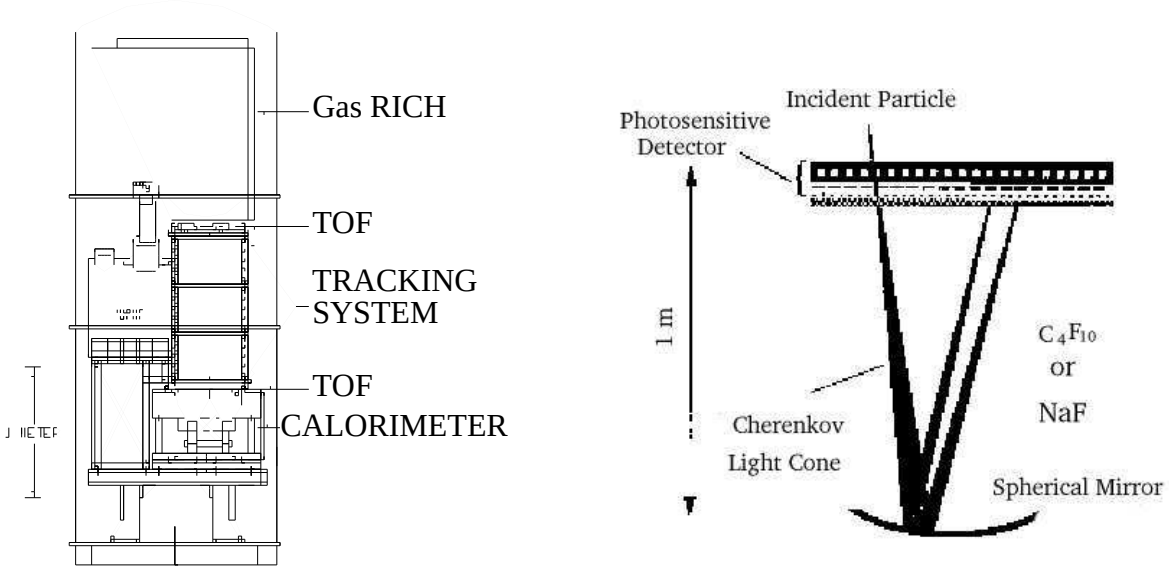

Figure 4.7: *Left: Schematic view of CAPRICE apparatus [?]. Right: Schematic view of the solid/gas RICH detector operating principles [?, ?].*

Figure ?? Left shows the CAPRICE spectrometer [?]. It includes from top to bottom:

a RICH detector, a TOF system, a tracking system consisting of DCs and a superconducting magnet, and silicon-tungsten imaging calorimeter. The details of this apparatus are described in a series of articles of CAPRICE [?, ?].

The RICH detector [?] shown in Figure ?? right, either installed with a solid NaF radiator, with a threshold Lorentz factor γ of 1.5 [?], or filled with high-purity perfluorobutane (C_4F_{10}) gas, with a γ threshold about 20 [?], is designed to identify antiprotons in cosmic rays in a large background of electrons, muons and pions. A spherical mirror is placed on the bottom of the radiator box, in order to reflect back the photons emitted along the particle trajectory onto a photosensitive MWPC. Photons are converted, by photoelectric effect, into photoelectrons which are amplified and detected on the matrix pad plane equipped in the MWPC volume. The profile of ring-like image on the matrix pad plane then reads out the velocity of particles. Such a layout can identify Z=1 particles with rigidities up to 50 GV/c [?] and with an angular resolution less than 2 mrad [?]. The TOF system consists of two layers of plastic scintillators, one placed above the tracking system and the other below. Each layer is divided into two paddles, each of which has two PMTs. The signal from each PMT is split into two parts: one is sent to an analog-to-digital converter and the other to a time-to-digital converter [?]. Thus, the TOF system provides both ionisation losses, dE/dx, and timing information and is used to identify albedo particles. The spectrometer consists of 3 sets of DCs, MWPCs and a superconducting magnet, with an average spatial resolution better than 100 μm [?] and with an average MDR of 300 GV/c [?]. The calorimeter is used to identify electromagnetic showers. The electromagnetic calorimeter consists of 8 silicon planes, giving x and y-coordinate projection readouts [?]. These silicon planes are interleaved with layers of tungsten convertors, each of which is one radiation length thick, $X_0 \simeq$ 3.5 mm [?]. The segmentation of the silicon planes into strips provides information on the longitudinal and lateral profiles of the interactions along the total deposited energy [?]. Thus, particles are identified by the combined energy release information with the event topology.

4.3.4 Alpha Magnetic Spectrometer (AMS)

The Alpha Magnetic Spectrometer (AMS) will be the first large acceptance detector to be put into space and collect data during a long period of time. AMS configuration on the precursor flight in 1998 (AMS01) is shown in Figure ?? and its working principle is schematically shown in Figure ??. AMS01 consisted of a large full acceptance magnetic spectrometer, about 0.82 m^2sr [?], based on a permanent Nd-Fe-B magnet, surrounding a 6 layer high precision silicon tracker and sandwiched between the 4 planes of the TOF scintillator system. A scintillator Anti-Coincidence Counter (Veto Counters) is located on the magnet inner wall and also an aerogel threshold Čerenkov detector, with n=1.035, providing the anti-coincidence protection against background particles and the noise outside the acceptance. A thin shielder on the top and the bottom sides would absorb low energy particles on the Earth radiation belts [?]. The complete system provides an effect geometric acceptance of 0.3 m^2sr [?].

The magnet is constructed by using high grade Nd-Fe-B as a permanent magnet in

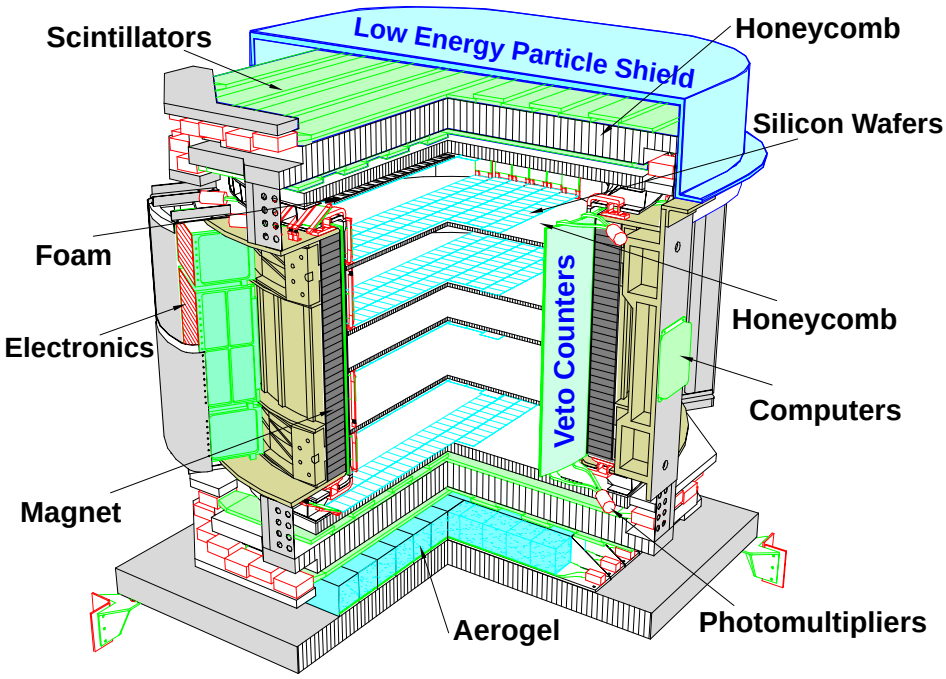

Figure 4.8: *AMS01 configuration for the June 1998 Shuttle precursor flight STS91. Picture is from the AMS Collaboration.*

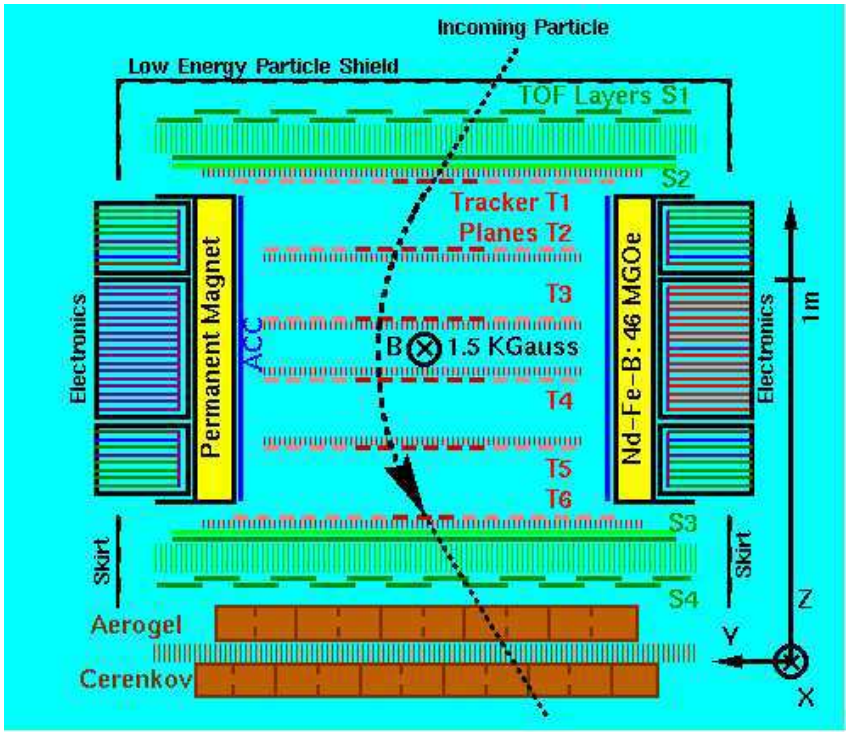

Figure 4.9: *The working principle AMS01. Picture is from the AMS Collaboration.*

a cylindrical shape with magnetic flux $BL^2 = 0.15$ T m^2, weighting less than 2 tons. A charged particle which traverses the spectrometer undergoes a dipole field orthogonal to the cylinder axis so that it triggers the experiment through the TOF system S1 to S4, which also provide measurements of the particle velocity β, with a typical resolution of 100 ps [**?**], over a distance of about 1.4 m. The curvature of the tracks is measured on the six layers of silicon double sided detectors (Trackers). The amount of material traversed by a particle is very small, less than 3% of the radiation length X_0 [**?**]. The momentum resolution of the Silicon Tracker is about 8% with rigidities between 1 and 10 GV [**?**] while at low momentum, the resolution is limited by multiple scattering. At high energy, its MDR is about 500 GV [**?**]. Both TOF system and the Silicon Tracker measure dE/dx, allowing a multiple verification of the charge magnitude of the particle.

In the second flight, AMS detector, AMS02, shown in Figure **??**, will be launched in 2005 and installed on the International Space Station (ISS) for a mission scheduled for 3 years. AMS02 will include a TOF system, Transition Radiation Detector (TRD), Silicon Microstrip Tracker (TRK), Anticoincidence (Veto) Counter (ACC), RICH and Electromagnetic Calorimeter (ECAL). All the working principles of these issues have been discussed in previous sections. Here, its particular features are summarised as follows [**?**, **?**, **?**]:

- discrimination capability of separating e^- from hadrons over a very wide range of energy beyond 1 TeV: $e/h > 10^2$ in TRD and $e/h > 10^3$ in ECAL;
- for Z=1 particles, velocity resolution $\frac{\triangle\beta}{\beta} \approx 4 \times 10^{-3}$ for $1.3 \leq P \leq 5$ GeV/c/n and $\frac{\triangle\beta}{\beta} \approx 1 \times 10^{-3}$ for $4.5 \leq P \leq 13$ GeV/c/n can be achieved by RICH;
- isotope separation up to $A \approx$ 25-30 at best, over a momentum range from about 1-2 GeV/c/n up to about 13 GeV/c/n, depending on the choice of the type of radiator;
- identification of chemical elements up to $Z \approx 26$, $A \approx 50$, over the full momentum range measured by the spectrometer, i.e., from threshold up to TeV/n range;
- contribution to the high level of redundancy of high purity samples of e^+ and $\bar{p}$ by the e^+/p and $e^-/\bar{p}$ discrimination capability of RICH, with momentum range up to 10 GeV/c/n;
- high efficiency rejection of albedo particles performed by RICH for particle momenta above the counter threshold, 1-2 GeV/c/n.

With its powerful discrimination capability, high accuracy, and also high statistics prospects of the cosmic ray elements over the specific energy range, AMS02 on ISS is expected to explore the profound understanding on cosmic ray astrophysics. It is also believed to be able to lower the limit of $\overline{He}/He$ ratio in the Galaxy, from 10^{-5} to 10^{-9} [**?**, **?**].

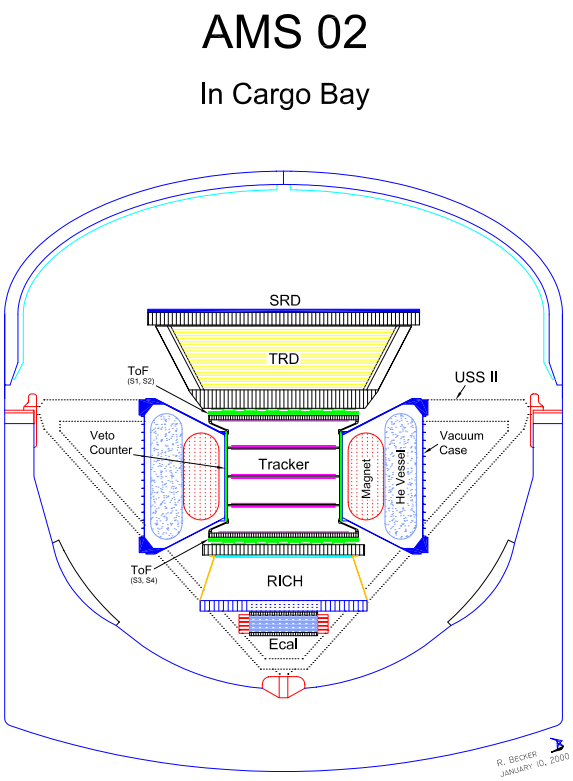

Figure 4.10: *AMS02 configuration. Picture is from the AMS Collaboration.*

Chapter 5

Theoretical Model of Cross Section of Antiproton Production in Proton-Induced Collisions

As discussed in Chapter ??, The distinctive spectral shape of the $\bar{p}$ flux with a maximum at 2 GeV and a sharp decrease towards lower energies makes antiprotons a unique probe of the models of the production source and mechanism, and also of the propagation condition in the Galaxy and of the flux modulation in the heliosphere as well. However, measuring the $\bar{p}$ flux in the neighbourhood of the Earth is a genuine challenge. The difficulties come from the requirement that antiprotons have to be distinguished from a large background of e^-, μ^- and π^-, with the latter produced around the detector because of its short lifetime. In addition, the measured flux is in fact a superposition of galactic antiprotons and a significant contribution of secondary atmospheric antiprotons from the collisions of cosmic ray particles with atmospheric nuclei. The first difficulty could be overcome by the progress in the identification techniques of detectors, such as IMAX [?, ?], MASS [?, ?], HEAT [?, ?], BESS [?, ?, ?, ?, ?, ?, ?], CAPRICE [?, ?, ?] and AMS [?]. Both secondary galactic and atmospheric antiprotons are produced in hadronic collisions by the same elementary reaction mechanism involving nucleon-nucleon collisions, between the incident cosmic ray flux and either ISM nuclei in the Galaxy, or atmospheric nuclei in the atmosphere. The correction of the total flux from the atmospheric contribution therefore needs to be carefully calculated since the accuracy on the evaluation of this component will set the limit of accuracy on the galactic flux. For simplicity, the antiproton flux can be described as the sum of all contributions:

$$\text{measured } \bar{p} \text{ flux} = \begin{cases} \text{secondary atmospheric } \bar{p} \\ + \text{ cosmic } \bar{p} = \begin{cases} \text{secondary galactic } \bar{p} \\ + \text{ primary } \bar{p} = \begin{cases} \bar{p} \text{ from the annihilation of dark matter} \\ + \bar{p} \text{ from the evaporation of primordial black holes} \\ + \bar{p} \text{ from other exotic sources...} \end{cases} \end{cases} \end{cases}$$

Therefore, in order to evaluate the contribution from the cosmic antiprotons, one has to know the contribution of the secondary atmospheric antiprotons. Under the same argument, one has to know the contribution from the secondary galactic antiprotons in order to evaluate the origin of the actual primary antiprotons. This goal is possible only if one can have a good description of the antiproton production cross section in nuclear interactions.

In this chapter, some elements of the theoretical approach to the mechanism and the $\bar{p}$ production cross section in nuclear interaction are discussed. In deriving the inclusive cross section, Quantum Field Theory (QFT) aspects, particle kinematics in the transformation between centre of mass system and laboratory system, Quark Counting Rules and Regge Phenomenology are also discussed.

5.1 Approach of Quantum Field Theory

Consider a hadronic reaction of the following form

$$a + b \longrightarrow c + d \tag{5.1}$$

where a, b are in the initial state i and c, d in the final state f. The cross section for the interaction (**??**) is defined as the transition rate W per unit incident flux of particle a per target particle b. Define n_a as the density of particles in the incident beam and v_i the relative velocity of a and b, then the flux of particles per unit time through unit area normal to the beam is

$$\phi = n_a v_i \tag{5.2}$$

Assume there are n_b particles in the target per unit area, each of an effective cross section σ, then the probability that any incident particle would collide the target is $n_b\sigma$, and the number of interactions per unit area per second is $n_a n_b \sigma v_i$. For each target, the transition rate W is therefore

$$W = \sigma\phi = \sigma n_a v_i \tag{5.3}$$

W is given by the product of the square of a matrix element M_{if} and a density of final states, or phase space factor, ρ_f [**?**]. M_{if} is the quantal transition amplitude which contains various dynamical features in the interaction: coupling strength, energy dependence, angular distribution and so on. The formula is given as [**?**]

$$W = \frac{2\pi}{\hbar}|M_{if}|^2\rho_f \tag{5.4}$$

In calculating the phase space factor ρ_f, one can restrict the particles to some arbitrary volume, which cancels in the calculation and can be taken as unity for convenience. Then,

$$\rho_f = \frac{dn}{dE_0} = \frac{d\Omega}{h^3}p_f^2\frac{dp_f}{dE_0}g_f \tag{5.5}$$

where E_0 is the total energy in the centre of mass frame; p_f is the final-state momentum in this frame, $|\boldsymbol{p}_c| = |\boldsymbol{p}_d| = p_f$; $d\Omega$ is the solid angle containing the final-state particles; g_f is a spin multiplicity factor. Eq. (??) refers to one particle of each type in the normalisation volume. From Eq. (??) and (??), with $n_a = 1$ and integrating over all angles of the products c and d, the cross section is then given as

$$\sigma = \frac{W}{v_i} = \frac{2(2\pi)^3}{h^4}|M_{if}|^2\frac{p_f^2 dp_f}{v_i dE_0}g_f \tag{5.6}$$

By the energy conservation

$$E_0 = E_c + E_d = \sqrt{p_f^2 + m_c^2} + \sqrt{p_f^2 + m_d^2} \tag{5.7}$$

this relation gives

$$\frac{dp_f}{dE_0} = \frac{E_c E_d}{E_0 p_f} = \frac{1}{v_f} \tag{5.8}$$

with $v_f = v_c + v_d$ as the relative velocity of c and d.

Take s_c and s_d to be the spins of particles c and d. The numbers of all possible substates for them are then $2s_c + 1$ and $2s_d + 1$ respectively. Thus, $g_f = (2s_c + 1)(2s_d + 1)$ [?]. Therefore, the cross section of the interaction (??) is obtained as

$$\sigma(a + b \longrightarrow c + d) = \frac{2(2\pi)^3}{h^4}|M_{if}|^2\frac{(2s_c + 1)(2s_d + 1)}{v_i v_f}p_f^2 \tag{5.9}$$

It has to be noted that σ in Eq. (??) is the cross section is derived only for initial state i and final state f. If, for example, an interaction between two particles a and b to a final state which contains n_f particles, Eq. (??) is then explored to a form of all possible states [?]

$$d\sigma = \frac{(2\pi)^4\delta^4(p_i - p_f)|M_{if}|^2}{4[(\boldsymbol{p}_a \cdot \boldsymbol{p}_b)^2 - m_a^2 m_b^2]^{1/2}}\prod_{j=1}^{n_f}\frac{d^3 p_j}{(2\pi)^3 2E_j} \tag{5.10}$$

The total σ is then the integral over the phase space for all possible states.

From Eq. (??) and (??), some important features in such an approach should be emphasised:

- Implied in Eqs. (??) and (??), σ is integrated over all angles so $|M_{if}|^2$ has been averaged over all possible initial spin states of a and b, and summed over all final spin and orbital-angular-momentum states involved;

- The exact form of $|M_{if}|^2$ is unknown. However, by first-order perturbation theory, where the interaction is assumed to be weak, $|M_{if}|$ can be interpreted as the overlap integral over the volume of the interaction potential H' and the initial and final state wavefunctions, ψ_i and ψ_f, i.e., $\int \psi_f^* H' \psi_i d\tau$. This interpretation holds provided $H' \ll H_0$, in which, H_0 is the unperturbed energy operator (Hamiltonian). Nevertheless, when the interaction is strong, $|M_{if}|$ cannot be calculated explicitly but Eq. (??) can be treated as the definition of $|M_{if}|$;

- $|M_{if}|^2$ is symmetric by assuming invariance of the interaction under time reversal and space inversion, both of which hold for strong interactions. Time reversal interchanges final and initial states and reverses all momenta and spins; space inversion then recovers the signs of momenta but leaves spins unchanged. Thus, suppose T is a suitable transition operator, then

$$\begin{array}{c} \\ \text{Time} + \text{Space} \\ \longleftrightarrow \end{array} \begin{array}{l} < f(\boldsymbol{p}_c, \boldsymbol{p}_d, s_c, s_d)|T|i(\boldsymbol{p}_a, \boldsymbol{p}_b, s_a, s_b) > \\ < i(\boldsymbol{p}_a, \boldsymbol{p}_b, -s_a, -s_b)|T|f(\boldsymbol{p}_c, \boldsymbol{p}_d, -s_c, -s_d) > \end{array} \tag{5.11}$$

  By summing over all $2s+1$ spin projections, from $-s$ to $+s$, it is obvious that the relation $|M_{if}|^2 = |M_{fi}|^2$ holds;

- Invariance (**??**) under time reversal and space inversion is not, however, applicable to weak interactions because of CP-violation [**?**]. But, first-order perturbation theory can still keep the validity of such a symmetry.

The interpretations of σ in (**??**) and (**??**) are theoretically valid but it would meet some difficulties in practice. In calculating the total σ, it requires all final states to be known but at high energies, the final state is often very complicated. In addition, in a single interaction, several particles could be produced and some of them could stay free out of the detector acceptance. In practice, it is less difficult to measure the inclusive cross section for the interaction [**?**], $a + b \longrightarrow c + X$, in which, c is the targeted production particle while X denotes all other particles whose production is allowed in this reaction but without being detected. The cross section is then completely given by the kinematics of incident particles a, b and the interested particle produced and also the mass of the recoiling system [**?**]. On the other hand, experiments can probably be sometimes designed to detect all the produced particles in the final state. These are called 'exclusive' while all detected particles are ensured to be the only ones produced in this collision event [**?**].

5.2 Threshold of Antiproton Production in Hadronic Collisions

For the $\bar{p}$ production threshold, consider a hadronic reaction $A + B \rightarrow \bar{p} + X$ where A is the incident particle while B is the target. According to the conservation of charge and the baryon number, the simplest hadronic reaction for the $\bar{p}$ production is

$$p + N \rightarrow \bar{p} + p + p + N \quad N: \text{ Nucleon} \tag{5.12}$$

Eq. (**??**) has a minimum possible mass of the recoiling particle as $M_{X,min} = 3m_p$ for a proton target. Since in the centre of mass frame, the net momentum of the system is zero before and after the collision. So, at the $\bar{p}$ production threshold, the invariant mass for the collision products $\bar{p}$ and X is

$$s = (E^*_{\bar{p}} + E^*_X)^2 = (4m_p)^2 = 16m_p^2 \tag{5.13}$$

Therefore, the threshold energy to produce an antiproton is the incident energy providing the system to have the same invariant mass. Then, one can obtain

$$s = (E^*_{p_{in}} + E^*_{p_t})^2 = m_p^2 + m_p^2 + 2m_p E^{Lab}_{p_{in}} = 16m_p^2 \tag{5.14}$$

where p_{in} and p_t are the incident and target protons respectively while the superscript Lab stands as the Lab frame. This relation gives

$$E^{Lab}_{p_{in}} = 7m_p \tag{5.15}$$

which is the minimum total energy needed to produce antiprotons in the hadronic $p + p$ reaction.

5.3 Total, Inelastic and Elastic Cross Sections

There are different definitions in interaction cross sections. The basic observable of hadron scattering processes, the total cross section σ_{total}, consists of two main contributions: the elastic cross section σ_{el} and the inelastic cross section σ_{inel}

$$\sigma_{total} = \sigma_{el} + \sigma_{inel}$$

where the elastic and inelastic cross sections can be decomposed into some more fundamental components.

Two colliding nuclei can be described in wave concept, in which, the incoming particles are represented by plane waves. The interactions between them give rise to some secondary waves whose superposition upon the incoming waves produces an interference patter. At large distance from the scattering centre, the total wave field consists of the original plane waves and a set of outgoing spherical waves that would represent the reaction products in various final states.

Figure **??** [**?**] shows the total and elastic pp cross sections in function of energy. The elastic cross section shown in the figure accounts for only a small fraction of the total cross section at high energies. So, at high energy, the elastic scattering is seen as the shadow of the inelastic cross section [**?**]. And, as shown in this figure, at low energy, hadron cross sections have shown a pattern with more complex structure; at high energy, however, the cross section appears to be smooth. Such a result suggests that, at high energy, the laws of the strong interactions would become simpler and merely follow the general assumptions independent of the details of the particle dynamics [**?**]. As derived in the previous section, in a $\bar{p}$-production collision, the energy threshold is $7m_p$. Above this energy, the inelastic cross section dominates the total cross section.

Most of the high energy elastic and total cross section data [**?**] have been usually interpreted in terms of the Regge Poles, i.e., in terms of the meson and the Pomeron exchanges between the two colliding particles. The elastic cross section can then be described by an amplitude which depends on the energy and the angular momentum

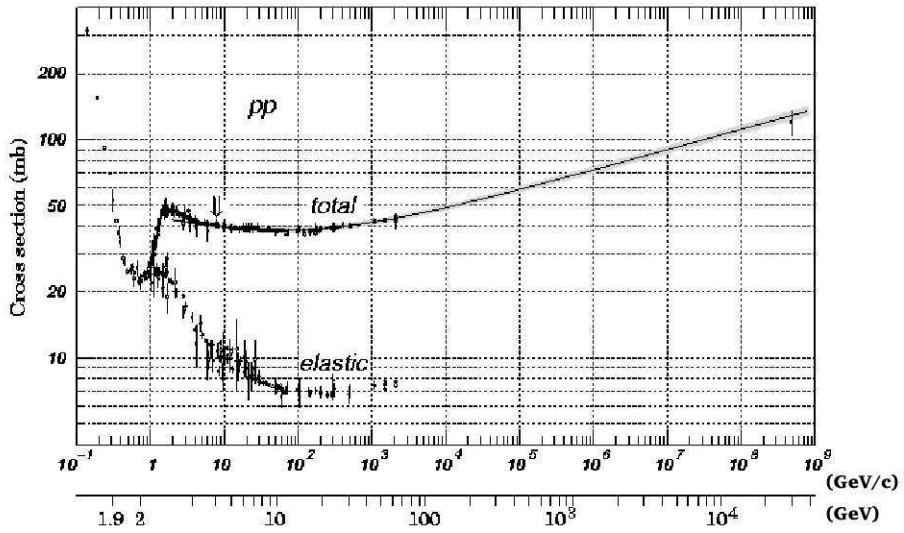

Figure 5.1: *Total and elastic cross section for pp collision as a function of laboratory beam momentum (upper scale) and total centre of mass energy (lower scale) [?].*

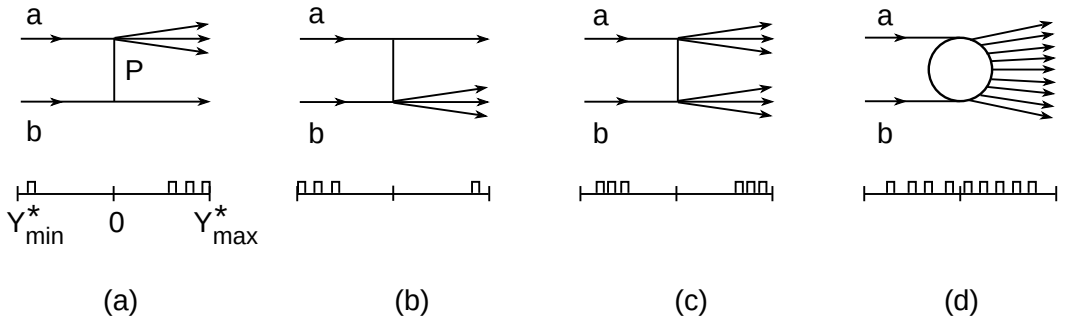

Figure 5.2: *Pictorial description of inelastic, small p_T processes with characteristic rapidity distributions [?]. P indicates Pomeron exchange. (a) Fragmentation of the beam particle a; (b) fragmentation of the target b; (c) double fragmentation of a and b; (d) central collision.*

[?, ?]. For the inelastic cross section σ_{inel}, it is more complicated but can be decomposed into some components:

$$\sigma_{inel} = \sigma_{sd,p} + \sigma_{sd,t} + \sigma_{dd} + \sigma_{nd} \tag{5.16}$$

where $\sigma_{sd,p}$ and $\sigma_{sd,t}$ are respectively the single diffractive cross section of the incident particle and the target which fragment into a number of particles. σ_{dd} is the double diffractive cross section and σ_{nd} is the non-diffractive part of the inelastic cross section. Figure ?? [?] shows pictorially various inelastic processes at low transverse momentum p_T. The properties of each component are described below.

Diffractive effects are prominent in nuclear collisions [?] since the nuclei which take part in a nuclear interaction have a spatial extension of well-defined size and shape. In addition, nuclear sizes happen to be usually larger compared with the de Broglie wavelength of the relative motion of two colliding nuclei at an energy at which, the strong interaction is involved, resulting in the diffraction condition

$$Rk \gg 1 \tag{5.17}$$

is satisfied [?, ?], where R is the typical nuclear size ($\approx$ fm) and k is the wave number. For $p + p$ collisions at high energy, the interaction becomes mostly absorptive, dominated by the many open inelastic channels [?]. Thus, with the strong absorption, the diffractive condition (??) is satisfied. This condition is in close analogy with the diffraction of a plane wave by a black disc in classical optics [?, ?, ?].

Since at high energy, the elastic cross section is like the shadow of the inelastic cross section, the elastic amplitude also has a diffractive character, well described by a single scalar amplitude [?, ?]. The elastic process and the single diffractive and double diffractive peripherical processes of the inelastic cross section, corresponding to small impact parameter collisions in Eq. (??), give rise to low multiplicity events at very forward angles while the non-diffractive cross section is the principal part of the inelastic cross section that gives rise to high multiplicity events and to particles emitted over a much wider CM angular range [?]. Most of the non-diffractive cross section concerns particles emitted with a low transverse momentum while a small part of the non-diffractive cross section gives rise to high p_T jets of particles emitted at relatively large angles due to the central collisions among the colliding particles. As it will be seen in the next chapter, the $\bar{p}$ production multiplicity in hadronic collisions has centrality in rapidity, the $\bar{p}$ is then mostly produced in central collisions.

5.4 Inclusive Cross Section

In an inclusive measurement, only one species of the final state particles is identified. The inclusive cross section is, however, obtained by summing the exclusive cross sections over all final states which include this particle. The approach to obtain the Lorentz invariant triple differential production cross section of the inclusive particle is here decomposed

into two-body nucleon-nucleon collision, nucleon structure functions and parton fragmentation function. The hadronic reaction can be viewed as interactions between partons involved in the nuclear interaction or the Pomeron exchange involved in the hadronic scattering at high energy. The mechanisms involved can be described by low-order perturbation in QCD and non-perturbative Regge Theory respectively.

5.4.1 Nucleon-Nucleon Interactions ($N-N$ Interactions)

In the scope of this work, the $\bar{p}$ production results from the strong interaction between two interacting nucleons or nuclei. Since the strong interaction force is short ranged, it means that the mean free path of hadrons in nuclear matter is comparable to or even smaller than the nuclear dimensions and the incident high energy particles make more or less direct hit on the target nucleus. Therefore, the high energy particle traverses the nucleus, suffering multiple scattering off the nucleons or partons (quarks, gluons) in the target nucleus. The space-time intervals between these interactions are also comparable to the range or characteristic time of the strong interaction itself as well. In most cases, the energy of the incident particle is so high that its de Broglie wavelength is small compared with the dimensions of the target nucleus and also the mean distance between nucleons in the nucleus. So, a quasi-classical estimate can be used for the nucleon-nucleon interactions. The cross section for nuclear interactions is, classically, the geometric cross section of the nucleus.

The size of the nucleus can be expressed approximately as [?]

$$R \simeq 1.2\ A^{1/3} \quad \text{fm} \tag{5.18}$$

where A is the mass number. Consider an incident high energy particle interacting with the nucleus. The effective size of an incident particle can be derived by means of Heisenberg's Uncertainty relation. For example, consider an incident proton with $E = 10$ GeV, its de Broglie wavelength is

$$\triangle x \simeq \frac{\hbar}{\gamma m_p c} \simeq 0.018 \quad \text{fm} \tag{5.19}$$

which is smaller than the proton size ($r \approx 1$ fm). Suppose all nucleons are averagely distributed in the volume of the nucleus, then the number of nucleons with which the proton interacts is just the number of nucleons along the trajectory across the nucleus. For example, the average number of nucleons the proton has interacted when it traverses a nucleus with an impact parameter $b = 0$ is

$$n(b=0) \simeq \frac{A}{\frac{4}{3}\pi R^3}(2R)\left[\pi r^2\right] \approx A^{1/3} \tag{5.20}$$

where R is the radius of the nucleus. For a nonzero impact parameter b, the average number of nucleons with which a proton has interacted along its trajectory across the

nucleus can be formulated. In average, therefore, the average number of nucleons a proton would interact when it traverses a nucleus can be classically formulated as

$$< n > \simeq \frac{1}{R}\int_0^R \frac{A}{\left[\frac{4}{3}\pi R^3\right]}\left(2\sqrt{R^2-b^2}\right)(\pi r^2)db \approx 0.82A^{1/3} \tag{5.21}$$

Eq. (**??**) is then a reasonable model of multiple scattering inside the nucleus of a nuclear collision. For example, a proton passing through an oxygen or a nitrogen nucleus along its diameter would interact, on average, with about $\sqrt[3]{16}$ and $\sqrt[3]{14}$ nucleons respectively. In case for a proton passing through the air, the average number of scattering nucleons is about $\sqrt[3]{14.47}$.

It has to be indicated that, in reality, a nucleus has a nuclear density distribution and the nucleons in a nucleus have their matter distribution $\rho(b)$ as well [**?**]. So, in the classical approach for the average number of nucleons that a proton has interacted along its trajectory across the nucleus should take $\rho(b)$ into account.

In modern language, the internal nucleon dynamics is described in the 'infinite momentum frame' [**?**], in which, the hadron is moving very fast, $p^\mu = (P, 0, 0, P)$ with $P \gg M$ with respect to the rest frame. In this frame, according to the Lorentz contraction, the longitudinal size of the hadron is contracted by a factor of M/P with respect to its size in the rest frame. Therefore, the nucleons seem to be distributed on a disc.

5.4.2 Kinematics in Two-Body System

In a two-particle collision process, suppose two particles a and b with four-momenta $p_a^\mu = (E_a, \boldsymbol{p}_a)$ and $p_b^\mu = (E_b, \boldsymbol{p}_b)$ are involved, in which, the values of p_a^μ and p_b^μ are normally determined by the experimental conditions. Different frames can be defined by requiring p_a^μ and p_b^μ to have some special values.

Although from the point of view of relativistic mechanics, all co-ordinate systems are equivalent; for practical purpose, however, two particle systems are of particular importance for the case of interest here: the laboratory system (LS) and the centre of mass system (CMS). The LS is tied to the observer, usually the target system (TS), consequently all direct observations are in the LS. Thus, it is convenient to use this frame for the experimental results. The CMS, which is tied to the centre of mass of a system of interacting particles in the incoming channel, is convenient since, in this frame, disintegration and collision processes for two particles have the maximum degree of symmetry. For the collisions between two particles with unequal mass, the case of $p + A$ or $A + A$ collisions, for example, the total momentum of the interacting particles in the CMS is equal to zero: $p_a^{\mu *} + p_b^{\mu *} = 0$, where the CMS quantities are denoted by an asterisk. Consequently, the directions of motion of these two interacting particles in the CMS always make an angle of 180^0. That is to say, they move towards each other before the collision but move apart in the opposite directions after the collision. Hence, their angular distributions are not changed by interchange with the direction of motion of the other particle. This could considerably simplify the interpretations of the colliding system. For such collisions, there is an axis of symmetry and it is always possible to

draw the relativistic transformation between the CMS and the Lab frames. However, one should keep in mind that, even though it is possible to simplify the interpretation of a system by choosing the reference frame, collisions could also be expressed in invariant forms independent of the reference frame.

As discussed above, an appropriate choice of the reference frame could simplify the interpretation of a system. In this work, the $\bar{p}$ production cross section is described in the CMS while the $\bar{p}$ production measurements were performed in the LS. Therefore, the transformation of the kinematics between the CMS and the LS is required. Note that in evaluating the atmospheric $\bar{p}$ flux, one should keep in mind that the atmospheric nuclei are actually in motion, but with velocities much smaller than those of the characteristic cosmic ray particles and the nucleons inside nuclei. According to Stephens [**?**], such a motion contributes only a tiny fraction to the secondary atmospheric $\bar{p}$ flux. Thus, the atmospheric target can be considered to be stationary and the TS then coincides with the LS.

Now, consider a collision process $a + b \to c + X$ where c is the inclusive particle [**?**]. The vectors p_a^μ and p_b^μ of the initial state $p_a^\mu + p_b^\mu$ of such a collision can be expressed in the CMS and the TS as follows:

$$p_a^{\mu *} = (E_a^*, 0, 0, P_a^*), \qquad p_a^{\mu T} = (E_a^T, 0, 0, P_a^T) \tag{5.22}$$

$$p_b^{\mu *} = (E_b^*, 0, 0, -P_a^*), \qquad p_b^{\mu T} = (m_b^T, 0, 0, 0) \tag{5.23}$$

where the direction of motion is chosen as the z axis. The Lorentz transformation equations are then

$$P_a^* = \gamma^{CM,T}(P_a^T - v^{CM,T}E_a^T), \quad E_a^* = \gamma^{CM,T}(E_a^T - v^{CM,T}P_a^T) \tag{5.24}$$

where $v^{CM,T}$ is the velocity of the CMS in the TS, given by

$$v^{CM,T} = \left.\frac{|\boldsymbol{p}_a + \boldsymbol{p}_b|}{E_a + E_b}\right|_T = \frac{P_a^T}{E_a^T + m_b} \tag{5.25}$$

This gives

$$v^{CM,T}\gamma^{CM,T} = \frac{P_a^T}{\sqrt{s}} \implies \gamma^{CM,T} = \frac{E_a^T + m_b}{\sqrt{s}} \tag{5.26}$$

where the invariant mass $\sqrt{s}$ of the system $p_a^\mu + p_b^\mu$ is defined as

$$s \equiv s_{ab} = (p_a^\mu + p_b^\mu)^2 = (E_a + E_b)^2 - (\boldsymbol{p}_a + \boldsymbol{p}_b)^2 \tag{5.27}$$

$\sqrt{s}$ is invariant in all frames and hence one can have, in particular

$$s = (E_a^* + E_b^*)^2 = (E_a^T + m_b)^2 - (P_a^T)^2 = m_a^2 + m_b^2 + 2m_bE_a^T \tag{5.28}$$

For the inclusive particle c, the energy and momentum can be written as [**?**]

$$E = m_T \cosh\xi, \quad Q = m_T \sinh\xi \tag{5.29}$$

in both the CMS and TS where $m_T = \sqrt{p_T^2 + m_0^2}$ is the transverse mass; p_T is the transverse momentum; $\xi = \frac{1}{2}\ln\frac{E+Q}{E-Q}$ is the rapidity; Q is the longitudinal momentum. Rapidities in the CMS and the TS, ξ^* and ξ^T, satisfy the relation

$$\xi^T = \xi^* + \xi^{CM,T}, \quad \xi^{CM,T} = \frac{1}{2}\ln\left(\frac{1+v^{CM,T}}{1-v^{CM,T}}\right) \tag{5.30}$$

with the domains [?]

$$-\ln\left(\frac{\sqrt{s}}{m_c}\right) \leq \xi^* \leq \ln\left(\frac{\sqrt{s}}{m_c}\right) \tag{5.31}$$

$$\ln\left(\frac{m_c}{m_b}\right) \leq \xi^T \leq \ln\left(\frac{s}{m_b m_c}\right) \tag{5.32}$$

In a production experiment, the kinematics of the inclusive particle is performed by measuring its momentum P, mass m, spatial angles θ and ϕ. Hence, the Lorentz invariant triple differential cross section can be calculated in terms of the different kinematical variables

$$\left(E\frac{d^3\sigma}{d^3p}\right)_{inv} = \frac{1}{2\pi m_T}\frac{d^2\sigma}{d\xi dm_T} = \frac{1}{2\pi p_T}\frac{d^2\sigma}{d\xi dp_T} \tag{5.33}$$

$$= \frac{E}{P^2}\frac{d^2\sigma}{d\Omega dP} = \frac{E}{2\pi P^2}\frac{d^2\sigma}{dP d\cos\theta} \tag{5.34}$$

where θ as the Lab angle between the measured inclusive particle and the incident particle direction, Ω as the solid angle and all others as defined above.

5.4.3 Quark Counting Rules

In the present framework, the production of antiprotons in a nuclear collision results from hadronic interactions. Since hadrons are made up of more fundamental parton constituents, the interaction can be described in terms of more elementary interactions of these constituents (quarks, antiquarks and gluons). In such interactions, the two hadrons may undergo the deep inelastic scattering.

Similar to the electromagnetic interaction in Quantum Electrodynamics (QED), which involves the exchange of the massless virtual photons (spin-1) between charged particles [?], the strong interaction is due to the exchange of the coloured massless gluons between coloured quarks [?], for which, the lowest order strong interaction potential that involves a single gluon exchange between a quark and an antiquark is [?]

$$V(r) = -\frac{4}{3}\frac{\alpha_s}{r} \tag{5.35}$$

where $\alpha_s = g_s^2/4\pi$ and g_s is the strong coupling constant. However, at higher order, the physical coupling strength becomes [?]

$$\alpha_s(Q^2) \simeq \alpha_s\left\{1 - \frac{\alpha_s b_0}{4\pi}\ln\left(\frac{Q^2}{\mu^2}\right) + \left[\frac{\alpha_s b_0}{4\pi}\ln\left(\frac{Q^2}{\mu^2}\right)\right]^2 + \cdots\right\} \tag{5.36}$$

$$\simeq \frac{\alpha_s}{1+(\alpha_s b_0/4\pi)\ln(Q^2/\mu^2)} = \frac{1}{(b_0/4\pi)\ln(Q^2/\Lambda^2)} \tag{5.37}$$

$$\Lambda^2 = \mu^2 \exp\left(-\frac{4\pi}{\alpha_s b_0}\right) \tag{5.38}$$

where $\mu^2 = |Q^2|$ at which α_s is measured, $Q^2 = -q^2$ in which, q is the four-momentum of the coloured gluon, $b_0 = \frac{11}{3}N_c - \frac{2}{3}N_f$ where N_c is the number of the colours (R: red, G: green, B: blue) and N_f is the number of the flavours of quark (d: Down, u: Up, s: Strange, c: Charm, b: Bottom, t: Top). Note that in Eq. (**??**)

$$\alpha_s(Q^2) \to \infty \quad \text{as} \quad Q^2 \to \Lambda^2 \tag{5.39}$$

so that the perturbation iteration breaks down at small Q^2. Therefore, one has

$$\alpha_s(r) \simeq \frac{1}{(b_0/4\pi)\ln(1/\Lambda r)} \tag{5.40}$$

Such a result indicates that the coupling strength becomes stronger when the separation r between the q and $\bar{q}$ increases, and, the perturbation iteration terminates as $r \to \frac{1}{\Lambda}$. This is because of the gluon self-coupling so that the exchanged gluons would attract each other, resulting that the colour lines of force between the interacting quarks are constrained to a tube-like region between these two quarks [**?**, **?**]. The increase of the interaction potential as the separation between two interacting quarks increases is supposed to be the origin of the confinement mechanism to prevent the quark from escaping from the hadron, providing that the free quark cannot be observed.

Figure **??** shows a possible parton diagram of the $\bar{p}$ production in pp collision. Two quarks from each proton scatter each other away from their parent protons. However, as discussed above, the colour lines of forces are stretched into tube-like forms, until the potential energy of the colour field is large enough to produce $q\bar{q}$ pairs. The first $q\bar{q}$ pair then breaks up the tube and, being the end points, they would form another two tubes with lower net energy. If the energy is still high enough, such a mechanism continues: the colour lines are stretched, another $q\bar{q}$ pair is produced, the tube is broken.... The process continues until the quark energy has degraded into clusters of quarks with zero net colour and low internal momentum. The cluster of quarks can then be confined and could hadronise into hadrons [**?**].

In evaluating the inclusive cross section, consider an inclusive interaction $AB \to CX$, where C is the inclusive particle, and X represents all other particles which could be produced in this interaction. Consider that the incoming particles A and B contain partons a and b, which scatter and produce partons c and d with a transverse momentum p_T. According to the Uncertainty Principle, the time interval τ within which parton scattering occurs is

$$\tau \sim \frac{\hbar}{p_T c} \tag{5.41}$$

Partons c and d hadronise by confinement mechanism after some time interval. Figure **??** shows the diagram of such an interaction [**?**].

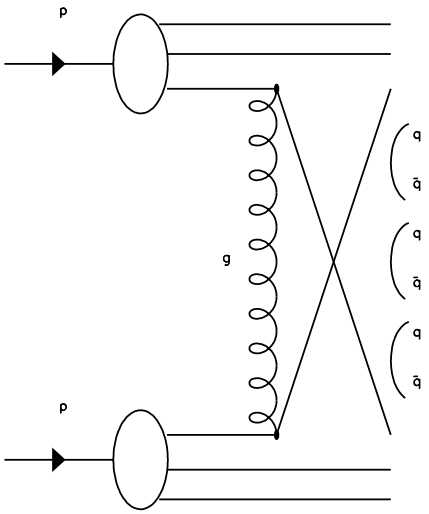

Figure 5.3: *A possible parton diagram of $\bar{p}$ production from pp collision. See the text for the related physics and the explanation of this figure.*

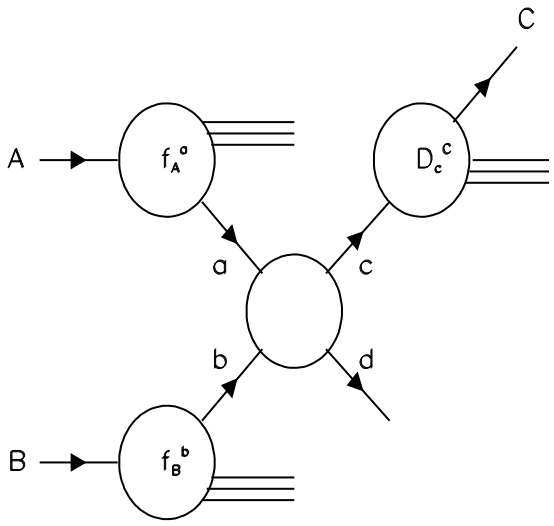

Figure 5.4: *The hadronic interaction $AB \to CX$ in terms of parton sub-process $ab \to cd$, the structure functions f_A^a, f_B^b and the fragmentation function D_c^C [?].*

The parton picture is mostly formulated also in the infinite momentum frame, in which, the nucleon is moving fast enough so that the longitudinal size of the nucleon is contracted by a factor of M/P with respect to its size in the rest frame, resulting that the partons in a nucleon look like to be distributed on a disc in this frame. In the infinite momentum frame, a structure function $f_A^a(x_a)$ is defined as the probability that, hadron A contains a parton a which carries a fraction $x_a = \frac{p_a}{p_A}$ of the momentum of A, with $0 \leq x_a \leq 1$. A fragmentation function $D_c^C(z_c)$ is defined as the probability that, the outgoing parton c produces a hadron C carrying a momentum fraction $z_c = \frac{p_C}{p_c}$, for which, $0 \leq z_c \leq 1$. Neglect any momentum a might have in direction transverse to the beam direction and, assume the masses of hadrons and partons as well are small compared with their momenta. So, under such constrains, the four-momenta of A and a can be written as

$$p_A^\mu \simeq (p_A, 0, 0, p_A), \quad p_a^\mu \simeq (p_a, 0, 0, p_a) = x_a(p_A, 0, 0, p_A) \tag{5.42}$$

By the definition in Eq. (??), the invariant variables for $AB \to CX$ are

$$s \equiv (p_A^\mu + p_B^\mu)^2 \simeq 2\boldsymbol{p}_A \cdot \boldsymbol{p}_B \tag{5.43}$$

$$t \equiv (p_A^\mu - p_C^\mu)^2 \simeq -2\boldsymbol{p}_A \cdot \boldsymbol{p}_C \tag{5.44}$$

where $\sqrt{-t}$ is the defined invariant four-momentum transfer from A to C [?]. For the parton sub-process, $ab \to cd$, the invariant variables as defined in Eqs. (??) and (??) are given as

$$\bar{s} \equiv (p_a^\mu + p_b^\mu)^2 \simeq 2\boldsymbol{p}_a \cdot \boldsymbol{p}_b = 2x_a x_b \boldsymbol{p}_A \cdot \boldsymbol{p}_B = x_a x_b s \tag{5.45}$$

$$\bar{t} \equiv (p_a^\mu - p_c^\mu)^2 \simeq -2\boldsymbol{p}_a \cdot \boldsymbol{p}_c = -\frac{2x_a}{z_c}\boldsymbol{p}_A \cdot \boldsymbol{p}_C = \frac{x_a t}{z_c} \tag{5.46}$$

Assume that C is produced collinearly with c and the fragmentation function D_c^C depends only on z_c and is also independent of the nature of the initial state. Then the invariant cross section for $AB \to CX$ is the weighted sum of the differential cross section $\frac{d\sigma}{d\bar{t}}$ of all possible contributing scatterings, over all momentum space [?, ?]:

$$E_C \frac{d^3\sigma}{d^3 p_C}(AB \to CX) = \sum_{abcd} \int_0^1 \int_0^1 dx_a dx_b f_A^a(x_a) f_B^b(x_b) \frac{1}{\pi z_c} \frac{d\sigma}{d\bar{t}}(ab \to cd)\, D_c^C(z_c) \tag{5.47}$$

Thus, if the structure functions, the fragmentation function and the cross sections for all parton sub-processes are known, the inclusive cross section for the hadron nuclear process $AB \to CX$ can be calculated via Eq. (??).

The exact form of parton-parton differential cross section is unknown. However, its first-order perturbation value can be derived by QCD, with a form [?, ?]

$$\frac{d\sigma}{dt} = \frac{\pi \alpha_s^2 |A|^2}{s^2} \tag{5.48}$$

where $\alpha_s = g_s^2/4\pi$, g_s is the strong coupling constant and s is the invariant total energy square E^2 of this two parton system. The amplitude $|A|^2$ corresponds to the quark type involved in the parton-parton interaction and is available in Standard QCD [?].

The structure function $f_A^a(x_a)$ can be determined by two extreme regimes: $x_a \to 1$ and $x_a \to 0$. Take the $\bar{p}$-production interaction $p + p \to \bar{p} + X$ for example. A proton is made up of 3 quarks, i.e., uud. So, it is direct that the proton structure functions should follow the relations

$$\int_0^1 [f_p^u(x) - f_p^{\bar{u}}(x)]dx = 2; \quad \int_0^1 [f_p^d(x) - f_p^{\bar{d}}(x)]dx = 1; \quad \int_0^1 [f_p^s(x) - f_p^{\bar{s}}(x)]dx = 0 \tag{5.49}$$

where x is the parton momentum fraction. All partons which make up the proton should carry all of the proton momentum. Thus

$$\sum_q \int_0^1 x f_p^q(x)dx \equiv 1 \tag{5.50}$$

For the regime of $x \to 1$, it means that one parton of the proton carries all the proton momentum. However, the partons in a proton are bounded and the proton momentum should be shared by all the parton constituents. So, the probability that a single parton has carried all the proton momentum is extremely small. Thus, the behaviour of the structure function is expected to be

$$f(x) \simeq (1 - x)^\alpha \qquad \text{as } x \to 1 \tag{5.51}$$

α is related to the parton number, $\alpha = 2n_s - 1$ [?], where n_s is the minimal counting number of partons whose momentum would vanish in this limit.

In the case of $x \to 0$, the parton model in this limit is related to the behaviour of hadronic scattering at high energy of the Regge Theory [?, ?]. This regime is called the 'Regge regime' [?, ?].

5.4.4 Regge Phenomenology

Quantum Chromodynamics (QCD) [?] has successfully described the strong interaction. However, its successes are limited to the perturbative regime where the strong coupling constant is small. Nevertheless, the elastic and diffractive scatterings between hadrons are non-perturbative and cannot currently be well described by QCD [?].

Similar to the electromagnetic QED interaction which involves the exchange of the massless virtual photons between charged particles and also strong QCD interaction which involves the exchange of coloured massless gluons between coloured quarks, the elastic and diffractive hadronic scatterings involve the exchange of the Pomeron [?, ?], in which the Pomeron is a colour singlet with the quantum numbers of the vacuum, and other mesons like the pion or the rho meson and their related families located on the Regge trajectory.

For the scattering process $AB \to CX$, s defined in Eq. (??) is the square of the centre of mass energy while t defined in Eq. (??) gives the scattering angle. But, the exchanged particle involved in the scattering forms in the t-channel process $AC' \to B'D$, for which, t gives the energy while s, in turn, gives the scattering angle. So, these two channel are related by crossing [?] and have presented the same scattering amplitude [?] but involve

different regions of the variables s and t [?]. Figure ?? shows an example of the s-channel and t-channel diagrams for the elastic meson-meson scattering.

The scattering involving the particle exchange can be described by the One-Particle-Exchange Model [?]. Suppose the exchanged particle in a hadronic scattering has rest mass M_J with a spin J. Then in the s-channel, the scattering amplitude associated with such kind of exchanged particle is [?, ?]

$$A_J(s,t) = -\frac{(g'_J)^2\ (-t)^J}{s - M_J^2} \quad \Longrightarrow \quad A(s,t) = -\sum_J \frac{(g_J)^2\ (-t)^J}{s - M_J^2} \tag{5.52}$$

Similarly, in the t-channel, the scattering amplitude can be written as [?]

$$A_J(t,s) = -\frac{(g'_J)^2\ (-s)^J}{t - M_J^2} \quad \Longrightarrow \quad A(t,s) = -\sum_J \frac{(g_J)^2\ (-s)^J}{t - M_J^2} \tag{5.53}$$

where g_J is the coupling constant. And, by the Principle of Crossing Symmetry [?], one should have

$$A(s,t) = A(t,s) \tag{5.54}$$

However, Eqs. (??) and (??) have met a problem since there exists a singularity, or pole, at points $s = M_J^2$ or $t = M_J^2$. In addition, the amplitude descriptions in Eqs. (??) and (??) are divergent at high energy when J is large since the amplitudes grows as s^J and t^J. Therefore, the singularity and the unphysical region should be excluded. These difficulties can be resolved by the Regge Theory [?, ?, ?, ?], which can give the collective effect of the exchanged particles.

A possible way to solve this difficulty was suggested by Regge in 1959 [?] who raised an argument that the poles in the scattering amplitude correspond to the exchange of particles carrying fixed angular momenta [?, ?] and treated the angular momentum as a continuous, complex variable [?] and the exchange particles in a hadronic scattering have to follow some constraints in their related angular momenta [?, ?]. These objects with complex angular momentum are referred to as the Regge poles.

In Figure ??, since the scattering is dominated by exchange of particles (poles) in the momentum-transfer, or say, t-channel, one can describe the scattering amplitude in the partial wave form $A_J(E)$, $E = t$, in which, J is the angular momentum and the index J, for the Jth partial wave contributing to the scattering, implies the angular dependence $P_J(\cos\theta)$. $P_J(\cos\theta)$ is the Legendre polynomial and the scattering angle θ is determined by Eq. (??)

$$t \equiv (p_A^\mu - p_C^\mu)^2 = m_A^2 + m_C^2 - 2E_A E_C + 2|\boldsymbol{p}_A||\boldsymbol{p}_C|\cos\theta \tag{5.55}$$

The simplest case in which, $m_A = m_B = m_C = m_D = m$ in a scattering $AB \to CD$ will give the scattering angle as

$$\cos\theta = 1 + \frac{2s}{t - 4m^2} \tag{5.56}$$

for the t-channel. The angular momentum is written as a function as $\alpha(E)$, with real and imaginary parts as $J = \mathrm{Re}(\alpha(E))$. The function of $\alpha(E)$ then shows the Regge trajectory. So, since the function $\alpha(E)$ is complex, the trajectory might locate in the complex angular momentum plane. When the pole exchange is involved in the scattering, the trajectory starts off along the negative real axis and it might cross the origin along the positive axis due to the dependence of the strength of the scattering potential as energy increases. The particles involved might have a bound state of energy (smaller than the threshold) E_1 and $J = 1$, which correspond to $\mathrm{Im}(\alpha(E)) = 0$ and $\mathrm{Re}(\alpha(E))$ is some integer. As the energy increases further and becomes greater than the threshold, the trajectory leaves the real axis and enter the complex plan, so that the function $\alpha(E)$ acquires a positive imaginary part. But, whenever the trajectory pass a point with $\mathrm{Re}(\alpha(E)) = n$, an integer, one can have an unbound state with energy E_n and with the angular momentum n. Therefore, the Regge trajectory will connect all poles [?]. A general way to achieve this is to consider the particles lying on a single linear trajectory [?]

$$\alpha(t) = \alpha_0 + \alpha' t \tag{5.57}$$

such that $\alpha(t)$ passes through integer values of J at $t = m_J^2, J = 0, 1, 2, \ldots$. α_0 in Eq. (??) is defined as the Regge intercept of the Regge trajectory [?]. Empirically, the Regge slope is approximately a constant, with a value [?]

$$\alpha' \simeq 1 \quad \mathrm{GeV}^{-2} \tag{5.58}$$

Figure ?? shows an example of such a trajectory connecting some of the lighter meson state in the $p - n$ scattering. The detail in the derivation of the Regge trajectory is given in Appendix ??.

Now, return to the behaviour of the structure function $f_A^a(x)$ to see what $f_A^a(x)$ would be like in the Regge regime. Since the particles in motion can be represented by plane waves, the scattering amplitude can be taken as the superposition of the partial wave amplitudes. So, in the t-channel, the scattering amplitude can be written as [?, ?]

$$A(s,t) = \sum_{J=0}^{\infty} (2J+1) A_J(t) P_J(\cos\theta) \tag{5.59}$$

where $A_J(t)$ is the partial wave amplitude and is taken the form as [?]

$$A_J(t) = \frac{R(t)}{J - \alpha(t)} \tag{5.60}$$

with $R(t)$ as the residue function. In Eq. (??), one finds that there is a Regge pole in the partial wave amplitude at $J = \alpha(t)$. With such partial wave amplitude, Eq. (??) then becomes

$$A(s,t) = \sum_{J=0}^{\infty} (2J+1) \frac{R(t)}{J - \alpha(t)} P_J(\cos\theta) \tag{5.61}$$

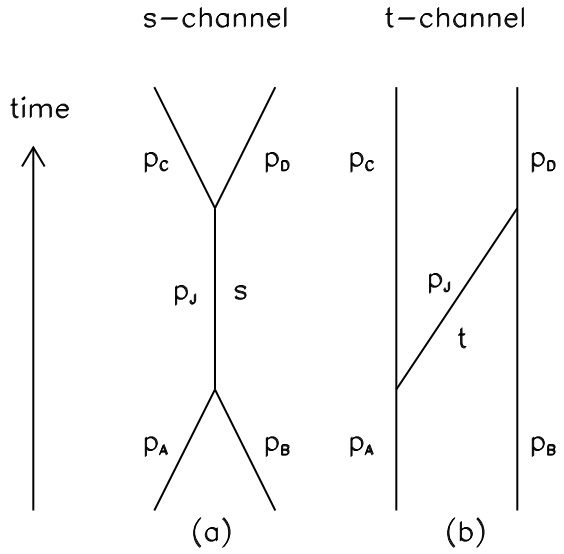

Figure 5.5: *(a) An s-channel diagram for elastic meson-meson scattering. (b) A t-channel diagram for elastic meson-meson scattering.*

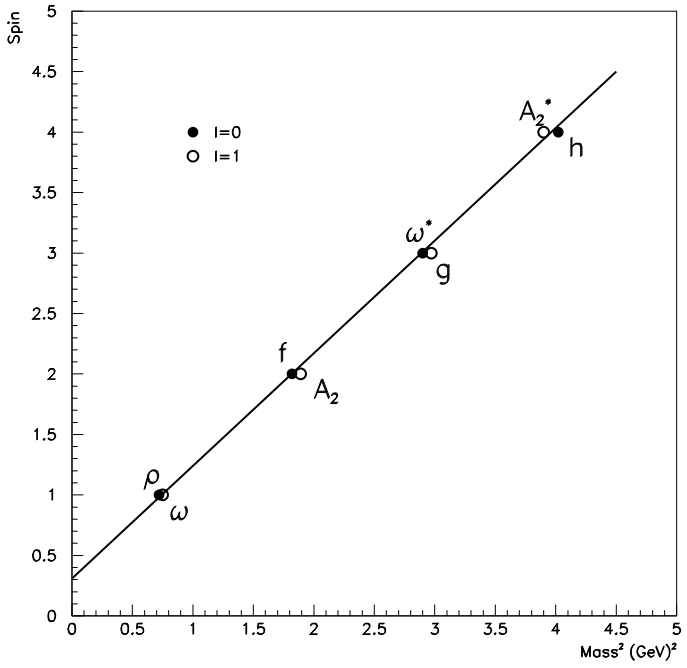

Figure 5.6: *Chew-Frautschi plot of meson Regge trajectory. Figure is reproduced from Ref. [?].*

Now consider the asymptotic case for which, $s \to \infty$ at a fixed t. The scattering angle in Eq. (??) in the asymptotic case gives $\cos\theta \propto (-s)$. So, at the poles, the Legendre polynomial will become

$$P_{J=\alpha(t)}(-\cos\theta) \propto \left(\frac{s}{s_0}\right)^{\alpha(t)} \tag{5.62}$$

where s_0 is a normalised parameter with dimension GeV^2 [?]. So, if one supposes that the Regge poles dominate the scattering, then, with the relation in (??) substituted in Eq. (??), one can have the scattering amplitude

$$A(s,t) \propto R(t)\left(\frac{s}{s_0}\right)^{\alpha(t)} \tag{5.63}$$

In addition, in Eq. (??), one has the relation

$$\frac{d\sigma}{dt} \propto \frac{|A|^2}{s^2} \propto R^2(t)\left(\frac{s}{s_0}\right)^{2\alpha(t)-2} \tag{5.64}$$

According to the optical theorem [?], the total cross section associated with the scattering amplitude $A(s,t)$ together with the relation in (??) is given as [?]

$$\sigma_{total} \simeq \frac{1}{s}\mathrm{Im}(A(s,t=0)) \propto s^{\alpha(0)-1} \tag{5.65}$$

And, in the Parton Model, the asymptotic limit $s \to \infty$ is related to the x dependence in the structure function in the limit $x \to 0$ [?]. In addition, the total scattering cross section obtained by the Parton Model appears as [?, ?]

$$\sigma_{total} \propto \sum_{q,\bar{q}} e_q^2 x f_A^q(x) \tag{5.66}$$

Therefore, taking Eqs. (??) and (??) together, the structure function in the Regge regime becomes

$$f_A^q(x) \propto x^{-1}s^{\alpha(0)-1} \propto x^{-\alpha(0)} = x^{-\alpha_{0,i}} \quad \text{as } x \to 0 \tag{5.67}$$

where $\alpha_{0,i}$ indicates the Regge intercept of the relevant Regge trajectory for the exchanged particle of type i. For example, if the scattering involves the exchange of Pomeron, then $\alpha_0 \simeq 1$ [?, ?]; for reggeon $(\rho, \omega, a_2, f_2 \ldots)$, $\alpha_0 \simeq 0.5$ [?, ?]; for pion, $\alpha_0 \simeq 0$ [?]; for u and d quarks, $\alpha_0 \simeq 0.5$ [?].

Finally, taking Eq. (??) and Eq. (??) altogether, the structure function can be written as [?]

$$f_A^a(x) \simeq C_A^a x^{-\alpha}(1-x)^{2n_s-1} \tag{5.68}$$

where C_A^a is the normalisation determined by Eqs. (??) and (??).

5.4.5 Fragmentation Function

The fragmentation function in Eq. (??) can be determined by the sum rules and the limiting behaviours as $z \to 1$ and $z \to 0$.

By the definition of $D_c^C(z_c)$, one can obtain the direct result

$$\sum_C \int_0^1 z D_q^C(z) dz \equiv 1 \tag{5.69}$$

And, by the charge conservation, it requires $D_q^C(z)$ to satisfy

$$\sum_C e_C \int_0^1 [D_q^C(z) - D_{\bar{q}}^C(z)] dz \equiv e_q \tag{5.70}$$

The averaged multiplicity of the hadron of type C is given as

$$< n_C >= \sum_{q,\bar{q}} \int_{z_{min}}^1 D_q^C(z) dz \tag{5.71}$$

where z_{min} is the lowest value in z needed to form the hadron C.

As $z \to 1$, it means that the hadron C has taken all the parton momentum. Such a case is quite rare. So, one expects

$$D_q^C(z) \simeq (1-z)^\alpha \qquad \text{as } z \to 1 \tag{5.72}$$

in which, $\alpha = 2n_s - 1$ where n_s is the minimal possible number of partons which are left behind by the hadron during the hadronisation [?].

In the case of $z \to 0$, it means that the hadron C doesn't appear at all in the hadronisation. So, the probability that the hadron C is produced from the parton c vanishes. Thus, one expects

$$D_q^C(z) \simeq z^{-1} \qquad \text{as } z \to 0 \tag{5.73}$$

Taking Eqs. (??) and (??) altogether, the fragmentation function can be obtained as

$$D_q^C(z) \simeq D_q^C z^{-1}(1-z)^{2n_s-1} \tag{5.74}$$

where D_q^C is the normalisation constant constrained by Eqs. (??) and (??) [?].

Chapter 6

Parametrised Antiproton Production in $p+p$, $p+A$ and $A+A$ Collisions

The parametrisation of the antiproton production cross section in $p+p$ and $p+A$ collisions was given by the multiple scattering approach in nucleon-nucleus collisions, the Parton Model and the Regge phenomenon discussed in Chapter **??**. An improved parametrisation is presented here based on the Kalinovskiĭ, Mokhov and Nikitin (KMN) parametrisation [**?**] and least χ^2 fitting. This reparametrisation is then compared with the experimental measurements. By the 3-dimensional analysis, its self-consistence has been shown. The $\bar{p}$ mean multiplicity distribution in hadron-hadron collisions can be evaluated from this reparametrisation and is fitted by means of a dedicated functional form. According to the analysis of the $\bar{p}$ mean multiplicity distribution, the energy range of the validity of this formula is inferred.

The secondary atmospheric antiprotons originate from cosmic ray particles interacting with the atmospheric nuclei. Nevertheless, cosmic rays consist of about 12% helium and the atmosphere consists of mostly nitrogen and oxygen. Therefore, in order to correctly evaluate the secondary atmospheric $\bar{p}$ flux, the contribution of antiprotons produced in the collisions between these nuclei has to be taken into account. That is to say, the $\bar{p}$ production in some specific nucleus-nucleus collisions has to be evaluated. The $\bar{p}$ mean multiplicity in nucleus-nucleus collisions is proposed as a scaling of that in $p+p$ collisions, based on the Wounded Nucleon Model descibed in Section **??** [**?**]. The values of the $\bar{p}$ mean multiplicity in nucleus-nucleus collisions are then calculated due to the parametrised $\bar{p}$ cross section in the present work. Comments about the $\bar{p}$ production calculated in these kinds of hadronic collisions are given in the last section.

6.1 KMN Parametrisation of Inclusive Antiproton Production in $p+A$ Collisions

By taking into account the qualitative predictions of hadronic partons model and the Regge phenomenology as well, Kalinovskiĭ, Mokhov and Nikitin [**?**] proposed a parametrised

effective proton-nucleus inclusive cross section for the process $p + A \to \bar{p} + X$

$$\left(E\frac{d^3\sigma}{d^3p}\right)_{inv} = \sigma_{inel}^{total}\, C_1 A^{b(p_T)}(1-x)^{C_2}\exp(-C_3 x)\Phi(p_T) \quad (6.1)$$

$$\Phi(p_T) = \exp(-C_4 p_T^2) + C_5\frac{\exp(-C_6 x_T)}{(p_T^2+\mu^2)^4} \quad (6.2)$$

where

$$b(p_T) = \begin{cases} b_0 p_T, & p_T \le \Gamma \\ b_0\Gamma, & p_T > \Gamma \end{cases}$$

where $C_1 - C_6$, b_0, Γ and μ^2 are free parameters.

From the discussion of inclusive cross section of nuclear interactions in Chapter **??**, the term of $A^{b(p_T)}$ in (**??**) incorporates the A dependence of the cross section, A being the mass number of the target; the term of $(1-x)^{C_2}$ is the form originating from quark counting rules in the Parton Model of hadronic interactions; $\exp(-C_3 x)$ is characterised by Regge regime; $x = \frac{E^*}{E^*_{max}}$ is the scaling variable, in which, E^* and E^*_{max} are the total energy of the inclusive particle and its maximum possible energy in the centre of mass frame respectively: $E^*_{max} = \frac{s - M^2_{X,min} + m_p^2}{2\sqrt{s}}$, in which, $M_{X,min} = 2m_p + m_N$ is the minimum possible mass of the recoiling particle in the relevant process and $\sqrt{s}$ is the invariant mass of the system; m_N in $M_{X,min}$ is the nucleon mass; p_T is the transverse momentum of the inclusive particle; $x_T = \frac{2p_T}{\sqrt{s}}$ is the transverse variable; σ_{inel}^{total} is the total reaction cross section of the collision and is described by Eqs. (**??**) and (**??**). The characteristic of the terms in Φ will be discusses later in Section **??**.

As it will be shown below, this parametrisation described in Eqs. (**??**) and (**??**) is not in good agreement with the experimental data using the original KMN parameters [**?**] over the low energy range for the inclusive particle. Hence, a reparametrisation based on this modified KMN parametrisation has been performed on a set of data, by applying the χ^2 minimisation procedure and using the MINUIT package [**?**].

6.2 MINUIT: Function Minimisation and Error Analysis

The MINUIT package [**?**], available from the CERN Program Library, is conceived as a tool to find the minimum value of a multi-parameter function and analyse the shape of the function around the minimum. The principal application is foreseen for statistical analysis, working on χ^2 or log-likehood functions, to compute the best-fit values and also the uncertainties of the parameters, including correlations between the parameters.

For a quick review on the function and running procedure of MINUIT, one can refer to the reference manual [**?**].

6.3 Reparametrisation of Inclusive Antiproton Production in $p + A$ Collisions

The χ^2 minimisation procedure is based on the MINUIT package. The set of experimental data taken into account includes the measurements from Sugaya *et al.* [?], Abbott *et al.* [?], Allaby *et al.* [?] and Eichten *et al.* [?], corresponding to the incident proton energies from 12 GeV to 24 GeV/c and the measured $\bar{p}$ transverse momentum range extending up to about 1 GeV/c. Table ?? shows some characteristics of the included experiments. The original parameters of the KMN parametrisation were taken as the starting values for the minimisation procedure.

Since the original KMN parametrisation doesn't present a good agreement with the experimental data, the modification of functional terms based on the original KMN parametrisation was proposed. The behaviour of the function terms Φ_1 and Φ_2 in the original KMN parametrisation were first observed.

Figure ?? shows the behaviour of the first and the second terms of Φ in function of p_T, corresponding to the centre of mass energy $\sqrt{s}$ = 5, 6, 7, 8, 9 and 10 GeV by the original KMN parametrisation [?]; $\Phi = \Phi_1 + \Phi_2$, for which, $\Phi_1 = \exp(-C_4 p_T^2)$ and $\Phi_2 = C_5 \exp(-C_6 x_T)/(p_T^2+\mu^2)^4$. By investigating each term in the function Φ in Eq. (??), one can notice that the second term in Φ is of significant magnitude for low transverse momentum p_T range, at least comparable to the first term.

As it is shown in the figure, Φ_2 is significantly similar to Φ_1 at low p_T over the entire range of $\sqrt{s}$ while in high energy systems in which $\sqrt{s}$ is high, Φ_2 is much greater than Φ_1 and will dominate Φ at high p_T range. In this case, Φ_2 cannot be treated as the modification term in Φ in the original KMN parametrisation. And, in independent searches over individual sets of data, it shows that good fits were obtained for energies $E > 12$ GeV with only Φ_1. In addition, in nuclear collisions, the probability of large p_T scattering is small so that the term Φ_2 is required for only low energies. Therefore, in order to enforce the above points to be satisfied, an energy-dependent cutoff function was introduced to the function Φ. Hence, Φ in Eq. (??) was modified to the form as

$$\Phi(p_T) = \exp(-C_4 p_T^2) + C_5 \frac{\exp(-C_6 x_T)}{(p_T^2 + \mu^2)^4} \exp(-\alpha\sqrt{s}) \tag{6.3}$$

The choice of this energy-dependent term $\Phi_3 = \exp(-\alpha\sqrt{s})$ is purely technical and the resultant term of $\Phi_2\Phi_3$ in the revised Φ in Eq. (??) then contributes only at low energies. The modified parametrisation is then investigated and the new parameters are then given based on the experimental results.

Combining all the experimental data [?, ?, ?, ?] and quoting the new forms of the inclusive cross section in (??) and (??), the χ^2 minimisation performed with MINUIT has been achieved and the best fitting parameters are obtained. The results are shown in Table ??. The difference between the new set of parameters and those from the original KMN parametrisation [?] is also shown in the same table.

In minimising χ^2, it has to be noted that, the error of measurement reported by Sugaya *et al.* is only about 1$\sim$2% [?]. This small error would drastically constrain the least χ^2

fitting. However, such a small error is not realistic because even if the statistical errors are small, the systematic error coming from the uncertainties from the calibration of incident beam intensity, and the spectrometer acceptance, etc, would give an overall uncertainty of the order of about 15% [?, ?]. So, in evaluating the best fitting χ^2, the experimental error bars of data from Sugaya *et al.* [?] had to be set to more realistic values in the optimisation procedure.

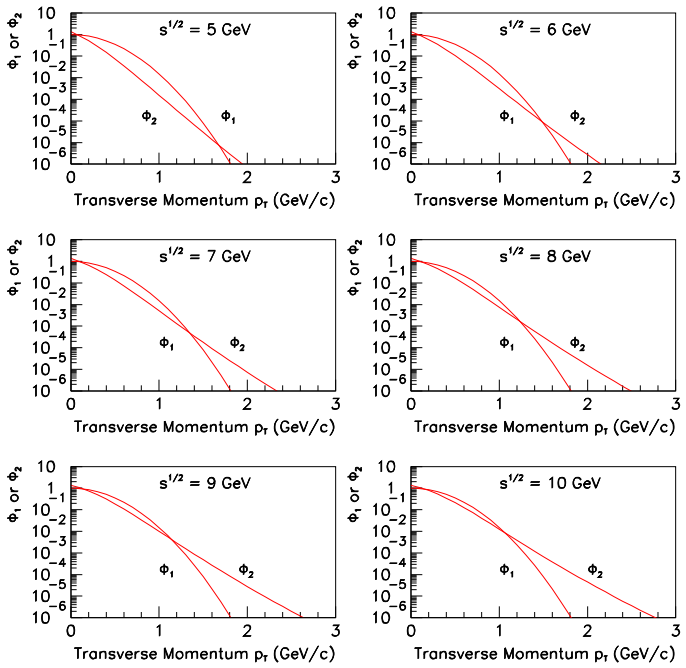

Figure 6.1: *The behaviour of the first and the second terms, Φ_1 and Φ_2, of Φ defined in Eq. (??) in the original KMN parametrisation [?] as a function of the transverse momentum p_T for centre of mass energy $\sqrt{s}$ as 5, 6, 7, 8, 9 and 10 GeV.*

6.4 Reparametrised Antiproton Production in $p+p$ and $p+A$ Collisions

The results are then compared with the experimental data together with the original KMN parametrisation [?]. Figure ?? shows the frame dependent $\bar{p}$ production cross section in the laboratory

$$\frac{d^2\sigma}{d\Omega dP} = \frac{P^2}{E}\left(E\frac{d^3\sigma}{d^3p}\right)_{inv} \tag{6.4}$$

Table 6.1: *Summary of experiments and data included.*

Exp.	Type	E_{in}/P_{in}	$P_{\bar{p},max}$ (GeV/c)	$p_{T,\bar{p},max}$ (GeV/c)
Allaby *et al.* 1970 [?]	$p+p$	19.2 GeV/c	14.5	0.91
Allaby *et al.* 1970 [?]	$p+Al$	19.2 GeV/c	14.5	0.91
Eichten *et al.* 1972 [?]	$p+Be$	24.0 GeV/c	18.0	1.068
Eichten *et al.* 1972 [?]	$p+Al$	24.0 GeV/c	18.0	1.068
Abbott *et al.* 1993 [?]	$p+Al$	14.6 GeV/c		0.78
Sugaya *et al.* 1998 [?]	$p+C$	12.0 GeV	2.5	0.22
Sugaya *et al.* 1998 [?]	$p+Al$	12.0 GeV	2.5	0.22

Table 6.2: *Values of the parameters and χ^2 by Kalinovskiĭ [?] and this work first reported in Ref. [?]. Note that the two values of C_5 cannot be compared directly since they are concerned with different functions. See the text.*

parameters	KMN (1989)	this work
C_1	0.08	0.042257
C_2	8.6	5.9260
C_3	2.30	0.9612
C_4	4.20	2.1875
C_5	2.0	84.344
C_6	10.5	10.5
μ^2	1.1	0.092743
b_0	0.12	0.12
Γ	5.0	5.0
α		2.2429
χ^2 *per point*	7.30	0.544

in function of $\bar{p}$ momentum measured at the scattering angles of 5.1^0 for $p+C$ and $p+Al$ collisions at the incident energy $E = 12$ GeV; P and E are the $\bar{p}$ momentum and energy in the LS. As shown in the figure, the curve behaves quite smoothly. It has to be noted that, even if the threshold of the $\bar{p}$ production is $7m_p$, antiprotons can also be produced in a system with an energy below the threshold. This is called the subthreshold production. It is due to the effect of the Fermi motion of nucleons in the nucleus but is not included in the expression (**??**). In general, the effect of the Fermi motion is negligible for a system above the threshold. However, according to the measurements [**?**], the Fermi motion would contribute several percent to low energy $\bar{p}$ production.

On Figure **??** where the antiproton invariant distribution

$$\frac{1}{2\pi m_T}\frac{d^2n}{d\xi dm_T} = \frac{1}{\sigma_{total}^{inel}}\frac{1}{2\pi m_T}\frac{d^2\sigma}{d\xi dm_T} = \frac{1}{\sigma_{total}^{inel}}\left(E\frac{d^3\sigma}{d^3p}\right)_{inv} \tag{6.5}$$

is shown as a function of the antiproton transverse mass difference $dm_T = m_T - m_0$ for the incident momentum of 14.6 GeV/c for $p + Al$ collision; m_0 is the $\bar{p}$ rest mass. The $\bar{p}$ cross section is averaged over the rapidity range $1.0 \leq \xi \leq 1.6$, corresponding to the measured momentum acceptance [**?**].

In Figure **??**, the antiproton cross sections integrated over p_T [**?**]

$$\frac{dn}{d\xi} = \frac{1}{\sigma_{total}^{inel}}\frac{d\sigma}{d\xi} = \frac{1}{\sigma_{total}^{inel}}\int_0^{p_{T\,max}} 2\pi p_T \left(E\frac{d^3\sigma}{d^3p}\right)_{inv} dp_T \tag{6.6}$$

at an incident momentum of 19.2 GeV/c for $p + p$ and $p + Al$ collisions are plotted as a function of antiproton rapidity. In this figure, it can be noted that the antiproton production cross section is at its maximum as expected around mid-rapidity, i.e., $x_F = 0$, in which, x_F is the Feynman variable defined as the ratio between the longitudinal momentum and its maximum possible longitudinal value in the centre of mass frame, for both $p+p$ and $p+Al$ collisions. Figure **??** also provides the evidence that $\bar{p}$ multiplicity in $p + A$ collisions increases only slightly with the target mass and also the centrality. This results is consistent with the measurements reported by Abbott *et al.* [**?**].

Figure **??** shows the Lorentz invariant density defined as twice the differential invariant multiplicity [**?**]

$$\omega = 2\frac{E}{P^2}\frac{d^2n}{d\Omega dP} = \frac{2}{\sigma_{inel}^{total}}\left(E\frac{d^3\sigma}{d^3p}\right)_{inv} \tag{6.7}$$

plotted in function of the $\bar{p}$ momentum for $p + Al$ and $p + Be$ collisions at an incident momentum of 24 GeV/c. The antiproton production angles measured were at 17, 27, 37, 47, 57, 67, 87, 107 and 127 mrad. The values on the figure are multiplied by a power of 10^{-1}, i.e., 10^0 for 17 mrad, 10^{-1} for 27 mrad, 10^{-2} for 37 mrad etc.

In order to investigate the continuity properties of the functional forms used together with the incident beam energy, the target, etc, the parametrised $\bar{p}$ production cross section is plotted as a function of its variables over the whole variable ranges. Once the

conditions of an experiment to produce and measure the $\bar{p}$ production are given, the possible ranges of variables can be immediately determined from the reaction kinematics. Figure **??** shows the 3-dimensional plots of the reparametrised $\bar{p}$ production as a function of different variables respectively: $\bar{p}$ invariant distribution as a function of the transverse mass difference and rapidity at the incident momentum of 14.6 GeV/c for $p+Al$ collision, cross section as a function of $\bar{p}$ production momentum and scattering angle at the incident energy of 12 GeV for $p+C$ collision and also the Lorentz invariant density as a function of $\bar{p}$ production momentum and scattering angle at the incident momentum of 24 GeV/c for $p+Be$ collision. Figure **??** provides the evidence that this reparametrisation is valid under the constraints of the available experiments taken into account [**?**, **?**, **?**, **?**], due to the given incident beam energies and also the chosen targets. Under this investigation, this reparametrisation has shown the agreement with the experimental data for the incident nucleon energy at least up to about 24 GeV/n in the laboratory frame. The energy limit of the validity of this reparametrisation will be discussed in the next section.

6.5 Antiproton Multiplicity Distribution in $p+p$ and $p+A$ Collisions

In the past few decades, high quality beams became available at proton synchrotron with increasing energies at CERN, for example, Intersecting Storage Ring (ISR), PS, IHEP and SPS etc [**?**, **?**, **?**, **?**], Fermilab (FNAL) Tevatron [**?**, **?**, **?**] and Brookhaven AGS [**?**] and Relativistic Heavy Ion Collider (RHIC) [**?**]. The experimental data of the cross section and the multiplicity distribution of charged hadrons in high energy hadron-hadron collisions then provide important informations of the internal structure of hadrons, i.e., the compound of nuclear dynamics with QCD which is regarded as the underlying theory of strong interactions.

However, the mean secondary charged particle multiplicity produced is quite low up to the incident beam energy $E \approx 30$ GeV [**?**, **?**]. The low multiplicity is partially due to the fact that a leading hadron would keep a considerable fraction of its incident energy [**?**]. Such a fact is referred to as the leading particle effect [**?**, **?**]. For example, in the case of $p+p$ collisions, a final state proton would still keep an average half of the incident energy [**?**] and thus would contribute a great fraction in the final charged particle multiplicity. Thus, the experiments were improved by applying the methods using an electronic detector, i.e., a set of multiwire proportional chambers inside the Split Filed Magnet (SFM) detector at CERN ISR [**?**, **?**]. The principal advantage of such methods is the possibility of analysing much larger event samples, but the resulting small statistical errors necessitate a thorough and lengthy study of possible systematic effects and errors. Another advantage is the use of inclusive trigger with the SFM, enabling a single charged particle anywhere in the phase space sufficient to trigger the detector. In addition, because of the magnetic field, the particles produced at small angles due to the inelastic collisions will be swept out into the tracking chambers, making it possible to separate the inelastic and non-single-diffractive events.

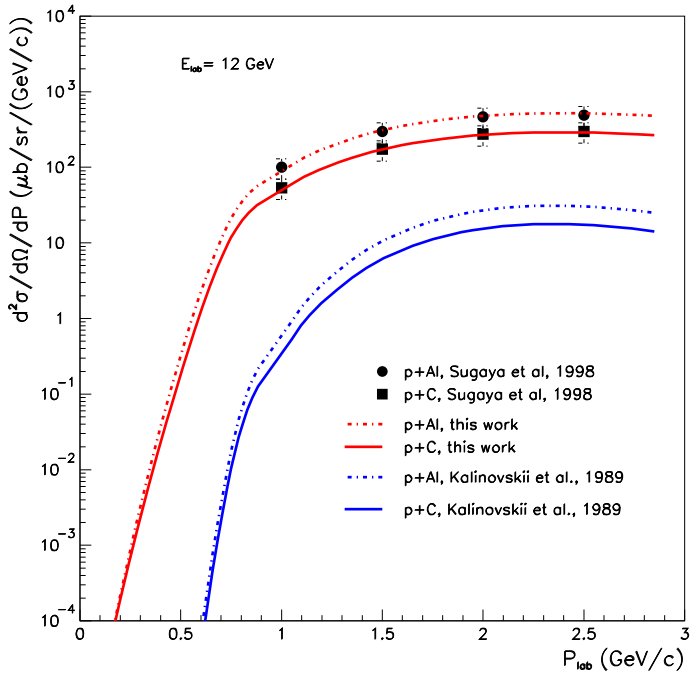

Figure 6.2: *Antiproton cross sections measured at* 5.1^0 *in function of antiproton production momentum for* $p+C$ *and* $p+Al$ *collisions at an incident energy of 12 GeV compared with the experimental data [?] and the KMN parametrisation [?].*

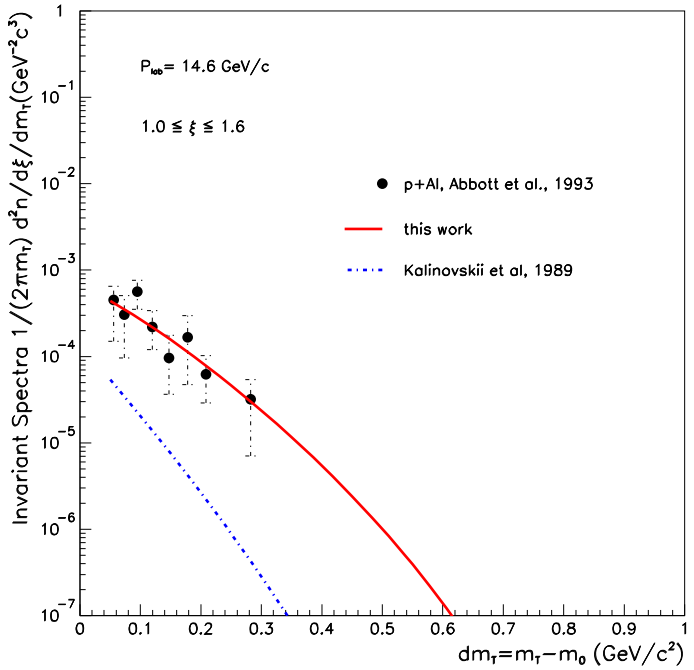

Figure 6.3: *Antiproton invariant spectra in function of antiproton production transverse mass difference* $dm_T = m_T - m_0$ *for* $p+Al$ *collision at an incident momentum of 14.6 GeV/c compared with the experimental data [?] and the KMN parametrisation [?].*

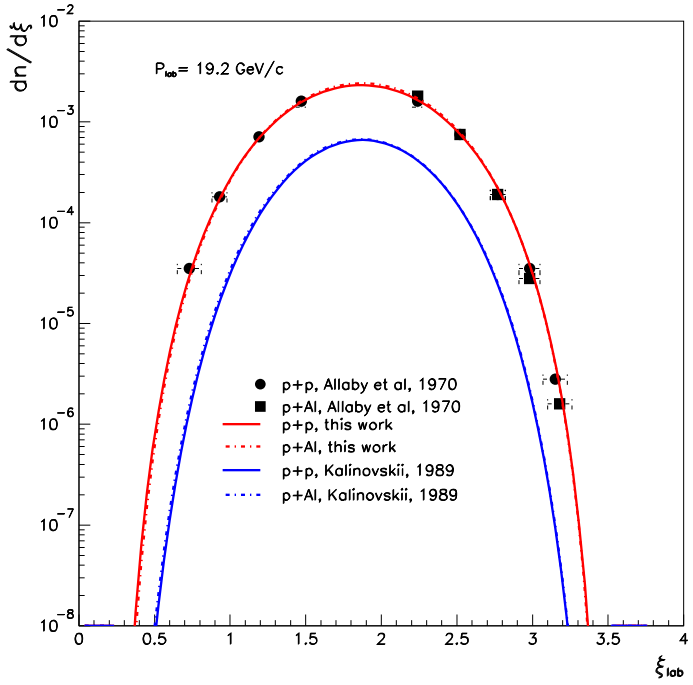

Figure 6.4: *Antiproton spectra $dn/d\xi$ in function of antiproton production rapidity ξ for $p+p$ and $p+Al$ collisions at an incident momentum of 19.2 GeV/c compared with the experimental data [?] and the KMN parametrisation [?].*

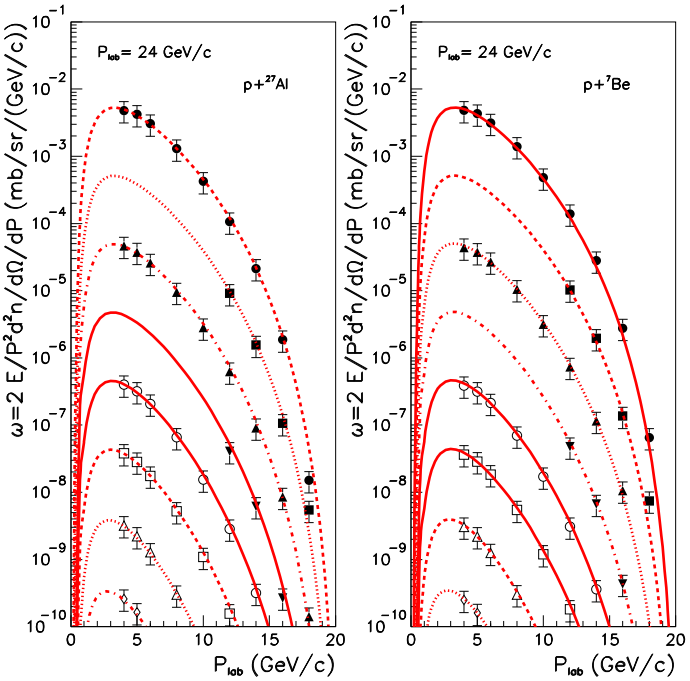

Figure 6.5: *Antiproton Lorentz invariant density in function of antiproton production momentum for $p+Al$ and $p+Be$ collisions at an incident momentum of 24 GeV/c compared with the experimental data [?]. The measurement angles are 17, 27, 37, 47, 57, 67, 87, 107 and 127 mrad from top to bottom. The density is plotted and multiplied by a power of 10^{-1}, i.e., 10^{0} for 17 mrad, 10^{-1} for 27 mrad, 10^{-2} for 37 mrad etc.*

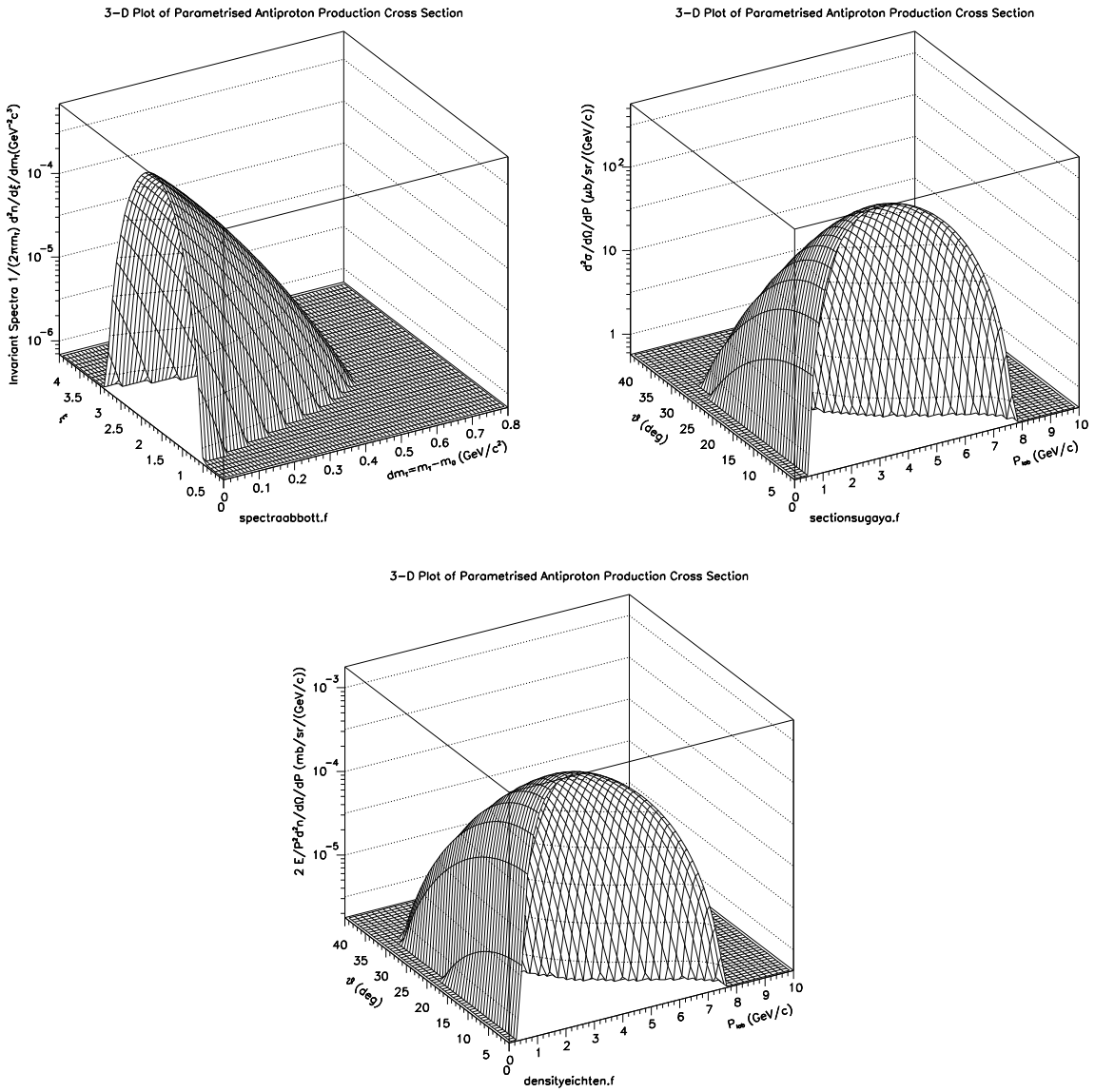

Figure 6.6: *3-dimensional plots of the reparametrised $\bar{p}$ production in three types: the $\bar{p}$ invariant spectrum in function of the transverse mass difference and rapidity at incident momentum of 14.6 GeV/c for $p+Al$ collision (Top Left), $\bar{p}$ production cross section in function of $\bar{p}$ production momentum and scattering angle at the incident energy of 12 GeV for $p+C$ collision (Top Right) and the Lorentz invariant density in function of $\bar{p}$ production momentum and scattering angle at the incident momentum of 24 GeV/c for $p+Be$ collision (Bottom).*

The experimental results [?, ?, ?] of the multiparticle production in high energy hadron-hadron collisions indicate that, if the charged particles are produced randomly and independently, their multiplicity distribution could obey a Poisson distribution [?]. The deviations from a Poisson distribution are then a hint of the underlying production processes, and also a source of information about the nuclear medium effects [?].

The multiplicity of particles created in high-energy hadron collisions follows a distribution with a long tail, qualitatively similar to the distribution of ionisation energy loss (Landau distribution). The produced hadron multiplicity is generally described in terms of the Koba-Nielsen-Olesen (KNO) variables [?], i.e., $z = \frac{N}{<N>}$, the ratio between the multiplicity and the average multiplicity of the particles produced at the centre of mass energy $\sqrt{s}$. However, it is found that the KNO scaling is violated in high energy collisions [?, ?]. Therefore, another parametrised hadron-nucleus multiplicity distribution in terms of $\ln\sqrt{s}$ is introduced [?, ?, ?]. The multiparticle production in the hadronic collision can be also understood as the cascade processes in the collision [?, ?], for which, cascading means that N particles are originally emitted in the collision and each gives rise to n_c^i particles. So, one says that n_c^i particles belong to a clan, whose ancestor is the i^{th} original particle. In Chapter ?? about the analysis of secondary antiprotons which will be discussed later, one will find that almost all secondary antiprotons are produced after the first collision. Therefore, almost each secondary antiproton belongs to an independent incident particle. The multiplicity distribution of particle in a single clan may vary from case to case but its average is found to obey a specific relation [?, ?, ?].

Figure ?? [?, ?] shows the measurement data of the mean multiplicity distributions of both charged and negative secondaries produced in $p+p$ collisions in the whole phase space as a function of the centre of mass energy. Figure ?? shows the mean multiplicity distribution of antiprotons produced calculated for $p+p$ collision [?] by the reparametrisation combining Eqs. (??), (??) and the parameters in Table ??. In Figure ??, it has to be noted that the original data (black circles) were measured by removing the single-diffractive parts in total cross section so that the corrected ones are given by estimating 10 $\sim$ 15% in contribution to its multiplicity [?]. The corrected values from the experimental data are also shown in the figure. Hence, after such a correction, the calculated $\bar{p}$ mean multiplicity distribution has shown a good agreement with the experimental data up to $\sqrt{s} = 25$ GeV. For $\sqrt{s} \geq 30$ GeV, the parametrisation underestimates the $\bar{p}$ mean multiplicity. The difference between the calculations and the measurements becomes larger at larger energies but still remains close to the experimental uncertainty of the available experiments.

It has to be noted that, when $\sqrt{s}$ is reaching 1 TeV, the calculated $\bar{p}$ mean multiplicity will turn out to decrease. Such a decrease is not physically expected. This has provided the upper energy limit of the validity of this parametrisation which is beyond the range of interest of this work.

The mean multiplicity distributions for separated types of charged secondaries and for all charged particles are available from experiments such as the SFM [?, ?], the E710 [?, ?] and the UA5 [?]. The mean multiplicity distribution for all charged particles in $p+p$ collisions is customarily expressed as the centre of mass energy dependence in a

form of a polynomial in terms of $\ln s$ [?, ?, ?, ?]

$$< n >= A + B \ln s + C \ln^2 s \tag{6.8}$$

or in the formula [?]

$$< n >= A + B \ln s + C s^{-1} \tag{6.9}$$

The constants in Eqs. (??) and (??) are determined by the fitting procedure. Note that a threshold value for the multiplicity was used in the parametrisations (??) and (??) [?, ?, ?]. Also note that the leading particle contribution has been included in the factor A [?]. In these results, the mean multiplicity of each type of charged particle appears in a similar shape to that of the all charged particles. Therefore, the $\bar{p}$ mean multiplicity distribution in $p+p$ collisions could be described by using the same functional forms shown in Eqs. (??) and (??). The constants for the $\bar{p}$ mean multiplicity distribution in form of (??) was reported [?] while the constants for the $\bar{p}$ mean multiplicity distribution in form of (??) was determined in this work, by the best fitting. The constants for these two parametrisations are shown in Table ??.

Table 6.3: *Constants for the parametrised $\bar{p}$ mean multiplicity distributions in $p+p$ collisions described in forms of Eq. (??) [?, ?, ?] and Eq. (??) [?].*

Parametrisation	A	B	C
$< n_{\bar{p}} >= A + B \ln s + C \ln^2 s$	-0.20	0.039	0.37
$< n_{\bar{p}} >= A + B \ln s + C s^{-1}$	0.09562	-0.0530	0.00751

Figure ?? shows the $\bar{p}$ mean multiplicity distributions in $p+p$ collisions as a function of the centre of mass energy in the whole phase space from four different origins: the experiment [?] together with its corrected values, the values calculated by the revised parametrisation of the $\bar{p}$ production from Eqs. (??) and (??), and the parametrisations from Eqs (??) [?, ?, ?] and (??) [?]. In this figure, both these two parametrisations of the $\bar{p}$ mean multiplicities have shown a better agreement with the experimental data than the results calculated by this work for the centre of mass energy $\sqrt{s} > 25$ GeV. Nevertheless, it has to be indicated that, according the functions used in the parametrisations (??) and (??), these two parametrisations have the following lower limits of the validity: $\sqrt{s} = 6.4$ GeV, i.e., the incident nucleon energy $E \simeq 20.89$ GeV for the parametrisation (??); $\sqrt{s} = 5.37$ GeV, i.e., the incident nucleon energy $E \simeq 14.43$ GeV for the parametrisation (??). However, the energy range below these limits is still important to the $\bar{p}$ production in nuclear interactions for the present work. On the other hand, as it will be discussed later, for the interest of study on the $\bar{p}$ origins, the energy range $E > 200$ GeV is of less importance. This arguments will be briefly outlined in advance in the next section while the details will be discussed in Chapter ??.

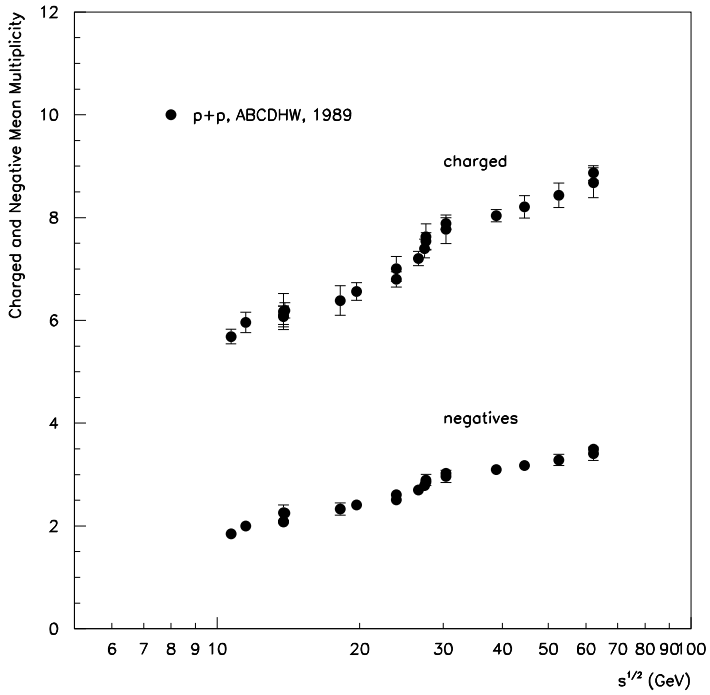

Figure 6.7: *The measured mean multiplicity distributions of the charged and negative particles produced in $p + p$ collision in the whole phase space as a function of the centre of mass energy [?, ?].*

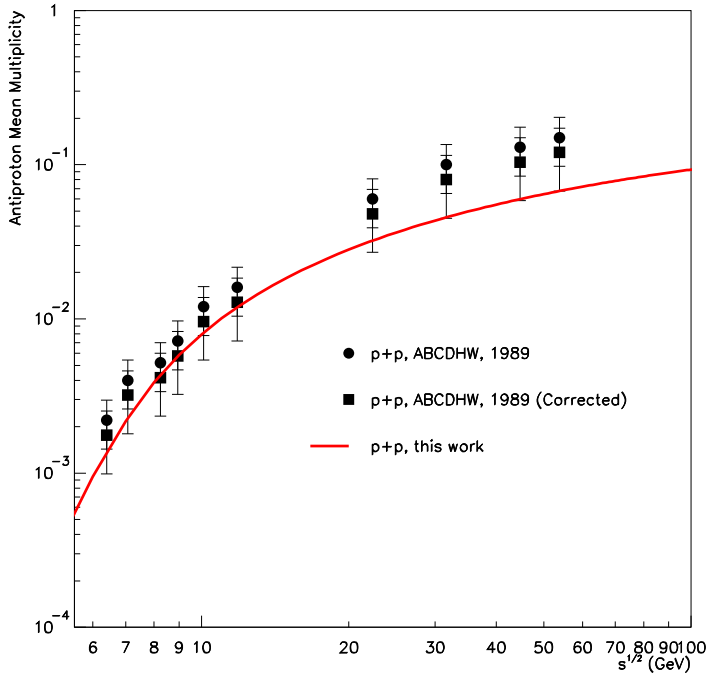

Figure 6.8: *Antiproton mean multiplicity distribution in the whole phase space calculated by the revised parametrisation in $p + p$ collision. The results are compared with the experimental data [?].*

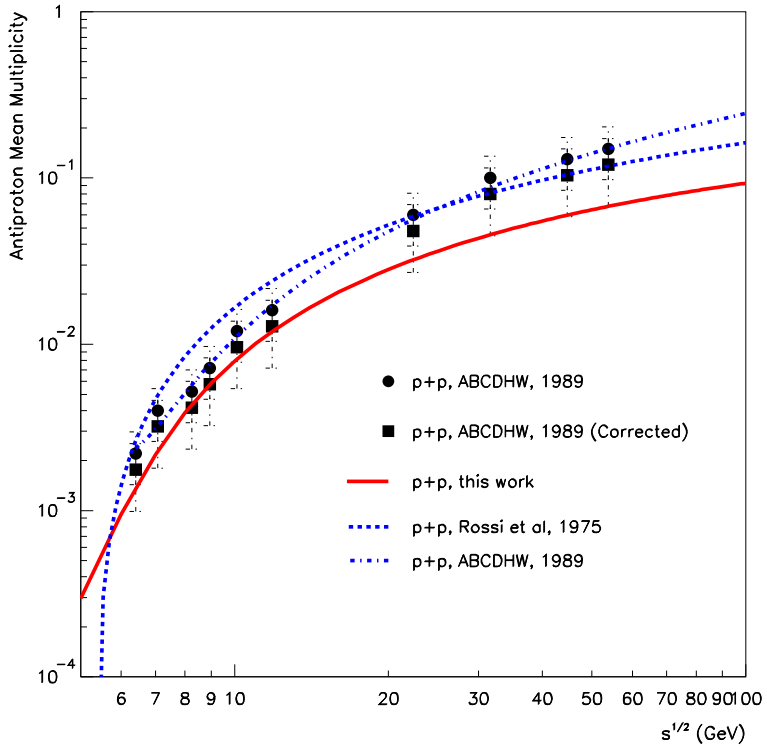

Figure 6.9: *Same data as in Figure* ?? *compared with the values calculated in this work and the parametrisations of Eqs. (??) and (??). See the text for the discussions.*

6.6 Antiproton Production in Nucleus-Nucleus Collisions

The parametrised $\bar{p}$ production cross section achieved in this work was first applied to evaluate the secondary galactic $\bar{p}$ flux [?] whose results are in a good agreement with the measured flux [?]. It has to be noted that, due to the material composition: about 88% of proton and 12% of helium in cosmic rays and about 90% protons and 10% of helium being assumed in the ISM, $p+p$ collisions are the dominant process for the secondary $\bar{p}$ production in the Galaxy but the $\bar{p}$ production in p-nucleus and nucleus-nucleus collisions (especially $p+He$ and $He+He$ collisions) should also be taken into account [?] while the $\bar{p}$ production from such processes will enhance the $\bar{p}$ flux as a whole and also shift its low energy tail [?] (see Figure ??).

The same argument also holds in the evaluation of the secondary atmospheric $\bar{p}$ flux. In the material composition in the atmosphere, there are about 80% nitrogen and 20% oxygen. Therefore, in order to correctly evaluate the secondary atmospheric $\bar{p}$ flux, in

addition to the $\bar{p}$ production in p-nucleus collisions, it is mandatory to include some other nucleus-nucleus collisions, especially $He + He$, $He + N$ and $He + O$ collisions. (In the atmosphere, $He + N$ and $He + O$ collisions are extremely dominant.) However, the available experimental data for the $\bar{p}$ production in these $A + A$ collisions are quite few.

In determining the $\bar{p}$ production cross section in nucleus-nucleus collisions, some approaches are currently applied: it is determined either by the Monte Carlo simulation technique (DTUNUC) [?, ?, ?, ?], or by approximations based on the cross section of nucleon-nucleon collisions, for example, the Wounded Nucleon Model [?, ?]. In this work, the approach considered is the Wounded Nucleon Model since:

- According to the measurements [?], this model has successfully predicted the multiparticle production of 200 GeV/c protons, pions and kaons on Au, Ag and Mg targets. In addition, the measurements on the charged particle multiplicity distributions in the experiments WA97 and NA57 [?] in $Pb + Pb$ collisions at 158 A GeV/c have been well described by the Wounded Nucleon Model within the centrality range.

- For the cosmic ray issue, the measurements of charged particle multiplicity distributions in the central rapidity region in $p + p$, $p + \alpha$ and $\alpha + \alpha$ collisions at the CERN ISR at the centre of mass energy $\sqrt{s} = 31.5$ and 44 GeV/n [?] and $\sqrt{s} = 88$ and 125 GeV/n [?] have shown that the data are better fitted with the Wounded Nucleon Model than with other models.

- The $\bar{p}$ mean multiplicity distributions in $p + p$ and $p + A$ collisions derived by the parametrisation developed in this work has shown a good agreement with the experimental data within the most important and interested energy range so that it has provided the precise module of scaling.

As discussed in the previous chapter, each type of charged particle in $p+p$ collisions has similar energy dependence multiplicity distribution. In this work therefore, the Wounded Nucleon Model will be used to relate the $\bar{p}$ multiplicity in nucleus-nucleus collision to that in $p + p$ collision. This idea is to be experimentally tested because up to now, it is still lacking in the direct experimental data.

6.6.1 Wounded Nucleon Model

The basic assumption of the Wounded Nucleon Model [?, ?] is that, in a nuclear collision, the average multiplicity is proportional to the number of wounded nucleons and each wounded nucleon contributes, on the average, only once to a multiplicity equal to half of that produced by a free nucleon-nucleon collision, for which, a wounded nucleon means a nucleon which has undergone at least one inelastic collision in such a process. A wounded nucleon contributes only once to the multiplicity even if it might be struck several times by other nucleons. Such an assumption was derived from a formation time argument, i.e., most of the hadrons emitted from the wounded nucleons of nucleus A are only formed after A has passed nucleus B [?]. The only physical inputs to this model

are the density distribution of the nucleons inside the nucleus and the nucleon-nucleon cross section [?]. The average number of wounded nucleons in one nucleus and also the probability of n wounded nucleons in a collision are then given by the nucleon-nucleon cross section and the impact parameters too [?, ?].

By this model, the multiplicity of particles produced in a nucleus-nucleus collision is proportional to the number of wounded nucleons which is the sum of wounded nucleons in nucleus A and in nucleus B:

$$< n_{AB} > \;=\; \frac{1}{2}(\omega_A + \omega_B) < n_{NN} > \;=\; \frac{1}{2}\left(A\frac{\sigma_{pB}}{\sigma_{AB}} + B\frac{\sigma_{pA}}{\sigma_{AB}}\right) < n_{NN} > \qquad (6.10)$$

where ω_A and ω_B are the numbers of wounded nucleons in nucleus A and nucleus B respectively; A and B are the mass numbers of nucleus A and nucleus B, σ_{pA} and σ_{pB} are the nucleon-nucleus A and the nucleon-nucleus B total reaction cross sections; σ_{AB} is the total reaction cross section for the collision between nuclei A and B.

Consider the limiting case of the expression (??) by taking $A = B = p$. Then

$$< n_{pp} > \;=\; \frac{1}{2}\left(1 \cdot \frac{\sigma_{pp}}{\sigma_{pp}} + 1 \cdot \frac{\sigma_{pp}}{\sigma_{pp}}\right) < n_{NN} > \;\equiv\; < n_{pp} > \qquad (6.11)$$

So, Eq. (??) is self-consistent. In addition, by the relation (??), an application for a collision between nucleon and nucleus A can be written as

$$< n_{pA} > \;=\; \frac{1}{2}\left(A\frac{\sigma_{pp}}{\sigma_{pA}} + 1\right) < n_{pp} > \qquad (6.12)$$

Therefore, with the available well described total reaction cross sections σ_{pA}, σ_{pB} and σ_{AB}, the $\bar{p}$ production multiplicity in nucleus-nucleus collisions based on the Wounded Nucleon Model in Eq. (??) can be directly obtained.

6.6.2 Antiproton Mean Multiplicity Distribution in Nucleus-Nucleus Collisions

For the $\bar{p}$ production in nucleus-nucleus collision, one can then use Eq. (??) to determine the $\bar{p}$ mean multiplicity, in which, $< n_{pp} >$ can be calculated by the parametrised $\bar{p}$ production cross sections developed in this work together with the total reaction cross sections σ_{pA}, σ_{pp} and σ_{AB}. Since the total reaction cross section remains almost constant at the incident energy $E \geq 2$ GeV/n [?], much smaller than the threshold of the $\bar{p}$ production, up to the interested energy range $E = 200$ GeV, one can therefore apply the well described total inelastic cross sections of nucleon-nucleon, nucleon-nucleus and nucleus-nucleus collisions, in Eqs. (??), (??) and (??) [?, ?], to evaluate the values of the multiplicity $< n_{AB} >$ in Eq. (??). So, the scaling relations for the $\bar{p}$ mean multiplicity, from Eqs. (??) and (??), in $He+He$, $He+N$ and $He+O$ collisions are found simply as a constant multiplier:

$$< n_{HeHe} > \;=\; 1.359 < n_{pHe} > \;=\; 1.684 < n_{pp} > \qquad (6.13)$$

$$< n_{HeN} > \;=\; 1.552 < n_{pN} > \;=\; 2.502 < n_{pp} > \qquad (6.14)$$

$$< n_{HeO} > \;=\; 1.578 < n_{pO} > \;=\; 2.613 < n_{pp} > \qquad (6.15)$$

where $< n_{pHe} >$, $< n_{pN} >$ and $< n_{pO} >$ are determined by integrating the parametrised $\bar{p}$ production cross section over the kinematic variables. Note that the constant multipliers obtained above donot show a proposed simple A-dependent scaling rule as [?]

$$< n_{AB} > \quad = \quad A^{1/3} < n_{pB} > \tag{6.16}$$

It has to be indicated that, at very high energy, above several hundred GeV, the total reaction cross section doesn't remain constant any more but turns to increase with the increasing incoming energy. For an example of the total cross section of pp collision, see Figure ??. The total reaction cross section at such high energies might show a stronger A-dependence [?]. However, this energy level is beyond the interest of the current work.

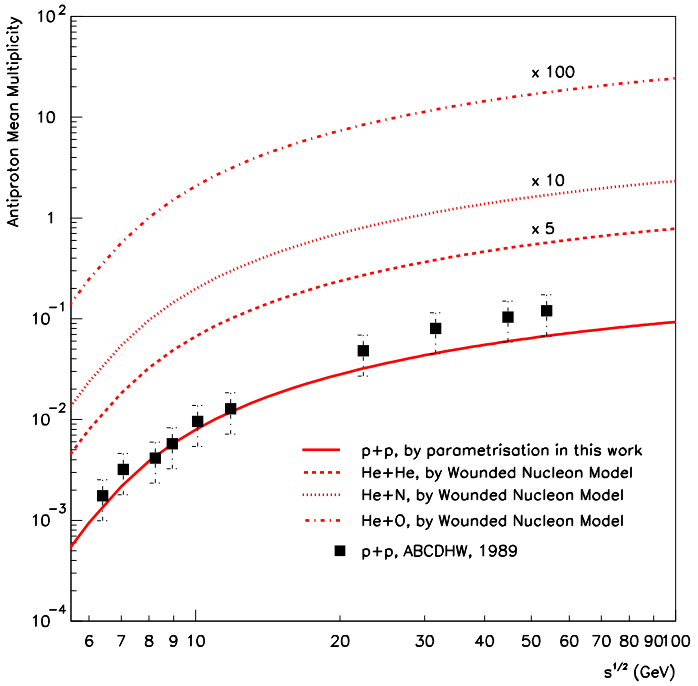

Figure 6.10: *The $\bar{p}$ multiplicity distributions in $He + He$, $He + N$ and $He + O$ collisions scaled by the Wounded Nucleon Model based on the parametrised $\bar{p}$ production cross sections in $p + p$ and $p + A$ collisions in this work, together with the experimental data in $p + p$ collision [?]. The values of $< n_{HeHe} >$, $< n_{HeN} >$ and $< n_{HeO} >$ are multiplied by a factor of 5, 10 and 100 separately.*

Figure ?? shows the $\bar{p}$ multiplicity distribution in $He+He$, $He+N$ and $He+O$ collisions which are derived by the Wounded Nucleon Model in the definition (??) based on the parametrised $\bar{p}$ production in $p+p$ collision achieved in this work. The experimental data for the $\bar{p}$ multiplicity in $p+p$ collision [?] are also shown in the figure for comparison. Since

there is no available direct measurements on the $\bar{p}$ mean multiplicity in nucleus-nucleus collisions, the comparison between the evaluated secondary $\bar{p}$ flux in the neighbourhood of the Earth by including He-type collisions and the $\bar{p}$ flux measurements in balloon or space experiments can play a role to investigate the acceptability of such a scaling rule used in this work.

6.7 Comments on the Parametrised Inclusive Antiproton Production

In conclusion, a parametrisation for the $\bar{p}$ production in $p+p$ and $p+A$ collisions has been developed. This parametrisation has shown a good agreement with the experimental data for incident nucleon energy at least up to 24 GeV/n in the laboratory frame. By the analysis of the $\bar{p}$ mean multiplicity distribution, this parametrisation would be able to extend to higher energies. The $\bar{p}$ production in $A+A$ collisions, an approach based on the Wounded Nucleon Model is presented by scaling the parametrised $\bar{p}$ production in $p+p$ collisions developed in this work.

With this parametrisation, it is now possible to evaluate the secondary galactic $\bar{p}$ flux and the secondary atmospheric $\bar{p}$ flux as well, since both of them are produced from the same nuclear mechanisms. In the discussions in Chapter **??**, one knows that the $\bar{p}$ flux contributed by the $\bar{p}$ exotic origins such as the evaporation of primordial black holes or the supersymmetric neutralino annihilation spreads over the low energy range. Their contribution could be distinguishable in the energy range $E \leq 1$ GeV, in which, there is the hope to search for these $\bar{p}$ exotic origins. Recall Figure **??** about the $\bar{p}$ contribution from the three origins: galactic secondaries, neutralino annihilation and the evaporation of primordial black holes. In order to observe if this parametrisation could sufficiently evaluate the secondary antiprotons, both galactic and atmospheric, providing the good tool to study this issue, the $\bar{p}$ production flux at some energy levels are investigated: $E =$ 1 GeV, while below which, the $\bar{p}$ exotic origins will make a distinguishing shape in the $\bar{p}$ flux; $E = 2$ GeV, at which, the secondary galactic $\bar{p}$ flux would have a peak and the contribution of the $\bar{p}$ flux from the evaporation of primordial black holes and the neutralino annihilation would shift or flatten the peak; $E = 4$ and $E = 6$ GeV while the contribution of the $\bar{p}$ flux from the neutralino annihilation would still have the influence to the peak at $E = 2$ GeV. This parametrisation is found to be sufficient for this purpose because of the following facts which will be discussed in detail later in Chapter **??**: about 96% of all antiprotons below 6 GeV are produced by the incident nucleons with energies $E \leq 200$ GeV/n; incident nucleons with $E \leq 20$ GeV/n produce about 25% of all antiprotons with energies $E \leq 1$ GeV; incident nucleons with energies $E \leq 50$ GeV/n produce about 70% of all antiprotons with energies $E \leq 2$ GeV and about 90% of antiprotons with energies $E \leq 4$ GeV are produced by the incident nucleons with energies $E \leq 100$ GeV/n. Hence, one can conclude that the incident energies up to $E \simeq 200$ GeV/n are the most important and sufficient to evaluate the secondary $\bar{p}$ flux with a good precision while such an energy range still lies in the good validity range of this parametrisation.

Chapter 7

Evaluation Technique of Secondary Atmospheric Antiproton Flux

With the $\bar{p}$ production in $p+p$, $p+A$ and $A+A$ collisions developed in the previous chapter, the secondary atmospheric $\bar{p}$ flux at different altitudes are calculated by Monte Carlo simulation, including both p-incident and He-incident collisions in the atmosphere. In addition to the $\bar{p}$ production in the hadronic collisions in the atmosphere, some elements have to be taken into account in the calculation. In this chapter, the simulation technique is introduced and the background applied in the calculation, such as cosmic ray flux, The solar modulation, particle propagation in the geomagnetic field, the atmospheric model and the cross section between the produced antiproton and the atmospheric nuclei, are discussed. the application of this technique to other atmospheric particles is outlined in the last section. The results are shown and discussed in the next chapters.

7.1 Simulation Technique of Secondary Atmospheric Antiproton Flux

The simulation approach used here is based on the research programme developed for the atmospheric particles below the geomagnetic cutoff [?]. This simulation was applied and improved in a series of articles by the AMS group at the Institut des Sciences Nucléaires de Grenoble: for atmospheric protons [?], for atmospheric electrons and positrons [?], and for light nuclei [?] in near earth orbit, for atmospheric muons and neutrinos [?, ?], for atmospheric antineutrons [?], and for this work on atmospheric antiprotons [?, ?].

This simulation [?] was developed to study the flux of secondary particles produced in the atmosphere due to the interactions between incident cosmic ray particles and the atmospheric nuclei, and also to investigate which part and by which mechanism the incident cosmic ray flux reaching the Earth would generate the secondary spectra. It also provides the possibility to study its dynamical status with respect to the trapping process observed for other populations of particles in the neighbourhood of the Earth.

The simulation applies the relations between the creation flux at the creation altitude

and the detection flux at the detection altitude:

$$N_{CR} = \Phi_{CR} \cdot 4\pi \cdot S_{CR} \cdot t \tag{7.1}$$

$$N_D = \bar{\Phi}_D \cdot 4\pi \cdot S_D \cdot t = \int (\Phi_D(\theta) 2\pi \sin\theta d\theta)\, S_D \cdot t \tag{7.2}$$

where Φ is the particle flux, S is the sphere area and t is the time scale. N_{CR} is the total cosmic ray particle number created on the creation sphere and N_D is the total detected particle number on the virtual detection sphere. The subscripts CR and D stand as 'creation' and 'detection'. By Eqs. (??) and (??), the average detection flux can be written as

$$\begin{aligned} \bar{\Phi}_D &= \frac{N_D}{\Omega S_D t} = \frac{N_D}{\Omega S_D (N_{CR}/\Phi_{CR} 4\pi S_{CR})} = \frac{S_{CR}}{S_D} \cdot \frac{4\pi}{\Omega} \cdot \Phi_{CR} \cdot \frac{N_D}{N_{CR}} \\ &= \frac{S_{CR}}{S_D} \cdot \frac{4\pi}{\Omega} \cdot \Phi_{CR} \cdot \frac{S_D(\triangle N_D/\triangle S)}{N_{CR}} \end{aligned} \tag{7.3}$$

In Eq. (??), $\frac{\triangle N_D}{\triangle S}$ is the particle mean count number on the cross area $\triangle S$, in which, $\triangle S$ is the band area of the geomagnetic latitude range on the virtual detection sphere and $\triangle N_D$ is determined by counting the particle crossing number upon the virtual sphere at the chosen detection altitude during particle propagation. Ω corresponds to the detection acceptance angle of the spectrometer required in the simulation.

7.1.1 Cosmic Ray Flux and Solar Modulation

The atmospheric $\bar{p}$ flux in this work is simulated by interacting cosmic ray particles with atmospheric nuclei. Cosmic ray particles are generated near the Earth at a distance of 2000 km, by applying their abundances and energy distributions at TOA [?], about 88% of protons and 12% of heliums, with the energy distributions $\propto E^{-2.74}$ (See Figure ??), corrected for the solar modulation effect [?]. The modulation is considered up to a radial distance of about 10 terrestrial radii (4 Störmer length units [?]) as to ensure the generation points to be always in the relevant initial conditions for the geomagnetic field [?]. The other types of cosmic ray particles are neglected due to their low abundances.

For cosmic ray particles propagating in the Solar system, they suffer the solar modulation which is a function of the particle energy and the radial distance [?, ?]

$$N(E)_{modulated} = \frac{E_k^2 + 2mE_k}{(E_k + Ze\Phi(r))^2 + 2m(E_k + Ze\Phi(r))} N_{unmodulated}(E_k + Ze\Phi(r)) \tag{7.4}$$

where $\Phi(r)$ is the solar modulation parameter and is given in Eq. (??). The parameter Φ varies between 350 and 1500 MV from the solar minimum to the solar maximum.

Thus, with the measured cosmic ray at TOA, the generated cosmic ray flux at the generating distance can be evaluated for the purpose of the present work.

7.1.2 Geomagnetic Field

Charged cosmic ray particles propagate under the geomagnetic field. The geomagnetic field consists of two parts, the internal field (main field) of the Earth itself and the external field driven by the Solar Wind plasma. The main field is coupled with some minor disturbances which come from the motion of charged particles in ionosphere, the Van Allen belts [**?**], and the Solar Wind. The main field dominates the geomagnetic field up to about 10 R_E where the internal field and the interplanetary magnetic field merge. Beyond 10 R_E, the Solar Wind becomes dominant and the magnetosphere is formed due to the interactions between the Solar Wind and the Earth main field.

The realistic geomagnetic field is a multipole field. The geomagnetic field used in the present work is the International Geomagnetic Reference Field (IGRF) model [**?**], which is the best fit to the multipole field by compiling the geomagnetic field measurements underwent all over the world, at both low and high altitudes. Based on the IGRF model, the numerical model [**?**, **?**] is used to calculated the related geomagnetic information needed for the present work.

For the analytic reason, a simplified dipole field is frequently used. In a dipole field, an analytic rigidity cutoff can be formulated as [**?**, **?**]:

$$R_{cutoff} = \frac{M\cos^4\lambda}{r^2(1+\sqrt{1-\zeta\cos\theta_{EW}\cos^3\lambda})^2} = \frac{59.6\cos^4\lambda}{(r/R_E)^2(1+\sqrt{1-\zeta\cos\theta_{EW}\cos^3\lambda})^2} \quad (7.5)$$

where M is the dipole moment, λ is the geomagnetic latitude, r is the radial distance, ζ is the sign of the particle charge and θ_{EW} is the incident angles from the east to the west. This rigidity cutoff indicates the minimum energy with which a cosmic ray particle can arrive at the Earth and also the minimum energy with which a particle in the Earth neighbourhood can escape from the geomagnetic field. This rigidity cutoff can play an important role in the atmospheric secondary $\bar{p}$ correction. Discussions will be given in the next chapter.

Figure **??** shows the rigidity cutoff, for a particle with positive charge, in function of the geomagnetic latitude with some different incident East-West angles of $0^0, 45^0, 90^0, 135^0$ and 180^0, at the AMS altitude 380 km. Figure **??** shows the rigidity cutoff for a positively charged particle in function of the incident East-West angle with some different geomagnetic latitudes at the same altitude. The East-West angle θ_{EW} is defined as the angle between the particle momentum and the direction normal to the meridian plane in geographic coordinate: in the geographic coordinate, a particle crosses a meridian plane at a point $(\boldsymbol{r}, \theta, \phi)$ giving the East-West angle

$$\theta_{EW} = \cos^{-1}(\zeta\cos\theta\cos\phi) \quad (7.6)$$

$\theta_{EW} = 0$ corresponds to a particle with a positive charge arriving from the geomagnetic east.

Each curve in in Figures **??** and **??** gives the important information for the particle propagation in the geomagnetic field: particles below the curve are trapped by the geomagnetic field while above the curve, the particles can escape from the Earth.

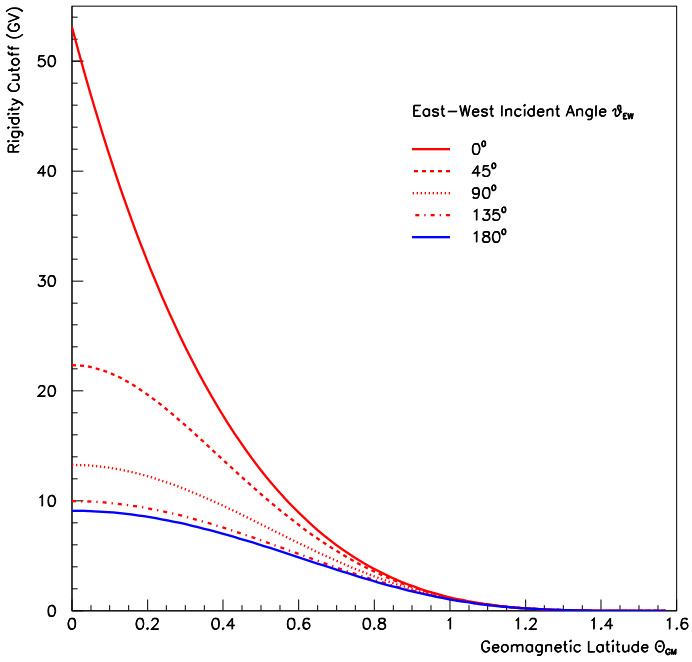

Figure 7.1: *The rigidity cutoff, for a positively charged particle ($\zeta = +1$), in function of the geomagnetic latitude for several incident angles at the altitude 380 km. $\theta_{EW} = 0$ is defined for particles coming from the east. The East-West effect is clearly seen: the particles with positive charges coming from the east have suffered a stronger rigidity cutoff ($\approx$ 55 GV at the equator) than those coming from the west ($\approx$ 10 GV at the equator).*

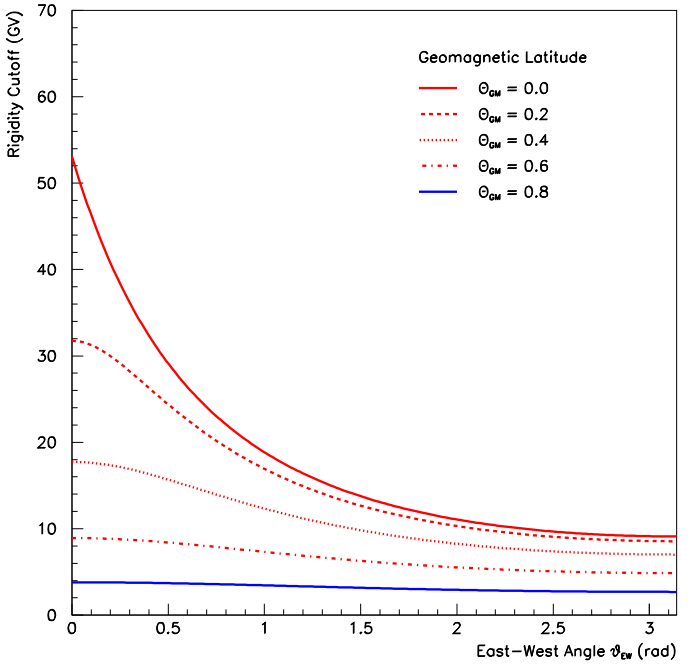

Figure 7.2: *The rigidity cutoff for a positively charged particle in function of the East-West angle for several geomagnetic latitudes at the altitude 380 km. $\theta_{EW} = 0$ for East-bound particles.*

From Figures ?? and ??, an important feature can be observed. For particles of positive charges coming from the eastern direction would suffer stronger geomagnetic rigidity cutoff than those with the same charge sign coming from the western direction. As one can see in the figures, for positively charged particles coming from the west, the rigidity cutoff around the equator is about 10 GV while the rigidity cutoff around the equator increases to about 55 GV for particles with positive charges coming from the east. This phenomenon is referred to as the East-West effect.

Although the realistic geomagnetic field is a multipole, the analysis under the assumption of the geomagnetic dipole will give the principal characteristics related to the geomagnetic field. In the realistic multipole, the field can be treated as the dipole approximation with disturbances.

7.1.3 Equations of Motion

As discussed in Section ??, in a more realistic consideration on the multipole geomagnetic field, the equations of motion become more complicated. However, the expressions of equations of motion for charged particles propagating in a magnetic field are still valid

$$\frac{mv}{e}\frac{d^2x}{ds^2} = H_y\frac{dz}{ds} - H_z\frac{dy}{ds} \tag{7.7}$$

$$\frac{mv}{e}\frac{d^2y}{ds^2} = H_z\frac{dx}{ds} - H_x\frac{dz}{ds} \tag{7.8}$$

$$\frac{mv}{e}\frac{d^2z}{ds^2} = H_x\frac{dy}{ds} - H_y\frac{dx}{ds} \tag{7.9}$$

with $m = m_0\gamma = m_0(1-\beta^2)^{-1/2}$ and m_0 is the particle rest mass. Now in multipole geomagnetic field, there is no simple form for each component of the field vector H like the dipole. In the present work, the particle propagating in the geomagnetic field is approached by applying numerically the 4th order adaptive Runge-Kutta integration of equations of motion, with the related geomagnetic information numerically calculated by the IGRF model [?, ?, ?].

7.1.4 Atmospheric Model

The cosmic ray particles are allowed to interact with the nuclei in the atmosphere during their propagation. The atmosphere can roughly be characterised as the region from sea level to an altitude about 1000 km, where neutral gases can still be detected [?]. Below 50 km, the atmosphere are assumed to be homogeneously mixed and can be treated as a perfect gas. Above 80 km, the hydrostatic equilibrium gradually breaks down as diffusion and vertical transport become important. The major species in the upper atmosphere are N_2, O, O_2, H and He. Temperature-oriented nomenclature differentiates the strata of the atmosphere as follows: the troposphere, from sea level up to about 10 km, where the temperature decreases; the stratosphere, from 10 km up to about 45 km, where the temperature increases; the mesosphere, from 45 km up to about 95 km,

where the temperature decreases again; the thermosphere, from 95 km to about 400 km, where the temperature increases again; and the exosphere, above about 400 km, where the temperature is constant.

Some atmospheric reference models are available nowadays. In the present work, the Mass Spectrometer Incoherent Scatter Empirical (MSISE) model [**?**] is applied.

The MSIS empirical model [**?**] is based on data measured from seven satellites and numerous rocket probes. This model provides the estimates of temperature, and the densities of N_2, O, O_2, H, Ar and He. Low-order spherical harmonics are used to describe the major variations through out the atmosphere including latitude, annual, semiannual, and simplified local time and longitude variations.

Figure **??** [**?**] shows the atmospheric density distributions in function of the altitude for different atmospheric compositions. As seen in the figure, in addition to nitrogen and oxygen, although some other elements also exist in the atmosphere, they show very minor contribution in the particle collisions due to their thin composition. For example, at the altitude of 1 km, the density of the most abundant atmospheric element other than nitrogen and oxygen, argon, is about 10^{-6} g/cm^3. So, the mean length for a collision between a cosmic ray particle and the argon nucleus in the atmosphere can be estimated as

$$l \simeq \frac{\xi}{m\rho_m} \simeq \quad 600 \quad \text{km} \tag{7.10}$$

where ξ is the mean amount of matter traversed by the cosmic ray particles in the atmosphere, $\xi \simeq 60$ g/cm^2. At the altitude of 100 km, the density of other atmospheric compositions is comparable to that of nitrogen and oxygen. However, the atmospheric density is very small at this altitude and the mean length for a collision of a cosmic ray particle with the atmospheric nuclei turns out to be around 6×10^7 km. Thus the collision rate of cosmic ray particles with atmospheric nuclei other than nitrogen and oxygen is found to be inefficient so the collisions of cosmic ray particles with atmospheric nuclei except nitrogen and oxygen are negligible. Therefore, the treatment by taking nitrogen and oxygen as the only compositions of the atmosphere is good enough for the purpose of the present work.

By integrating the atmospheric density over the altitude, the residual atmosphere can be obtained. The result is shown in Figure **??**. The altitude in the unit of residual atmosphere is frequently used in most of related work. For reference, keep in mind that at the BESS altitude altitude 36.50 km, the residual atmosphere is $x = 5.0$ g/cm^2; at the CAPRICE altitude 36.05 km, $x = 5.5$ g/cm^2; at the AMS altitude 380 km, $x \simeq 10^{-8}$ g/cm^2; at the BESS 1999 altitude 2.770 km, $x = 742$ g/cm^2.

7.1.5 Cross Section of Antiproton with Atmospheric Nuclei

Once an antiproton is produced in the atmosphere, it might interact with the atmospheric nuclei during its propagation. An antiproton may undergo elastic scattering on atmospheric nuclei. The cross section for this process has been shown to be peaked in

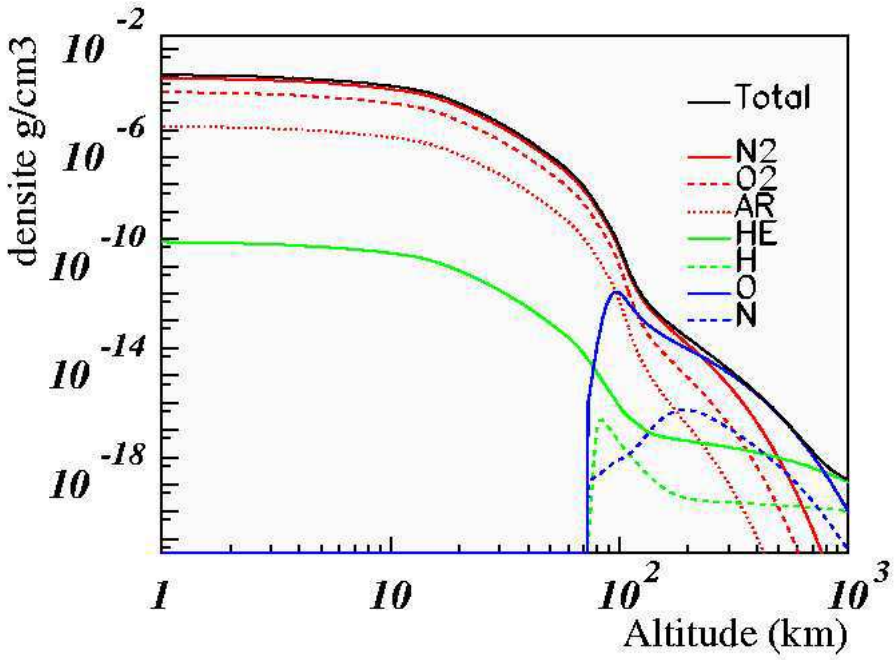

Figure 7.3: *The density distributions of the atmospheric compositions in function of the altitude [?]. The density of the sum of all compositions is also shown.*

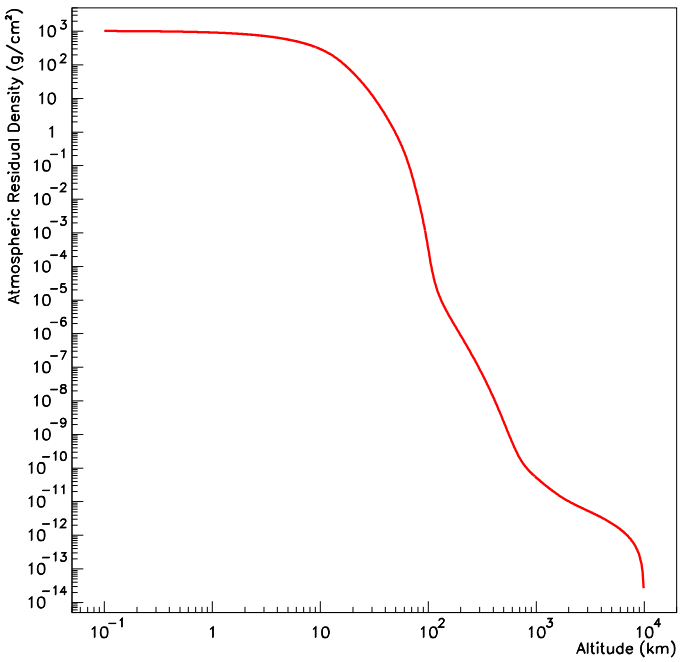

Figure 7.4: *The residual atmosphere in function of the altitude.*

the forward direction [?]. So, the corresponding $\bar{p}$ energy loss due to this process is neglected. The antiproton might also annihilate on the atmospheric nucleus in a collision, or survive from the inelastic scattering with the atmospheric nuclei. Both annihilation and non-annihilation interactions contribute to the $\bar{p}$ inelastic cross section

$$[\sigma_{\bar{p},A}]_{inel}^{total} \approx \sigma_{\bar{p},A}^{ann} + \sigma_{\bar{p},A}^{non} \tag{7.11}$$

The $\bar{p}$ annihilation cross section for the annihilation process $\bar{p} + A \to X$ is found to become small at the $\bar{p}$ incident kinetic energy $E_{\bar{p}} \geq 10$ GeV [?]. And, the $\bar{p}$ annihilation length in the atmosphere can be approximatedly described as [?]

$$\xi_{\bar{p},A}^{ann} \simeq \frac{70.5}{(E_{\bar{p}}/\mathrm{GeV})^{-0.47} - 0.0476} \quad (\mathrm{g/cm^2}) \tag{7.12}$$

At $E_{\bar{p}} = 1$ GeV, $\xi_{\bar{p},A}^{ann} \simeq 71$ g/cm^2 is comparable to the mean free path of cosmic ray particle in the atmosphere, $\xi_{CR,A} \simeq 60$ g/cm^2, while at $E_{\bar{p}} = 2$ GeV, $\xi_{\bar{p},A}^{ann}$ turns be twice of $\xi_{CR,A}$. Thus, $\sigma_{\bar{p},A}^{ann}$ would appear to be more important to the atmospheric secondary $\bar{p}$ flux at $E_{\bar{p}} \leq 1$ GeV. At higher energies, the total inelastic cross section for $\bar{p}+A$ collisions can then be approximately described by the $\bar{p}$ non-annihilation cross section.

The experimental data on the antiproton-nuclei annihilation cross sections [?, ?, ?] have shown that the inelastic cross section for $\bar{p}+A$ collision has an A dependence, being described by [?, ?, ?]

$$[\sigma_{\bar{p},A}]_{inel}^{total} = \sigma_0 A^{\alpha} \tag{7.13}$$

The values of σ_0 and α depend on the value of the total collision cross section for particle interactions with nucleons [?]. The behaviour of the parameters σ_0 and α indicates the possibility of Coulomb influence on the annihilation processes at low momenta [?]. Note that at high energies, the total cross section increases, and the index α approaches the black disc limit of $\frac{2}{3}$ [?, ?, ?, ?].

Figure ?? shows an example of the total inelastic cross section for $p + C$ and $\bar{p} + C$ collisions [?, ?, ?] in function of the kinetic energy of the incoming hadron. The curve for $p + C$ collision is obtained from the parametrised inelastic cross section in Eqs. (??) and (??). As to obtain the inelastic cross section for $\bar{p} + A$ collisions, one can apply the $A^{2/3}$ dependence from the available experimental data of $\bar{p}$-nucleus collisions [?, ?, ?].

The $\bar{p}$ non-annihilation process $\bar{p}+A \to \bar{p}'+A$ comes from the fact that the antiprotons which interact with atmospheric nuclei do not necessarily disappear in the annihilation. There is a probability that an antiproton can survive from such an interaction but with an energy lower than that of the incident antiproton and the target nucleus is excited to a resonance. Since the mean free path for the $\bar{p}$ non-annihilation cannot be directly measured on air targets, a scaling approach based on the $\bar{p}$ non-annihilation cross section in $\bar{p} + C$ collisions is suggested as

$$\sigma_{\bar{p},A}^{non}(E_{\bar{p}}) = \sigma_{\bar{p},C}^{non}(E_{\bar{p}}) \frac{[\sigma_{\bar{p},A}(E_{\bar{p}})]_{inel}^{total}}{[\sigma_{\bar{p},C}(E_{\bar{p}})]_{inel}^{total}} \tag{7.14}$$

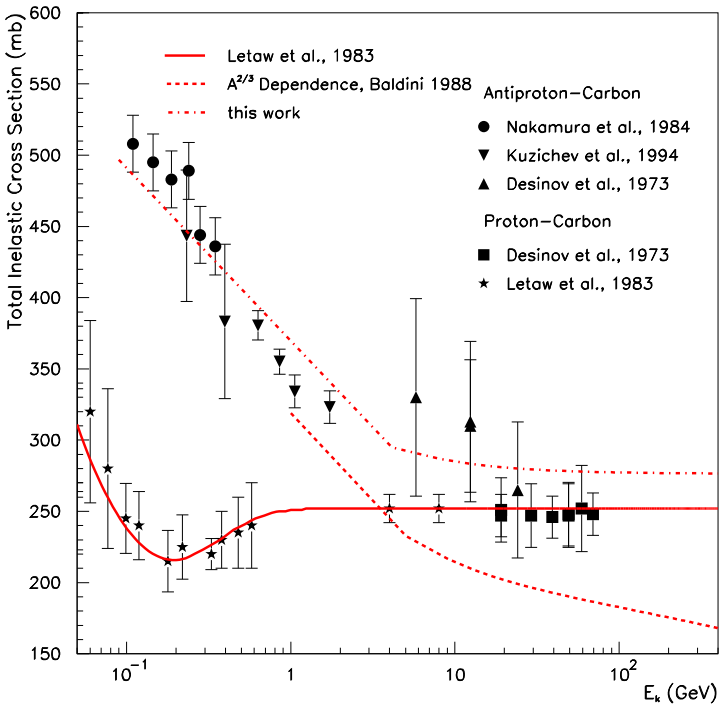

Figure 7.5: *The total inelastic cross section for $p + C$ [?, ?] and $\bar{p} + C$ [?, ?, ?] collisions as a function of the kinetic energy of the incoming hadron. The curve for $p + C$ collision is parametrised by Eqs. (??) and (??) [?]. The inelastic cross section in $\bar{p} + C$ collision is more complicated since the values of the parameter σ_0 is not a simple function of energy [?, ?]. See the text for the discussions on the curves of inelastic cross section in $\bar{p} + C$ collisions.*

where $\sigma^{non}_{\bar{p},C}(E_{\bar{p}})$ and $[\sigma_{\bar{p},C}(E_{\bar{p}})]^{total}_{inel}$ are available from the experiments of $\bar{p} + C$ collisions [?, ?, ?]. $[\sigma_{\bar{p},A}]^{total}_{inel}$ can be obtained by applying the $A^{2/3}$ dependence based on the experimental data of $\bar{p}$ -nucleus collisions [?, ?, ?]. Thus, the $\bar{p}$ annihilation cross section is then obtainable. Based on the experimental data, a parametrised $[\sigma_{\bar{p},A}]^{total}_{inel}$ obtained by best fitting is used for the present work

$$[\sigma_{\bar{p},A}(E_{\bar{p}})]^{total}_{inel} \approx 1000 \left(\frac{A}{46}\right)^{0.67} \cdot \left(0.68 + \frac{0.228}{p}\right) \quad \text{(mb)} \tag{7.15}$$

where p is the $\bar{p}$ incident momentum. The curve of $[\sigma_{\bar{p},C}(E_{\bar{p}})]^{total}_{inel}$ from expression (??) is shown in Figure ??.

However, the $A^{2/3}$ dependence might be too over simplified. In Figure ??, the curve of the inelastic cross section for $\bar{p} + C$ collisions by scaling $[\sigma_{\bar{p},p}]^{total}_{inel}$ to carbon target

according to the relation of $A^{2/3}$ dependence is shown for comparison. $[\sigma_{\bar{p},p}]^{total}_{inel}$ is taken as the parametrised form [?]

$$[\sigma_{\bar{p},p}(E_{\bar{p}})]^{total}_{inel} \approx 38 + 38p^{-0.96} - 0.169\log^2(p) \quad \text{(mb)} \tag{7.16}$$

It is seen that these two results differ with each other a lot. The divergence between this curve and the data should indicate that the coefficient σ_0 in Eq. (??) might be A dependent as well.

It has to be indicated that, in the present work, the $\bar{p}$ non-annihilation process as a process of $\bar{p}$ energy loss has not been included. However, the contribution to the $\bar{p}$ flux due to the non-annihilation effect is found to be small over the overall results [?, ?, ?], but one should keep in mind that, due to Eqs. (??) and (??), this effect would become a little bit more significant at low energy.

With all above background included, the simulation for the $\bar{p}$ production in the atmosphere is then obtainable: cosmic ray particles are generated and propagate under the solar modulation effect and the geomagnetic field. After reaching the Earth atmosphere, the cosmic particles could collide with the atmospheric nuclei along their propagation and produce secondary particles with the production cross sections and also the multiplicities developed in this work. Each secondary particle is then propagating and is allowed to collide other nuclei as the same as the step discussed previously. Each particle in its propagation undergoes an energy loss by ionisation and, each event propagates until the particle disappears while either it collides with a nucleus, or it is stopped in the atmosphere, or it escapes to outer space beyond twice of the production altitude [?]. Therefore, during the particle propagation, a reaction cascade can develop through the atmosphere. The interaction products are then counted, both upwards and downwards, when they cross the virtual sphere at the chosen detection altitude. The particles are counted each time when they cross the detection altitude. Hence, the trapped particles will contribute more statistically weightedly corresponding to their numbers of crossing. In the simulation process, some empirical cuts constrained to the kinematics of the initial particles can be performed as to significantly save the computer time by removing the inappropriate events. For example, unlike the spallation cross sections that determine the observed ratio of nuclei [?, ?], the cross section for the $\bar{p}$ production has a high threshold. So, an energy cutoff to the incident energy would first reject the irrelevant incident nucleons.

7.2 Remarks on Simulation Results

The calculation by this simulation has successfully explained the high p flux observed by AMS in its precursor flight in 1998 [?] below the geomagnetic cutoff to be secondaries originating from the cosmic rays interacting with the atmospheric nuclei [?]. The secondary atmospheric $\bar{p}$ flux reproduced at the balloon altitudes by this simulations have provided the correction to the galactic $\bar{p}$ flux at the Top of the Atmosphere (TOA) [?, ?] and the reproduced secondary atmospheric $\bar{p}$ flux at low altitude has provided a test proposition of the $\bar{p}$ calculation against the previous results [?]. In addition, the reproduced

secondary atmospheric leptons [?, ?, ?] have been reported to show a good agreement with the AMS measurements [?, ?] and the e^+ over e^- flux ratio below the geomagnetic cutoff was reported to result from the geomagnetic East-West effect combined with other effects [?]. It was also reported [?], using this simulation, the possible sources of light nuclei observed by the AMS below the geomagnetic cutoff [?] as the fragmentation of the incident cosmic ^4He on the atmospheric nuclei and also the nuclear coalescence from proton and ^4He induced reactions. The simulated flux of ^2H, ^3H and ^3He, ^4He were shown to be compatible with the AMS measurements [?].

In the next two chapters, the calculated secondary atmospheric $\bar{p}$ flux at different altitudes will be compared with the measurements. The results will be also analysed and discussed systematically.

Chapter 8

Flux of Secondary Atmospheric Antiprotons

Some balloon experiments such as IMAX [?, ?], MASS [?, ?], HEAT [?, ?], BESS [?, ?, ?, ?, ?, ?, ?] and CAPRICE [?, ?, ?], and the space experiment AMS [?] have collected some new data whose analyses have provided the determination of the cosmic $\bar{p}$ flux over an energy range extending from about 0.18 GeV to 49 GeV. In the balloon experiments, the values of the $\bar{p}$ flux at TOA was obtained by subtracting the atmospheric $\bar{p}$ component obtained from a calculation by Stephens [?] from the values of the measured total $\bar{p}$ flux.

In this chapter, the atmospheric $\bar{p}$ flux at both high balloon altitudes and the AMS satellite altitude are calculated. The $\bar{p}$ production at these altitudes are analysed and discussed. The $\bar{p}$ flux at TOA is modified by correcting for the calculated atmospheric $\bar{p}$ component. A potential experiment at a low terrestrial altitudes is raised to test the calculations of the atmospheric $\bar{p}$ production used for the $\bar{p}$ flux correction at TOA in different works and also the identification capability of the existing or future detectors. Comments are given at the end of this chapter.

8.1 Antiproton Flux at Balloon Altitudes

8.1.1 Analysis of Antiproton Production from Simulation

Table ?? shows the produced $\bar{p}$ population in function of the incident cosmic ray energies which generate the atmospheric $\bar{p}$ production at a balloon altitude 36.05 km, the CAPRICE measurement altitude, above which, the residual atmosphere is $x \simeq 5.5$ g/cm^2. The table gives the $\bar{p}$ population plotted in several energy ranges. It is seen that about 96% of all antiprotons below 6 GeV are produced by the incident nucleons with energies $E \leq 200$ GeV/n; incident nucleons with $E \leq 20$ GeV/n produce about 25% of all antiprotons with energies $E \leq 1$ GeV; incident nucleons with energies $E \leq 50$ GeV/n produce about 70% of all antiprotons with energies $E \leq 2$ GeV and about 90% of antiprotons with energies $E \leq 4$ GeV are produced by the incident nucleons with energies $E \leq 100$ GeV/n.

Hence, one can conclude that the incident energies up to $E \simeq 200$ GeV/n provide most of the secondary atmospheric $\bar{p}$ flux. According to the discussions in Chapter **??**, this has proven the evident applicability of the parametrised $\bar{p}$ production in nuclear collisions developed in this work for the interested purposes. Therefore, for the current work of interest, cosmic ray particles with energies from threshold up to 200 GeV/n are the most important.

Table 8.1: *The atmospheric fractional $\bar{p}$ production population in function of the incident cosmic ray nucleon kinetic energy, for the produced atmospheric antiprotons with energies up to 1, 2, 4 and 6 GeV. Unit of energy is in GeV.*

$E_{CR} \setminus E_{\bar{p}}$	0-1	0-2	0-4	0-6
8	0.2%	0.1%	0.03%	0.03%
10	1.9%	1.6%	0.85%	0.57%
15	11.8%	10.9%	7.03%	5.30%
20	23.9%	23.2%	17.7%	14.1%
50	73.3%	69.7%	65.7%	61.3%
100	88.9%	88.8%	87.5%	85.4%
200	96.7%	96.6%	96.2%	95.4%

Figure **??** shows some basic features of the simulated antiproton flux. The four histograms show respectively, (a) the rank distribution of the antiprotons, (b) the thickness of matter crossed by particles, (c) the altitude distribution of the $\bar{p}$ collision points, and (d) the altitude distribution of the $\bar{p}$ production points. It is seen in Figure **??** (a) that, about 90% antiprotons are produced at the first collision (rank = 1) but some antiprotons would originate from up to the 9th collision generation (rank = 9) in the atmospheric cascade for a given incident cosmic ray particle. The thickness of matter crossed by the particles distributes over a range extending up to about 550 g/cm^2, i.e., about 9 collision lengths. The altitude distribution of the $\bar{p}$ production has a maximum around 35 km, with a mean value about 45 km.

Figure **??** shows the two dimensional plot of the $\bar{p}$ rank versus the incident energy of cosmic ray particles which generate the $\bar{p}$ production. It is seen that, the atmospheric $\bar{p}$ component comes mostly from the generating cosmic ray particles with energies around 50 GeV/n. This fact comes from that, the cosmic ray particles with energies from the threshold of the $\bar{p}$ production up to this energy range have contributed more than 90% of population of cosmic ray particles. Cosmic ray particles of lower energy could also generate the production of antiprotons with large rank. It is seen that, cosmic ray particles with energies about 30 GeV/n could still generate the $\bar{p}$ production after 4 collisions.

Figure **??** shows an important feature of results with the scatter plot of the geomagnetic latitude of the $\bar{p}$ detection versus their number of crossing at the detection altitude of 36.05 km. It is seen that antiprotons have more crossings on the detection surface in

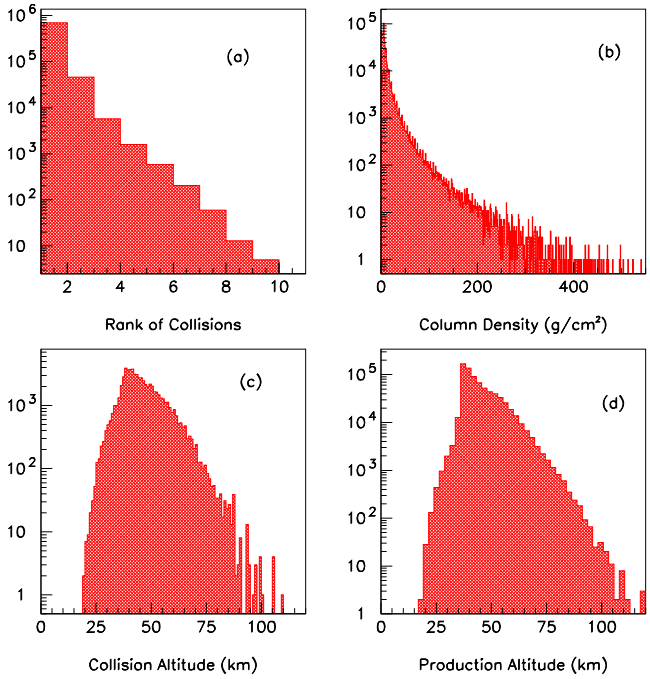

Figure 8.1: *Analysis of the $\bar{p}$ production at a balloon altitude $x = 5.5\ g/cm^2$: (a) The $\bar{p}$ rank distribution of collisions in the atmosphere, (b) the thickness of matter crossed, (c) the altitude distribution of the $\bar{p}$ collisions and (d) the altitude distribution of the $\bar{p}$ production.*

the equatorial region. However, it doesn't show any evident region of large crossing multiplicity, i.e., the region in which the antiprotons are trapped by the geomagnetic field. The reason for this will be discussed together with the same issue at the AMS altitude in Section **??**.

In the histogram of the $\bar{p}$ production altitude distribution in Figure **??** (d), it is found that, a great deal of antiprotons are produced below the detection altitude of 36.05 km. These antiprotons produced below the detection altitude are first investigated.

8.1.2 Production of Atmospheric Antiprotons below 36.05 km

In Figure **??**, the crossing number of the antiprotons produced below the detection surface is plotted (left). It is seen in the figure that some antiprotons could cross the detection surface up to 5 times, providing that they cross the surface upwards. However, why is there no upward $\bar{p}$ flux measurement reported at a balloon altitude? In this work, if an antiproton is produced below the detection altitude and if it crosses the detection

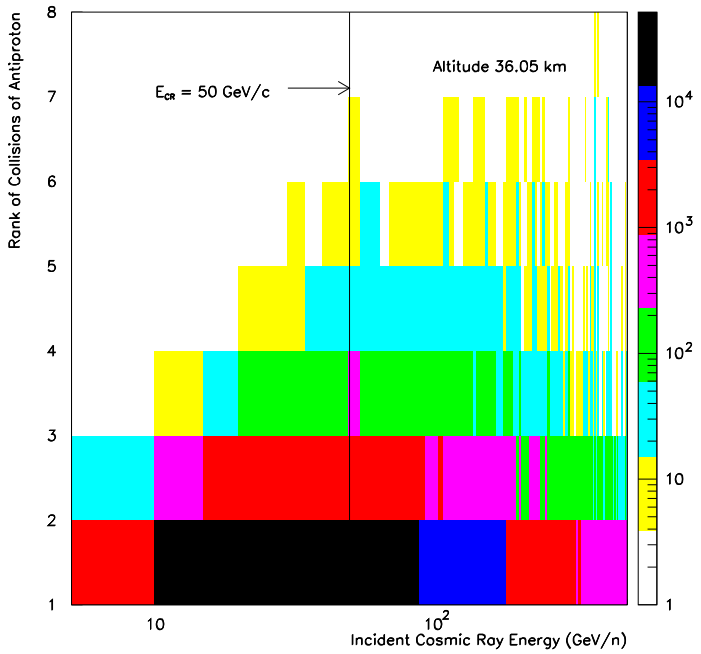

Figure 8.2: *Two dimensional plot of the $\bar{p}$ rank distribution versus the incident energy of the generating cosmic ray particles.*

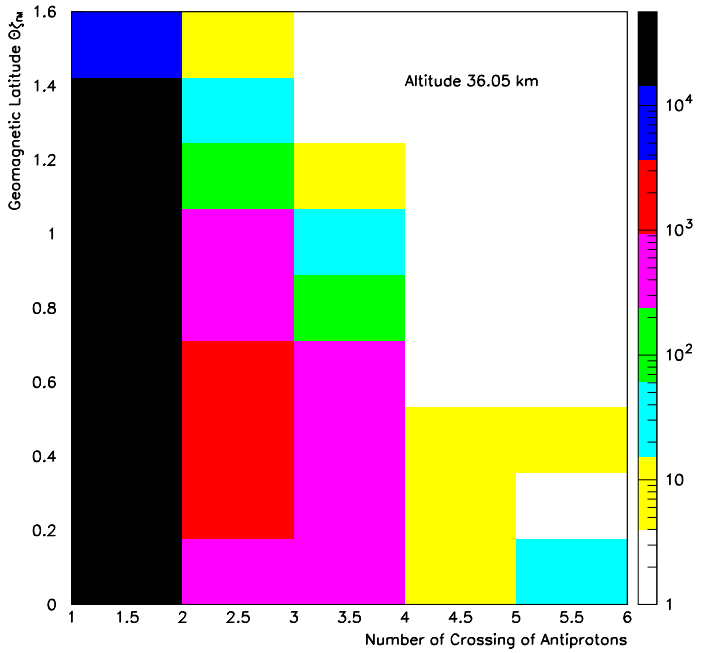

Figure 8.3: *Two dimensional plot of the distribution of the geomagnetic latitude versus the number of crossing of the antiprotons at the detection altitude of $x = 5.5\ g/cm^2$.*

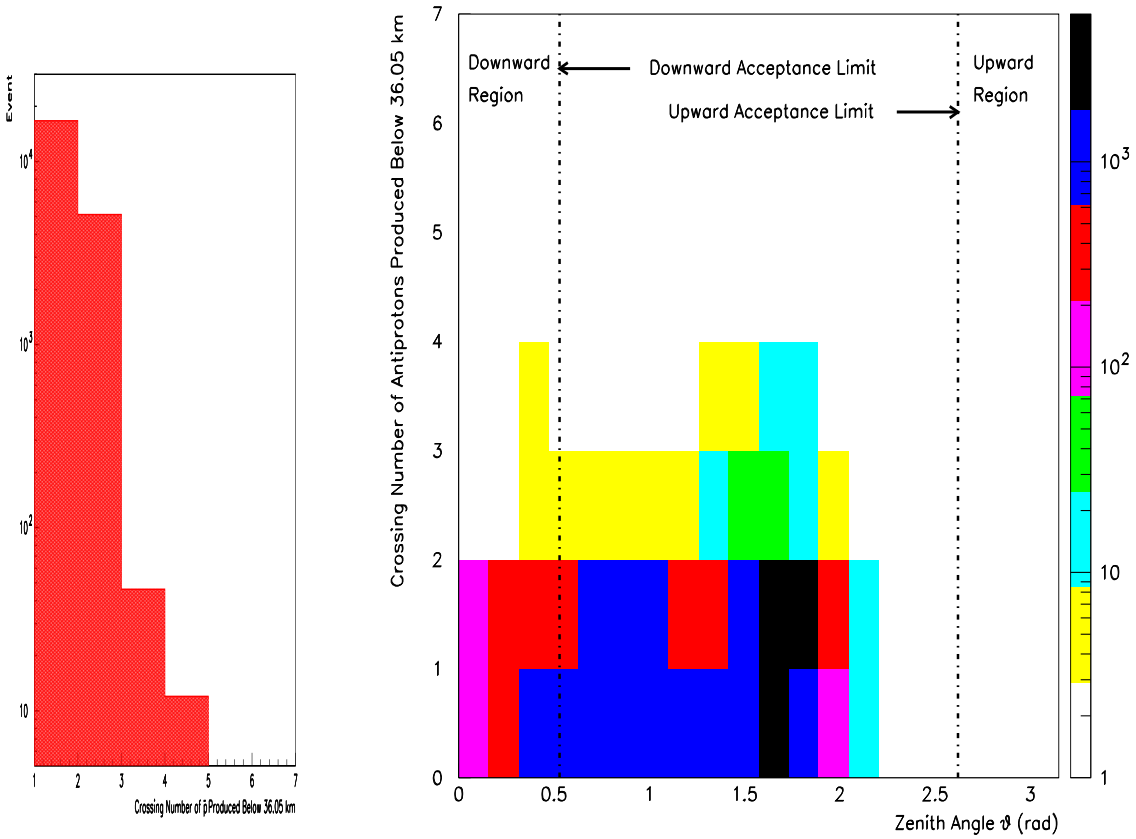

Figure 8.4: *Crossing number on the detection surface of the antiprotons produced below the detection altitude $x = 5.5\ g/cm^2$ (Left) and the two dimensional plot of the crossing number versus the zenith angle for these antiprotons (Right).*

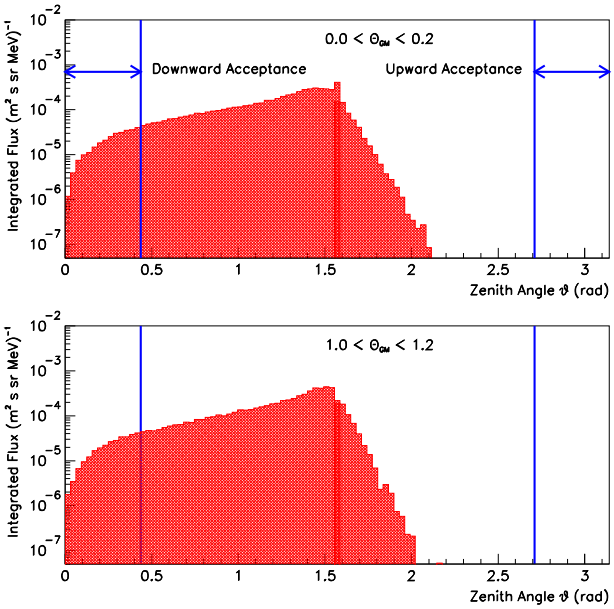

Figure 8.5: *The zenith angular distributions of the $\bar{p}$ flux at a balloon altitude 36.05 km ($x = 5.5\ g/cm^2$) for two different geomagnetic latitude regions: $0.0 < \theta_{GM} < 0.2$ and $1.0 < \theta_{GM} < 1.2$, over the full angular range. Antiprotons are crossing the detection surface from below with angles greater than about 65.5^0 ($\theta \geq 2$ rad).*

surface from below. If the crossing angle is smaller than the CAPRICE acceptance angle [?, ?, ?], the event is not validated. It is found that all particles crossing the detection surface from below correspond to angles outside the CAPRICE acceptance. The two dimensional plot of the crossing number of all antiprotons which are produced below the detection altitude versus their corresponding zenith angles in Figure ?? (right) has shown that, even though a great amount of antiprotons are produced below the detection altitude, all these antiprotons have crossed the detection surface outside the detector acceptance. Qualitatively, at a balloon altitude, the window for detecting the upward antiprotons is small. An upward $\bar{p}$ to be detected is most likely generated by a cosmic ray particle about tangent to the sphere of the altitude. So, such a $\bar{p}$ has to be produced at a greater scattering angle so as to fly into the acceptance angle. In Chapter ??, however, it has been shown that, the $\bar{p}$ production cross section at large scattering angles is very small. Figure ?? shows the two dimensional plot of crossing number on the detection surface versus the zenith angle for the antiprotons produced below the detection altitude $x = 5.5$ g/cm^2. It is seen in this figure that, in the upward region, i.e., zenith angle $\theta > \pi/2$, there is no event with $\theta > 2.2$ rad. So, the probability of detecting upward antiprotons at a high balloon altitude is quite small. Nevertheless, at high detection altitudes, for example, the AMS altitude of 380 km, the detection window for upward particles becomes larger and the antiprotons produced below the high detection altitudes have more chance to fly into the detector acceptance angle. This will be shown in next section.

Quantitatively, this phenomenon can be well understood by investigating the $\bar{p}$ zenith angle distribution. Figure ?? shows the $\bar{p}$ integrated flux in function of the zenith angle at an altitude of $x \simeq 5.5$ g/cm^2, in two different geomagnetic latitude regions: $0.0 < \theta_{GM} < 0.2$ and $1.0 < \theta_{GM} < 1.2$. The CAPRICE geometrical acceptance for upward and downward particles are also shown in the figure. By the definition, $\theta = 0^0$ corresponds to downwards, where θ is the angle with respect to the zenith direction. One can see that all antiprotons cross the detection surface from below with angles greater than about 60^0, which is larger than the acceptance angle considered here. Thus, the analysis of the $\bar{p}$ zenith angle distribution has provided the evidence that, at a balloon altitude, the upward $\bar{p}$ flux is unlikely to be detected with the currently available detectors [?]. The reason that no upward antiprotons have been detected is thus made more clear for the balloon experiments [?, ?, ?].

8.1.3 Atmospheric Antiproton Flux at Top of Atmosphere (TOA)

To determine the p and $\bar{p}$ flux at TOA from a balloon experiment, some factors have to be taken into account. Firstly, the loss and the production of particles due to the interaction in the material of the payload have to be considered. And, the production of secondary antiprotons and protons in the atmosphere have to be determined. So far, for the balloon experiments, the calculation by Papini, Grimani and Stephens [?] for the proton, and the calculation by Stephens [?] for the antiproton have been applied. Secondly, the transmission of the particles through the geomagnetic field has to be included so

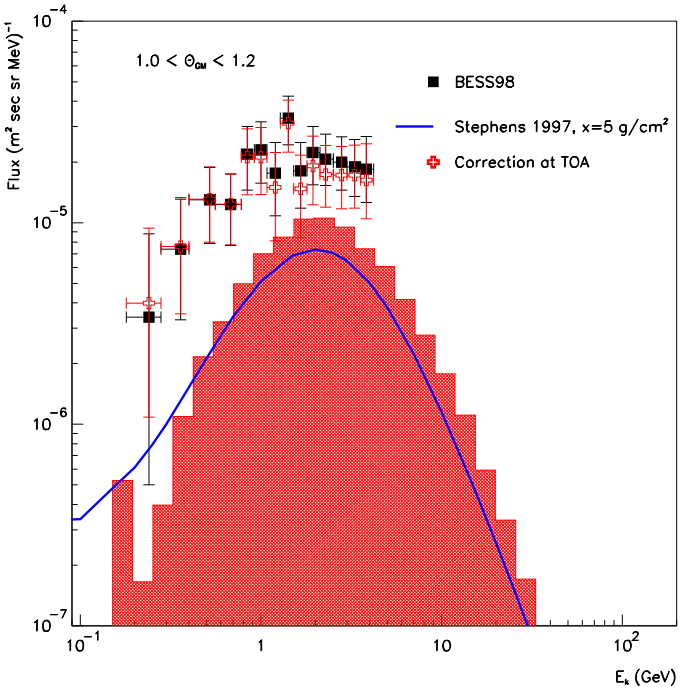

Figure 8.6: *Cosmic $\bar{p}$ distribution deduced in the BESS 1998 measurements [?], and the atmospheric $\bar{p}$ flux used to correct the raw flux measurements calculated in the original work (curve) [?] and in the current work (histogram). The cosmic $\bar{p}$ flux corrected by using the results calculated in the current work is shown as open crosses.*

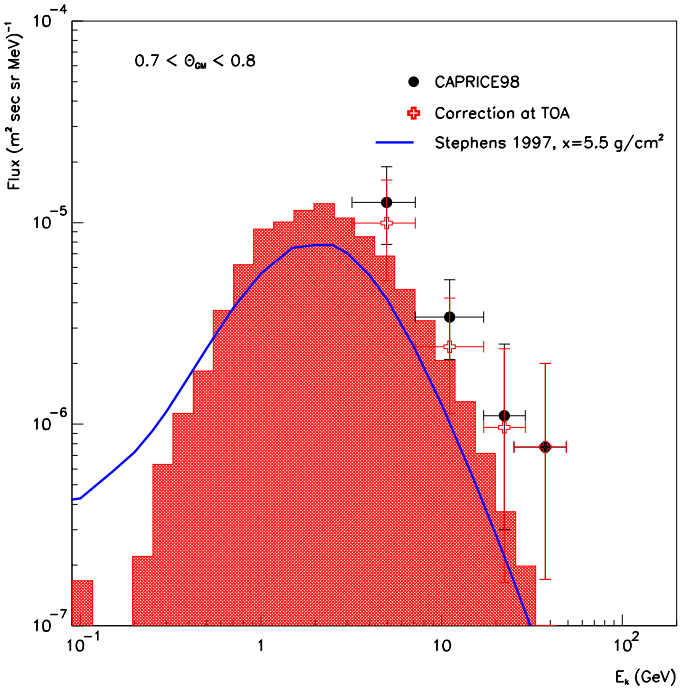

Figure 8.7: *Results for the CAPRICE 1998 measurements [?]. Same definitions are given as those given in Figure* **??**.

that the correction factor for the geomagnetic effect has to be determined [?]. With the correction terms included, the $\bar{p}$ flux at TOA have been reported [?, ?]. They are now shown on Figures ?? and ?? together with the simulated atmospheric $\bar{p}$ flux and the applied reference values for the $\bar{p}$ production correction by Stephens [?].

Figures ?? and ?? show respectively the data points obtained from the measurements for the cosmic $\bar{p}$ flux in BESS 1998 [?] and CAPRICE 1998 [?], in which, the contribution of the corrected atmospheric $\bar{p}$ flux is based on the calculation curves by Stephens [?]. The atmospheric $\bar{p}$ flux calculated from the present work are also shown (histograms). On both figures, the deduced cosmic $\bar{p}$ flux are obtained by adding back the original atmospheric $\bar{p}$ correction [?] and subtracting the new values evaluated in this work. It is seen that, the present work provides the atmospheric $\bar{p}$ flux on average about 20% higher than the reference values of Stephens for energies $E_k > 0.5$ GeV, while for energies $E_k < 0.5$ GeV, the calculated atmospheric $\bar{p}$ flux is lower than the original. Thus, the current work has corrected the $\bar{p}$ flux at TOA to become about 10-15% lower than the originally deduced, for kinetic energies above 1-2 GeV. However, at low energies, $E_k < 0.5$ GeV, the $\bar{p}$ flux at TOA is, conversely, modified upwards by a factor of about 10-15%. Nevertheless, it has to be noted that, the $\bar{p}$ flux at $E_k < 0.5$ GeV needs to be corrected by considering the non-annihilation effect which is not yet included in the present work.

Figure ?? shows the contribution fractions of the total atmospheric $\bar{p}$ flux due to cosmic protons and heliums respectively, in two geomagnetic latitude regions $1.0 < \theta_{GM} < 1.2$ and $0.7 < \theta_{GM} < 0.8$, according to the BESS 1998 [?] and the CAPRICE 1998 [?] measurements. It is seen that, the He-induced atmospheric $\bar{p}$ flux contributes about $25-30\%$ of the total atmospheric $\bar{p}$ flux in the medium energy range. The calculated contribution by this work due to the cosmic heliums then confirms the preliminary estimates reported earlier [?, ?], in which, the cosmic heliums were not included yet and a 15-20% more in the atmospheric $\bar{p}$ flux evaluated previously was proposed. Therefore, after including the cosmic heliums, an entire contribution fraction of about 25-30% from heliums is expected. Note that at high and low energies, the values are coupled with large uncertainties. These uncertainties come from the poor statistics of He-induced $\bar{p}$ production at these extreme energies. The fraction distributions for cosmic ray protons and heliums have well indicated this conclusion.

8.2 Antiproton Flux at Satellite Altitudes

8.2.1 Analysis of Antiproton Production from Simulation

In this section, the simulated atmospheric $\bar{p}$ production at the AMS altitude is investigated. As to understand the discussion about the atmospheric $\bar{p}$ production, it is good to take this section together with Section ?? for comparison.

Figure ?? shows the geomagnetic latitude of the $\bar{p}$ detection versus their number of crossings of the AMS altitude 380 km. Unlike the antiprotons detected at a high balloon altitude shown in Figure ??, this figure shows that the events with large crossing multiplicities are strongly correlated with low latitudes, showing that a population of trapped

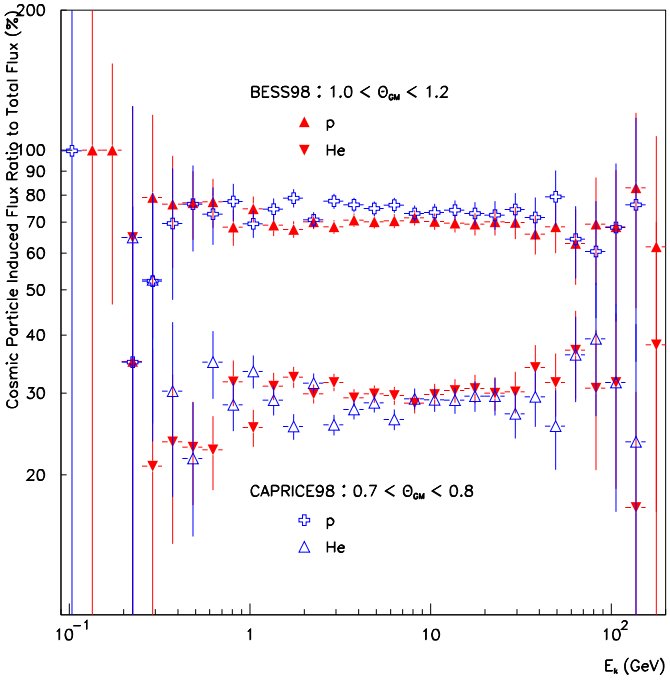

Figure 8.8: *The contribution fraction to the total atmospheric $\bar{p}$ flux for cosmic protons and heliums, calculated at the altitudes of the BESS 1998 [?] and the CAPRICE 1998 [?] measurements.*

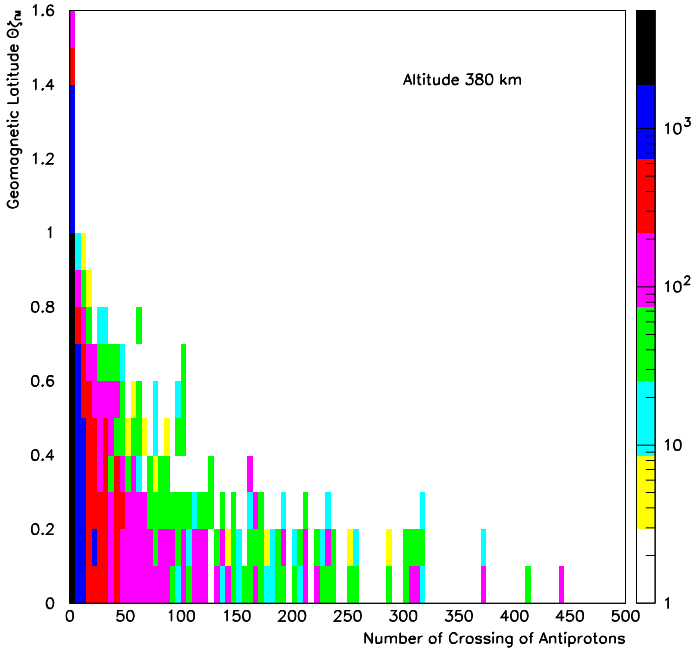

Figure 8.9: *Two dimensional plot of the distribution of the geomagnetic latitude versus the number of crossing of the antiprotons at the AMS detection altitude 380 km.*

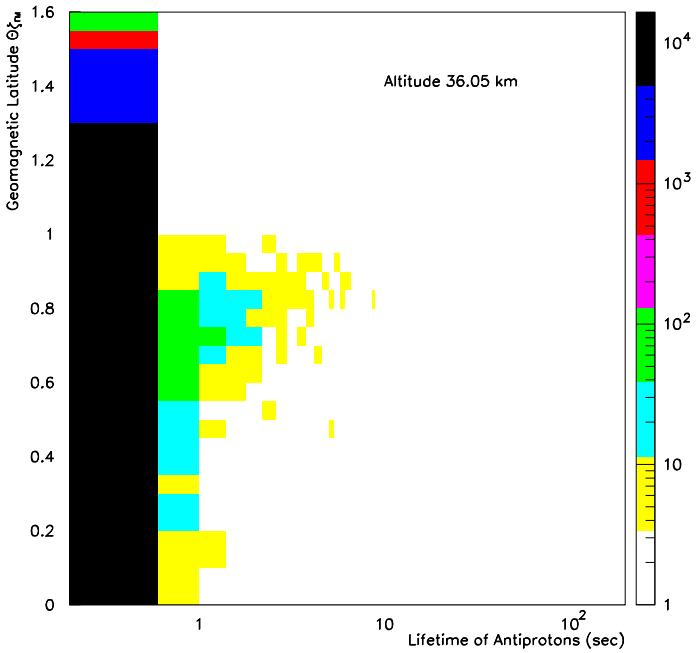

Figure 8.10: *Two dimensional plot of the geomagentic latitude versus the lifetime of the produced antiprotons for the balloon detection altitude 36.05 km.*

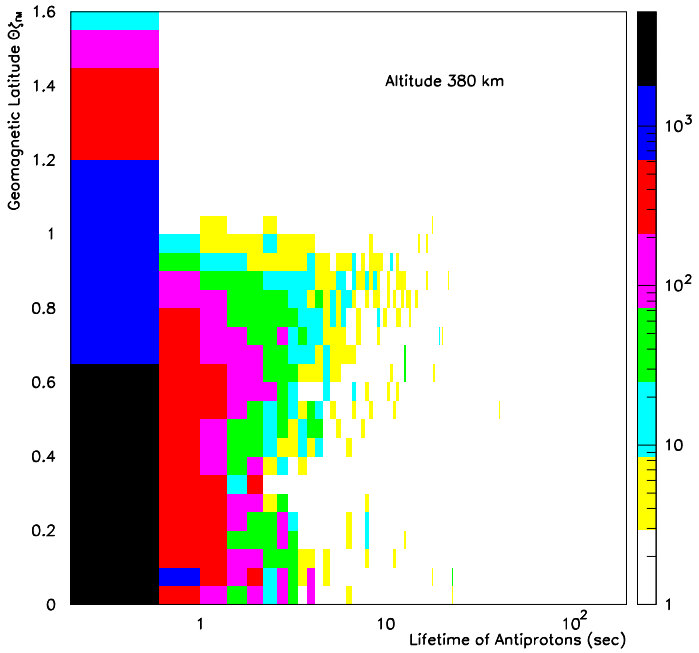

Figure 8.11: *Two dimensional plot of the geomagentic latitude versus the lifetime of the produced antiprotons for the AMS detection altitude 380 km.*

particles confined in the geomagnetic latitude region $\theta_{GM} \simeq \pm 0.3$, which is expected to be the most experimentally observable. In order to understand this difference between these two altitudes, the lifetimes of the produced antiprotons are plotted. Figures ?? and ?? show the two dimensional plots of the geomagnetic latitude versus the $\bar{p}$ lifetime for the altitudes 36.05 and 380 km respectively. It is seen that, a population of longlived antiprotons, with lifetimes up to 10 sec at the altitude of 36.05 km and about 50 sec at 380 km, is found in the polar and the subpolar regions. At the balloon altitude 36.05 km, the antiprotons populated in the equatorial region are quite shortlived. However, at the AMS altitude 380 km, a population of longlived antiprotons can be seen in the equatorial region, some of which have the lifetime up to dozens of seconds. These longlived antiprotons in the equatorial region could have long flight path and could undergo large crossings on the virtual detection sphere at the altitude. Nevertheless, for the longlived antiprotons in the polar and subpolar regions, most of them are found to have only one or two crossings during their flight paths.

Figure ?? shows the $\bar{p}$ integrated flux in function of the zenith angle at the AMS altitude in two different geomagnetic latitude regions: $0.0 < \theta_{GM} < 0.2$ and $0.8 < \theta_{GM} < 0.9$. The AMS acceptance is shown in both downward and upward regions. Figure ?? shows the two dimensional plot of the geomagnetic latitude versus the $\bar{p}$ zenith angle. Conversely with lower altitude in Figure ??, the $\bar{p}$ integrated zenith angular flux shows that upward antiprotons should be detected at this altitude. According to Figures ?? and ??, an important feature has to be emphasised. At the AMS altitude, the expected downward atmospheric $\bar{p}$ flux is found comparable to the upward $\bar{p}$ flux in the equatorial region. This comes from the fact that, in the equatorial region, a high population of particles are trapped and confined. Such a result was also observed in the p flux below the geomagnetic cutoff in the AMS 1998 measurements [?, ?]. Furthermore, even in a high geomagnetic latitude region, the downward $\bar{p}$ flux is still higher than the upward $\bar{p}$ flux. This is an effect of the constraint of the zenith angular effect. In evaluating the particle flux, the acceptance angle of the detector has to be considered. For example, for AMS, the acceptance angle for the antiproton is about 30^0 with respect to zenith [?, ?] which is indicated in Figure ??. But, it is seen in Figure ?? that, the mean angle for the upward $\bar{p}$ trajectories in the geomagnetic latitude region $0.8 < \theta_{GM} < 0.9$ is about 1.9 rad. In Figure ??, it is seen that, in the near equatorial region, both downward and upward $\bar{p}$ flux are comparable while in subpolar region, the upward $\bar{p}$ flux would naturally be expected to be larger than the downward $\bar{p}$ flux. However, the mean zenith angle for the upward antiprotons in this region also becomes much larger than the maximal angle of detector acceptance, thus resulting in the downward $\bar{p}$ flux to be larger than the upward $\bar{p}$ flux. So, from Figures ?? and ??, the reason that the downward $\bar{p}$ flux is still more detectable than the upward $\bar{p}$ flux at the AMS altitude is made clear as to result from the constraint of the acceptance angle of the current available spectrometer.

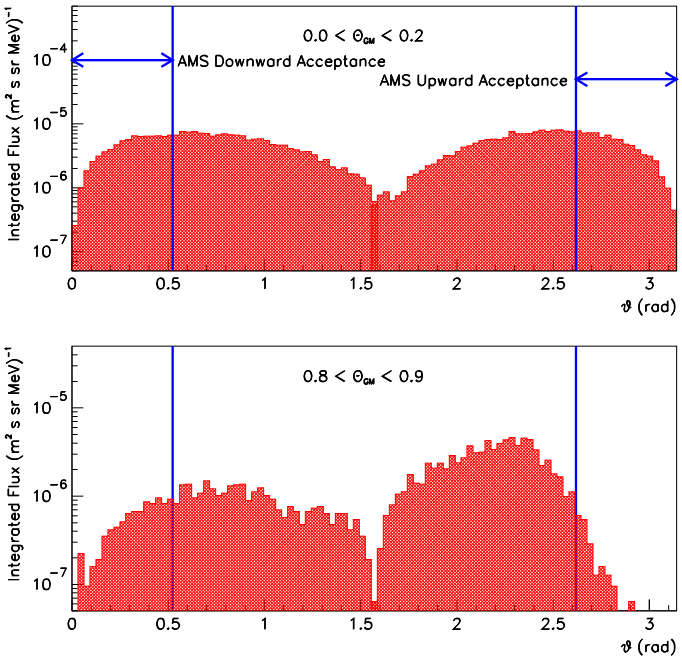

Figure 8.12: *The zenith angular distributions of the $\bar{p}$ flux at the AMS altitude 380 km in two different geomagnetic latitude regions: $0.0 < \theta_{GM} < 0.2$ and $0.8 < \theta_{GM} < 0.9$. The definitions for upward and downward particles are the same as in Figure* **??**. *The AMS acceptance angle is also shown.*

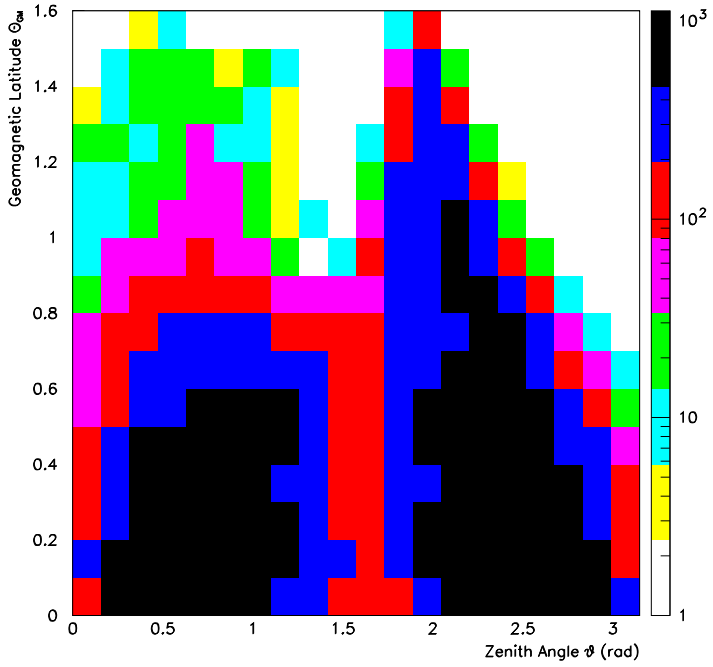

Figure 8.13: *Two dimensional plot of the geomagnetic latitude versus the zenith angle of antiprotons produced in the whole atmosphere at the AMS altitude 380 km.*

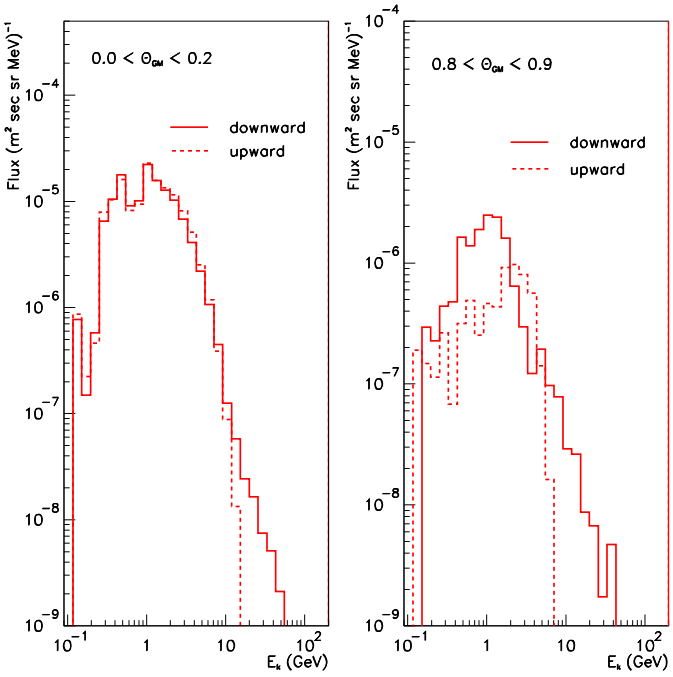

Figure 8.14: *Expected atmospheric $\bar{p}$ flux calculated in the present work at the AMS altitude 380 km in two geomagnetic latitude regions: $0.0 < \theta_{GM} < 0.2$ and $0.8 < \theta_{GM} < 0.9$. for the downward $\bar{p}$ flux (solid line) and the upward $\bar{p}$ flux (dashed line).*

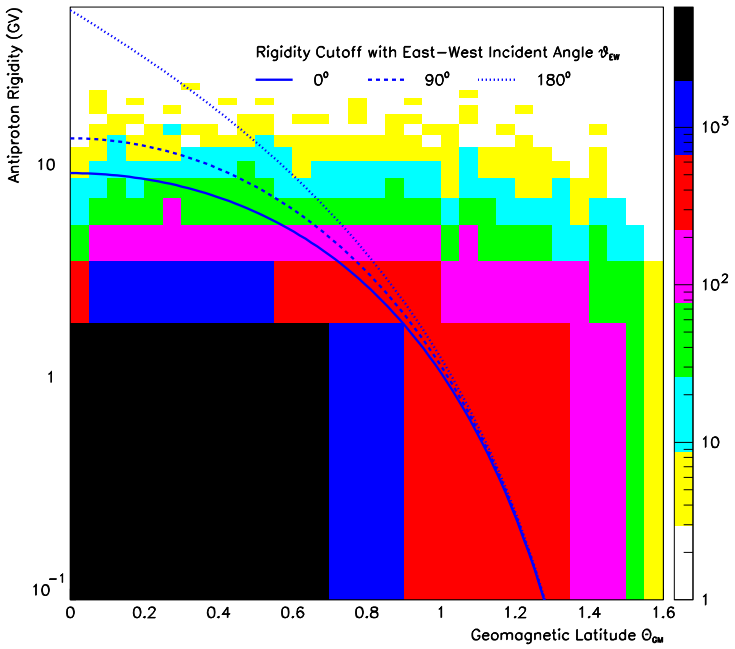

Figure 8.15: *Two dimensional plot of the $\bar{p}$ rigidity versus the geomagnetic latitude together with the rigidity cutoff for several incident angles at the altitude 380 km. The East-West angle $\theta_{EW} = 0$ for particles coming from the east.*

8.2.2 Antiproton Flux at the AMS Altitude

Figure ?? shows the expected atmospheric $\bar{p}$ flux at the AMS altitude in two different regions of geomagnetic latitude, equatorial ($0.0 < \theta_{GM} < 0.2$) and subpolar ($0.8 < \theta_{GM} < 0.9$), for both downward and upward antiprotons. It is clearly seen that, unexpectedly, the predicted atmospheric $\bar{p}$ flux at this altitude is still of the same order of magnitude as the cosmic $\bar{p}$ flux obtained in Figures ?? and ??. This phenomenon comes from the prediction that, as shown in Figure ??, at this altitude, a great deal of particles are trapped by the geomagnetic field in the region close to the equator, resulting in the atmospheric antiprotons re-enter many times the detection surface as protons do [?]. This result has shown that, the future satellite measurements of the $\bar{p}$ flux, such as AMS, PAMELA, etc., should therefore have to be corrected from the atmospheric contribution and could suffer from more uncertainties [?, ?]. So, an appropriate procedure as to extract the cosmic $\bar{p}$ component from the measurements should consist of simultaneously and consistently processing both satellite and balloon altitude data in order to consider constraint as much as possible the calculations, using the same approach as in this work [?, ?]. Otherwise, in order to reduce the atmospheric $\bar{p}$ component at this altitude, the measurements could be underwent in a region close to the geomagnetic pole, where the atmospheric downward $\bar{p}$ contribution entering the spectrometer turns to be relatively small.

As to improve the evaluation of the cosmic $\bar{p}$ flux from the correction of atmospheric $\bar{p}$ component, the rigidity cutoff upon the antiprotons detected at the detection altitude can be taken into account. Figure ?? shows the two dimensional plot of the $\bar{p}$ rigidity versus the geomagnetic latitude at the AMS altitude 380 km. The rigidity cutoff in function of the geomagnetic latitude is also shown in the same figure with some incident angles of 0^0, 90^0 and 180^0. Each curve would provide some important information: cosmic ray particles with rigidities below the cutoff have no chance to penetrate through the geomagnetic field into the lower atmosphere; particles with rigidities below the cutoff cannot escape from the geomagnetic field either, i.e., such particles will be trapped by the geomagnetic field. Given a detected particle, whether it is above or below the rigidity cutoff can be immediately determined by its kinematics and the experiment constraint: the rigidity can be known from the measured momentum; with the measured momentum and the position of the detection, the East-West angle of the particle can be calculated; the geomagnetic latitude is determined by the position of the detection. With such kinetic and experimental information, it is possible to determine if the detected particle at the given altitude is above or below the rigidity cutoff. Those particles which are bounded (trapped) are secondaries of atmospheric origin. Thus, all those particles which are bounded by the geomagnetic field can in principle be removed for the atmospheric production correction. As shown in Figure ??, by the rigidity cutoff upon the antiprotons will first filter a great deal amount of atmospheric secondary antiprotons with rigidities below 10 GV in the geomagnetic latitude region $\Theta_{GM} < 0.7$. It is seen that, in high geomagnetic latitude region, a significant amount of antiprotons could escape from the geomagnetic field, even though their rigidities are quite low. However, in the subpolar and polar geomagnetic region, the atmospheric secondary $\bar{p}$ component will turn to be small compared with the

cosmic $\bar{p}$ flux.

On the other hand, as to distinguish cosmic and atmospheric secondary particle spectra experimentally, a trajectory tracing programme [?] can be used to trace particle trajectories backwards and forwards through the geomagnetic field using their measured momenta. Particles are defined as cosmic rays if they are traced backwards to reach a radial distance greater than $10R_E$; particles are defined as atmospheric secondaries if they are traced backwards to reach TOA, defined at an altitude of about 40 km. The time scale between the source and sink is defined as the lifetime of a particle, for which, the source is defined as the position where particles generate the secondary particle production at TOA while the sink is defined as the position where particles re-enter the atmosphere at TOA. By this way, two distinct components are observed: short lifetime ($<$ 200 ms) particles are detected over all the geomagnetic latitudes and long lifetime ($>$ 200 ms) particles are detected essentially at $|\theta_{GM}| < 0.3$. This result is consistent with Figure ?? in which, it is seen that the antiprotons trapped in the geomagnetic field with large crossing multiplicities strongly correlate to the geomagnetic latitude region $\theta_{GM} \simeq \pm 0.3$.

Figure ?? shows the $\bar{p}$ measurements in the AMS 1998 flight [?]. Note the region of geomagnetic latitude for the data points is the polar region $1.0 < \theta_{GM} < 1.2$. In this region, the atmospheric $\bar{p}$ component is found to be negligible from the $\bar{p}$ measurement at the AMS altitude. In this figure, the $\bar{p}$ flux at TOA in measurements of BESS 1998 [?] and CAPRICE 1998 [?] corrected by the atmospheric $\bar{p}$ component calculated in this work are also given. The corrected $\bar{p}$ flux at TOA agrees with the AMS measurements within the measurement uncertainty. Therefore, with the data compared in this figure, the $\bar{p}$ flux measured by AMS in polar geomagnetic region is a good approximation ($\sim 1\%$) to the exact cosmic $\bar{p}$ flux as for protons [?, ?].

8.3 Antiproton Flux at Ground Level

The idea to consider the $\bar{p}$ flux at ground level is to investigate the confidence level of the atmospheric $\bar{p}$ flux calculated in this work since at very low altitudes, all the antiprotons are supposed to be secondarily produced. If the $\bar{p}$ flux at these low altitudes are measurable, it is then possible to observe the trustworthiness of different calculations of the atmospheric $\bar{p}$ production used for the correction.

Figures ?? and ?? show respectively the expected atmospheric $\bar{p}$ flux calculated by the same simulation programme in this work in wide geomagnetic latitude regions from equatorial to subpolar: $0.0 < \theta_{GM} < 0.2$ and $0.7 < \theta_{GM} < 0.8$ at ground level and $0.2 < \theta_{GM} < 0.3$ and $1.0 < \theta_{GM} < 1.2$ at an altitude of 4 km. It can be found that at ground level, the $\bar{p}$ flux is about $0.78 \times 10^{-2} s^{-1} m^{-2} sr^{-1}$ but at the altitude of 4 km, this value would raise to $18.6 \times 10^{-2} s^{-1} m^{-2} sr^{-1}$. These values are small but still large enough to be measured by current existing large acceptance detectors like BESS and CAPRICE or by the future detector AMS. Therefore, an experiment at a low altitude can be proposed to distinguish the reliability of the atmospheric $\bar{p}$ production for the correction between the calculations by Stephens [?] and by this work. This idea was first raised in [?, ?] and

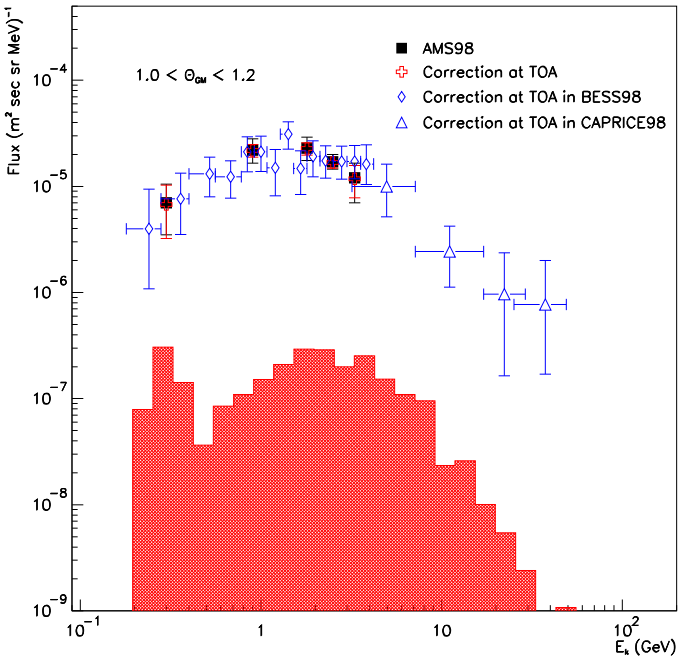

Figure 8.16: *The downward $\bar{p}$ flux measurement by AMS 1998 [?], together with the simulated atmospheric $\bar{p}$ flux histogram at the AMS altitude and the corrected cosmic $\bar{p}$ flux performed in this work. The corrected $\bar{p}$ flux at TOA from the measurements in BESS 1998 [?] and CAPRICE 1998 [?] are also given.*

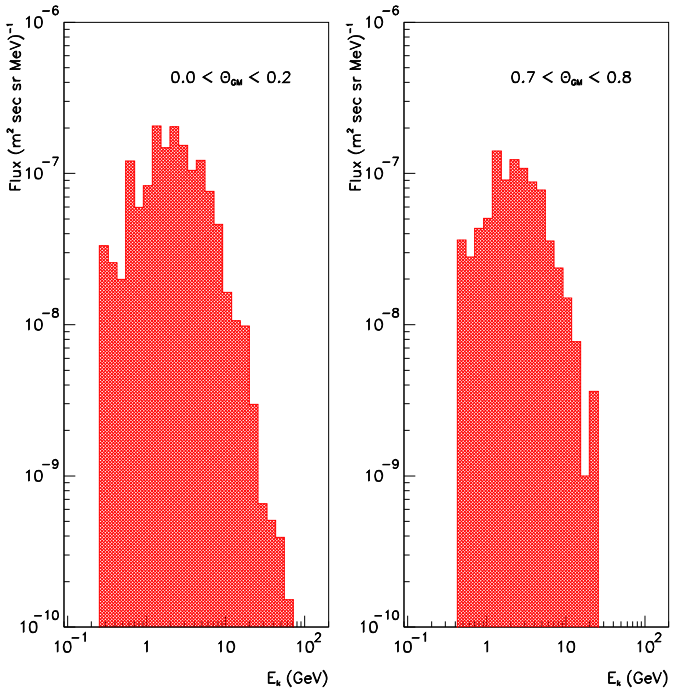

Figure 8.17: *Expected atmospheric $\bar{p}$ flux at sea level for two geomagnetic latitude regions:* $0.0 < \theta_{GM} < 0.2$ *and* $0.7 < \theta_{GM} < 0.8$.

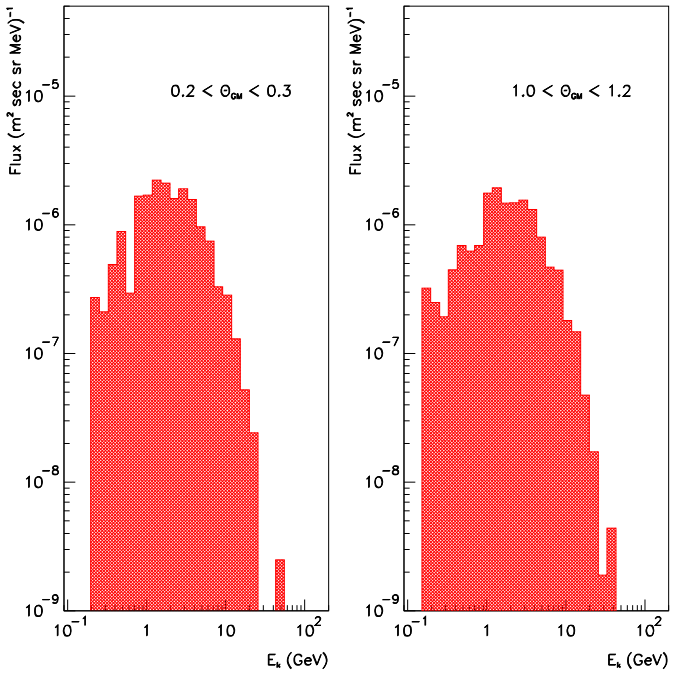

Figure 8.18: *Expected atmospheric $\bar{p}$ flux at the altitude 4 km for two geomagnetic latitude regions:* $0.2 < \theta_{GM} < 0.3$ *and* $1.0 < \theta_{GM} < 1.2$.

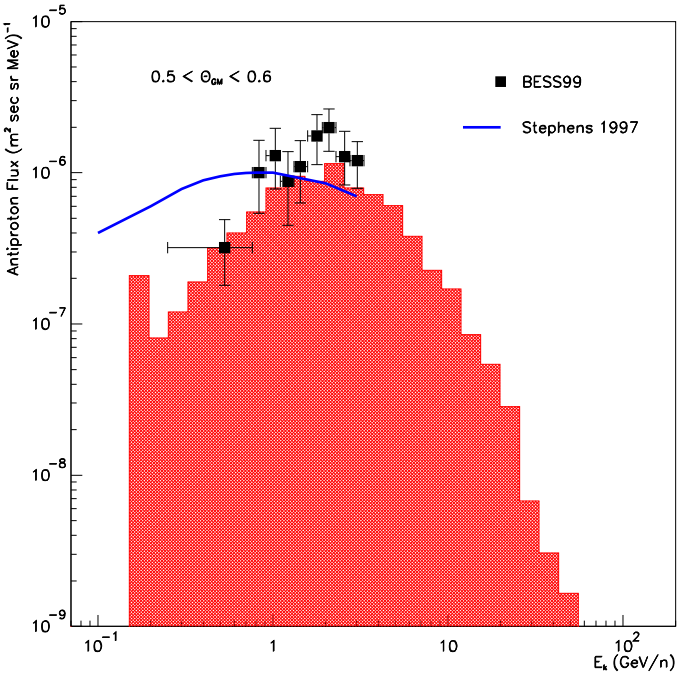

Figure 8.19: *The $\bar{p}$ flux measured in the BESS 1999 experiment [?] at the altitude 2770 m in the geomagnetic latitude region* $0.5 < \theta_{GM} < 0.6$, *together with the expected $\bar{p}$ flux calculated by Stephens [?] and by the current work.*

was soon supported by the results in the BESS 1999 measurements [?] performed at an altitude of 2770 m.

Figure ?? shows the $\bar{p}$ data measured in BESS 1999 at 2770 m [?], together with the calculations by Stephens [?] and by this work. Disagreement between the measurement data and the calculation of Stephens is clearly seen. However, the calculation by the present work has shown a good agreement with the measurements with uncertainties lying within the error bars. This result has then shown the consistency between the measurements and the present calculations, at least in the energy range in which the measurements were performed. In addition, it has also provided the evidence of more confident applicability of the present work than the original calculations previously applied.

8.4 Comments on Secondary Atmospheric Antiprotons

In summary, the secondary $\bar{p}$ flux produced by cosmic protons and heliums on the atmospheric nuclei have been calculated, and are found significantly larger than the evaluation in previous works. With the correction, the $\bar{p}$ flux at TOA is then modified downwards. The expected $\bar{p}$ flux at the satellite altitude for the future AMS experiment at the International Space Station (ISS) appears to be of the same order of the magnitude at high balloon altitudes, indicating that it should be taken into account in the future measurements of the cosmic $\bar{p}$ flux at this satellite altitude. The $\bar{p}$ at terrestrial altitudes expected from the calculations in our works are found to be small but measurable and could thus provide good grounds of testing both the calculations of the atmospheric $\bar{p}$ component in different works and the identification capability of the existing or future devices. The low altitude measurements of BESS 1999 have supported this conclusion.

It must be pointed out that, although the $\bar{p}$ production cross section is rather accurately known for the $\bar{p}$ energy above about 1 GeV, over the incident energy range discussed in Chapter ??, it is less well known for low energy $\bar{p}$ production, say, below about 0.5 GeV. The values calculated for the $\bar{p}$ flux should then be taken with care for low energy antiprotons. The forthcoming experimental programmes HARP at CERN PS [?, ?] and MIPP at Fermilab [?], aiming at systematic measurements of cross section of astrophysical interest should fulfill this requirement in the near future.

Chapter 9

Trajectories of Secondary Atmospheric Antiprotons at Very High Altitudes Above the Earth

In this chapter, the atmospheric $\bar{p}$ flux at very high altitudes are investigated. It is found that there are always some residual atmospheric antiprotons, both outward and inward, even at a very high altitude. The discussion of these antiprotons by investigating their final states is given. The trajectories of some types of characteristic atmospheric antiprotons are discussed pictorially.

9.1 Antiproton Flux at Very High Altitudes

The motivation to look at the atmospheric $\bar{p}$ flux at very high altitudes is based on the considerations as follows. In Chapter **??**, it has been shown that, even at the AMS satellite altitude, the expected atmospheric $\bar{p}$ flux still cannot be neglected, indicating that the $\bar{p}$ flux measurements at this altitude would suffer from more uncertainties and have to be taken into account the correction of the atmospheric $\bar{p}$ component all the time. Thus, it might be an interesting question to ask at which altitude, the expected atmospheric $\bar{p}$ flux vanishes so that the $\bar{p}$ flux measured at this altitude will become the exact cosmic $\bar{p}$ flux. This idea is immediately proven not very practical after evaluating the atmospheric $\bar{p}$ flux up to very high altitudes, since it can be seen that there are still some residual atmospheric secondary antiprotons at very high altitudes.

Figures **??**, **??**, **??** and **??** show respectively the integrated atmospheric $\bar{p}$ flux in function of the zenith angle in two different geomagnetic latitudes $0.0 < \theta_{GM} < 0.2$ and $0.7 < \theta_{GM} < 0.8$, at altitudes from 600 km up to 2800 km. Note that the values of $\bar{p}$ flux at different altitudes are multiplied by a power of 10 for comparison. The flux are evaluated by the same method discussed in Chapters **??** and **??**.

It is clearly seen in these figures that, above the AMS altitude, at least up to 2800 km, there are still some residual atmospheric antiprotons with the flux magnitude of about

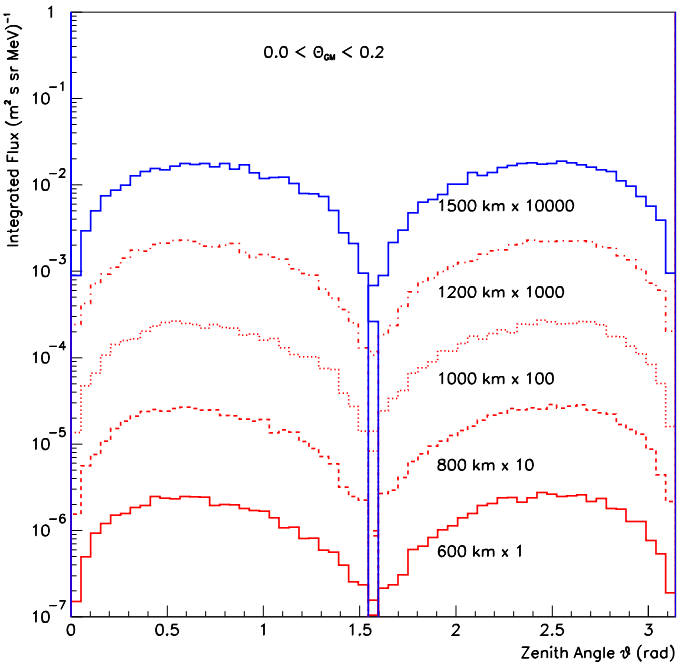

Figure 9.1: *The zenith angular distributions of the atmospheric $\bar{p}$ flux in the geomagnetic latitude region $0.0 < \theta_{GM} < 0.2$ at the altitudes of 600, 800, 1000, 1200 and 1500 km. The values are multiplied by a power of 10, i.e., 10 for 800 km, 100 for 1000 km etc as indicated on the figure. The definitions of upward and downward particles are the same as in Chapter* **??**.

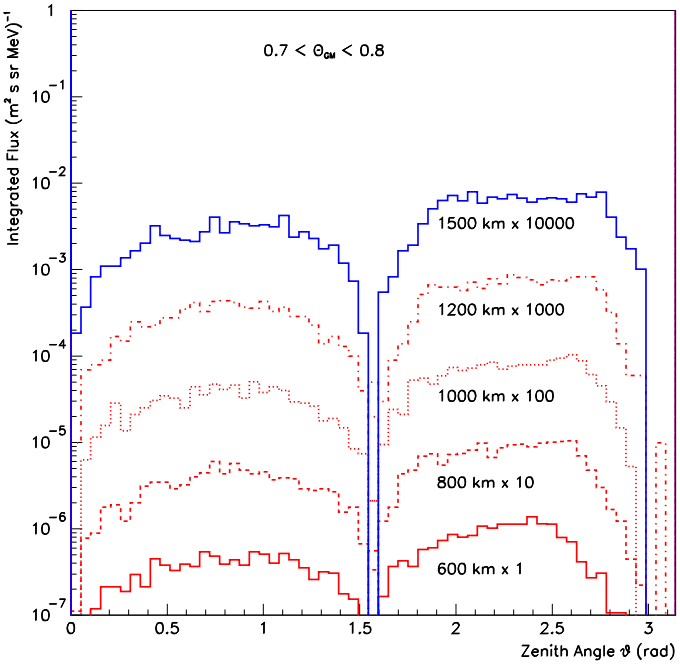

Figure 9.2: *The zenith angular distributions of the atmospheric $\bar{p}$ flux in the geomagnetic latitude region $0.7 < \theta_{GM} < 0.8$ at the same altitudes as in Figure* **??**. *The multiplication factors on flux and the definitions of upward and downward particles are also the same.*

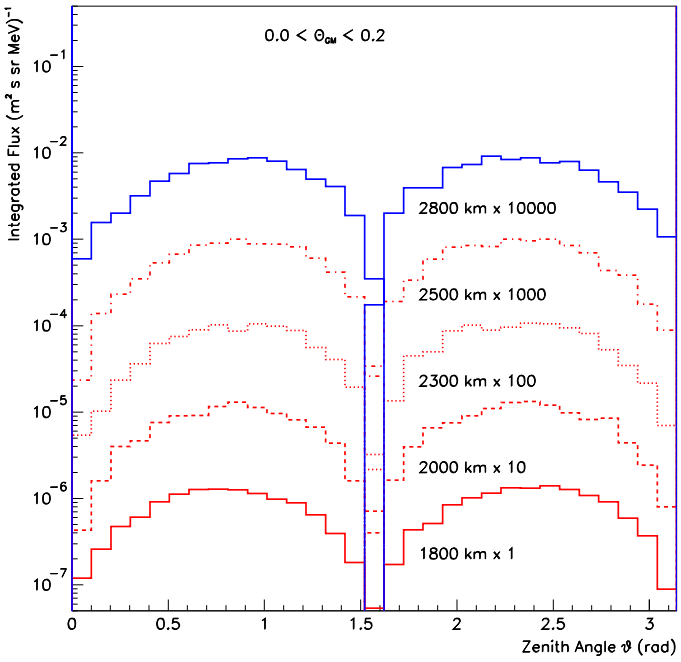

Figure 9.3: *The zenith angular distributions of the atmospheric $\bar{p}$ flux in the geomagnetic latitude region $0.0 < \theta_{GM} < 0.2$ at the altitudes of 1800, 2000, 2300, 2500 and 2800 km. The values are multiplied by a power of 10, i.e., 10 for 1800 km, 100 for 2000 km etc. The other definitions and the configuration in the figure are the same as in Figure* **??**.

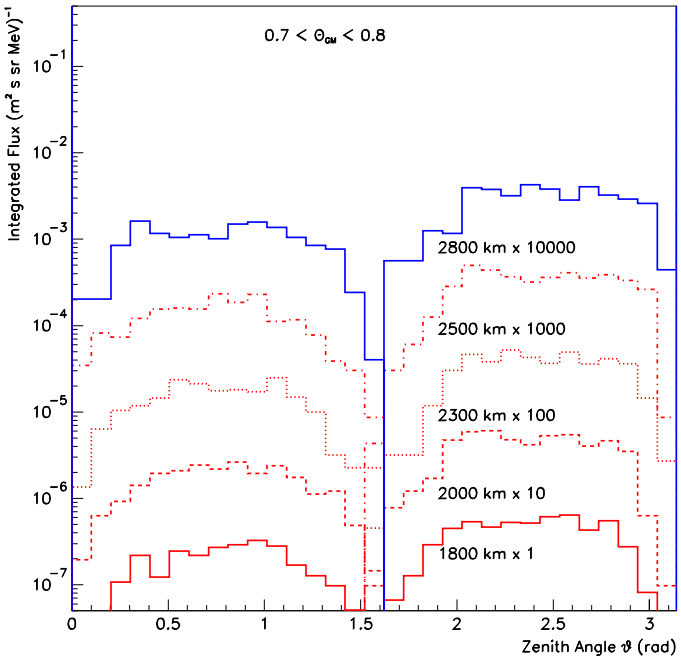

Figure 9.4: *The zenith angular distributions of the atmospheric $\bar{p}$ flux in the geomagnetic latitude region $0.7 < \theta_{GM} < 0.8$ at the same altitudes as in Figure* **??**.

some percent up to 10% of the evaluated cosmic antiprotons discussed in Chapter **??**. Thus, the idea to find an altitude at which the atmospheric $\bar{p}$ flux vanishes doesn't seem practical. In addition, it can also be seen in the figures that, from equatorial to subpolar regions, both upward and downward atmospheric $\bar{p}$ flux are still comparable to each other at very high altitudes but it is seen the upward atmospheric $\bar{p}$ flux becomes larger than the downward atmospheric $\bar{p}$ flux over the full angular range as the altitude increases, as naturally expected. In the discussions in Chapter **??**, all atmospheric antiprotons are produced below the altitude of about 100 km. Thus, the fact that both upward and downward atmospheric $\bar{p}$ flux are comparable at high altitudes implies that, at a high altitude, after outward atmospheric antiprotons cross the virtual detection sphere at this altitude, most of them should return to cross this sphere again, contributing as the inward flux. The overall outward flux is higher than the inward flux as expected for particles produced in the atmosphere.

Figures **??** shows the atmospheric $\bar{p}$ spectral distributions of flux, both upward and downward, in the equatorial region $0.0 < \theta_{GM} < 0.2$ at the altitudes of 1800, 2000, 2300, 2500 and 2800 km. Note the values at different altitudes are multiplied by a power of 10 for comparison. Figure **??** shows the integrated flux for atmospheric antiprotons, both upward and downward, in function of altitude from 100 km to 2800 km in the same geomagnetic latitude region. It is seen that, at the altitude of about 500 km, the upward and downward atmospheric $\bar{p}$ flux are almost of the same value while above 500 km, the upward flux becomes larger than the downward flux and below 500 km, the downward flux becomes larger than the upward flux. The deviation between these two flux increases with altitudes away from 500 km while both flux are seen to reach their maximum at an altitude around 750 km. Such a result is impressing.

Figure **??** show some features of the antiprotons which can cross the virtual sphere at the altitude of 2800 km. The simulation programme used in the present work provides the statistics of the final state of each produced particle. Thus, the final states of all produced antiprotons are investigated here. The definitions for the signatures used for the particle final state are given in Table **??**, while Figure **??** (a) and (b) show the final states of the antiprotons crossing the virtual sphere at the altitude of 2800 km, both outwards and inwards. It is seen that, the numbers of both outward and inward antiprotons which are finally annihilated in the interactions with atmospheric nuclei are comparable to each other. This implies a fact that, even at the altitude of 2800 km, most of outward atmospheric antiprotons would turn around after some duration, cross the the virtual sphere, re-enter again the atmosphere, collide with atmospheric nuclei and finally become annihilated in the atmosphere. This provides the reason that both downward and upward atmospheric $\bar{p}$ flux at high altitudes to be still comparable to each other. In addition, also in the histograms Figure **??** (a) and (b), it can be seen that a fraction of outward antiprotons escape the Earth (with the final state signature 4). These antiprotons would cross the virtual sphere at the altitude outwards only once, or one time more than the number of their inward crossings if they could turn around. So, this histogram are consistent with the natural expectation of the upward atmospheric $\bar{p}$ flux at high altitudes being higher than the downward $\bar{p}$ flux. Therefore, the histograms of the final states of

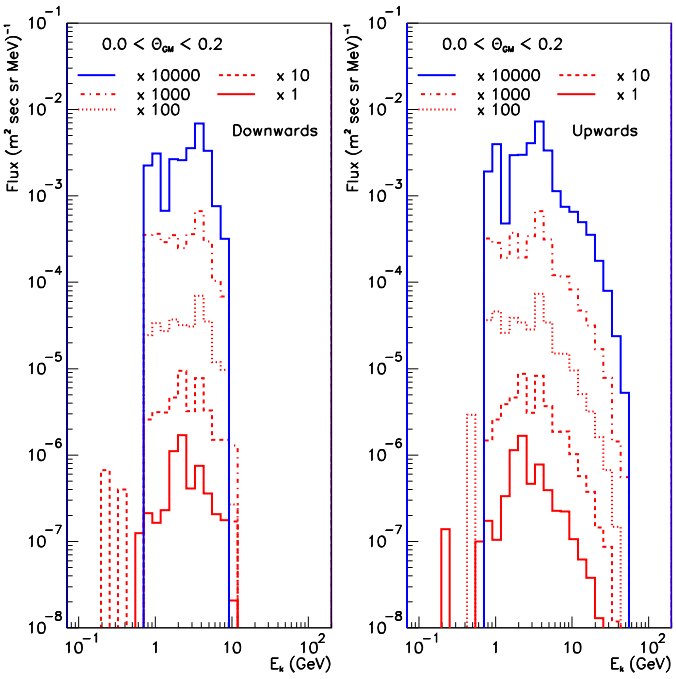

Figure 9.5: *The downward and upward atmospheric $\bar{p}$ flux in the geomagnetic latitude region $0.0 < \theta_{GM} < 0.2$ at the altitudes (from bottom to top) of 1800, 2000, 2300, 2500 and 2800 km. The values are multiplied by a factor of 10, i.e., 10 for 1800 km, 100 for 2000 km etc as indicated on the figure.*

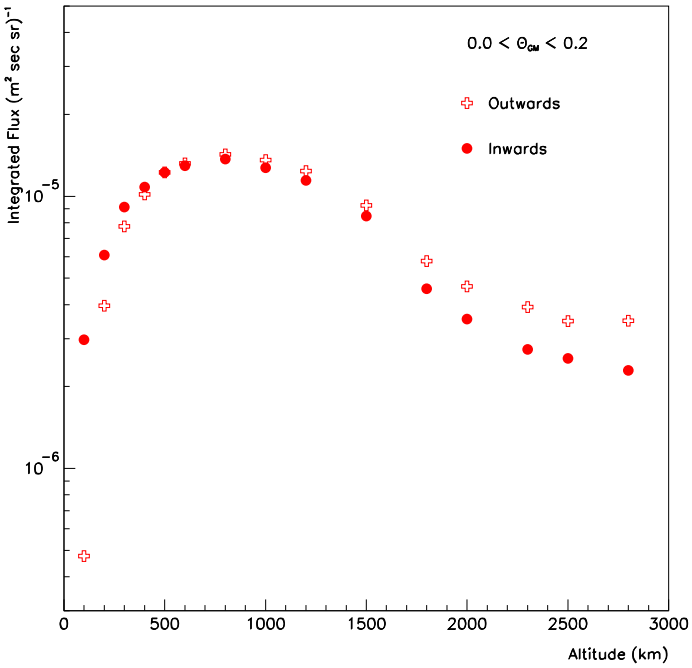

Figure 9.6: *The upward and downward atmospheric $\bar{p}$ integrated flux in function of altitude, from 100 km to 2800 km. The deviation between upward and downward flux increases in both directions from the altitude of 500 km.*

atmospheric antiprotons in Figure ?? (a) and (b) agree to the inference made earlier in this section.

From the previous discussion, it is concluded that a great amount of atmospheric antiprotons could undergo round trips during their propagation near the Earth after their production. Thus, these antiprotons could be longlived. Figure ?? (c) and (d) show respectively the distributions of lifetime of atmospheric antiprotons at the altitude of 2800 km and their numbers of bounce during their lifetimes. It is seen that some atmospheric antiprotons can live as long as 100 sec, with a number of bounce up to 100 times. In fact, some events with much longer lifetime, of about 500 sec, can be found in the simulationu results. So with their long lifetime and long journey distance, there are expected to be some residual atmospheric antiprotons bounded by the Earth geomagnetic field even at very high altitudes.

9.2 Trajectories of Atmospheric Antiprotons

The simulation programme used in the present work also provides the recording of the particle trajectories. The circulation radius of a charged particle propagating in a magnetic field depends on its charge, momentum and the magnetic field:

$$p\cos\alpha = 0.3ZBr \tag{9.1}$$

where p is the particle momentum in GeV/c, Ze the charge, α the pitch angle, B the magnetic field in tesla, and r the radius of curvature in meters. However, the charged particle trajectory near the Earth is complicated since the Earth geomagnetic field is a multipole, and, the propagating particles might interact with the atmosphere during their paths, by energy loss, or nuclear collisions. Therefore, the particle trajectory near the Earth is not uniform since the Earth geomagnetic field and the kinematic configurations of particles vary with time and their positions.

The particle trajectories are evaluated in the same simulation technique with the consideration of particle equations of motion in the Earth multipole geomagnetic field, the atmospheric structure and the interactions of particles with atmospheric nuclei discussed in Chapter ??. Some examples of $\bar{p}$ trajectories near the Earth are given as follows.

9.2.1 Examples of Atmospheric Antiproton Trajectory Near the Earth

In this section, some examples of the atmospheric $\bar{p}$ trajectories are given. The figure in each example gives the three dimensional plot of the $\bar{p}$ position with the Earth sphere, the plot of the antiproton z coordinate versus the position on the meridian plane and also the projection of the $\bar{p}$ position onto xy plane. Some configurations, such as the particle kinetic energy, rank of collision, the particle final state, the lifetime and the number of bounce around the Earth, are also shown in the figure.

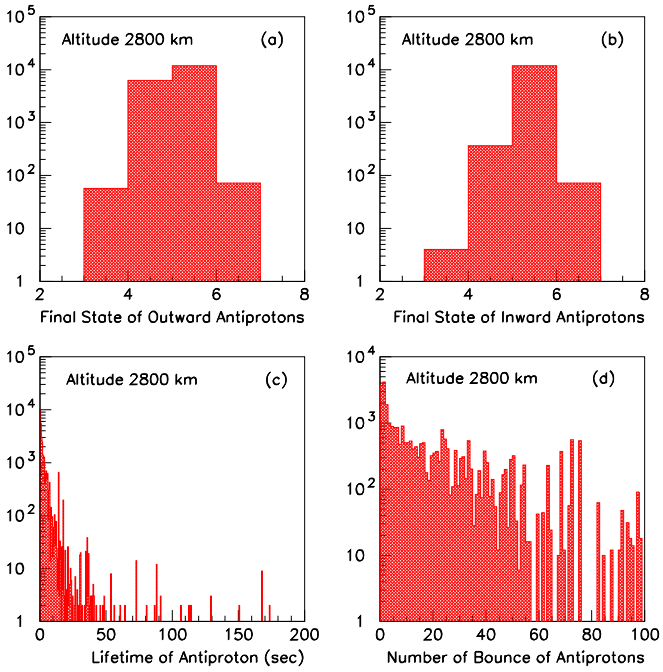

Figure 9.7: *(a) The distribution of the final states of outward atmospheric antiprotons at the altitude of 2800 km. See definitions in Table* **??**. *(b) Same as (a) for inward atmospheric antiprotons. (c) The distribution of lifetimes of atmospheric antiprotons crossing the altitude of 2800 km. (d) The distribution of bounces of atmospheric antiprotons crossing the altitude of 2800 km.*

Table 9.1: *Definitions of the signatures used for the particle final states.*

Signature	Configuration
3	trapped (over long duration, $t > 2000$ sec)
4	escaping
5	annihilated in interaction with atmospheric nuclei
6	stopped by energy loss ($E < E_{cut}$)

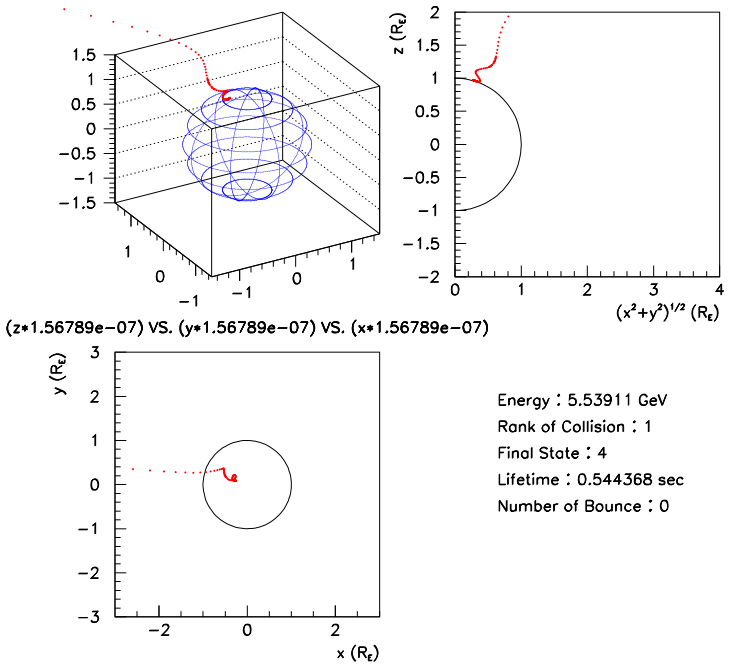

Figure 9.8: *An example of the shortlived atmospheric $\bar{p}$ trajectory in the polar region. This antiproton finally escapes to infinity.*

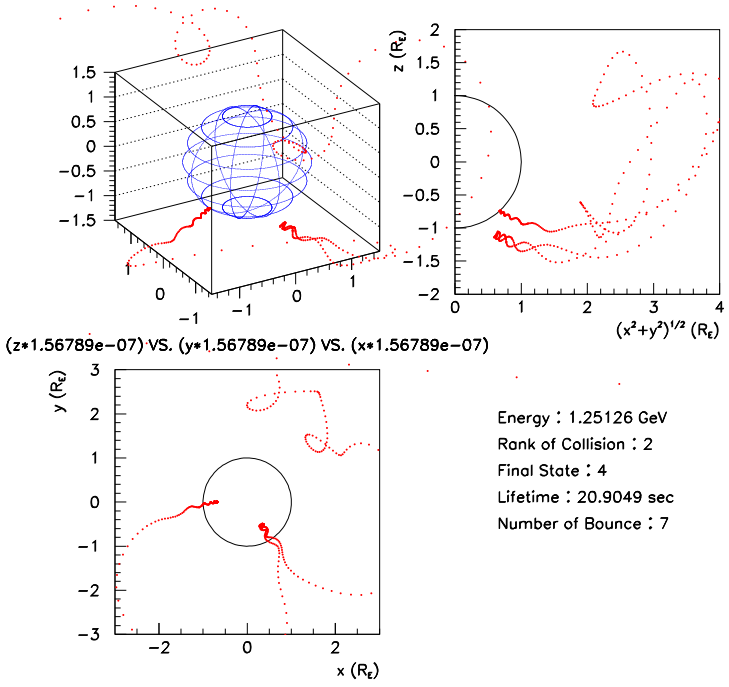

Figure 9.9: *An example of a longlived atmospheric $\bar{p}$ trajectory in the subpolar region with large crossings. This $\bar{p}$ finally escapes to infinity.*

Figure ?? shows a typical trajectory of a longlived atmospheric $\bar{p}$ in the subpolar and polar regions. In Figure ??, it has been shown that a large population of longlived atmospheric antiprotons is found in the polar region. More than 90% of these antiprotons would cross only once the virtual sphere at high altitudes, even though they are longlived. As it can be seen in Figure ??, the antiproton recoils in a vertical direction away from the Earth. It is found that most particles in the polar region can escape the Earth because of the low geomagmetic rigidity cutoff.

A longlived $\bar{p}$ produced in the subpolar or polar region could also cross the virtual detection sphere at high altitudes more than once. Shown in Figure ??, a produced $\bar{p}$ which is longlived and finally escapes to infinity can cross the sphere 7 times at the altitude of $2R_E$. However, it is found that such antiprotons are quite few in the $\bar{p}$ population, less than 1% according to the simulation.

Figures ?? and ?? show the examples of the trajectories of atmospheric antiprotons, both shortlived and longlived, in low geomagnetic latitude region. It is found that both shortlived and longlived antiprotons can contribute to large crossing multiplicity at high altitudes. This result agrees to the discussion in the previous chapter. It is also seen in Figure ?? that, the antiproton could be trapped with the trajectory within a wide domain, speading up to about $3R_E$ away from the geocentric origin. Also note that these trajectories are those for the atmospheric antiprotons which can cross the virtual sphere at the altitude 2800 km. It should be emphasised that, in both Figure ?? and Figure ??, the antiprotons are finally annihilated in the interactions with atmospheric nuclei. However, even though they could cross the altitude 2800 km many times, their ranks of collision are just one. In the simulation result moreover, some longlived antiprotons with hundreds of bounces but with their ranks of collision of 1, are seen. So, this implies that the trajectory of a charged particle in the realistic Earth geomagnetic field is extremely complicated and it seems impossible to well explain the particle trapped trajectories at such high altitudes in terms of of usual variables.

9.3 Remarks on Atmospheric Antiproton Flux at Very High Altitudes

It is found that there are always some residual atmospheric antiprotons which could cross the virtual sphere at very high altitudes, both inwards and outwards. This implies that it is not practical trying to measure the pure cosmic $\bar{p}$ flux in the neighbourhood of the Earth. Therefore, the correction of secondary atmospheric $\bar{p}$ flux will be always required to evaluate the cosmic $\bar{p}$ flux. Hence, it turns to be more practical to correct the secondary atmospheric antiprotons by applying some other efforts discussed in the previous chapter, such as the analysis of the rigidity cutoff or the particle forward and backward tracing. These methods are supposed to filter away most of the absolute atmospheric antiprotons.

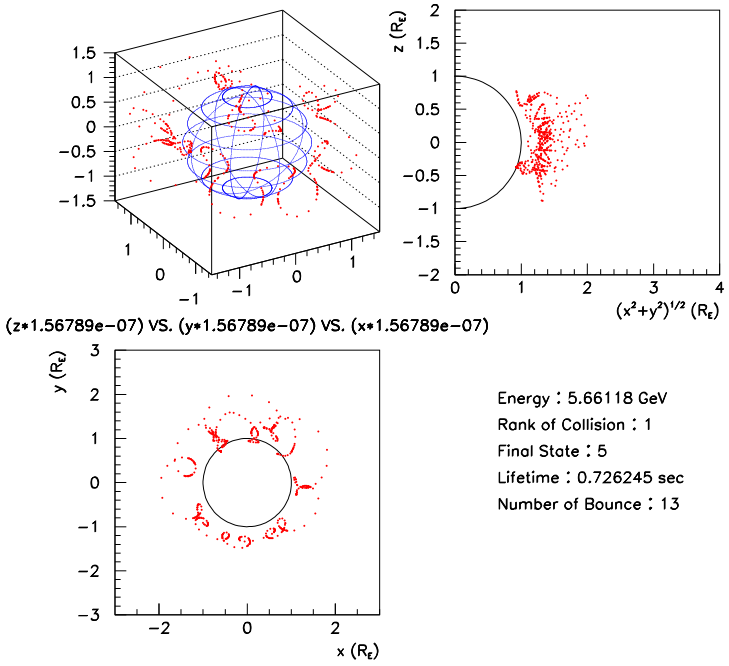

Figure 9.10: *An example of the trajectory of a shortlived atmospheric $\bar{p}$ with large crossing multiplicity at high altitude in the equatorial region. The $\bar{p}$ is annihilated in the interaction with atmospheric nuclei finally.*

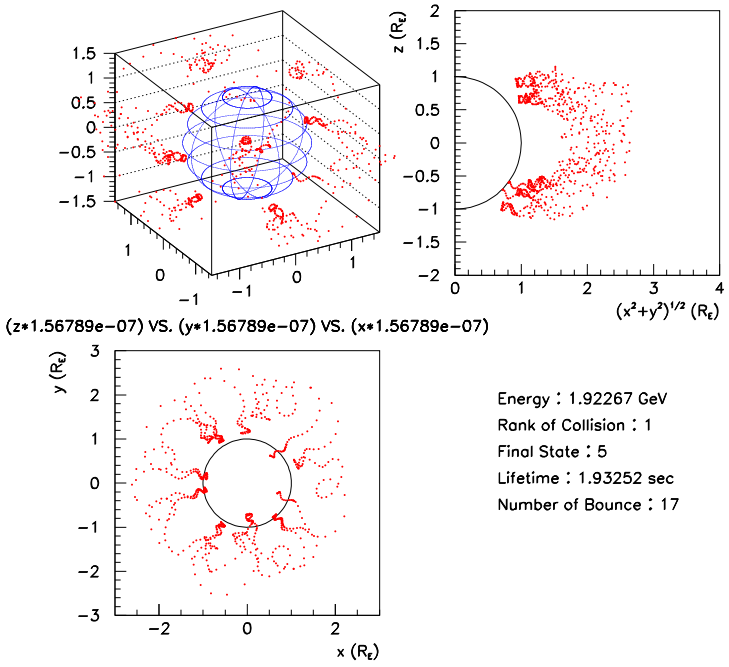

Figure 9.11: *An example of the trajectory of a longlived atmospheric $\bar{p}$ with very large crossing multiplicity in the equatorial region. This $\bar{p}$ is also annihilated in the interaction with atmospheric nuclei at the end of its lifetime.*

Chapter 10

Flux of Atmospheric Protons at Low Altitudes

In this short chapter, the proton flux at different altitudes are evaluated by the present simulation, and compared with the experimental data. The deviations observed for the proton flux at the altitudes of 5.75 km and 2.77 km between the simulated flux and the measurements are discussed. Although a careful investigation of the proton flux at low altitudes is not the principal object of this thesis, it provides some useful indication on the consistency of the approach.

10.1 Atmospheric Proton Flux at Low Altitudes

The absolute flux and spectra of cosmic protons are essential and fundamental references to cosmic ray study. Their interstellar spectrum, which in principle could be derived from the measurements at TOA of the Earth by demodulating the observed spectra for solar modulation, is very important to understand the Galactic propagation and acceleration mechanisms of cosmic ray particles. The protons which enter the Earth atmosphere can give rise to secondary particle production: the antiprotons, whose interest of study has been discussed in the previous chapters of this thesis; the neutrinos, which are the decay product of muons or pions, are of special interest in view of so-called 'atmospheric neutrino anomaly' [?]. A precise understanding of cosmic p flux could then help reduce the uncertainty in the neutrino flux calculation. This is of great importance for understanding the apparent deficit of muonlike neutrinos in underground neutrino detection experiments [?].

Measurements of the p energy spectrum have been performed in various experiments at different altitudes. In the AMS 1998 experiment [?, ?], a high flux proton component was observed below the geomagnetic cutoff and can be well accounted for as the secondary particles originating from the interactions of cosmic ray particles with the atmospheric nuclei [?]. At high balloon altitudes, early experiments [?, ?] have reported p spectra different by a factor as large as 2, for energies $E \geq 10$ GeV. Such differences might come from the imprecise or incomplete knowledge of detector efficiencies [?]. More current

experiments like BESS [?, ?] and CAPRICE [?] etc., are able to measure the detector efficiencies more accurately and the p spectra at TOA measured by these experiments have shown a good agreement at energies $E \geq 10$ GeV. However, at energies $E < 10$ GeV, the reported p spectra at TOA have shown a disagreement as large as a factor of about 2. The difference at the energy range $E < 10$ GeV might come from the less correct knowledge of detector efficiencies at low energies or the incomplete understanding of the atmospheric proton production in this energy range.

Just like the antiprotons discussed in the previous chapters, the measured protons at high balloon altitudes should be a superposition of cosmic protons and atmospheric secondaries. Thus, for evaluating the p flux at TOA, one has to correct the measured p flux by subtracting the atmospheric p component. So far, in most balloon experiments, the calculations of atmospheric p flux by Papini, Grimani and Stephens [?] have been used. However, it was found [?] that, at a low altitude of 2770 m, the simulation results of GEANT/GHEISHA have reproduced the same shape of the measured p spectrum but the absolute flux deviates from the observed flux by a factor about 2 for low energy protons. Since at such a low altitude, all the protons measured should be secondaries, the deviation might firstly possibly come from the less correct estimate of atmospheric proton component. Therefore, in this chapter, the attention focuses on the atmospheric p flux at low altitudes for investigations.

Figure ?? shows the evaluated proton flux at some different altitudes, from 2.77 km to 29.93 km, together with the measurement results by different groups [?, ?, ?, ?, ?]. The p flux at the AMS altitude, both from the present work and the measurement [?, ?], are shown as the p flux at TOA. Note that a factor by a power of 10^{-1} is multiplied to the flux values, as indicated in the figure.

It is seen that, the simulation results of the present work do reproduce the same shape and magnitude of the p flux measurements at all altitudes except at the altitude of 5.75 km measured in the CAPRICE 1994 experiment [?]. Since the p flux measured at different altitudes by different groups have reported the same shape of the p flux, the apparent deviation of the p flux at the altitude of 5.75 km might indicate a less accuracy in the p flux measurement at this altitude performed in the CAPRICE 1994 experiment [?].

In addition, it is seen that, at the altitude of 2.77 km, the present simulation overestimates the p flux, deviating from the observed flux [?], by a factor of about 2 over the measurement energy. Therefore, the present work has shown the same deviation in the proton flux at the altitude of 2.77 km as reported [?]. However, it must be noted that most protons at low altitudes are produced as N^{th} rank of collision in the air cascade. At 2.77 km, for example, the mean rank of collision of protons is $N = 6.7$. So the production cross section of a proton detected at this altitude is $\sim (\sigma)^N$. Therefore, a small deviation of the calculated cross section from the experimental cross section could then easily account for the observed deviation factor of 2. According to simulation results, it is found that above the altitude of 20 km, the effect of the N^{th} rank of collision can be neglected since above this altitude, the protons of multi-ranks of collisions have contributed a population of only several percent of total proton amount, while below the altitude of 20 km, the phenomenon becomes more diverse and would require more careful investigations and

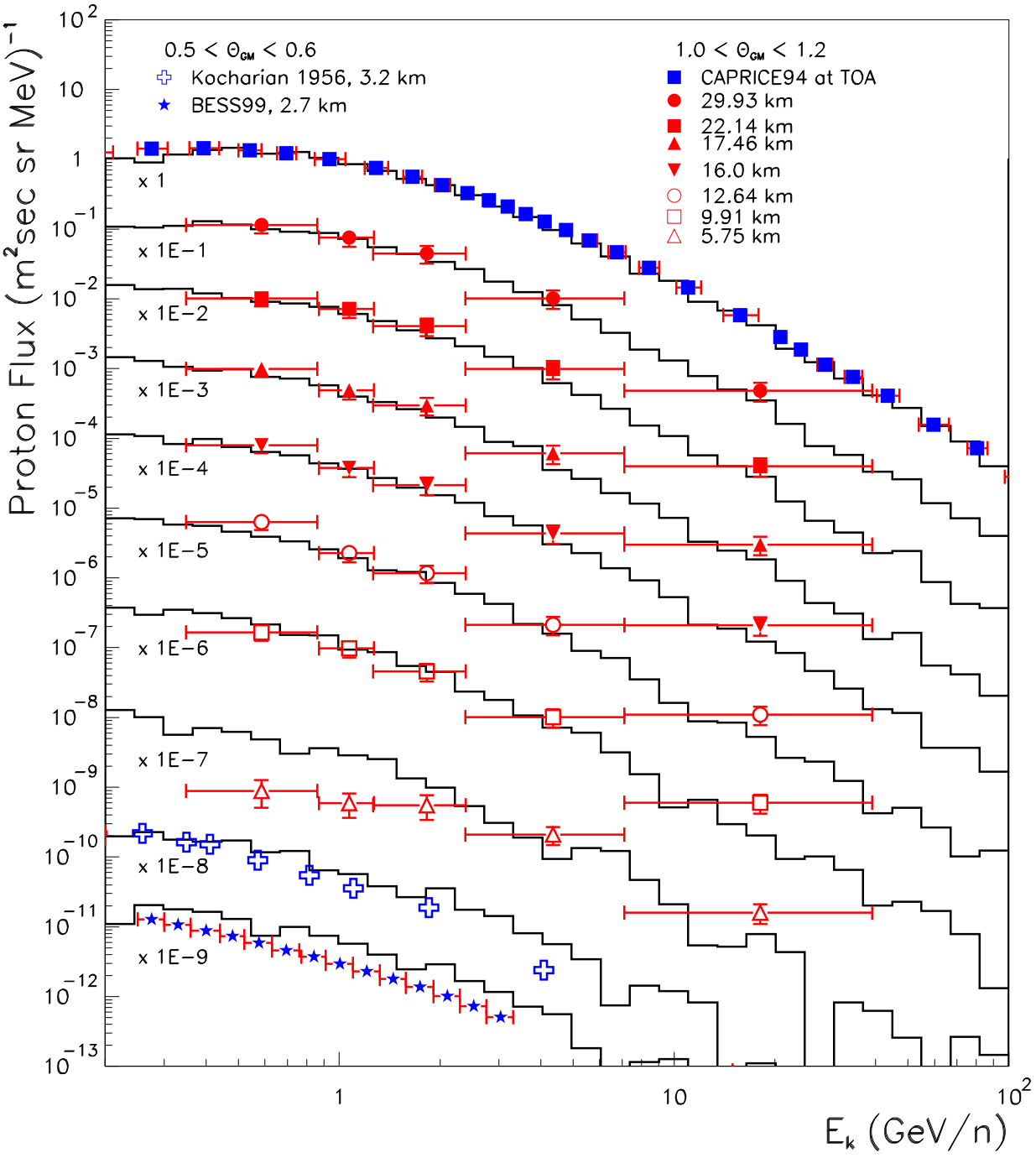

Figure 10.1: *The proton flux at different altitudes evaluated of the simulation results (solid lines) of the present work and the measurements [?, ?, ?, ?, ?]. The values are multiplied by a power of* 10^{-1}*, i.e.,* 10^{-1} *for 29.93 km,* 10^{-2} *for 22.14 km,..., up to* 10^{-9} *for 2.77 km.*

calculations. On the other hand, the deviation of the p flux at low energies might also suggest the corresponding cross section should be re-measured.

Conclusions and Perspectives

The present work in this thesis has met with success in some aspects which are outlined as follows.

For the $\bar{p}$ production in nuclear collisions, the parametrised inclusive cross section has been found to show a good agreement with the experimental data for incident nucleon energy at least up to 24 GeV/n in the laboratory frame, in $p+p$ and $p+A$ collisions. By the analysis of the $\bar{p}$ mean multiplicity distribution in $p+p$ collisions, this parametrisation was also shown to match the experimental data at least up to the centre of mass energy $\sqrt{s} \simeq 25$ GeV. This energy range is the most important for the related study of the primary $\bar{p}$ origins by the analysis of the cosmic $\bar{p}$ spectrum.

For the atmospheric $\bar{p}$ component, it was found that, the cosmic He-induced collisions contribute about 30% of the total atmospheric $\bar{p}$ component, and, the secondary atmospheric $\bar{p}$ flux used to correct the cosmic $\bar{p}$ flux at TOA in previous studies were probably underestimated. The expectedly more realistic corrections for the evaluations of the cosmic $\bar{p}$ flux at TOA have been given for different experiments. The accuracy of the present calculations on the atmospheric $\bar{p}$ flux has been confirmed by comparison with the $\bar{p}$ measurements at the altitude of 2.77 km, whose data have shown an apparent deviation compared with the previous calculations but are shown to be in good agreement with the present calculations. According to the present work, the identification window for the supersymmetric neutralinos by detecting antiprotons at balloon altitudes has been reduced.

Based on the analysis on the zenith angular distribution of the $\bar{p}$ flux, at both high balloon and satellite AMS altitudes, the reason that no upward antiprotons have been detected at high balloon altitudes is now well explained.

It was also found that, even at the AMS altitude, the atmospheric $\bar{p}$ flux in the equatorial region still has the same magnitude of the evaluated cosmic $\bar{p}$ flux. It implies that the correction of the atmospheric $\bar{p}$ component onto the cosmic $\bar{p}$ flux is always necessary. On the other hand, in the subpolar and polar regions, the $\bar{p}$ flux measured by AMS is almost the exact cosmic $\bar{p}$ flux, with only about 2-3% of atmospheric $\bar{p}$ component. This means that in the future, AMS will provide more direct $\bar{p}$ measurements for the related studies.

At the AMS altitude, the particle crossing multiplicity is strongly correlated with low geomagnetic latitude while at balloon altitudes, this correlation is not obvious. By observing the atmospheric $\bar{p}$ trajectories with their lifetimes, such a correlation is now well understood.

The p flux calculated by the present work at different altitudes have shown the good agreements with the experimental data measured by different groups, except at low altitudes. The source of this deviation has been suggested to come from the multi-rank of collision in the air cascade, which amplifies minor deviation of the calculated cross section with respect to the experimental values. In addition, in order to investigate this problem more carefully, the re-measurements of the corresponding cross section is also suggested.

For future works, the secondary galactic $\bar{p}$ flux arriving at the Earth can be re-evaluated combining the results of the present work and the cosmic ray propagation. Thus, a better calculation for the galactic $\bar{p}$ flux can be expected. In addition, more attention should go in the future to the $\bar{p}$ flux, both cosmic and atmospheric, at energies $E < 0.5$ GeV. It is already seen that, the present work has reproduced the $\bar{p}$ flux consistent with the experimental data at energies above 0.5 GeV. For the study on the primary $\bar{p}$ origins, the energy range of $E < 1$ GeV is the most important. However, low energy $\bar{p}$ production is still not well known experimentally. So, future calculations should take low energy antiprotons into account with great care. The forthcoming experiments HARP and MIPP will provide more reliable information for this. With the better evaluation of $\bar{p}$ flux in the future, a better upper limit for the identification of the $\bar{p}$ primary origins, like the annihilation of supersymmetric neutralinos and the evaporation of primordial black holes could be given.

Above thousands of kilometres above the Earth, some residual atmospheric antiprotons can still be found. Their trajectories have shown great complexity. Therefore, it could be worth working on the dynamics of these antiprotons with complex trajectories.

The integrated atmospheric $\bar{p}$ flux has shown a particular distribution with altitude. At very high altitudes, up to thousands of kilometres, both outward and inward $\bar{p}$ flux which turn to be constant have been discussed in this thesis, by observing their trajectories. But, why do they have such specific distributions? Why do both upward and inward $\bar{p}$ flux have a peak at the altitude around 750 km? Why do these two flux meet each other at the altitude around 500 km? These questions are interesting and it is expected to have a better understanding of the dynamics of particles, from the neighbourhood of the Earth up to thousands of kilometres above the Earth, by answering these questions.

Appendix A

Regge Trajectory

In order to see the characteristic of the poles connected by the Regge trajectory, one can consider an s-t symmetric Veneziano scattering amplitude [**?**]

$$A(s,t) = g^2 \frac{\Gamma(-\alpha(s))\Gamma(-\alpha(t))}{\Gamma(-\alpha(s)-\alpha(t))} \tag{A.1}$$

where Γ is the gamma function and the angular momentum distribution $\alpha(x)$ is taken to depend linearly on x as

$$\alpha(x) = \alpha_0 + \alpha' x \tag{A.2}$$

The gamma function $\Gamma(-\alpha)$ obeys the relation

$$\Gamma(-\alpha) = \frac{\Gamma(-\alpha+1)}{-\alpha} = \frac{\Gamma(-\alpha+2)}{-\alpha(-\alpha+1)} = \frac{\Gamma(-\alpha+J+1)}{-\alpha(-\alpha+1)\cdots(-\alpha+J)} \tag{A.3}$$

Expand $\Gamma(-\alpha)$ at $-\alpha = -J$, then one can obtain

$$\Gamma(-\alpha) = \frac{\Gamma(1)}{(-J)(-J+1)\cdots(-\alpha+J)} = \frac{(-1)^J}{J!(-\alpha+J)} \tag{A.4}$$

So, $\Gamma(-\alpha)$ in Eq. (**??**) has poles at $-\alpha = 0, -1, -2, \ldots - J, \ldots,$. Thus, expanding $A(s,t)$ at $-\alpha(t) = -J$ by using Eq. (**??**), one can have

$$\begin{aligned} A(s,t) &= g^2 \frac{\Gamma(-\alpha(s))}{\Gamma(-\alpha(s)-J)} \cdot \frac{(-1)^J}{J!\,(-\alpha(t)+J)} \\ &= g^2(-\alpha(s)-1)(-\alpha(s)-2)\cdots(-\alpha(s)-J)\cdot \frac{(-1)^J}{J!\,(-\alpha(t)+J)} \\ &= g^2 \frac{(\alpha(s)+1)(\alpha(s)+2)\cdots(\alpha(s)+J)}{J!\,(-\alpha(t)+J)} \end{aligned} \tag{A.5}$$

Now, the singular poles happen at $-\alpha(t) = 0, -1, -2, \ldots, -J, \ldots,$. So, by including all poles, the scattering amplitude turns to be

$$A(s,t) = \sum_{J=0}^{\infty} g^2 \frac{(\alpha(s)+1)(\alpha(s)+2)\cdots(\alpha(s)+J)}{J!\,(-\alpha(t)+J)} \tag{A.6}$$

By taking $\alpha(x) = \alpha_0 + \alpha' x$ in Eq. (??), for the limiting case of $s \gg 1$, $A(s,t)$ is changed to

$$A(s,t) = \sum_{J=0}^{\infty} g^2 \frac{(\alpha' s)^J}{J!\,(-\alpha_0 - \alpha' t + J)} = -\sum_{J=0}^{\infty} g^2 \frac{(\alpha')^{J-1}}{J!} \cdot \frac{s^J}{t - \frac{J-\alpha_0}{\alpha'}} \tag{A.7}$$

By investigating Eq. (??) and Eq. (??), it shows that the scattering amplitude is the sum of all the amplitudes for the exchange of particles with spin J and mass M_J, following

$$M_J^2 = \frac{J - \alpha_0}{\alpha'} \quad \Longrightarrow \quad J = \alpha_0 + \alpha' M_J^2 \tag{A.8}$$

Eq. (??) represents that, in a hadronic scattering, the masses and the spins of the exchange particles should follow a special relation. The relation in Eq. (??) is called Regge trajectory with a Regge intercept α_0 and a Regge slope α'. So, in the high energy limit, hadron scattering amplitudes are controlled by the exchange of particles which lie on the Regge trajectory [?]. Empirically, the Regge slope is approximately a constant, with a value [?]

$$\alpha' \simeq 1 \quad \text{GeV}^{-2} \tag{A.9}$$

Bibliography

[1] R. Konig, *J. Geophys. Res.* **86**, (1981) 515

[2] R. L. Golden *et al.*, *Phys. Rev. Lett.* **43**, (1979) 1196

[3] S. Rudaz and F. W. Stecker, *AstroPhys. J.* **325**, (1988) 16

[4] A. Bottino, F. Donato, N. Fornengo and P. Salati, *Phys. Rev.* **D 58**, (1998) 123503

[5] L. Bergström, J. Edsjö and P. Ullio, *Proc. 26th ICRC*, 1999

[6] B. J. Carr, *AstroPhys. J.* **206**, (1976) 8

[7] A. Barrau, *Astropart. Phys.* **12**, (2000) 269

[8] A. N. Kalinovskiĭ, N. V. Mokhov and Yu. P. Nikitin, *Passage of High-Energy Particles through Matter*, American Institute of Physics. 1989

[9] P. D. B. Collins and A. D. Martin, *Hadron Interaction*, Adam Hilger Ltd., 1984

[10] R. K. Ellis, W. J. Stirling and B. R. Webber, *QCD and Collider Physics*, Cambridge University Press, 1996

[11] D. H. Perkins, *Introduction to High Energy Physics: Revised, Enlarged and Reset*, Addison-Wesley Publishing Company, 1982

[12] G. Alberi and G. Goggi, *Phys. Rep.* **74**, (1981) 1

[13] A. Białas, M. Bleszyński and W. Czyż, *Nucl. Phys.* **B 111**, (1976) 461

[14] S. A. Stephens, *Astropart. Phys.* **6**, (1997) 229

[15] B. R. Martin and G. Shaw, *Particle Physics*, John Wiley & Sons, 1997

[16] J. Wdowczyk and A. W. Wolfendale, *Ann. Rev. Nucl. Part. Sci.* **39**, (1989) 43

[17] T. K. Gaisser, *Cosmic Rays and Particle Physics*, Cambridge University Press, 1990

[18] M. S. Longair, *High Energy Astrophysics*, Vol. 1, 2, Cambridge University Press, 1992 (Vol. 1), 1994 (Vol. 2)

[19] W. R. Webber, A. Lukasiak, F. B. McDonald and P. Ferrando, *AstroPhys. J.* **457**, (1996) 435

[20] T. K. Gaisser, *Nuclear and Particle Astrophysics*, Ed. J. G. Hirsch and D. Page, Cambridge University Press, 1998

[21] R. J. Tayler, *Galaxy: Structure and Evolution*, Cambridge University Press, 1996

[22] The CRIS Collaboration, T. T. von Rosenvinge *et al.*, *Proc. 25th ICRC*, Vol 5, 1997

[23] D. J. Bird *et al.*, *AstroPhys. J.* **424**, (1994) 195

[24] S. Yoshida *et al.*, *Astropart. Phys.* **3**, (1995) 105

[25] Y. Sekido and H. Elliot, *Early History of Cosmic Ray Studies*, D. Reidel Publishing Company, 1985

[26] P. E. Hodgson, E. Gadioli and E. Gadioli Erba, *Introduction to Nuclear Physics*, Oxford Clarendon Press, 1997

[27] L. H. Ryder, *Quantum Field Theory*, Cambridge University Press, 1985

[28] F. Mandl, *Introduction to Quantum Field Theory*, Interscience Publishers, 1959

[29] V. Berezinsky, *9th Int. Workshop Neutrino Telescope*, 2001

[30] G. Sigl, *Science* **291**, (2001) 73

[31] J. A. Simpson, *Ann. Rev. Nucl. Part. Sci.* **33**, (1983) 323

[32] R. Ramaty, R. E. Lingenfelter and B. Kozlovsky, *Proc. Nuclei in the Cosmos V*, 1998

[33] R. Ramaty, E. Vangioni-Flam, Michel Cassé and K. Olive, *Proc. Astronomical Society of Pacific Conference*, 1999

[34] K. Greisen, *Phys. Rev. Lett.* **16**, (1966) 748

[35] G. T. Zatsepin and V. A. Kuzmin, *Pisma Zh. Experim. Theor. Phys.* **4**, (1966) 114

[36] V. S. Berezinskiĭ, S. V. Bulanov, V. A. Dogiel, V. L. Ginzburg and V. S. Ptuskin, *Astrophysics of Cosmic Rays*, North-Holland Publishing Company, 1990

[37] The SuperKamiokande Collaboration, Y. Fukuda *et al.*, *Phys. Rev. Lett.* **81**, (1998) 1562

[38] Y. Liu, L. Derome and M. Buénerd, *Proc. 27th ICRC*, 2001

[39] V. L. Ginzburg and S. I. Syrovatskiĭ, *The Origin of Cosmic Rays*, Oxford Pergamon Press, 1964

[40] R. A. Ong, *Particle and Nuclear Astrophysics and Cosmology in the Next Millennium*, Ed. E. W. Holb and R. D. Peccei, World Scientific Publishing Co., 1994

[41] N. Lund, *Cosmic Radiation in Contemporary Astrophysics*, Ed. M. M. Shapiro, D. Reidel Publishing Company, Dordecht, 1984

[42] B. Wiebel-Sooth, P. L. Biermann and H. Meyer, *Astron. Astrophy.* **330**, (1998) 389

[43] P. Papini, C. Grimani and S. A. Stephens, *Il Nuovo Cimento* **19C**, No. 3, (1996) 367

[44] P. Ferrando, *Proc. of the XXIII Internationl Conference of Cosmis Rays*, Ed. D. A. Leahy, R. B. Hicks and D. Venkatesan, World Scientific Publishing Co., 1994

[45] E. P. S. Shellard, *Foundation in Modern Cosmology*, Cambridge University Press, 1995

[46] The IMAX Collaboration, O. Reimer *et al.*, *AstroPhys. J.* **496**, (1998) 490

[47] E. S. Seo and V. S. Ptuskin, *AstroPhys. J.* **431**, (1994) 705

[48] W. R. Webber, J. C. Kish and D. A. Schrier, *Proc. 19th ICRC*, Vol 2, 1983

[49] A. Lukasiak *et al.*, *AstroPhys. J.* **423**, (1994) 426

[50] J. J. Connell, *AstroPhys. J.* **501**, (1998) 59

[51] N. E. Yanazak *et al.*, *Proc. 26th ICRC*, 1999

[52] A. W. Strong and I. V. Moskalenko, *AstroPhys. J.* **509**, (1998) 212

[53] M. A. Shea and D. F. Smart, *Proc. 19th ICRC*, 1985

[54] L. J. Gleeson and W. I. Axford, *AstroPhys. J.* **154**, (1968) 1011

[55] A. W. Labrador and R. A. Mewaldt, *AstroPhys. J.* **480**, (1997) 371

[56] Yu. Galaktionov and V. Shoutko, *AMS Internal Note 1997-05-10*

[57] W. Heinrich, *CERN SI 88-02*, 1988

[58] J. A. Simpson, *Phys. Rev.* **83**, (1951) 1175

[59] K. G. Pyle, *Proc. 23rd ICRC*, 1993

[60] Neutron Monitor Datasets, CLIMAX Group, *http://ulysses.uchicago.edu/NeutronMonitor/*

[61] M. Honda, T. Kajita, K. Kasahara and S. Midorkawa, *Phys. Rev.* **D 52**, No. 9, (1995) 4985

[62] W. R. Webber and J. A. Lezniak, *Astrophy. Sp. Sci.* **30**, (1974) 361

[63] The BESS Collaboration, T. Maeno *et al.*, *Astropart. Phys.* **16**, (2001) 121

[64] M. Walt, *Introduction to Geomagnetically Trapped Radiation*, Cambridge University Press, 1994

[65] C. Störmer, *Astrophy.* **1**, (1930) 237

[66] M. A. Huang, *Proc. 7th Taiwan Astrophysics Workshop*, 2000

[67] C. Störmer, *The Polar Aurora*, Oxford Clarendon Press, 1995

[68] A. E. Sandström, *Cosmic Ray Physics*, North-Holland Publishing Company, 1965

[69] M. S. Vallarta, *Progress in Elementary Partiles and Cosmic Ray Physics, Handbuch des Physik*, Springer, vol. 46/1, 1961

[70] Particle Data Group, Review of Particle Properties, *Eur. Phy. J.* **C**15, (2000) 1

[71] HiRes, Fly's Eye Group, *http://hires.physics.utah.edu/*

[72] P. Bhattacharjee and G. Sigl, *Phys. Rep.* **327**, (2000) 109

[73] U. Heinbach and M. Simon, *AstroPhys. J.* **441**, (1995) 209

[74] S. A. Stephens and R. L. Golden, *Adv. Space Res.* **9**, No. 12, (1989) 93

[75] M. Garcia-Munoz and J. A. Simpson, *AstroPhys. J.* **64**, (1987) 269

[76] L. H. Smith, A. Buffington, G. F. Smoot, L. W. Alvazrez and M. A. Wahlig, *AstroPhys. J.* **180**, (1973) 987

[77] W. R. Webber, *AIP Conf. Proc. 203,, Particle Astrophysics: The NASA Cosmic Ray Program for the 1990s and Beyond*, Ed. W. V. Jones, F. J. Kerr and J. F. Oremes, AIP, New York, 1990

[78] J. R. Letaw, R. Silberberg, and C. H. Tsao, *AstroPhys. J. Suppl.* **51**, (1983) 271

[79] G. D. Westfall *et al.*, *Phys. Rev.* **C 19**, (1979) 1309

[80] J. J. Engelmann *et al.*, *Astron. Astrophy.* **233**, (1990) 96

[81] I. V. Moskalenko, A. W. Strong, J. F. Ormes and M. S. Potgieter, *AstroPhys. J.* **565**, (2002) 280

[82] E. Fermi, *Phys. Rev.* **75**, (1949) 1169

[83] A. R. Bell, *Mon. Not. Roy. Astro. Soc.* **182**, (1978) 147

[84] P. O. Lagage and C. J. Cesarsky, *Astron. Astrophy.* **125**, (1983) 249

[85] A. Achterberg, Y. A. Gallant, J. G. Kirk and A. W. Guthmann, *Mon. Not. Roy. Astro. Soc.* **328**, (2001) 393

[86] V. Koch, G. Brown and C. Ko, *Phys. Lett.* **B 265**, (1991) 29

[87] C. Spieles *et al.*, *Phys. Rev.* **C 53**, (1996) 2011

[88] The NA44 Collaboration, I. G. Bearden *et al.*, *Phys. Rev.* **C 57**, (1998) 837

[89] T. Armstrong *et al.*, *Phys. Rev. Lett.* **79**, (1997) 3351

[90] R. Rapp and E. Shuryak, *Phys. Rev. Lett.* **86**, (2001) 2980

[91] U. Heinz *et al.*, *Nucl. Phys.* **12**, (1986) 1237

[92] S. Gavin *et al.*, *Phys. Lett.* **B 234**, (1990) 175

[93] R. L. Golden *et al.*, *AstroPhys. Lett.* **24**, (1984) 75

[94] S. A. Stephens and B. G. Mauger, *Astrophy. Sp. Sci.* **110**, (1985) 337

[95] W. Hu and S. Dodelson, *Ann. Rev Astron. & Astrophys.* **?**, (2002) ?

[96] G. F. Smoot and D. Scott, *Eur. Phys. J.* **C15**, (2000) 145

[97] K. Griest, *International School of Physics "Enrico Fermi" Course "Dark Matter in the Universe"*, 1995

[98] M. Kamionkowski, *1997 ICTP Summer School on High Energy Physics and Cosmology*, 1997

[99] J. Binney and S. Tremaine, *Galactic Dynamics*, Princeton University Press, Princeton, 1987

[100] E. W. Kolb and M. S. Turner, *The Early Universe*, Addison-Welsey Redwood, 1989

[101] S. Burles and D. Tytler, *AstroPhys. J.* **507**, (1998) 732

[102] M. Douspis, A. Blanchard, R. Sadat, J. G. Bartlett and M. Le Dour, *Astron. Astrophy.* **379**, (2001) 1

[103] S. D. M. White *et al.*, *Nature* **366**, (1993) 429

[104] M. S. Turner, *Phys. Scripta* **T85**, (2000) 210

[105] G. P. Holder and J. E. Carlstrom, *Microwave Foregrounds*, Ed. A. de Oliveria-Costa and M. Tegmark, The Astronomical Society of the Pacific, 1999

[106] The SCP Collaboration, S. Perlmutter *et al.*, *AstroPhys. J.* **517**, (1999) 565

[107] The HZSST Collaboration, B. Schmidt *et al.*, *AstroPhys. J.* **507**, (1998) 46

[108] The HZSST Collaboration, A. Riess *et al.*, *Astron. J.* **116**, (1998) 1009

[109] M. S. Turner, *Type Ia Supernovae: Theory and Cosmology*, Ed. Jens Niemeyer and James Truran, Cambridge University Press, 1998

[110] M. S. Turner, *The Proceedings of Physics in Collision*, Ed. M. Campbell and T. M. Wells, World Scientific, 1999

[111] K. G. Begeman *et al.*, *Mon. Not. Roy. Astro. Soc.* **249**, (1991) 523

[112] The SCP Collaboration, C. Alcock *el al.*, *Nature* **365**, (1993) 621

[113] The EROS Collaboration, E. Aubourg *el al.*, *Nature* **265**, (1993) 623

[114] The MACHO Collaboration, W. Sutherland *el al.*, *Proc. International Workshop on the Identification of Dark Matter*, 1996

[115] The OGLE Collaboration, A. Udalski *el al.*, *AstroPhys. J. Lett.* **436**, (1994) L103

[116] The DUO Collaboration, C. Alard *el al.*, *Astron. Astrophy.* **337**, (1998) L17

[117] M. S. Turner, *Phys. Rep.* **197**, (1990) 67

[118] G. Jungman, M. Kamionkowski and K. Griest, *Phys. Rep.* **267**, (1996) 195

[119] The AMS Collaboration, J. Alcaraz *et al.*, *Phys. Rep.* **?**, (2002) ?

[120] P. Nath and R. Arnowitt, *Proc. International Workshop on Aspects of Dark Matter in Astrophysics and Particle Physics*, 1996

[121] F. Mayet, *Ph.D. Thesis*, Université Joseph Fourier (Grenoble I), 2001

[122] J. Ellis, T. Falk, K. A. Olive and M. Schmitt, *Phys. Lett.* **B 388**, (1996) 97

[123] E. L. Wright, *AstroPhys. J.* **459**, (1996) 487

[124] T. K. Gaisser and R. K. Schaefer, *AstroPhys. J.* **394**, (1992) 174

[125] T. K. Gaisser, J. W. Bieber, R. Engle and T. Stanev, *Proc. 26th ICRC*, Vol 3, 1999

[126] P. Chardonnet, G. Mignola, P. Salati and R. Taillet, *Phys. Lett.* **B 384**, (1996) 161

[127] M. Simon, A. Molnar and S. Roesler, *AstroPhys. J.* **499**, (1998) 250

[128] J. W. Bieber *et al.*, *Phys. Rev. Lett.* **83**, (1999) 674

[129] P. Ullio, *Astron. Astrophy.* **?**, (2002) ?

[130] F. Donato *et al.*, *AstroPhys. J.* **536**, (2001) 172

[131] A. Buffington, S. M. Schindler and C. R. Pennypacker, *AstroPhys. J.* **248**, (1981) 1179

[132] J. F. Ormes, A. Moiseev and J. Wells, *Proc. 26th ICRC*, 1999

[133] L. C. Tan and L. K. Ng, *Phys. Rev.* **D 26**, No. 5, (1982) 1179

[134] L. C. Tan and L. K. Ng, *J. Phys. G.* **9**, (1983) 227

[135] L. C. Tan and L. K. Ng, *J. Phys. G.* **9**, (1983) 1289

[136] M. Simon and U. Heinbach, *AstroPhys. J.* **456**, (1996) 519

[137] I. V. Moskalenko, A. W. Strong and O. Reimer, *Astron. Astrophy.* **338**, (1998) L75

[138] D. Maurin, *Ph.D. Thesis*, Université de Savoie, 2001

[139] Y. Sugaya *et al.*, *Nucl. Phys.* **A 634**, (1998) 115

[140] The E-802 Collaboration, T. Abbott *et al.*, *Phys. Rev.* **C 47**, No. 4, (1993) 1351

[141] The E-802 Collaboration, T. Abbott *et al.*, *Phys. Rev.* **D 45**, No. 11, (1992) 3906

[142] J. V. Allaby *et al.*, *CERN Report No.* 70-12 (1970)

[143] T. Eichten *et al.*, *Nucl. Phys.* **B 44**, (1972) 333

[144] C. Y. Huang, *Proc. 6èmes Rencontres avec les Jeunes Chercheurs, Physique Nucléaire, Astroparticules & Astrophysique*, 2000

[145] Ching-Yuan Huang and Michel Buénerd, *Phys. Lett.* **B ?**, (2001) ?

[146] R. A. Mewaldt *et al.*, *Acta. Astronautica Suppl.* **35**, (1995) 267

[147] A. M. Ghez, B. L. Klein, M. Morris and E. E. Becklin, *AstroPhys. J.* **509**, (1998) 678

[148] P. J. E. Peebles, *Principles of Physical Cosmology*, Princeton University Press, 1993

[149] S. W. Hawking, *Mon. Not. Roy. Astro. Soc.* **152**, (1971) 75

[150] S. W. Hawking and B. J. Carr, *Mon. Not. Roy. Astro. Soc.* **168**, (1974) 399

[151] J. H. MacGibbon and B. J. Carr, *AstroPhys. J.* **371**, (1991) 447

[152] S. W. Hawking, *Nature* **248**, (1974) 30

[153] S. W. Hawking, *J. Math. Phys.* **43**, (1975) 199

[154] B. J. Carr, *Observational and Theoretical Aspects of Relativistic Astrophysics and Cosmology*, Ed. J. L. Sanz and L. J. Goicoechea, World Scientific Publishing Co., 1985

[155] J. Yokoyama, *Astron. Astrophy.* **318**, (1997) 673

[156] D. N. Page and S. W. Hawking, *AstroPhys. J.* **206**, (1976) 1

[157] K. Maki, T. Mitsui and S. Orito, *Phys. Rev. Lett.* **76**, No. 19, (1996) 3474

[158] J. H. MacGibbon, *Phys. Rev.* **D 44**, (1991) 376

[159] H. A. Bethe and W. Heitler, *Proc. Roy. Soc.* **146**, (1934) 83

[160] C. Grupen, A. Böhrer and L. Smolík, *Particle Detectors*, Cambridge University Press, 1996

[161] J. D. Jackson, *Classical Electrodynamics*, John Wiley and Sons, 1975

[162] P. V. Ramana Murthy and A. W. Wolfendale, *Gamma-Ray Astronomy*, Cambridge University Press, 1993

[163] R. C. Fernow, *Introduction to Experimental Particle Physics*, Cambridge University Press, 1986

[164] C. W. Fabjan and H. G. Fischer, *Particle Detectors*, CERN-EP/80-27, 1980

[165] The IMAX Collaboration, J. W. Mitchell *et al.*, *Phys. Rev. Lett.* **76**, (1996) 3057

[166] The IMAX Collaboration, E. A. Bogomolov *et al.*, *Proc. 20th ICRC*, 1987

[167] The BESS Collaboration, A. Yamamoto *et al.*, *Advances in Space Research*, **14** (1994) 75

[168] The BESS Collaboration, Y. Ajima *et al.*, *Nucl. Instr. and Meth.* **A 443**, (2000) 71

[169] The BESS Collaboration, A. Moiseev *et al.*, *AstroPhys. J.* **474**, (1997) 479

[170] The BESS Collaboration, T. Saeki *et al.*, *Phys. Lett.* **B 422**, (1998) 319

[171] The BESS Collaboration, S. Orito *et al.*, *Phys. Rev. Lett.* **84**, No. 6, (2000) 1078

[172] The BESS Collaboration, T. Sanuki *et al.*, *AstroPhys. J.* **545**, (2000) 1135

[173] M. Fujikawa, *Ph.D. Thesis*, University of Tokyo, 2001

[174] The BESS Collaboration, Y. Asaoka *et al.*, *Phys. Rev. Lett.* **88**, (2002) 051102

[175] The WiZard/CAPRICE Collaboration, M. Boezio *et al.*, *AstroPhys. J.* **487**, (1997) 415

[176] The WiZard/CAPRICE Collaboration, M. Boezio *et al.*, *AstroPhys. J.* **518**, (1999) 457

[177] The WiZard/CAPRICE Collaboration, M. Boezio *et al.*, *AstroPhys. J.* **561**, (2001) 787

[178] The WiZard/CAPRICE Collaboration, M. L. Ambriola *et al.*, *Nucl. Phys. Proc. Suppl.* **B 78**, (1999) 32

[179] M. Buénerd, ISN Internal Note, May 21, 1998

[180] The AMS Collaboration, R. Battiston, *Proc. XIII Rencontres de Physique: Results and Perspectives in Particle Physics*, 1999

[181] The AMS Collaboration, J. Alcaraz *et al.*, *Phys. Lett.* **B 461**, (1999) 387

[182] The AMS Collaboration, V. Plyaskin, *Surv. High Energy Phys.*, **13**, (1998) 177

[183] M. Buénerd, ISN Internal Note, October 15, 1999

[184] The MASS Collaboration, M. Hof *et al.*, *AstroPhys. J.* **467**, (1996) L33

[185] The MASS Collaboration, G. Basini *et al.*, *Proc. 26th ICRC*, 1999

[186] The HEAT Collaboration, C. R. Bower *et al.*, *Proc. 26th ICRC*, Vol 5, 2000

[187] The HEAT Collaboration, A. S. Beach *et al.*, *Phys. Rev. Lett.* **87**, (2001) 271101

[188] The BESS Collaboration, H. Matsunaga *et al.*, *Phys. Rev. Lett.* **81**, No. 19, (1998) 4052

[189] The BESS Collaboration, K. Yoshimura *et al.*, *Phys. Rev. Lett.* **75**, No. 21, (1995) 3792

[190] The WiZard/CAPRICE Collaboration, D. Bergström *et al.*, *AstroPhys. J.* **534**, (2000) L177

[191] L. I. Schiff, *Quantum Mechanics*, McGraw-Hill, New York, 1955

[192] Rino Castaldi and Giulio Sanguinetti, *Ann. Rev. Nucl. Part. Sci.* **35**, (1985) 351

[193] G. Giacomelli, *Proc. 1989 International Workshop on Multiparticle Dynamics*, 1989

[194] G. Giacomelli and R. Giacomelli, *Il Nuovo Cimento* **24C**, (2001) 575

[195] W. E. Frahn, *Diffractive Processes in Nuclear Physics*, Oxford University Press, 1985

[196] U. Amaldi, M. Jacob and G. Matthiae, *Ann. Rev. Nucl. Sci.* **26**, (1976) 385

[197] E. Byckling and K. Kajante, *Particle Kinematics*, John Wiley & Sons, 1973

[198] B. Andersson, *The Lund Model*, Cambridge University Press, 1998

[199] R. P. Feynman and R. D. Field, *Phys. Rev.* **D 15**, (1977) 2590

[200] Cheuk-Yin Wong, *Introduction to High Energy Heavy-Ion Collisions*, World Scientific Publishing Co., 1994

[201] R. P. Feynman, *Photon-Hadron Interactions*, W. A. Benjamin, Inc., 1972

[202] K. Goulianos, *Phys. Rep.* **101**, (1983) 169

[203] F. James, *MINUIT, Function Minimization and Error Analysis*, CERN Program Library Long Writeup D506, 1998

[204] The NA44 Collaboration, J. Dodd *et al.*, *Nucl. Phys.* **A 590**, (1995) 523

[205] The NA44 Collaboration, A. Sakaguchi *et al.*, *Nucl. Phys.* **A 638**, (1998) 103

[206] The NA35 Collaboration, T. Alber *et al.*, *Eur. Phys. J.* **C2**, (1998) 643

[207] M. Jacob, *Phys. Rep.* **315**, (1999) 7

[208] S. Matinyan, *Phys. Rep.* **320**, (1999) 261

[209] A. M. Rossi *et al.*, *Nucl. Phys.* **B 84**, (1975) 269

[210] The BNL-AGS Collaboration, K. Shigak *et al.*, *Nucl. Phys.* **A 590**, (1995) 519c

[211] The STAR Collaboration, C. Adler *et al.*, *Phys. Rev.* **C 64**, (2001) 031601

[212] The ABCDHW Collaboration, A. Breakstone *et al.*, *Phys. Rev.* **D 30**, (1984) 528

[213] C. P. Singh and M. Shyam, *Phys. Lett.* **B 171**, (1986) 125

[214] The ABCDHW Collaboration, A. Breakstone *et al.*, *Il Nuovo Cimento* **102A**, (1989) 1199

[215] Z. Koba, H. B. Nielsen and P. Olesen, *Nucl. Phys.* **B40**, (1972) 317

[216] The UA5 Collaboration, G. J. Alner *et al.*, *Z. Phys.* **C 32**, (1986) 133

[217] Ch. Pfeifer, S. Roesler, and M. Simon, *Phys. Rev.* **C 54**, No. 2, (1996) 882

[218] M. A. Faessler, *Phys. Rep.* **115**, (1984) 1

[219] D. H. Brick *et al.*, *Phys. Rev.* **D 39**, (1989) 2484

[220] The WA97 and NA57 Collaborations, F. Antinori *et al. Eur. Phys. J.* **C18**, (2000) 57

[221] The Axial Field Spectrometer Collaboration, T. Åkesson *et al.*, *Phys. Lett.* **119B**, (1982) 464

[222] L. Derome *et al.*, *Phys. Lett.* **B 489**, (2000) 1

[223] L. Derome, M. Buénerd and Y. Liu, *Phys. Lett.* **B 515**, (2001) 1

[224] L. Derome and M. Buénerd, *Phys. Lett.* **B 521**, (2001) 139

[225] Y. Liu, L. Derome and M. Buénerd, *ISN Internal Report 01-012* (to be pubilished)

[226] M. Buénerd, *Int. J. Mod. Phys.* **A???**, (2002) ???

[227] C. Y. Huang, L. Derome and M. Buénerd, *Proc. 27th ICRC*, 2001

[228] C. Y. Huang, L. Derome and M. Buénerd, *ISN Internal Report 01-019* (to be pubilished)

[229] J. S. Perko, *Astron. Astrophy.* **184**, (1987) 119

[230] L. A. Fish, M. A. Forman and W. I. Axford, *J. Geophys. Res.* **78**, (1973) 995

[231] R. L. Langel, *International Geomagnetic Reference Field 1995 Revision, J. Geomag. Geoelectr.* **47**, (1995), 2551

[232] N. A. Tsyganenko, *J. Geophys. Res.* **100A**, (1995) 5599

[233] N. A. Tsyganenko and D. P. Stern, *J. Geophys. Res.* **101A**, (1996) 27187

[234] R. A. Matzner, *Dictionary of Geophysics, Astrophysics and Astronomy*, CRC Press, 2001

[235] A. E. Hedin, *J. Geophys. Res.* **96A**, (1991) 1159

[236] E. Eisenhandler *et al.*, *Nucl. Phys.* **B113**, (1976) 1

[237] S. P. Denisov *et al.*, *Nucl. Phys.* **B61**, (1973) 62

[238] K. Nakamura *et al.*, *Phys. Rev. Lett.* **52**, (1984) 731

[239] V. F. Kuzichev, Yu. B. Lepikhin and V. A. Smirnitsky, *Nucl. Phys.* **A576**, (1994) 581

[240] A. S. Carroll *et al.*, *Phys. Lett.* **B 80**, (1979) 319

[241] A. Baldini, Flaminio, W. G. Moorhead, D. R. O. Norrison and H. Schopper, *Total Cross-Sections for Reactions of High Energy Particles (Including Elastic, Topological, Inclusive and Exclusive Reactions)*, Landolt-Börnstein New Series, Vol. I/12b, Ed. H. Schopper, Springer-Verlag, 1988

[242] The AMS Collaboration, J. Alcaraz *et al.*, *Phys. Lett.* **B 472**, (2000) 215

[243] The AMS Collaboration, J. Alcaraz *et al.*, *Phys. Lett.* **B 484**, (2000) 10

[244] The AMS Collaboration, J. Alcaraz *et al.*, *Phys. Lett.* **B 494**, (2000) 19

[245] The HARP Collaboration, M. G. Catanesi *et al.*, *CERN-SPSC/99-35*, 1999

[246] The HARP Collaboration, M. G. Catanesi *et al.*, *CERN-SPSC/2000-029*, 2000

[247] The MIPP Collaboration, http://ppd.fnal.gov/experiments/e907/e907.htm

[248] T. K. Gaisser *et al.*, *Phys. Rev.* **D 54**, (1996) 5578

[249] The LEAP Collaboration, E. S. Seo *et al.*, *AstroPhys. J.* **378**, (1991) 763

[250] The BESS Collaboration, J. Z. Wang *et al.*, *Proc. 26th ICRC*, 1999

[251] The WiZard/CAPRICE Collaboration, T. Francke *et al.*, *Proc. 26th ICRC*, 1999

[252] N. M. Kocharian, M. T. Aivazian, Z. A. Kirakosian and A. S. Aleksanian, *JETP.* **30**, No. 1956, (243)

List of Figures

List of Tables